AN EXPERIMENTAL AND NUMERICAL INVESTIGATION OF SPRAY ATOMIZATION IN LIQUID-PROPELLANT ROCKET ENGINES

A THESIS SUBMITTED TO
THE GRADUATE SCHOOL OF NATURAL AND APPLIED SCIENCES
OF
MIDDLE EAST TECHNICAL UNIVERSITY

BY

SENEM GÜLMEZ

IN PARTIAL FULFILLMENT OF THE REQUIREMENTS
FOR
THE DEGREE OF MASTER OF SCIENCE
IN
AEROSPACE ENGINEERING

SEPTEMBER 2021

Approval of the thesis:

AN EXPERIMENTAL AND NUMERICAL INVESTIGATION OF SPRAY ATOMIZATION IN LIQUID-PROPELLANT ROCKET ENGINES

submitted by **SENEM GÜLMEZ** in partial fulfillment of the requirements for the degree of **Master of Science** in **Aerospace Engineering, Middle East Technical University** by,

Prof. Dr. Halil Kalıpçılar
Dean, Graduate School of **Natural and Applied Sciences** _____

Prof. Dr. İsmail Hakkı Tuncer
Head of the Department, **Aerospace Engineering** _____

Assoc. Prof. Dr. Harika Senem Kahveci
Supervisor, **Aerospace Engineering, METU** _____

Examining Committee Members:

Prof. Dr. Serkan Özgen
Aerospace Engineering, METU _____

Assoc. Prof. Dr. Harika Senem Kahveci
Aerospace Engineering, METU _____

Assoc. Prof. Dr. Nilay Sezer Uzol
Aerospace Engineering, METU _____

Prof. Dr. Almıla Güvenç Yazıcıoğlu
Mechanical Engineering, METU _____

Assist. Prof. Dr. Sıtkı Uslu
Mechanical Engineering, TOBB ETU _____

Date: 10.09.2021

I hereby declare that all information in this document has been obtained and presented in accordance with academic rules and ethical conduct. I also declare that, as required by these rules and conduct, I have fully cited and referenced all material and results that are not original to this work.

Name Last name : Senem Gülmez

Signature :

ABSTRACT

AN EXPERIMENTAL AND NUMERICAL INVESTIGATION OF SPRAY ATOMIZATION IN LIQUID-PROPELLANT ROCKET ENGINES

Gülmez, Senem
Master of Science, Aerospace Engineering
Supervisor : Assoc. Prof. Dr. Harika Senem Kahveci

September 2021, 276 pages

Since the liquid rocket engines have been widely used in various flight applications, improving the efficiency and stability of those engines have become important. To achieve efficient combustion in the chamber, the injector must be carefully designed and characterized well. Although impinging jet injectors are widely used in several systems, the previous researches focused on mainly the characterization of like-doublets, thus, there is still a lack of understanding on the atomization of the other types of impinging injectors. In this study, triplet and pentad type of impinging injectors are examined both experimentally and numerically. Parameters that affect the spray distribution, velocity and droplet statistics are analyzed and a group of injectors for both injector elements are tested with a mechanical patternator, a PDA, and a high-speed camera. It is seen that while some parameters enhance the results obtained by triplet injectors, they either deteriorate the results obtained by pentad injectors or do not have an obvious effect. For numerical results, a CLSVOF technique with the AMR method is used to simulate the spray characteristics of doublet, triplet and pentad injectors. Results indicate that this numerical method can be used to analyze the performance of these injectors with a reasonable accuracy compared to experimental data.

Keywords: Injector, Triplet, Pentad, PDA, CLSVOF

ÖZ

SIVI YAKITLI ROKET MOTORLARINDA PÜSKÜRTÜCÜ ATOMİZASYONUNUN DENEYSEL VE SAYISAL ARAŞTIRMASI

Gülmez, Senem
Yüksek Lisans, Havacılık ve Uzay Mühendisliği
Tez Yöneticisi: Doç. Dr. Harika Senem Kahveci

Eylül 2021, 276 sayfa

Sıvı yakıtlı roket motorları çeşitli uçuş görevlerinde sıklıkla kullanıldığı için, bu motorların verimini ve kararlığını artırmak önemli hale gelmiştir. Yanma odasında verimli bir yanmanın sağlanması için püskürtücünün dikkatle tasarlanması ve iyi karakterize edilmesi gerekmektedir. Çarpışan jet tipi püskürtücüler çeşitli sistemlerde kullanılmasına rağmen, önceki çalışmalar çoğunlukla eşlenik dubletlerin karakterizasyonuna odaklanmıştır; bu yüzden diğer tip çarpışan püskürtücülerin atomizasyonunun anlaşılması için yeterli bilgi halen bulunmamaktadır. Bu çalışmada, çarpışan püskürtücü olan triplet ve pentad tipi püskürtücüler deneysel ve sayısal yöntemlerle incelenmiştir. Sprey dağılımı, hız ve damlacık istatistiklerini etkileyen değişkenler incelenmiş ve iki tip püskürtücüden oluşan püskürtücü grubu mekanik paternatör, PDA ve hızlı kamera ile test edilmiştir. Bazı değişkenlerin triplet püskürtücülerden elde edilen sonuçları iyileştirirken, pentad püskürtücülerden elde edilen sonuçları ya kötüleştirdiği ya da pek etkilemediği görülmüştür. Nümerik sonuçlar için, AMR metodu eşliğinde CLSVOF tekniği kullanılarak dublet, triplet ve pentad püskürtücülerin sprey karakteristiklerinin benzetimi yapılmıştır. Sonuçlar, bu sayısal yöntemin deneysel

veriye göre kabul edilebilir bir doğruluk seviyesinde sonuç verecek şekilde bu tip püskürtücülerin performansının incelenmesinde kullanılabileceğini göstermektedir.

Anahtar Kelimeler: Püskürtücü, Triplet, Pentad, PDA, CLSVOF

To my family

ACKNOWLEDGMENTS

The author wishes to express her deepest gratitude to her supervisor Assoc. Prof. Dr. Harika Senem Kahveci for her guidance, advice, criticism, encouragements and insight throughout the research.

Roketsan Inc. is gratefully acknowledged for granting access to the test setup to carry out experiments in this research. Also, I gratefully acknowledge METU Center for Wind Energy (RÜZGEM) for granting access to computational resources to perform simulations.

This thesis would not have been possible without the help and support of my colleagues at Roketsan Inc. First of all, I would like to express my gratitude to Mahmut Murat Göçmen for his friendship, encouragements and support. I also gratefully thank Aykut Sever for his support and efforts in the experiments from the very beginning to the end. The technical assistance of Salih Toker is gratefully acknowledged. I would like to thank Oğuz Korkmaz and Tolga Kurşun for their friendship and encouragements. I am also thankful to my manager Sevda Açık Akkuş for her understanding and support.

I also gratefully thank my friends Çiğdem Özçelik, Pakize Kumtepe Temiz, Ümmehan Mert, Gizem Altındaş and Parisa Moradi for their support and understanding during all these tough years.

Words cannot express how grateful I am to my big family: my parents, my sister and brother, and also, my cousins for their encouragements, support and unconditional love. Last but not least, I would like to thank my nephew Onur Asaf Erdal for making my day brighter with his little smile.

TABLE OF CONTENTS

LIST OF TABLES

TABLES

LIST OF FIGURES

FIGURES

LIST OF ABBREVIATIONS

ABBREVIATIONS

AMR	:	Adaptive Mesh Refinement
CLSVOF	:	Coupled Level Set and Volume of Fluid
DPM	:	Discrete Phase Model
LOX	:	Liquid Oxygen
LS	:	Level Set
MR	:	Momentum Ratio
PDA	:	Phase Doppler Anemometry
PDF	:	Probability Density Function
PDPA	:	Phase Doppler Particle Analyzer
PLIF	:	Planar Laser Induced Fluorescence
Re	:	Reynolds Number
SMD	:	Sauter Mean Diameter
SST	:	Menter's Shear Stress Transport
VOF	:	Volume of Fluid
We	:	Weber Number

LIST OF SYMBOLS

SYMBOLS

a	:	spray coefficient
A	:	area, m^2
A_{cell}	:	cell area, m^2
A_i	:	orifice area, inner orifice, m^2
A_o	:	orifice area, outer orifice, m^2
A_{pat}	:	quadrat of each patternator cell, m^2
b	:	spray coefficient
c	:	spray coefficient
C_D	:	discharge coefficient
d	:	orifice diameter, m
D	:	droplet diameter, µm
D_{10}	:	mean droplet diameter, µm
D_{32}	:	Sauter Mean Diameter, µm
$D_{droplet}$	:	droplet diameter, µm
$\overline{D}_{droplet}$	:	average droplet diameter, µm
D_i	:	orifice diameter, inner orifice, m
D_o	:	orifice diameter, outer orifice, m
$D_{pinhole}$	:	pinhole diameter, m
D_ω	:	cross-diffusion term
e	:	Euler's number
e_{i2}	:	error indicator
$f_{excitation}$	:	excitation frequency, Hz
$\vec{F}_{sf}$	:	force arising from surface tension effects, N
F_1	:	blending function
F_2	:	blending function

G_ω	:	generation of ω
G_k	:	production of turbulence kinetic energy
H_φ	:	Heaviside scaling function
k	:	mixing efficiency parameter
k	:	turbulence kinetic energy
l	:	orifice length, m
$L_{h,\ turbulent}$	:	Hydrodynamic entry length for turbulent flow
L_{imp}	:	impingement distance, m
L_{met}	:	measured liquid height of the patternator cell, m
L_{pat}	:	side length of the patternator cell, m
$\dot{m}$	:	mass flow rate, kg/s
$\dot{m}_i$	:	mass flow rate, inner orifice, kg/s
$\dot{m}_o$	:	mass flow rate, outer orifice, kg/s
$\vec{n}$	:	local interface normal
N	:	droplet count
N_i	:	number of droplet with specified diameter
$\overline{N}$	:	normalized droplet count
P	:	pressure, N/m^2
Q	:	volume fraction of droplets
q	:	phase number
q		Rosin-Rammler distribution constant
r	:	gradient volume weight
R	:	function of n independent variables
S	:	strain rate magnitude
S_k	:	user-defined source term
S_ω	:	user-defined source term
U	:	x component of velocity, m/s
$\vec{u}$	:	velocity field, m/s
$\vec{v}$	:	velocity field, m/s

V	:	y component of velocity, m/s
$V_{droplet}$	:	velocity of droplet, m/s
V_i	:	velocity, inner orifice, m/s
V_o	:	velocity, outer orifice, m/s
$\overrightarrow{V_u}$	:	x component of velocity, m/s
$\vec{\bar{V}}_u$	:	normalized x component of velocity, m/s
$\dot{V}_i$	:	volumetric flow rate, inner orifice, m^3/s
$\dot{V}_o$	:	total volumetric flow rate, outer orifices, m^3/s
$\overline{w}$	:	normalized mass flux
w_{001}	:	normalization factor equivalent to mass flux, $kg/m^2/s$
$w_{average}$	:	average mass flux over the patternator, $kg/m^2/s$
w_i	:	mass flux, inner orifice, $kg/m^2/s$
w_{local}	:	local mass flux measured by using the patternator, $kg/m^2/s$
w_o	:	mass flux, outer orifice, $kg/m^2/s$
W	:	z component of velocity, m/s
X	:	Rosin-Rammler distribution constant
x	:	x-axis of Cartesian coordinate
Y_k	:	dissipation of k due to turbulence
Y_ω	:	dissipation of ω due to turbulence
y	:	y-axis of Cartesian coordinate
y'	:	y-axis, converted 45° in the counterclockwise direction
z	:	z-axis of Cartesian coordinate
z'	:	z-axis, converted 45° in the counterclockwise direction
α	:	half impingement angle, deg
α	:	volume fraction
α	:	interface thickness
δ	:	uncertainty
δ	:	surface Dirac function
Δ	:	difference

ε	:	dissipation rate
Γ_k	:	effective diffusivity of k
Γ_ω	:	effective diffusivity of ω
κ	:	local mean interface curvature
μ	:	viscosity, N.s/m^2
μ_t	:	turbulent viscosity, N.s/m^2
ρ	:	density, kg/m^3
ρ_{fluid}	:	density of fluid, kg/m^3
ρ_i	:	density, inner orifice, kg/m^3
ρ_o	:	density, outer orifice, kg/m^3
σ	:	surface tension coefficient, N/m
σ_k	:	turbulent Prandtl number for k
σ_ω	:	turbulent Prandtl number for ω
φ	:	level-set function
ω	:	specific dissipation rate
ω_R	:	overall uncertainty of function
ω_x	:	uncertainty interval of independent variable
∂	:	symbol used to denote partial derivatives
$\nabla^2 f$	:	undivided Laplacian of the selected solution

CHAPTER 1

INTRODUCTION

Since liquid rocket engines have been extensively used for both civil and military applications, there is an increasing effort on the research in the field of the understanding of the combustion mechanism in order to design stable and efficient engines. Liquid rocket engines are used to convert the thermal energy that is obtained from the chemical reactions between fuel and oxidizer at a high chamber pressure to kinetic energy in order to obtain thrust. As it is understood, the physical phase of propellants determine the design of the engine significantly, hence, the rocket engines are named accordingly. In many liquid propellant rocket engines such as the F-1 engine in Saturn V, the upper stage in VEGA, and the Agena upper stage engine (Gill, 1976), impinging injectors were used because of their simplicity in design and fabrication, compatibility with storable and LOX/hydrocarbon propellants (Mouis, 1995), and atomization and mixing performance. One of the most challenging design phases of a liquid rocket engine is to specify the injector type and design parameters, as injectors are the keys to have a stable and efficient combustion in the chamber. The main objective of the injector is to supply the fuel and oxidizer at predefined proportions so that the reaction between them can give the highest energy level possible. In addition to this, the pressure drop due to injectors will increase the stability of the engine. The propellant combinations must be in liquid-liquid or liquid-gaseous phases.

Liquid-propellant rocket engine injectors are categorized in three groups that are straight injectors, centrifugal injectors and coaxial injectors (Wang, 2016). The straight injectors are subcategorized as impinging and non-impinging ones. Impinging injectors are used to mix and atomize the propellants in rocket engines,

where the injected oxidizer and fuel-liquid streams impinge on one another at a predetermined distance from the injector surface and at a defined impingement angle (Won, 2002). Figure 1.1 shows the cross-section and bottom views of selected impinging injectors. Doublets are one of the commonly used impinging injectors. They are used in many rocket engines such as F-1 engine in Saturn V, A-7 engine in Redstone, booster and stage 2 engines in Titan 1 (Gill, 1976).

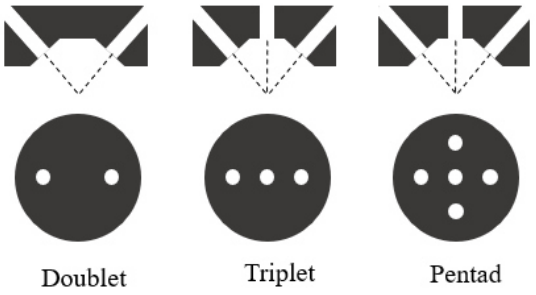

Figure 1.1. The Cross-section and Bottom View of Injectors

The like-doublet is the most commonly used doublet type. In like-doublet injectors, two streams of the same type of the propellant are injected on each other with a specified impingement distance and angle. At the impingement point, a liquid sheet spray is produced. The resultant spray forms in axial direction. Like-doublets are good at maintaining combustion stability and preventing reactive-stream demixing (Huzel, 1992). Despite these advantages, compared to the unlike-doublets with elements having different kinds of reactants, the like-doublets are not good at initial mixing. In order to increase the mixing of propellant combinations, hence, unlike-doublets can be used. In this type, a fuel stream is injected to oxidizer stream, and efficient mixing of propellants is obtained by the direct impact of propellants. In contrary to like-doublets, the disadvantage of this element is that the resultant spray may not be in the axial direction because of the momentum difference between the two jets. As a solution to this problem, symmetrical element configurations such as triplet and pentad injectors can be used. The triplet injector has three orifices one of which is placed at the center and the other two are placed at the outer with the same

geometric properties. The jets from the two outer orifices impinge on the central jet. Because of the symmetry of the outer streams, the axial spray can be obtained.

Table 1.1. Advantages and Disadvantages of Selected Types of Impinging Injectors (Gill and Nurick, 1976)

Injector Type	**Advantages**	**Disadvantages**
Unlike doublet	• Proven dependability • Good overall mixing • Simple to manifold • Extensively studied	• Blowapart with hypergolic propellants • Mixture ratio gradients • Sensitive to design tolerances • Performance sensitive to continuous throttling
Unlike triplet	• Good overall mixing • Axial spray distribution • Proven dependability	• Blowapart with hypergolic propellants • Sensitive to design tolerances • Performance sensitive to continuous throttling
Unlike pentad	• Good overall mixing • High performance • Applicable to very high or very low mixture ratio or density ratio	• Subject to blowapart with hypergolic propellants • Difficult to manifold • Wall compatibility problems • Performance sensitive to throttling • Tends to produce high heat flux to injector face
Like doublet	• Easy to manifold • Good mixing • Stable element • Not subject to blowapart • Proven dependability	• Requires increased axial distance to mix fuel and oxidizer • Sensitive to design tolerances

Another type of unlike impinging elements is the pentad which has four outer orifices located on the same circle and canted with a predefined impingement angle to the impingement point. The last orifice is located at the center, and the jets from the four outer orifices impinge on the central jet. Thus, the resultant spray is in axial direction and also symmetrical to the other two directions.

Atomization process is started with the transformation of liquid jets coming from injector orifices into liquid sheet. Oscillations on the liquid sheet cause the formation of ligaments. Then, these ligaments are broken into droplets (Ashgriz, 2016). In general, the outer orifices are designed to inject oxidizer and the center orifice injects fuel considering the high mixture ratio of propellant combinations. The spray characteristics such as droplet statistics, liquid wave, spray breakup length, and spray distribution are directly related to the injector element, therefore, these properties should be analyzed for the selected type of the injection element.

The advantages and disadvantages of impinging injector types are given in Table 1.1 taken from the study of Gill et al. (Gill and Nurick, 1976).

As a first step in designing an injector, the mixture ratio of the propellants and chamber pressure must be specified. The injector type is selected for the given mixture ratio of the propellants. Also, the desired pressure drop is specified depending on the combustion chamber pressure. 15 – 20% of the chamber pressure is suggested for the injector pressure drop. Mass flow rate of an orifice is calculated using the equation given in Equation *(1)*:

$$\dot{m} = AC_D\sqrt{2\rho\Delta P} \qquad (1)$$

In Equation *(1)*, $\dot{m}$ is the mass flow rate of the fluid, A is the orifice area, C_D is the discharge coefficient, ρ is the density of the fluid and ΔP is the pressure drop along the orifice. The area of the orifice is calculated by Equation *(2)*.

$$A = \pi\frac{d^2}{4} \qquad (2)$$

In Equation *(2)*, d is the orifice diameter. The orifice diameter d, and orifice length-to-diameter ratio, l/d, are determined simultaneously since the discharge coefficient of the orifice, C_D, is the function of both the velocity which is derived from the orifice diameter and length-to-diameter ratio. Several empirical relations are used to calculate the discharge coefficient, which is given in Table 1.2.

Table 1.2. Empirical Correlations of Discharge Coefficient of a Plain Orifice

Relation	l/d Ratio	Re	Source
$C_D = \dfrac{Re^{5/6}}{\dfrac{17.11l}{d} + 1.65Re^{0.8}}$ *(3)*	1.5-17	550-7000	(Nakayama, 1961)
$C_D = \left[1.23 + \dfrac{58\left(\dfrac{l}{d}\right)}{Re}\right]^{-1}$ *(4)*	2-5	100-150000	(Asihmin, Geller, Skobel'cyn, 1961)
$\dfrac{1}{C_D} = \dfrac{1}{C_{Dmax}} + \dfrac{20}{Re}\left(1 + 2.25\dfrac{l}{d}\right)$ *(5)* $C_{Dmax} = 0.827 - 0.0085\dfrac{l}{d}$ *(6)*	2-10	10-20000	(Lichtarowicz, Duggins, Markland, 1965)

The velocity of the liquid jets and Re and We numbers are determined upon the specification of the orifice diameter and the l/d ratio. The next step in the injector design is to specify the impingement angle and impingement distance. This selection is conducted in a way that the optimum distribution, mixing and SMD levels are achieved. If the desired efficiency is not obtained, the orifice diameter and the l/d ratio selections are conducted again.

1.1. Aim of This Study

Since the combustion efficiency, hence the performance of the engine is directly related to the spray quality produced by the injectors, spray characteristics of impinging injectors have been widely studied over the years. However, most of the

previous studies focused on especially doublet injectors, and there still remains the lack of understanding of physical mechanism of other impinging injector types. Therefore, the objective of this study is to investigate the spray characteristics of triplet and pentad type of impinging injectors with respect to various design parameters through experiments and numerical simulations.

1.2. Outline of the Thesis

This thesis consists of six chapters whose contens are given below.

Chapter 1 gives a brief overview about liquid propellant rocket engines. Atomization and combustion processes in the combustion chamber are explained. The advantages and disadvantages of various types of injectors are discussed. The objective of this thesis is explained.

Chapter 2 presents a comprehensive literature review on experimental and numerical studies on impinging injectors. The mechanical and optical measurements systems of the spray characteristics are discussed with flow visualization methods. The numerical methods used for simulating the primary and secondary atomization are mentioned.

Chapter 3 provides information on the test setup that is used in the current study. It also presents the accuracy of the measurement of the flow components and uncertainty analysis of the presented experimental data.

Chapter 4 presents the test matrix conducted as a part of this thesis in order to investigate the effects of the selected design parameters on the spray characteristics. The results of these tests are also given in this chapter.

Chapter 5 discusses the numerical techniques and models that are used to simulate the selected test cases. In addition, the details of the validation cases and the comparison of all analyses with experimental data are given.

Chapter 6 briefly summarizes all work done in this thesis and gives some recommendation for future work.

CHAPTER 2

LITERATURE REVIEW

The combustion efficiency, thus, the performance of the engine is directly related to the spray quality produced by the injectors, hence, spray characteristics of impinging injectors have been widely studied over the years. There have been many experimental and numerical studies performed to investigate this topic over the years up to this date. In this section, first the experimental studies will be summarized, which will be later followed by a discussion on research that used numerical techniques.

Several experimental techniques are used in spray characterization. In 1953, Rupe studied the liquid phase mixing of a pair of impinging jets and obtained some ground rules for the design of rocket engine injectors (Rupe, 1953). Heidmann et al. studied the effects of increased jet velocity using the sprays of two impinging jets (Heidmann, Priem and Humphrey, 1957). They revealed that when the velocity increases, the spray pattern changes from a closed liquid rim to the waves of drops. At a fully developed spray, the frequency of the waves increased with injection velocity and decreased with impingement angle. On the other hand, it did not change with jet diameter or impingement length. In 1959, Elverum and Morey generated empirical correlations to obtain the optimum mixture-ratio distribution of doublet, triplet, and pentad types of injector element (Elverum and Morey, 1959). In 1972, Hoehn et al. studied the effects of non-circular orifice geometries and compared the results they obtained with those from the circular ones in terms of mixing efficiencies (Hoehn, Rupe and Sotter, 1972). A comprehensive study was published in 1985 by Ferrenberg et al. in order to investigate the atomization and mixing performance of several injector types (Ferrenberg, Hunt and Duesberg,

1985). An important conclusion of the study is that the Elverum-Morey criteria, which states that optimum mixture-ratio distribution for triplet injectors is obtained when the correlation defined in Equation *(7)* reaches 0.66, are not valid for triplets with sharp-edged entry and low L/D orifices. It was recommended that the relation in Equation *(8)* should be maximized to obtain the best mixing efficiency. This is possible by increasing momentum at the outer orifices that is a function of orifice diameter, density and velocity of the propellant used.

$$k = \left(\frac{\dot{m}_o}{\dot{m}_i}\right)^2 \cdot \frac{\rho_i}{\rho_o} \cdot \left(\frac{A_i}{2A_o}\right)^2 \quad (7)$$

$$k = \left(\frac{D_o}{D_i}\right)^{0.29} \cdot \left(\frac{\rho_o}{\rho_i}\right)^{0.56} \cdot \left(\frac{V_o}{V_i}\right)^{0.25} \quad (8)$$

Vassallo et al. conducted experiments to analyze the effect of flow rate on two and four impinging jet injectors (Vassallo, Ashgriz, and Boorady, 1992). The tests of two-jet injector showed that with the increase of flow rate, the droplet diameter and volume flux were increased along the spray fan in contrary to the decrease at the center. The experiments involving four jet injectors showed that up to a critical flow condition that is $Re = 4750$, the droplet diameters and velocities increase with flow rate. Further increase caused a decrease in droplet diameters and velocities in the measurement area other than the center of the spray fan. Ryan et al. (Ryan, Anderson, Pal, Santoro, 1993) investigated the effects of flow properties and injector geometric parameters on the droplet diameter, sheet break-up length and surface wave of like-doublet injectors. Break-up length and wave results were obtained from images taken by a high speed camera. The velocity and diameter of the droplets were taken by a Phase Doppler Particle Analyzer (PDPA). Ashgriz et al. used a linear patternator consisting of a group of 20 square brass tubings with a side length of 3.175 mm each, and analyzed the mixing mechanisms of different injector sprays utilizing a food coloring dye (Ashgriz, Brocklehurst, Talley, 1995).

Kang et al. used a Phase Doppler Particle Analyzer (PDPA) in order to study the effects of mixture ratios on droplet size and velocity distributions obtained from split-triplet injectors, and they derived some empirical correlations predicting the

mean diameter distributions (Kang, Lee, Kwon, Oh and Yu, 2002). Lai et al. performed a study on the spray characteristics such as spray pattern, mean droplet size and mixture ratio of an unlike-doublet impinging-jet at different jet velocities (Lai, Huang and Chu, 2004). They studied the effects of momentum ratio on mixture ratio distribution from unlike-doublet injectors by using a mechanical patternator. They also obtained SMD measurements by using a laser diffraction-sizing device, as well as performing flow visualization by using a single exposure camera and a stroboscope with appropriate lighting. It was concluded that unlike-doublet spray pattern has similarity to like-doublet ones. Droplet sizes decrease with increase in velocity of fluid jets. Also, mixture ratio and deviation angle of the resultant spray agree well with the theoretical calculations. Cho et al. focused on the effects of the orifice diameter ratios of the unlike-doublet and split-triplet injectors on the mixing performance by using immiscible fluids. They used a 14 x 14 cm quadrilateral plain-faced collector that was divided into 400 equal squares (Cho, Lee and Yoon, 2004).

Another study with four-jet (split triplet) impinging injectors was carried out by Jung et al. in 2005 (Jung, Lim, Yoon and Koo, 2005). Based on their experiments using triplet and split triplet injectors, they concluded that despite their spray characteristics being more sensitive to momentum ratio compared to those of split-triplets, the triplets were also performing better at mixing than the latter. Another finding from this study was that increasing the impinging angle led to a more uniform mixing of the injector sprays, however, an excessive increase caused triplets to have reduced mixing efficiency. In 2006, Jung et al. studied the breakup characteristics of a like-doublet injector in terms of breakup length and wavelength that are functions of orifice entrance shape, propellant type, impingement angle, injection pressure and velocity (Jung, Khil and Yoon, 2006). It was found that turbulent flow decreases the wavelength of the liquid sheet and increases the break-up length.

In 2015, Sweeney et al. studied the effects of impingement angle and distance of like-doublet injectors and jet velocity on spray characteristics by using high-speed

cameras for flow visualization and a two-component PDPA for droplet statistics (Sweeney and Frederick, 2015). In another study, Sweeney et al. also investigated the effects of the jet break-up length-to-impingement distance ratio of like doublet injectors on primary atomization characteristics (Sweeney and Frederick, 2016). It was observed that when the jet break-up length-to-jet impingement distance ratio was greater than 1.5, the break-up mechanism was considerably affected by this ratio, and depending on the Weber number, a ruffled sheet or fully-developed pattern was seen. In the case where the jet break-up length-to-jet impingement ratio was equal to 1, an unsteady flat sheet was seen, which was sensitive to the disturbances caused by the combustion chamber and resulted in fluctuations. When the ratio was smaller than 1, they observed that only large droplets passed and collided at the impingement point and flat sheet was not obtained, which is considered as poor atomization and mixing of the spray.

Indiana et al. looked into the drop size distribution of two impinging jets over a wide range of Reynolds number and Weber number by using a PDA (Indiana, Bellenoue and Boust, 2015). Inoue et al. investigated cold-flow characterization of injectors to determine the characteristic velocity of thrusters by using a mechanical patternator and an absorbance spectrometer (Inoue, Fujii and Daimon, 2017). The spectrometer was calibrated with several combinations of a colored oxidizer simulant and a fuel simulant before the test to be able to determine the local mixture ratio of the liquid inside the test tubes. Additionally, they visualized the injector spray by the help of a high-speed camera and investigated the fuel and oxidizer distribution on a specified plane using the PLIF technique. It was observed that the SMD is inversely proportional to injection pressure and impingement angle. In 2017, Atyam et al. studied the characterization of different additive-manufactured injector concepts by using an optical patternator and a dual PDA system to measure droplet diameters (Atyam and Sojka, 2017).

Xia et al. performed a series of experiments (Xia, Khezzar, Alshehhi and Hardalupas, 2017). They used a high-speed camera and a PDA in their experiments to investigate the droplet size and velocity characteristics of a water-air impinging-

jet atomizer by changing the water jet velocity, airflow rate, and impinging angle (Xia, Khezzar, Alshehhi and Hardalupas, 2017). In a follow-up study, they studied impinging opposed jets with and without impinging air jets in order to investigate the effects of flowrates on the droplet size and velocity distributions (Xia, Khezzar, Alshehhi and Hardalupas, 2018). They found that increase in water flowrates causes increase in SMD while increase in air flowrate leads to smaller droplets, hence smaller SMD. In a third study, they also analyzed the flow regimes and break-up length of two impinging jets as a function of Reynolds number, velocity and impingement angle (Xia, Khezzar, Bojanampati and Molki, 2019). Break-up regimes were in agreement with those observed in previous studies. The measured values of break-up length were found smaller than the theoretical values.

In another recent study, Kiaoulias et al. conducted a study in order to investigate the effects of inlet orifice geometry, diameter and length-to-diameter ratio on the pressure drop and breakup length (Kiaoulias, Travis, Moore and Risha, 2019). The study showed that increase in length-to-diameter ratio leads to increase in breakup length. Pressure drop is proportional to length-to-diameter and inversely proportional to diameter. They also pointed out that diameter of 0.51 mm and length-to-diameter ratio of 5 resulted in larger pressure drop and longer break-up length with a sharp-edge orifice instead of a chamfered one.

All of the above studies showed that although the interest in understanding the physics of impinging jet atomization with experimental methods has been increasing since 1950s, the studies mainly gathered around on several aspects of characterization of doublet injectors, but only few of them focused on the fundamental spray characterization of triplet injectors, and less number of studies exists with pentad injectors.

Some spray atomization studies have been carried out both experimentally and numerically, while some of them have purely focused on the numerical aspects. Arienti et al. (Arienti, Soteriou, Eckett, Sussman and Jensen, 2013) developed a numerical method to simulate the liquid flow, breakup and atomization by the

Coupled Level Set and Volume of Fluid (CLSVOF) method with the Adaptive Mesh Refinement (AMR) technique. They selected Ryan's low and high velocity jets cases for comparisons (Ryan, Anderson, Pal, Santoro, 1993) which were explained in the previous section. They also compared the particle density distribution of different refinement levels with the experimental data given in the study of Anderson et al. (Anderson, Ryan, Santoro, Hewitt, 1995). Results indicated that the smaller mesh size improved the computational accuracy.

Cenik et al. (Cenik, Suer, and Uslu, 2019) analyzed the effects of different meshes on the spray characteristics of like-doublet impinging jet injectors by using the VOF method in star CCM+ with a user-defined adaptive mesh refinement. They compared their findings with the experiment results of Anderson et al (Anderson, Ryan, Santoro, and Hewitt, 1995). In addition, Cenik et al. (Cenik, Suer, and Uslu, 2019) performed simulations for triplet injectors with different inlet velocity conditions and indicated that an increase in velocity leads to formation of smaller droplets.

Chen et al. (Chen and Yang, 2012) performed a numerical study on simulation of the formation and breakup of the impinging jets at different Reynolds and Weber numbers by using a Volume of Fluid (VOF) method with AMR. They showed that the numerical results are in good agreement with experimental results.

Another study was conducted by Zheng et al. (Zheng, Nie, Feng and Wu, 2015) to analyze the influences of the impingement angle on two like-doublet configurations experimentally and to compare the results of the numerical method developed with the experimental data. In the numerical study, the Coupled Level-Set and Volume of Fluid method is used in order to capture the interface between liquid and gas. Evaluation criterion was selected as the Sauter Mean Diameter (SMD). The results indicate that both SMD values of experimental data and numerical results decrease slightly when the impingement angle increases. However, the numerical results had an error varying between 11% and 35% compared to the experimental results.

Balasubramanian et al. (Balasubramanian, Kumar, Nakod, Schütze and Rajan, 2020)

analyzed the break-up mechanism and particle distribution of the doublet injector case studied by Zheng et al. (Zheng, Nie, Feng and Wu, 2015). They used the coupled VOF and Discrete Phase Model (DPM) with the AMR technique. It was shown that the SMD values are similar to those obtained by Zheng et al. (Zheng, Nie, Feng and Wu, 2015). However, it was seen that the velocity magnitudes obtained along the spray centerlines for the two impingement angles were calculated differently by each numerical method.

CHAPTER 3

EXPERIMENTAL SETUP

In this thesis, a series of experiments were performed using different types of injectors. The facilities of Roketsan Inc. were set up and used for this research. In order to supply the required mass flow rate to injectors for selected test cases, a feeding system pressurized by gas tanks is used. As a part of PDA, transmitting and receiving optics on a traverse system is used for the velocity and droplet statistics of the spray on the measurement plane. Since the traverse system can move in three directions, it enables the measurement to be obtained point by point in the plane. Also, a monosize droplet generator is used for the control of PDA calibration. In addition, a mechanical patternator is used for measurements of mass flux distributions. In the test setup, a video camera and a high-speed camera are used. The former is used for the spray angle measurements and the latter is used for the flow visualization of the selected test case. The details of test setup will be given in the following sections.

3.1. Feeding System

The schematic of the feeding system is given in Figure 3.1. The system has two similar feeding lines constructed separately in order to provide different mass flow rates to the inner and outer orifices. The gas tanks are filled with highly-pressurized nitrogen, and the pressure is reduced via a pressure regulator to a level that is required to achieve the desired mass flow rates for the tests. The water tank is separated from the pneumatic part of the system by a solenoid valve, while the high-pressure tank and the regulator are protected from the retrace of the water with the help of a one-way check valve. Relief valves that open when a certain pressure level is reached are located above the water tanks so that they could be

kept from the higher pressure than the design value. The solenoid valves are located below the water tanks to isolate them from the remaining part of the feeding system, which includes filters, calibrated flow meters needle valves that are used for sensitive regulation of flow, and finally the ball valves placed at the top of the injectors.

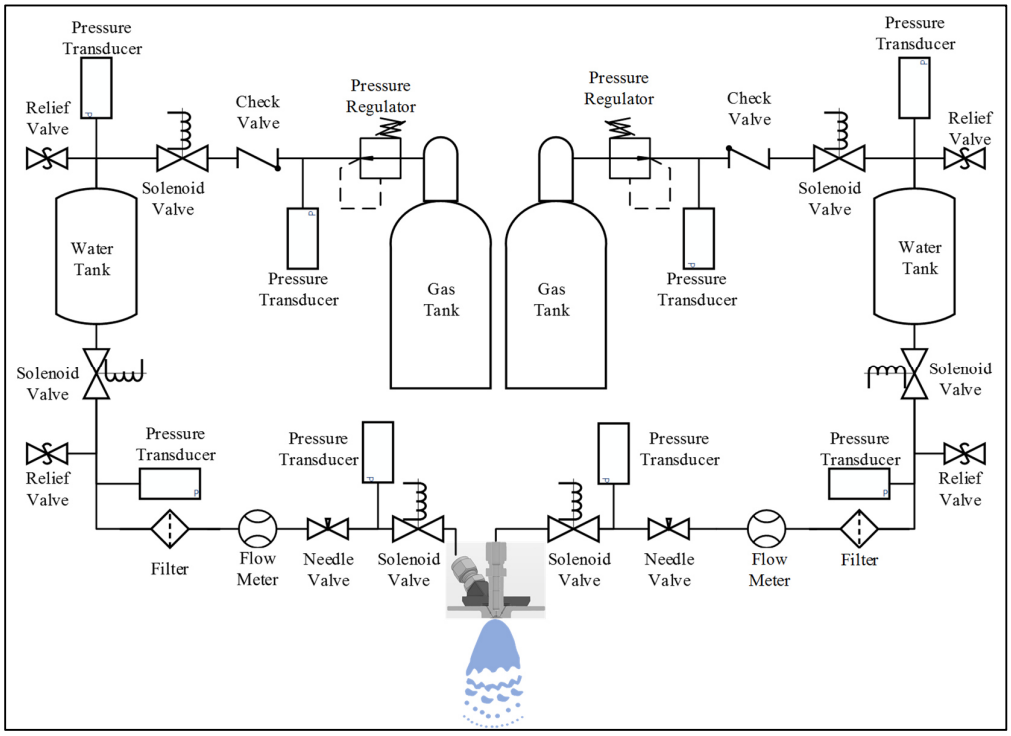

Figure 3.1. The Schematic of Feeding System

3.2. PDA

The velocity, droplet count and the Sauter Mean Diameter (SMD) distribution measurements are conducted at 30 mm below the impingement point by a three-dimensional PDA system manufactured by Dantec Dynamics. It can be seen in Figure 3.2 that the transmitting and receiving optics are mounted on a traverse system that moves in three directions across the spray to monitor the changes in the

properties of interest within the volume of the spray. In the system, three separate laser sources are used to generate three laser beams with wavelengths of 514.5, 488 and 532 nm. Each laser beam is at first split into two beams, followed by a 40 MHz of frequency shift applied to one of the beams in each pair in order to capture the velocity of the droplets in the opposite direction. The two pairs of the laser beams are projected by the horizontal transmitter. The two transmitters make the vertical and horizontal beams coincide at a point 500 mm away from the surface. The third pair of beams is projected by the other transmitter that is aimed at an angle of 20° to the horizontal axis. The intersection of the laser beams from the two transmitters produces a measurement volume. The receiver is mounted at an angle of 70° to the vertical axis in order to capture the light scattering from the droplets inside the probe volume, and the signals obtained are processed by the BSA P600 signal processor. The BSA Flow Software 6.50 is used to tabulate the measurement results.

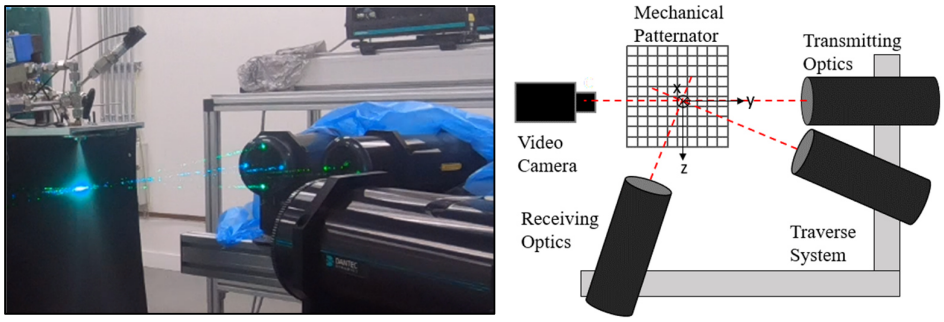

Figure 3.2. The PDA and Schematic of the Measurement System

3.3. Patternator

A mechanical patternator given in Figure 3.3 is placed at 80 mm and 480 mm below the impingement point of the injector sprays, for the measurement of mass flux distribution. The 100 mm x 100 mm sized patternator consists of 100 plexiglass tubes with a length of 30 cm each. An additively manufactured separator

is placed above the plexiglass tubes in order to decrease their wall thickness from 4 mm to 0.3 mm so that it will not disturb the injector sprays at the measurement plane.

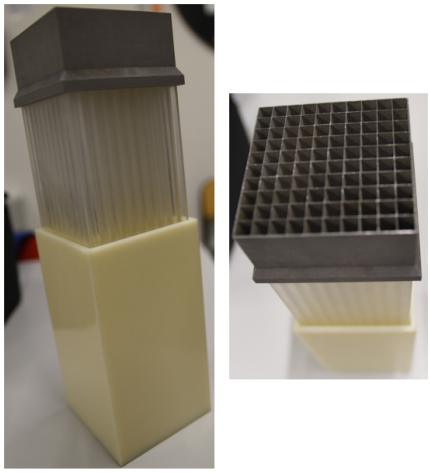

Figure 3.3. Mechanical Patternator

Patternator measurements are conducted for 2 different time durations. For each time duration two tests are carried out. In order to calculate the mass flux, first the average of two tests is found for both time durations. Then, the difference between the two averaged values is calculated and used for mass flux calculation.

3.4. High-Speed Camera

The i-Speed 716-R camera was used for the flow visualization of the primary atomization of sprays. The i-Speed 716-R is a colored camera with a memory of 96 GB and it has a 2048 × 1536 pixel sensor resolution with a pixel size of 13.5 µm. This enables the camera to take 5315 fps during 4.1 seconds with the highest resolution (iX Cameras, 2020). It has a global exposure shutter that exposes all pixels of the array, simultaneously, enabling to capture the moment. The minimum allowable shutter time is 1µs that can be reduced to 289 ns in fast mode. The high-speed camera test setup is given in Figure 3.4.

Figure 3.4. High-Speed Camera

In this study, the high-speed camera is used with a resolution of 5000 fps @ 1536 × 1536 at a shutter speed of 1/100000 sec. Also, a Nikon Nikkor AF-S DX Nikkor 35mm f/1.8G lens was used with the high-speed camera. This lens has a focal length of 35 mm, view angle of 44°, minimum aperture of f/22 and maximum aperture of f/1.8 (Nikon).

3.5. Video Camera

A Nikon D750 video camera installed next to the mechanical patternator was used to visualize the sprays for the measurements of spray angles in the same setup. The lens used with the camera was Tokina 24-70mm f/2.8 Pro FX. The focus length is 24-70 mm. The minimum aperture is f/22 and the maximum aperture is f/2.8. The angle of view is 84°-34°29' (Tokina).

3.6. Monosize Droplet Generator

For the calibration of the PDA system, a monodisperse droplet generator with a signal generator was used. The model of the droplet generator is MTG-01-G3 which was manufactured by FMP Technology. The model of the signal generator is TOELLNER TOE 7404. The droplet generator given in Figure 3.5 can produce droplet chains with a very small diameter depending on the pinhole diameter, operating pressure, working fluid and excitation frequency.

The equations used for the calculation of the velocity and the diameter of droplets are given in Equation *(9)* and Equation *(10)*, respectively:

$$V_{droplet} = \sqrt{\frac{2\Delta P}{\rho_{fluid}}} \qquad (9)$$

In Equation *(9)*, $V_{droplet}$ is the velocity of the droplets, ΔP is the pressure drop along the droplet generator, ρ_{fluid} is the density of the fluid.

$$D_{droplet} = \left(\frac{3V_{droplet}D_{pinhole}^2}{2f_{excitation}}\right)^{\frac{1}{3}} \qquad (10)$$

In Equation *(10)*, $D_{droplet}$ is the diameter of the droplets, $D_{pinhole}$ is the diameter of the pinhole used in the monosize droplet generator, $f_{excitation}$ is the excitation frequency that is used for the monosize droplet generator.

Figure 3.5. Monodisperse Droplet Generator

3.7. Results of Monosize Droplet Generator

In order to test the calibration of PDA system, several tests were conducted by using monosize droplet generator since the diameter and the velocity of droplets

coming from this system are known. For these tests, parameters for the droplet generator are given in Table 3.1.

Table 3.1. Parameters of Droplet Generator

Working Fluid	**Pinhole Diameter**	**Pressure Drop**	**Excitation Frequency**
Water	50 µm	6.1 bar	180000 Hz

Two PDA tests were conducted for the measurements. Results were evaluated over 10000 samples and are given in Table 3.2.

Table 3.2. Droplet Generator PDA Measurement Results

	Droplet Generator	**Test 1**	**Test 2**	**Unit**
$V_{droplet}$	34.96	34.71	34.84	m/s
$\overline{D}_{droplet}$	89.98	90.34	88.33	µm

Table 3.2. shows the calculated velocity and size of the droplet and the results of the tests. Since the calculations are based on the pressure measured at the inlet of the droplet generator, expected velocity and diameter of droplets have some uncertainties, which is derived in Section 3.9.

The repeatability of the PDA measurements based on these two experiments are calculated as 0.3% and 2.2% for velocity and diameter, respectively.

The density histograms of Test 1 and Test 2 are given in Figure 3.6. Similar distribution trends were seen for these measurements. Between 80% and 90% of all measurements have almost the same droplet size for both tests.

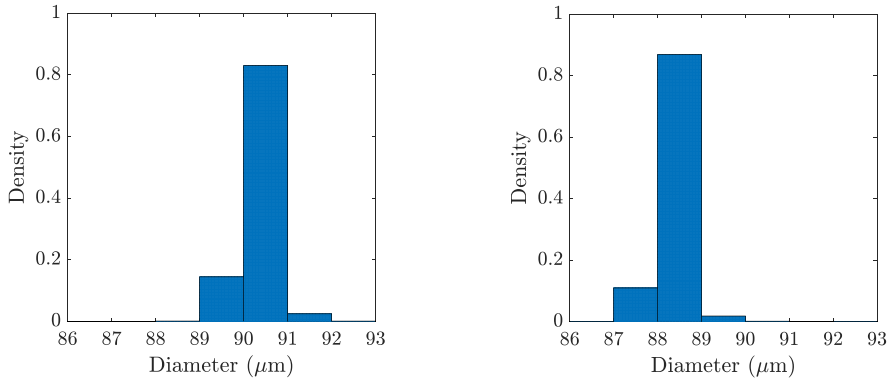

Figure 3.6. Density Histograms of Diameter Measurements

3.8. Test Injectors

In this section, the details of the test injectors will be discussed. The cross-section of an injector is given in Figure 3.7 in order to define the selected parameters.

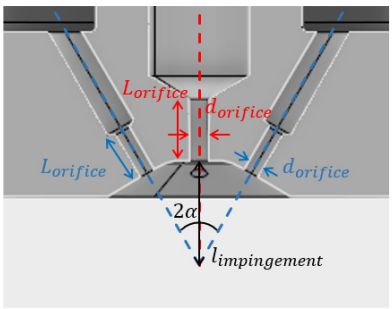

Figure 3.7. Cross-section of an Injector

In triplet and pentad injectors, there is one orifice at the center and at the outer, two orifices are positioned with an angle of 180° on the same plane with respect to the inner orifice. In pentads, there are four outer orifices that are located with an angle of 90°. In order to eliminate the secondary effects arising from the differences in the orifices, for this thesis study, all orifices that are in the center and at the outer parts are identical in each test configuration in terms of their diameters and lengths.

Hence, all orifices can be defined only one common diameter and length. The orifice diameter is one of the design parameters that was investigated in this research.

Table 3.3. Test Parameters of Injectors

Parameters	**Range**	**Code**
Injector Type	Triplet / Pentad	T / P
Impingement Angle	45° / 60° / 90°	45 / 60 / 90
Orifice Diameter	0.8 / 1.0 / 1.2 mm	08 / 10 / 12
Orifice l/d Ratio	3 / 5 / 8	3 / 5 / 8
Impingement Distance	5 / 8 / 10 mm	5 / 8 / 1

Another parameter is the ratio of the orifice length to the orifice diameter. The distance from the orifice surface to the impingement point is the third design parameter. And finally, the angle between outer orifices is defined as impingement angle and it is the last geometric parameter that was examined.

The ranges of selected test parameters are given in Table 3.3. Also, injectors are defined with their geometric parameters and named in the given order from top to bottom.

In addition, the effect of the total momentum ratio of the outer orifices to the inner orifice is investigated and this parameter will be called as the momentum ratio herefrom.

18 injector configurations were manufactured according to the parameter range given in Table 3.3. The list of the tests performed in this study is given in Table 3.4. Further details will be given in CHAPTER 4.

The test injectors can be seen in Figure 3.8.

Table 3.4. List of Tests Performed With Injectors

	Code	MR	Patternator	PDA	Camera	High-Speed Camera
01	T601055	1.99	X	X	X	X
02	T601055	4.32	X	X	X	
03	T601055	8.34	X	X	X	
04	T601055	12.91	X	X	X	
05	T601058	12.70	X	X	X	
06	T601051	12.86	X	X	X	
07	T601035	13.01	X	X	X	
08	T601085	12.96	X	X	X	
09	T601255	12.75	X	X	X	
10	T600855	12.67	X	X	X	
11	T451055	2.20	X	X	X	
12	T901055	2.07	X	X	X	
13	T901055	3.19	X	X	X	
14	T901055	6.21	X	X	X	
15	T901055	8.93	X	X	X	
16	T901055	11.73	X	X	X	
17	P601055	4.17	X	X	X	
18	P601055	16.05	X	X	X	
19	P601058	16.03	X	X	X	
20	P601051	15.98	X	X	X	
21	P601035	16.06	X	X	X	
22	P601085	16.27	X	X	X	
23	P601255	16.32	X	X	X	
24	P600855	16.15	X	X	X	
25	P451055	16.03	X	X	X	
26	P901055	16.04	X	X	X	

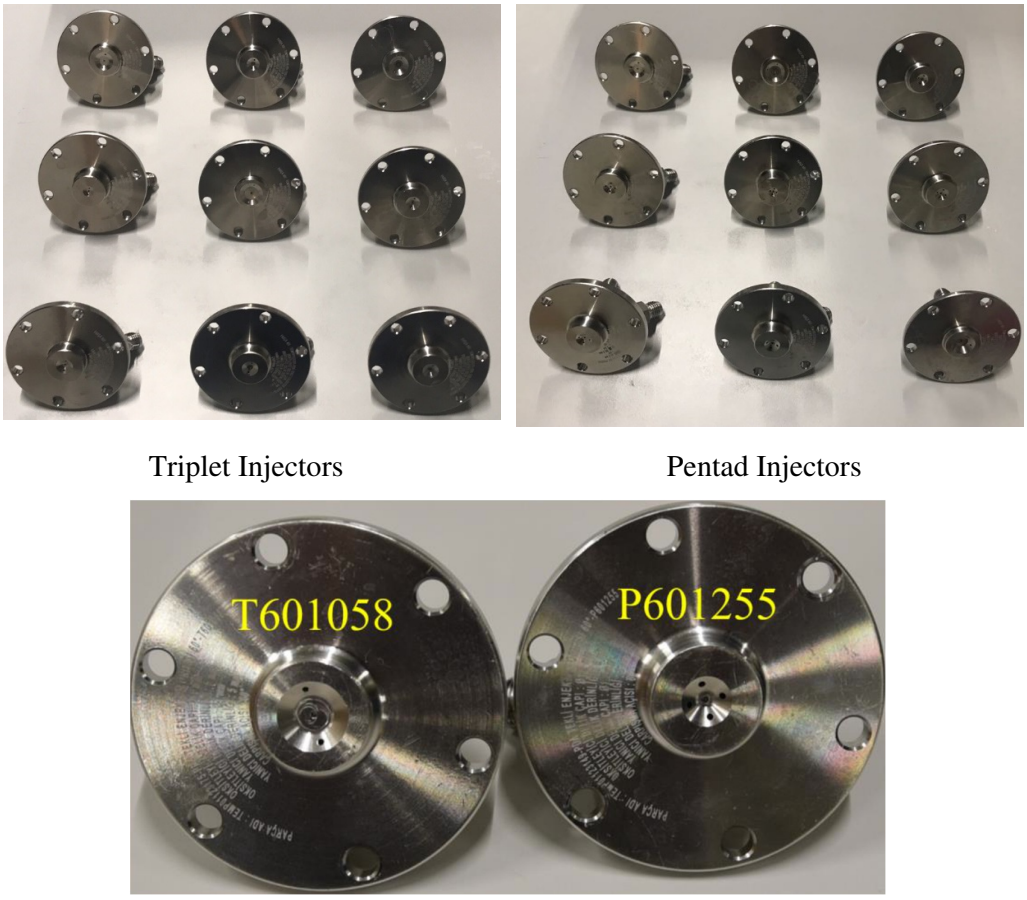

Triplet Injectors Pentad Injectors

Figure 3.8. Test Injectors

3.9. Uncertainty Analysis

Uncertainties of measurement devices propagate through the experimental data since several combinations of them are used in obtaining the results. In this section, the methods of calculating the uncertainty estimates for each parameter are given. Uncertainty calculations are done by using the error propagation technique defined by Kline and McClintock (Kline and McClintock, 1953) and are given in *(11):*

$$\omega_R = \sqrt{\left(\frac{\partial R}{\partial x_1}\omega_{x_1}\right)^2 + \left(\frac{\partial R}{\partial x_2}\omega_{x_2}\right)^2 \ldots + \left(\frac{\partial R}{\partial x_n}\omega_{x_n}\right)^2} \qquad (11)$$

Here, R is the function of n independent variables, ω_x represents the uncertainty interval of independent variables and ω_R shows the overall uncertainty of function R. In this section, uncertainty analyses of results were derived by using the error propagation technique derived above.

3.9.1. Velocity and Droplet Diameter Calculations of Monosize Droplet Generator

Recalling the equation of the velocity of droplets Equation *(9)* generated by the monosize droplet generator,

$$V_{droplet} = \sqrt{\frac{2\Delta P}{\rho_{fluid}}} \qquad (9)$$

By using the error propagation technique, the uncertainty of the velocity is calculated as given in Equation *(12):*

$$\omega_{V_{droplet}} = \sqrt{\frac{1}{2\rho_{fluid}\Delta P}}\,\omega_{\Delta P} \qquad (12)$$

Here, $\omega_{V_{droplet}}$ is the uncertainty is the velocity of the droplets. In the same way, the uncertainty of the droplet diameter can be obtained. Recalling Equation *(10)*,

$$D_{droplet} = \left(\frac{3V_{droplet}D_{pinhole}^2}{2f_{excitation}}\right)^{\frac{1}{3}} \qquad (10)$$

The uncertainty of the droplet diameter is calculated by using Equation *(13)*,

$$\omega_{D_{droplet}} = \frac{\left(\frac{3D_{pinhole}^2}{2f_{excitation}}\right)^{\frac{1}{3}}}{3V_{droplet}^{2/3}}\,\omega_{V_{droplet}} \qquad (13)$$

In this equation, $\omega_{D_{droplet}}$ shows the uncertainty of the droplet diameter. The pressure sensor used for this measurement is Trafag's model 8287 with an accuracy of 0.5%. Using Equation *(12)* and Equation *(13)*, the uncertainties in the measurements of velocity and droplet size of the monodisperse droplet generator described in Section 3.7 are calculated as 0.57 m/s and 0.86 µm, respectively.

3.9.2. Normalized Mass Flux Measurements

The relation of the normalized mass flux measurement is given in Equation *(14)* as follows:

$$\overline{w} = \frac{w_{local}}{w_{average}} \qquad (14)$$

In this equation, $\overline{w}$ is the normalized mass flux, w_{local} is the mass flux measured by using the patternator and $w_{average}$ is the average mass flux over the patternator. Rearranging the equation,

$$\overline{w} = \frac{\rho L_{met}}{\frac{\dot{m}_i + \dot{m}_o}{100 A_{pat}}} \qquad (15)$$

Here, ρ is the density of fluid, L_{met} is the measured liquid height of the patternator cell per second, $\dot{m}_i$ is the mass flow rate of the inner orifice, $\dot{m}_o$ is the total mass flow rates of outer orifices, A_{pat} is the quadrat of each patternator cell. Then, the equation becomes as follows:

$$\overline{w} = 100 \frac{L_{met} L_{pat}^2}{\dot{V}_i + \dot{V}_o} \qquad (16)$$

In Equation *(16)*, L_{pat} is the side length of a patternator cell, $\dot{V}_i$ is the volumetric flow rate of the inner orifice and $\dot{V}_o$ is the total volumetric flow rate of the outer orifices.

Thus, by using the error propagation technique, the uncertainty of the normalized mass flux measurement is calculated by Equation *(17)*,

$$\omega_{\overline{w}} = \sqrt{\left(100\frac{L_{pat}^2}{\dot{V}_i + \dot{V}_o}\right)^2 \omega_{L_{met}}^2 + \left(200\frac{L_{met}L_{pat}}{\dot{V}_i + \dot{V}_o}\right)^2 \omega_{L_{pat}}^2 + \left(-100\frac{L_{met}L_{pat}^2}{(\dot{V}_i + \dot{V}_o)^2}\right)^2 \left(\omega_{\dot{V}_i}^2 + \omega_{\dot{V}_o}^2\right)} \qquad (17)$$

Here, $\omega_{\overline{w}}$ is the uncertainty of the normalized mass flux measurements, $\omega_{L_{met}}$ is the uncertainty of the length measurement of the patternator cell, $\omega_{L_{met}}$ is the uncertainty of the side length of the patternator cell, $\omega_{\dot{V}_i}$ and $\omega_{\dot{V}_o}$ are the uncertainties of the volumetric flow rates of inner and outer orifices, respectively.

The accuracy of the flowmeters used in the both feeding lines are Omega FLR-1000 series with an accuracy of 0.5%. The uncertainty of the side length of the patternator is 50 µm and the uncertainty coming from the measurement of the tube length is 0.5 mm. The maximum uncertainty of the normalized mass flux is found as 0.20 by taking the mass flowrates and tube length as large as possible.

3.9.3. Normalized Velocity Measurements

The relation of the normalized axial velocity measurement is given in Equation *(18)* as follows:

$$\bar{\vec{V}}_u = \frac{\overrightarrow{V_u}}{\frac{\dot{m}_o V_o + \dot{m}_i V_i}{\dot{m}_o + \dot{m}_i}} \qquad (18)$$

In this equation, $\bar{\vec{V}}_u$ is the normalized U velocity, $\overrightarrow{V_u}$ is the U velocity measured by PDA, V_o is the mean velocity of an outer orifice, V_i is the mean velocity of the inner orifice. The other normalized velocity measurements are calculated in the same way. Multiplying the numerator and denominator of the right-hand side of Equation *(18)* by A that is the area of each orifices, it becomes:

$$\bar{\bar{V}}_u = \frac{\rho A \overrightarrow{V_u}}{\frac{\dot{m}_o \rho V_o A + \dot{m}_i \rho V_i A}{\dot{m}_o + \dot{m}_i}} = \frac{\rho A \overrightarrow{V_u}}{\frac{\dot{m}_o^2 + \dot{m}_i^2}{\dot{m}_o + \dot{m}_i}} \qquad (19)$$

By using Equation *(19)*, the uncertainty of the normalized axial velocity measurement is calculated by Equation *(20)*:

$$\omega_{\bar{\bar{V}}_u} = \sqrt{\begin{aligned} &\left(\frac{\rho A \overrightarrow{V_u}}{\frac{\dot{m}_o^2 + \dot{m}_i^2}{\dot{m}_o + \dot{m}_i}}\right)^2 \omega_{\overrightarrow{V_u}}^2 \\ &+ \left(-\frac{\rho A \overrightarrow{V_u}}{\left(\frac{\dot{m}_o^2 + \dot{m}_i^2}{\dot{m}_o + \dot{m}_i}\right)^2} \frac{2\dot{m}_o(\dot{m}_o + \dot{m}_i) - (\dot{m}_o^2 + \dot{m}_i^2)}{(\dot{m}_o + \dot{m}_i)^2}\right)^2 \omega_{\dot{m}_o}^2 \\ &+ \left(-\frac{\rho A \overrightarrow{V_u}}{\left(\frac{\dot{m}_o^2 + \dot{m}_i^2}{\dot{m}_o + \dot{m}_i}\right)^2} \frac{2\dot{m}_i(\dot{m}_o + \dot{m}_i) - (\dot{m}_o^2 + \dot{m}_i^2)}{(\dot{m}_o + \dot{m}_i)^2}\right)^2 \omega_{\dot{m}_i}^2 \end{aligned}} \qquad (20)$$

In this equation, $\omega_{\bar{\bar{V}}_u}$ is the uncertainty of the normalized U velocity, $\omega_{\overrightarrow{V_u}}$ is the uncertainty of the U velocity measured by PDA, $\omega_{\dot{m}_i}$ and $\omega_{\dot{m}_o}$ are the uncertainties of the mass flow rates of inner and outer orifices, respectively. The uncertainties of the other normalized velocity measurements are calculated in the same way.

The maximum error in the velocity measurements done with the droplet generator described in Section 3.7 is calculated as 2.3% and 2% for Test 1 and Test 2, respectively. The maximum uncertainty of the normalized velocity distribution becomes 0.04 by taking the maximum velocity and mass flow rates among the tests.

3.9.4. Normalized Droplet Count Measurements

The relation of the normalized droplet count measurement is given in Equation *(21)*:

$$\overline{N} = \frac{N}{\dot{m}_o + \dot{m}_i} \qquad (21)$$

Here, $\overline{N}$ is the normalized droplet count, N is the droplet count measured by PDA and the uncertainty of the normalized droplet count measurement is calculated using Equation *(22)*:

$$\delta_{\overline{N}} = \sqrt{\left(\frac{N}{(\dot{m}_o + \dot{m}_i)^2}\right)^2 \delta_{\dot{m}_o}^2 + \left(\frac{N}{(\dot{m}_o + \dot{m}_i)^2}\right)^2 \delta_{\dot{m}_i}^2} \qquad (22)$$

The uncertainty becomes 0.6 #/g/s for the greatest number of droplet count and mass flowrates among the tests.

3.9.5. Droplet Diameter Measurements

The maximum error of diameter measurements is found as 1.4% and 2.8% for Test 1 and Test 2, respectively.

CHAPTER 4

EXPERIMENTAL INVESTIGATION

This chapter is divided into three main parts as triplet injectors, pentad injectors and comparison of these injector types. In each section, the effects of selected design parameters will be investigated in terms of mass flux, velocity and droplet distributions.

4.1. Triplet Injectors

In this section, the effects of impingement distance, orifice l/d ratio, orifice diameter, impingement distance and momentum ratio on the spray characteristics of triplet injectors will be discussed in terms of mass flux, velocity distributions, droplet statistics and spray angles.

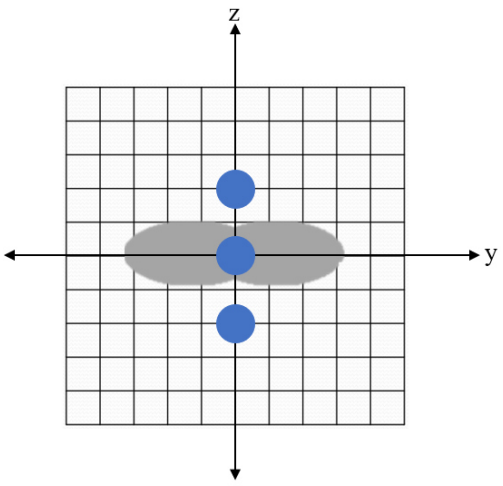

Figure 4.1. The Schematic of the Distribution of Triplet Injectors

Figure 4.1 shows the distribution of triplet injectors. In the figure, blue circles represent the injector orifices. Since the orifices are positioned along the z-axis, the resultant spray grows along the y-axis. Hence, in this section, the comparison of different test cases will be evaluated along y and z-axes.

Mass flux measurements used in the following sections were obtained by using the mechanical patternator defined in the CHAPTER 3. The patternator was positioned at 80 mm below the impingement point for triplet injector test cases, except the one with T451055 (triplet injector with 45° impingement angle, 1 mm orifice diameter, 5 of orifice l/d ratio and 5 mm impingement distance) due to the mass flux distribution characteristics of this injector, which will be explained in detail in the related section.

Velocity distributions and droplet statistics were obtained by PDA at a plane 30 mm below the impingement point of each injector without any exceptions. It should be noted that PDA collects the data on droplets. This means that the rest of the spray such as liquid sheet, ligaments and spherical atomized particles cannot be obtained in these measurements. Therefore, the evaluation on the results should be carried out by taking this fact into consideration.

Table 4.1 shows the test list of the triplet injectors. As it is seen, for each test configuration, measurements are performed with the patternator, PDA and the video camera. While the selected test parameter is investigated, all other measured parameters are kept constant. This includes the momentum ratio, MR, which was maintained approximately around the same value among the compared cases other than those investigating the effect of MR itself. In order to accomplish this, the mass flow rates supplied to the inner and outer orifices were adjusted accordingly. In the table, it is seen that slight variations exist among the compared test cases in terms of momentum ratio due to the pressurizing system of the test setup. In order to eliminate the effect of these variations, the mass flux, droplet count and velocity distributions are normalized, which will be presented in the following sections.

Table 4.1. Test Map of Triplet Injectors

No	Code	Injector Type	MR	Imp. Angle (°)	Orifice Diameter (mm)	Orifice l/d Ratio	Imp. Distance (mm)
1	T601055	Triplet	1.99	60	1.0	5	5
2	T601055	Triplet	4.32	60	1.0	5	5
3	T601055	Triplet	8.34	60	1.0	5	5
4	T601055	Triplet	12.91	60	1.0	5	5
5	T601058	Triplet	12.70	60	1.0	5	8
6	T601051	Triplet	12.86	60	1.0	5	10
7	T601035	Triplet	13.01	60	1.0	3	5
8	T601085	Triplet	12.96	60	1.0	8	5
9	T601255	Triplet	12.75	60	1.2	5	5
10	T600855	Triplet	12.67	60	0.8	5	5
11	T451055	Triplet	2.20	45	1.0	5	5
12	T901055	Triplet	2.07	90	1.0	5	5
13	T901055	Triplet	3.19	90	1.0	5	5
14	T901055	Triplet	6.21	90	1.0	5	5
15	T901055	Triplet	8.93	90	1.0	5	5
16	T901055	Triplet	11.73	90	1.0	5	5

The momentum ratio is defined as the ratio of the total momentum through the outer orifices to that through the inner orifice as given in Equation *(23)*, where $\dot{m}_i$ is the mass flow rate through the inner orifice and $\dot{m}_o$ is the total mass flow rate through the outer orifices. V_i and V_o represent the flow velocity through the inner and outer orifices, respectively.

$$MR = \frac{\dot{m}_o V_o}{\dot{m}_i V_i} \qquad (23)$$

Spray angle measurements conducted by a video camera lead to better understanding of the spread of sprays. A representation for the spray angle measurements in triplet injectors is given in Figure 4.2. In this study, the spray angles were found on the xy plane, while the change in xz plane was not examined. Results were analyzed based on the change of the angle along the xy plane only.

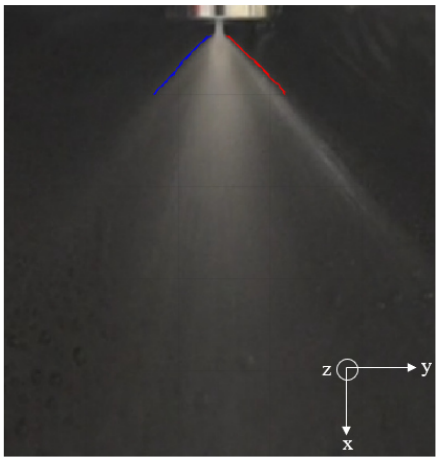

Figure 4.2. A Representation of Spray Angle Measurements in Triplet Injectors

4.1.1. The Effect of Impingement Distance

In this section, the effect of impingement distance for triplet injectors on normalized mass flux, velocity, droplet count distributions, droplet statistics and spray angles will be discussed. The orifice l/d ratio, orifice diameter, impingement angle and momentum ratio were kept constant while the following results were obtained.

4.1.1.1. Normalized Mass Flux Distribution

Figure 4.3 shows the mass flux distribution of triplet injectors with different impingement distances. As it is seen, with the increase of the impingement distance, the peak flux value at the center decreases slightly. This could be the result of the flow at the outlets of the orifices becoming more turbulent as approaching the

impingement point. This result is in the same trend with the doublet injector study performed by Heidmann et al. (Heidmann and Humphrey, 1952). Heidmann and others studied the effect of the free jet length before the impingement.

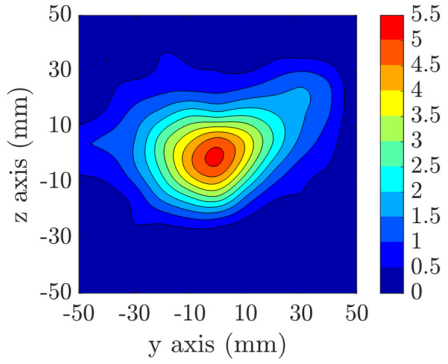

a) Injector T601055, impingement distance= 5 mm

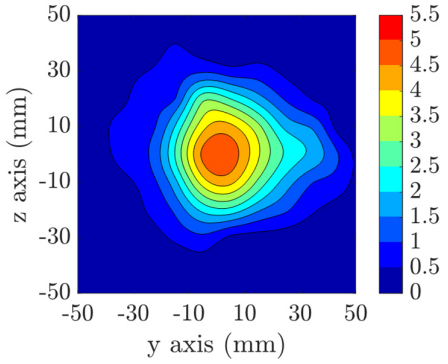

b) Injector T601058, impingement distance = 8 mm

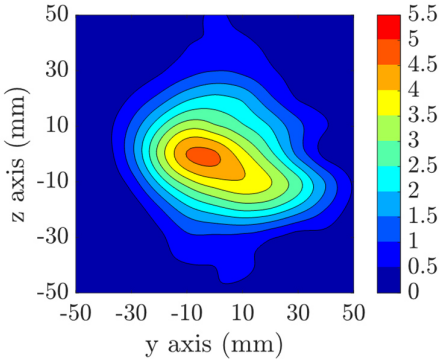

c) Injector T601051, impingement distance = 10 mm

Figure 4.3. The Effect of Impingement Distance on Normalized Mass Flux Distribution

Figure 4.4 shows the normalized mass flux distributions of triplets with different impingement distances. Along the y-axis, with the increase of impingement distance from 5 mm to 10 mm, the peak mass flux value decreases by 10% at the center.

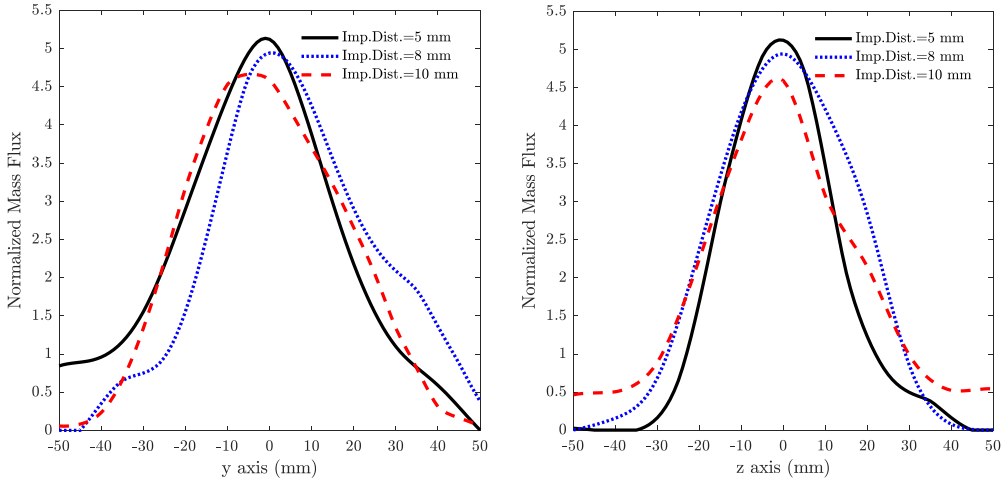

a) along y-axis b) along z-axis

Figure 4.4. Comparison of the Effect of Impingement Distance on Normalized Mass Flux Distributions at y and z-axes

4.1.1.2. Normalized Droplet Count

Figure 4.5 shows the normalized droplet count distribution of triplet injectors at different impingement distances. As it is seen, with the increase of the impingement distance, the normalized droplet count decreases in coherence to the peak normalized mass flux values. When the disturbances on the liquid jets increase, the resultant spray becomes more instable, thus, the behavior of the breakup of the sheets and the generation of droplets deteriorate similar to what happens with doublet injectors.

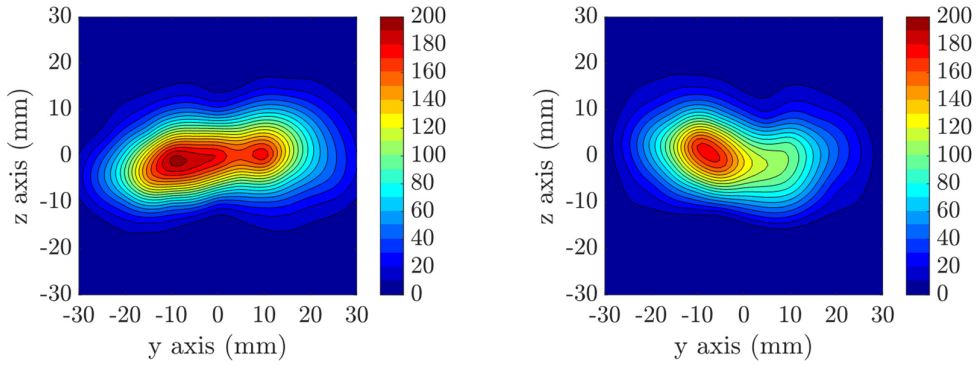

a) Injector T601055, impingement distance= 5 mm

b) Injector T601058, impingement distance = 8 mm

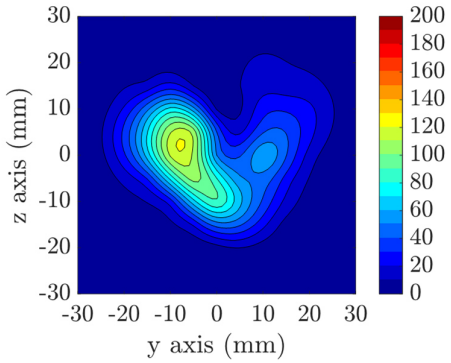

c) Injector T601051, impingement distance = 10 mm

Figure 4.5. The Effect of Impingement Distance on Normalized Droplet Count

Also, the irregularities of the droplet distribution become apparent on the injector with 10 mm impingement distance. The uneven increase of droplet count along the z-axis can be linked to the pre-impingement behavior of the liquid jets.

Figure 4.6 shows the normalized droplet count distributions of triplet injectors along y-axis with different impingement distances. With the increase of the impingement distance from 5 mm to 10 mm, the peak value of the normalized droplet count is decreased by almost 50%. The decrease on the count is kept along the axis in the same manner. Since the highest mass flux values for each injector are generally obtained along the y-axis, the distinct decrease in the droplet count in this region

may be interpreted as leading to a reduction in the efficiency of the combustion process.

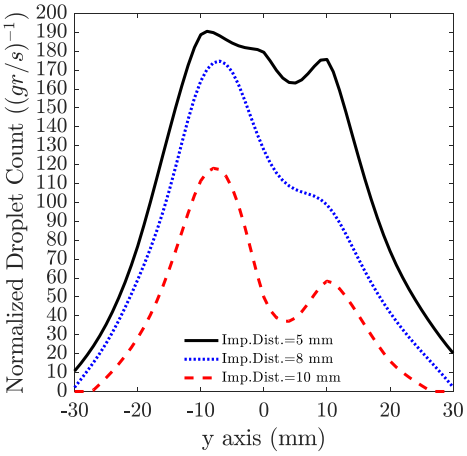

Figure 4.6. Comparison of the Effect of Impingement Distance on Normalized Droplet Count along y -axis

4.1.1.3. Normalized Axial Velocity

Figure 4.7 shows the normalized axial velocity distribution of the sprays from the triplet injectors with different impingement distances. As it is seen, with the increase of impingement distance, the highest velocity at the center decreases which is parallel to the results of mass flux and droplet count. Also, similar to the previous findings, the asymmetry on the velocity distribution along the z-axis increases with the triplet injector with 10 mm impingement distance.

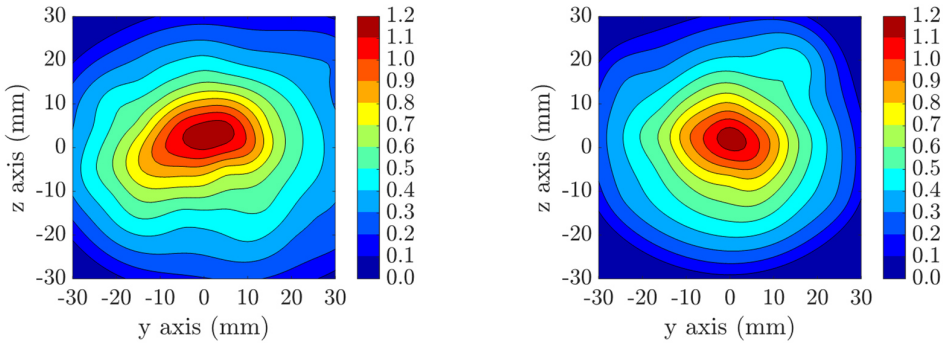

a) Injector T601055, impingement distance = 5 mm

b) Injector T601058, impingement distance = 8 mm

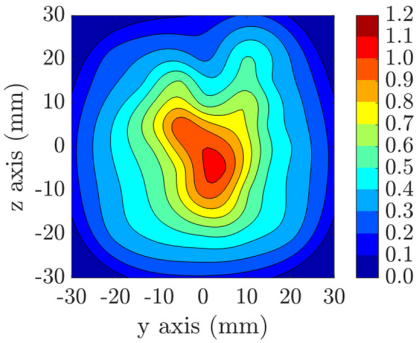

c) Injector T601051, impingement distance = 10 mm

Figure 4.7. The Effect of Impingement Distance on Normalized Axial Velocity

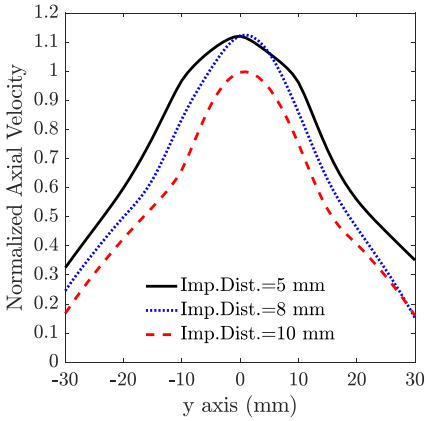

Figure 4.8. Comparison of the Effect of Impingement Distance on Normalized Axial Velocity at y-axis

Figure 4.8 shows the normalized axial velocity distributions of sprays from triplet injectors with different impingement distances. With the increase of the impingement distance from 5 mm to 10 mm, the highest value of the mass flux is decreased by 10% at the center.

4.1.1.4. Normalized V Velocity

The normalized V velocity distributions of the sprays obtained with the triplet injectors at different impingement distances are given in Figure 4.9.

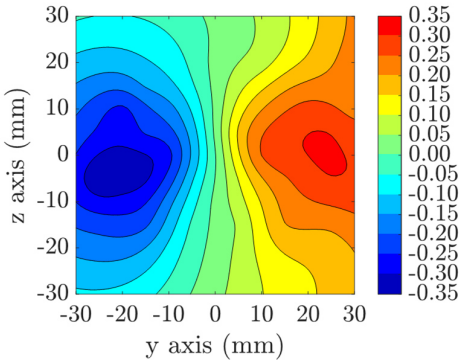

a) Injector T601055, impingement distance= 5 mm

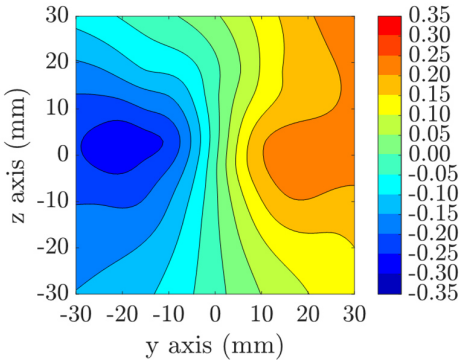

b) Injector T601058, impingement distance = 8 mm

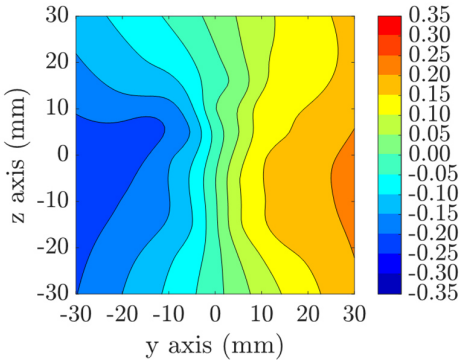

c) Injector T601051, impingement distance = 10 mm

Figure 4.9. The Effect of Impingement Distance on Normalized V Velocity

The normalized V velocity distribution shows the dispersion of the spray along the y-axis. As it is expected from the normalized mass flux distribution, the magnitude of the normalized V velocity distribution becomes smaller with the increase in the impingement distance, which results in significant drop in the normalized droplet count. The comparison of the V velocity distribution along the y-axis is given in the Figure 4.10.

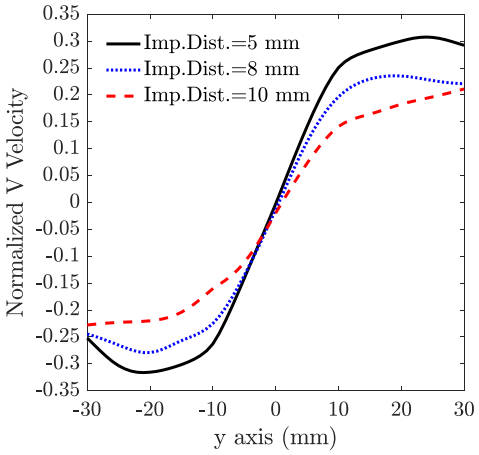

Figure 4.10. Comparison of the Effect of Impingement Distance on Normalized V Velocity at y-axis

4.1.1.5. Normalized W Velocity

The normalized W velocity distributions obtained with triplet injectors at different impingement distances are given in Figure 4.11.

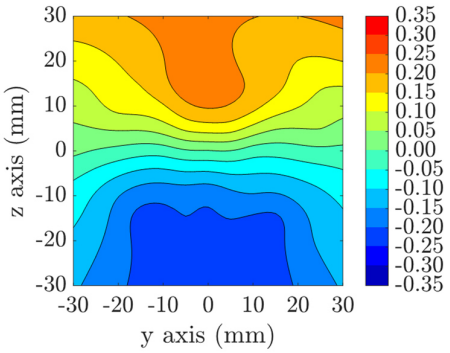

a) Injector T601055, impingement distance= 5 mm

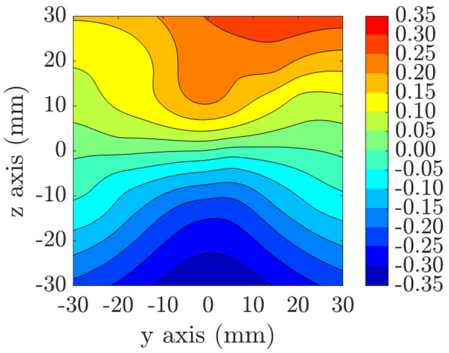

b) Injector T601058, impingement distance = 8 mm

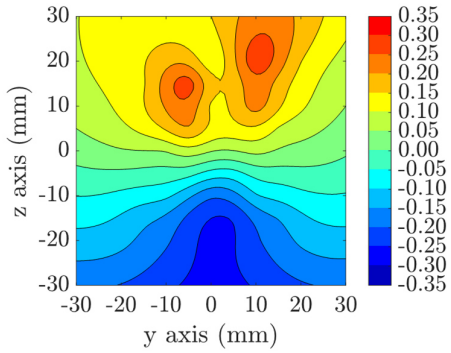

c) Injector T601051, impingement distance = 10 mm

Figure 4.11. The Effect of Impingement Distance on Normalized W Velocity

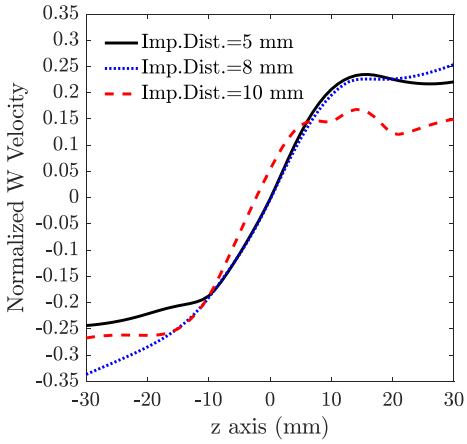

Figure 4.12. Comparison of the Effect of Impingement Distance on Normalized W Velocity at z-axis

The asymmetrical behavior of the normalized W velocity distribution increases with the impingement distance, which is consistent with previous results. The distortion on the normalized W velocity distribution becomes apparent along the z-axis in Figure 4.12, especially for the injector with 10 mm impingement distance. This result shows that the eddies on the liquid jets also affect the W velocity distributions of the sprays.

4.1.1.6. Normalized Velocity Magnitude

The normalized velocity magnitude distributions of the sprays obtained by the triplet injectors at different impingement distances are given in Figure 4.13. The distribution for the impingement distance of 10 mm shows similarities to the random distribution of the normalized mass flux and droplet count distributions.

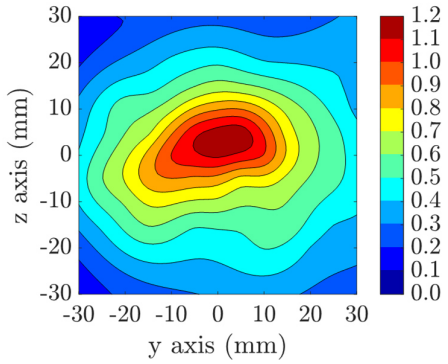

a) Injector T601055, impingement distance= 5 mm

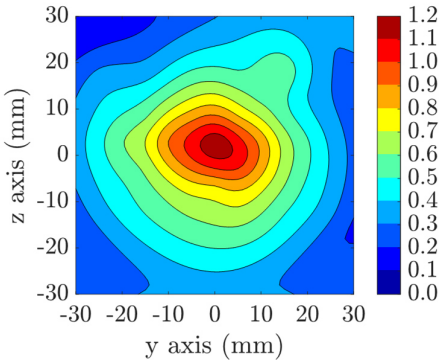

b) Injector T601058, impingement distance = 8 mm

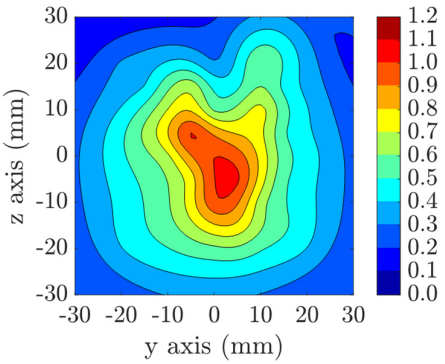

c) Injector T601051, impingement distance = 10 mm

Figure 4.13. The Effect of Impingement Distance on Normalized Velocity Magnitude

Along the y-axis, the magnitude of the velocity distribution shows similar trends to the axial velocity distribution as expected. As Figure 4.14 shows, the apparent reduction of the dispersion of the spray along the y-axis can be correlated with the normalized velocity distributions obtained at different impingement distances.

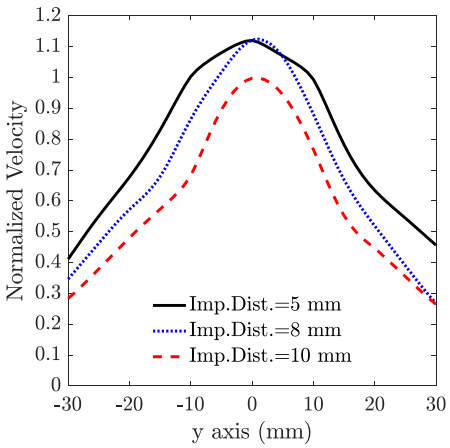

Figure 4.14. Comparison of the Effect of Impingement Distance on Normalized Velocity Magnitude at y-axis

4.1.1.7. SMD Distribution

The Sauter Mean Diameter (SMD), also represented as D_{32}, is the equivalent diameter defined as the ratio of the total volume to the total surface area of the droplets. It is calculated by using Equation *(25)* (Lefebvre and McDonell, 2017), where D_i is the droplet diameter and N_i is the number of droplets with that diameter:

$$SMD = D_{32} = \frac{\sum N_i D_i^3}{\sum N_i D_i^2} \qquad (24)$$

The SMD distributions obtained by the injectors at different impingement distances are given in Figure 4.15. In contrary to the droplet count distribution, the minimum SMD is generally obtained in the center where the highest axial velocity is obtained. Liquid sheets break up into ligaments due to the impact waves on the surface. At the impingement point, the lateral velocity is minimized at the center and it increases as it gets away from the center.

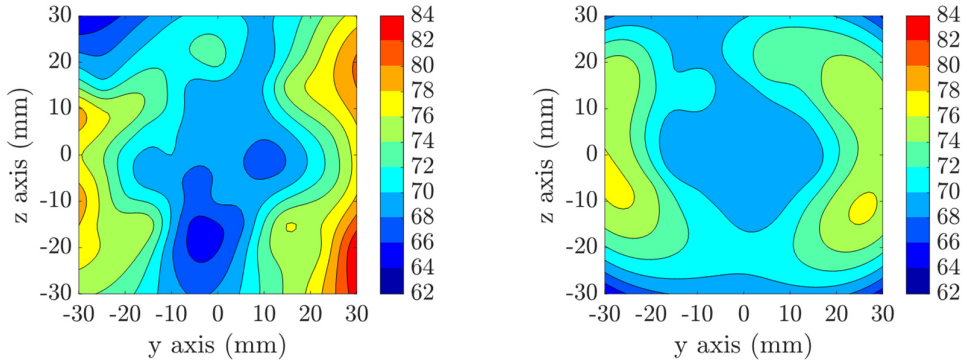

a) Injector T601055, impingement distance= 5 mm

b) Injector T601058, impingement distance = 8 mm

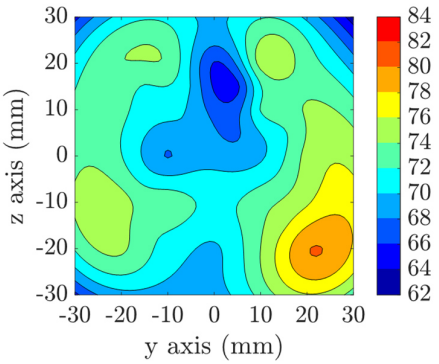

c) Injector T601051, impingement distance = 10 mm

Figure 4.15. The Effect of Impingement Distance on SMD

The spray progresses both in the axial and lateral directions. The sheet becomes thinner in the lateral direction compared to the axial direction and fluctuations on the edge of the liquid sheet easily breaks up into ligaments with a smaller effect of velocity. The liquid sheet can progress in the axial direction for a longer time before it breaks up into ligaments because the thickness of the liquid sheet can be preserved for a long time. The comparison of the SMD distribution along the y-axis is given in Figure 4.16. The SMD does not have an apparent trend with respect to the impingement distance, although the impingement distance greatly affects both mass flux and droplet count distributions.

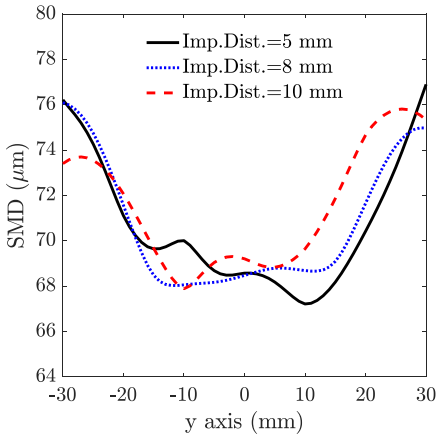

Figure 4.16. Comparison of the Effect of Impingement Distance on SMD at y-axis

4.1.1.8. Rosin-Rammler Distribution

Rosin-Rammler distribution is used for expressing the droplet size distribution of each test case. The distribution can be expressed by the Equation *(25)* (Lefebvre and McDonell, 2017):

$$1 - Q = exp - \left(\frac{D}{X}\right)^{q} \qquad (25)$$

Here, Q shows the fraction of the total volume of droplets with diameter smaller than D. D is the diameter. X and q are distribution constants.

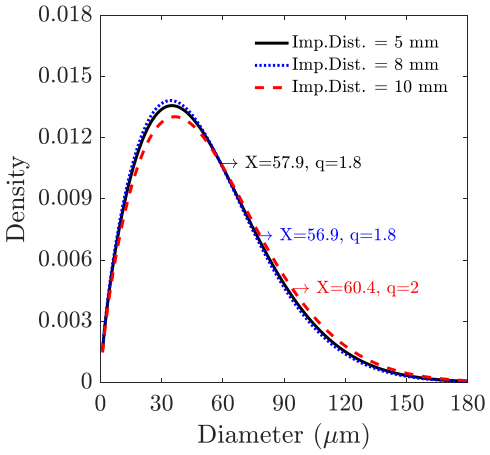

Figure 4.17. Comparison of Rosin-Rammler Distributions

The Rosin-Rammler distributions of injectors with different impingement distances are shown in Figure 4.17. Neither X nor q changes significantly with respect to the impingement distance, similar to what is observed with the SMD distributions.

4.1.1.9. Total Normalized Droplet Count

Total normalized droplet count decreases as a function of the impingement distance, which is given in Figure 4.18.

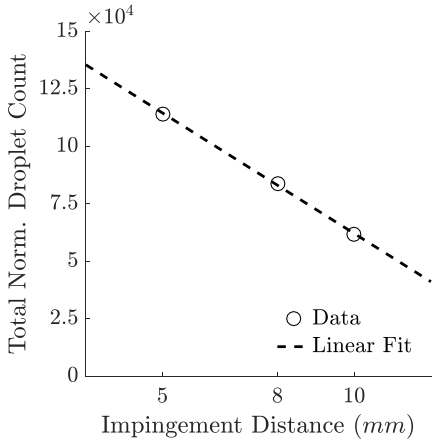

Figure 4.18. Comparison of the Effect of Impingement Distance on Total Normalized Droplet Count

4.1.1.10. Mean D10

The arithmetic mean diameter (D_{10}) is calculated by using Equation *(26)* (Lefebvre and McDonell, 2017), where D_i is the droplet diameter and N_i is the number of droplets with that diameter:

$$D_{10} = \frac{\sum N_i D_i}{\sum N_i} \qquad (26)$$

Figure 4.19 shows that the mean diameter is proportional to the impingement distance.

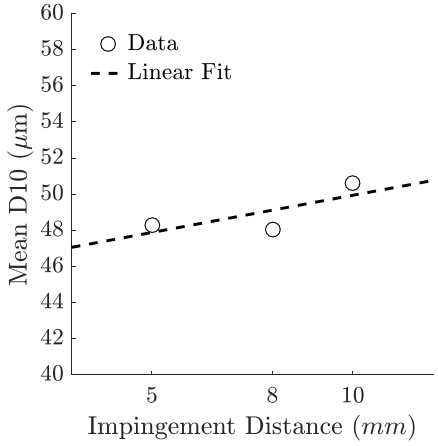

Figure 4.19. Comparison of the Effect of Impingement Distance on Mean D10

4.1.1.11. Mean SMD

The variation in the mean SMD as a function of the impingement distance is given in Figure 4.20. The mean SMD is almost insensitive to the impingement distance.

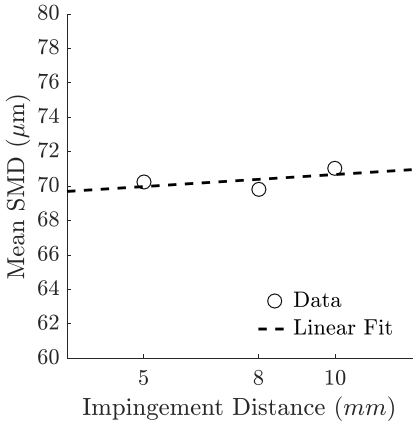

Figure 4.20. Comparison of the Effect of Impingement Distance on Mean SMD

4.1.1.12. Spray Angle

The effect of the impingement distance on the spray angle is given in Figure 4.21. With an increase of the impingement distance, the spray angle becomes smaller.

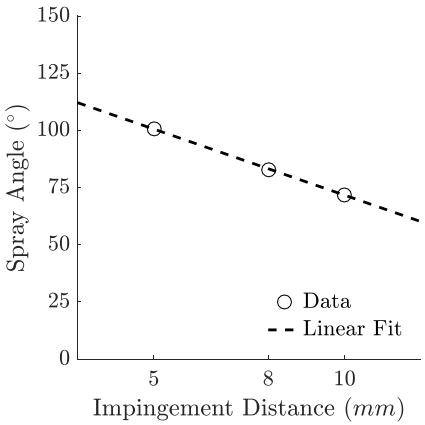

Figure 4.21. Comparison of the Effect of Impingement Distance on Spray Angle

4.1.2. The Effect of Orifice l/d Ratio

In this section, the effect of the orifice l/d ratio of triplet injectors on the normalized mass flux, velocity, droplet count distributions, droplet statistics and spray angles will be discussed. Impingement distance, orifice diameter, impingement angle and momentum ratio were kept constant while the following results were obtained.

4.1.2.1. Normalized Mass Flux Distribution

Figure 4.22 shows the mass flux distribution of triplet injectors with different orifice l/d ratios. In each case, the inner orifice had the same l/d ratio with the outer orifices. As it is seen, with the increase of l/d ratios, the highest flux value at the center increases slightly. In order to obtain the fully-developed turbulent flow, the required length-to-diameter ratio of the orifice can be found as 13.5 and 17 for the inner and outer orifices, respectively, by using the empirical correlation given by Bhatti and Shah (Bhatti and Shah, 1987) in Equation (27):

$$L_{h,\ turbulent} = 1.359 D Re_D^{1/4} \qquad (27)$$

where $L_{h,\ turbulent}$ is defined as the hydrodynamic entry length for turbulent flow. This value can be approximated as 10 for practical use by Equation (28) as follows (Zhi-qing, 1982):

$$L_{h,turbulent} \approx 10D \qquad (28)$$

which is also supported by the study of Kiaoulias et al. (Kiaoulias et al., 2019). They did experiments with orifices with the same orifice diameter and different orifice l/d ratio in order to investigate the flow behavior and showed that the stability of the jet at the exit of the orifice increases with l/d of 10, however, further increase in this ratio cannot affect the flow behavior since it reaches the fully turbulent flow inside the orifice.

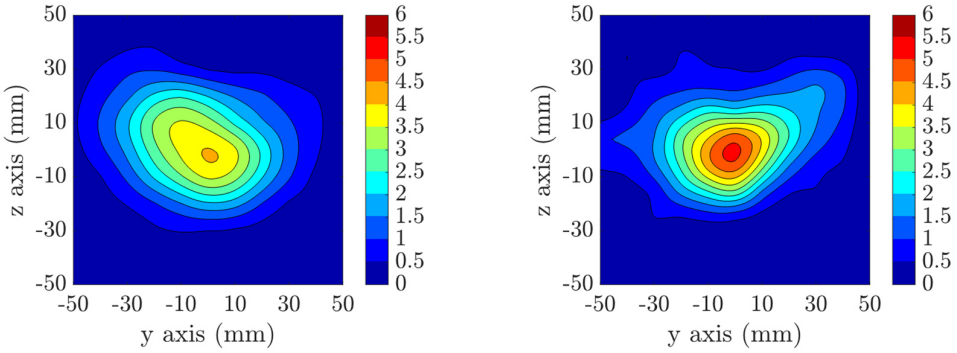

a) Injector T601035, orifice l/d ratio = 3 b) Injector T601055, orifice l/d ratio = 5

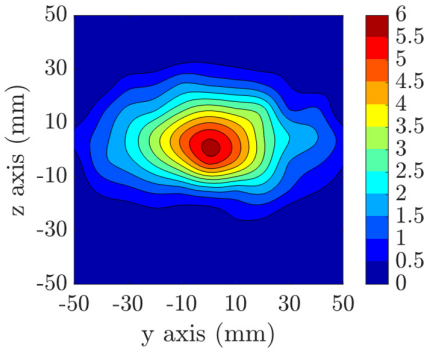

c) Injector T601085, orifice l/d ratio = 8

Figure 4.22. The Effect of Orifice l/d Ratio on Normalized Mass Flux Distribution

Yet, since the length-to-diameter ratios of the orifices tested in this study are still smaller than those suggested by the empirical correlation (Cengel et al. 2006) or shown by Kiaoulias et al. (Kiaoulias et al., 2019), with the increase of the length of the orifice, the disturbances on the flow becomes smaller, increasing the liquid sheet breakup length.

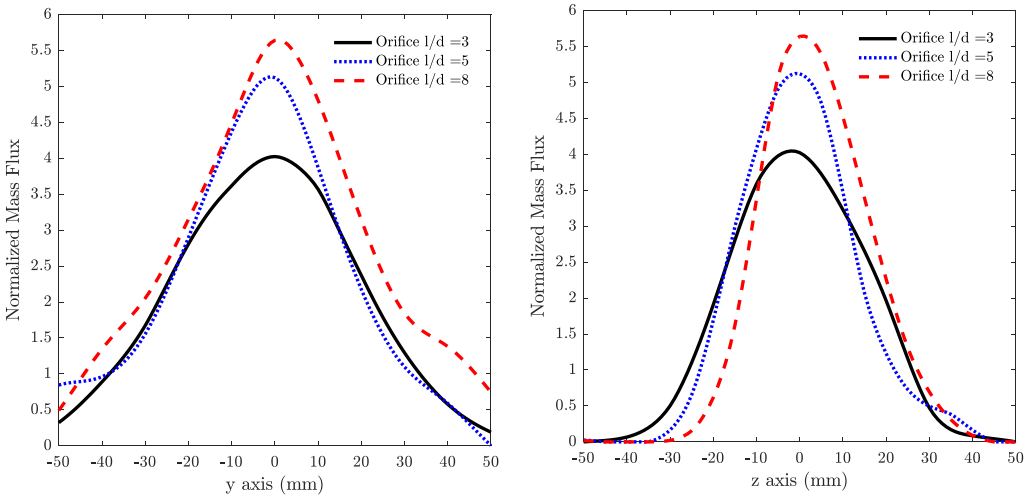

a) along y-axis b) along z-axis

Figure 4.23. Comparison of the Effect of Orifice l/d Ratio on Normalized Mass Flux Distributions at y and z-axes

Figure 4.23 shows the normalized mass flux distributions obtained with triplet injectors with different orifice l/d ratios. Along the y-axis, an increase in l/d clearly increases the highest mass flux values at the center. The increase of the l/d ratio and the decrease of the impingement distance show similar trends in terms of normalized mass flux distribution; however, the change is more observable with the parameter of length-to-diameter ratio.

4.1.2.2. Normalized Droplet Count

The normalized droplet count distributions of injectors with different orifice l/d ratios are given in Figure 4.24. The distributions show that the highest normalized

droplet count is obtained with the orifice l/d ratio of 5. It was discussed that the increase of the orifice l/d ratio increases the stability of the orifice streams, hence, the resultant liquid sheet. Because of this reason, the fully atomized droplets for l/d = 8 may be further downstream of the measurement plane that is 30 mm below the impingement point.

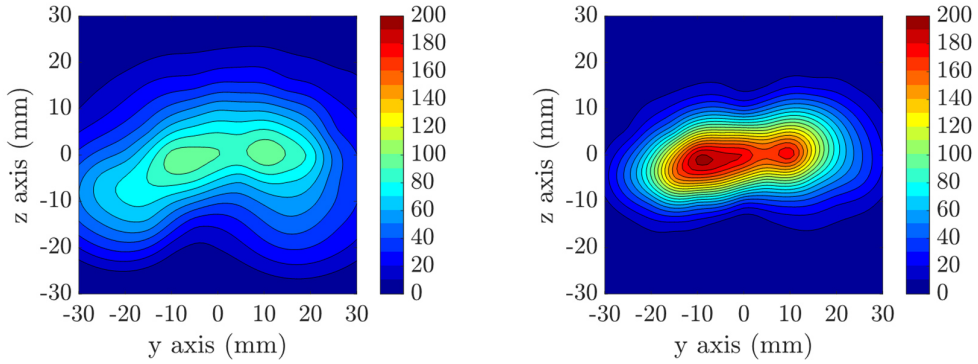

a) Injector T601035, orifice l/d ratio = 3 b) Injector T601055, orifice l/d ratio = 5

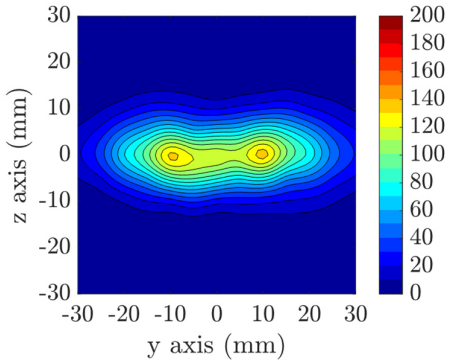

c) Injector T601085, orifice l/d ratio = 8

Figure 4.24. The Effect of Orifice l/d Ratio on Normalized Droplet Count

The comparison of the normalized droplet count along the y-axis is given in Figure 4.25. The increase of the l/d ratio from 3 to 5 results in a 100% increase in the normalized droplet count. Further increase of orifice l/d ratio from 5 to 8 reduces the normalized droplet count distribution, which shows that the liquid sheet breaks into ligaments and then more droplets form further away from the impingement point.

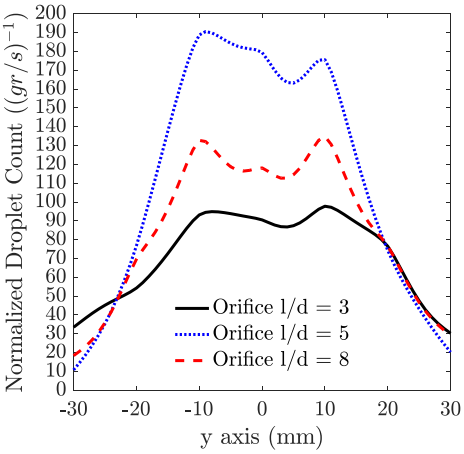

Figure 4.25. Comparison of the Effect of Orifice l/d Ratio on Normalized Droplet Count at y-axis

4.1.2.3. Normalized Axial Velocity

The normalized axial velocity distribution is given in Figure 4.26. The normalized axial velocity distribution at orifice l/d ratio of 3 shows a different distribution than the others while the other two shows very similar trends. This result also shows that the fully-developed flow cannot be obtained with l/d of 3.

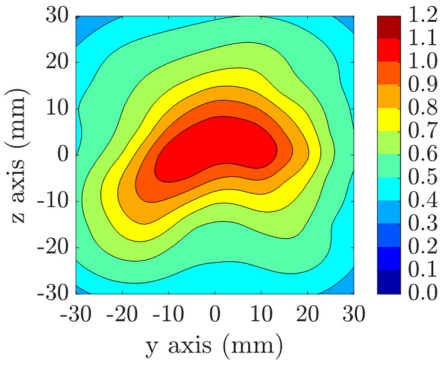

a) Injector T601035, orifice l/d ratio = 3

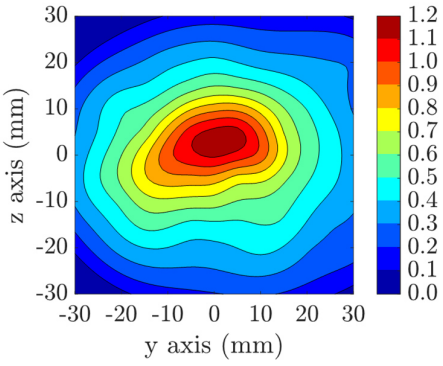

b) Injector T601055, orifice l/d ratio = 5

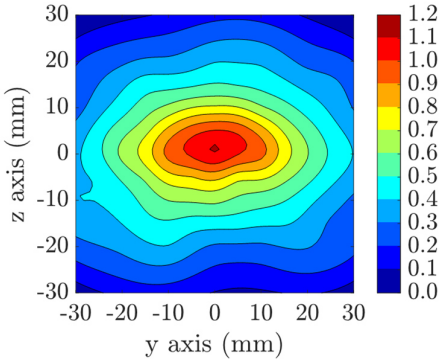

c) Injector T601085, orifice l/d ratio = 8

Figure 4.26. The Effect of Orifice l/d Ratio on Normalized Axial Velocity

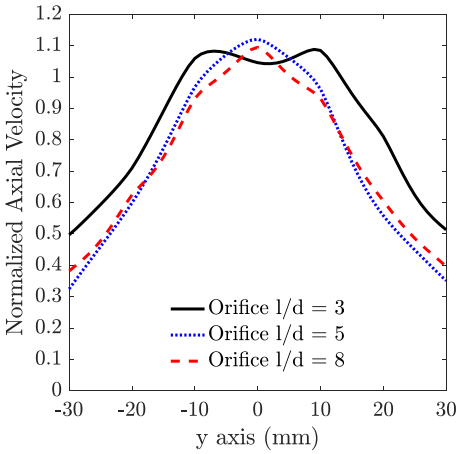

Figure 4.27. Comparison of the Effect of Orifice l/d Ratio on Normalized Axial Velocity at y-axis

The normalized axial velocity distribution along the y-axis is given in Figure 4.27. This result indicates that the fully-developed turbulent flow can be obtained with l/d ratio of 5 for this test case.

4.1.2.4. Normalized V Velocity

The normalized V velocity distribution of injectors with different orifice l/d ratios can be seen in Figure 4.28.

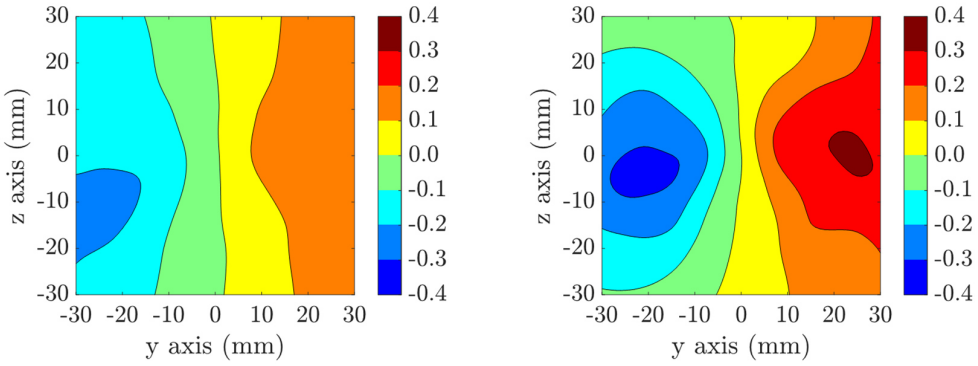

a) Injector T601035, orifice l/d ratio = 3 b) Injector T601055, orifice l/d ratio = 5

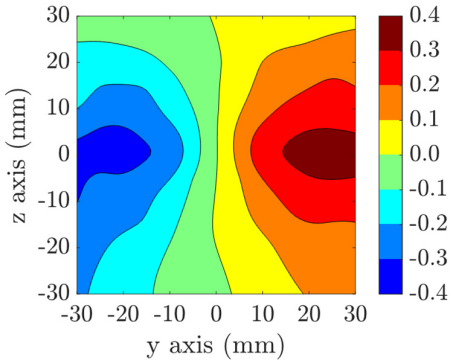

c) Injector T601085, orifice l/d ratio = 8

Figure 4.28. The Effect of Orifice l/d Ratio on Normalized V Velocity

The injectors with orifice l/d ratios of 5 and 8 show similarities on the normalized V velocity distributions like the normalized axial velocity. The injector with orifice l/d ratio of 3 has a smaller normalized V velocity in terms of magnitude. Figure 4.29 shows the V velocity distribution along the y-axis.

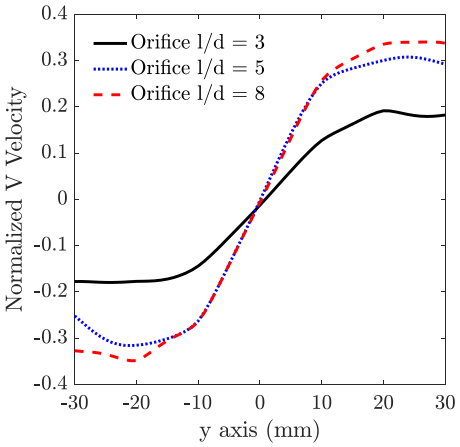

Figure 4.29. Comparison of the Effect of Orifice l/d Ratio on Normalized V Velocity at y-axis

4.1.2.5. Normalized W Velocity

The normalized W velocity distributions of injectors with different orifice l/d ratios are given in Figure 4.30. The injectors with the orifice l/d ratios of 5 and 8 show similarities on the normalized W velocity distributions like the normalized axial and V velocity distributions. The injector with the orifice l/d ratio of 3 has a smaller normalized W velocity in terms of magnitude similar to the V velocity distribution. Figure 4.31 shows the W velocity distributions with respect to the orifice l/d ratio.

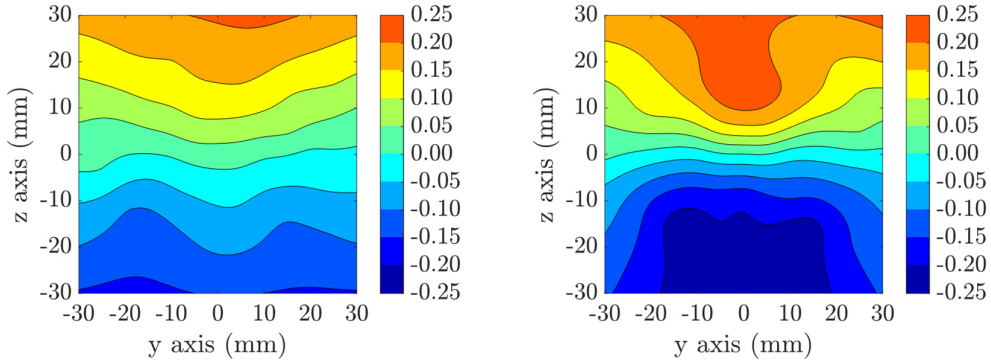

a) Injector T601035, orifice l/d ratio= 3 b) Injector T601055, orifice l/d ratio= 5

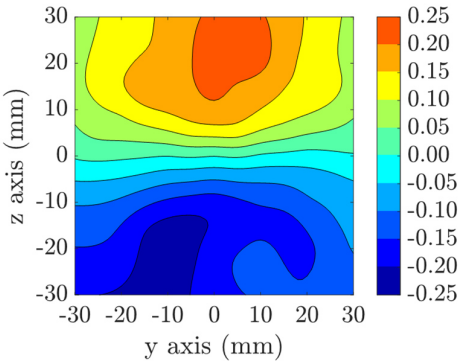

c) Injector T601085, orifice l/d ratio= 8

Figure 4.30. The Effect of Orifice l/d Ratio on Normalized W Velocity

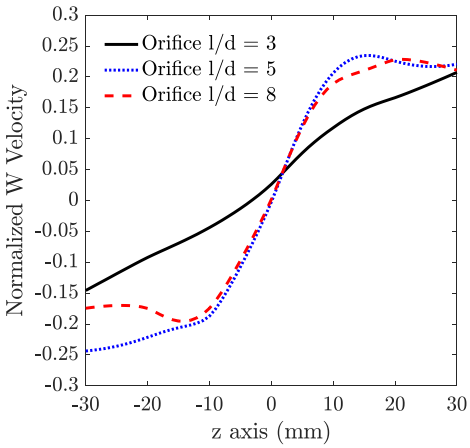

Figure 4.31. Comparison of the Effect of Orifice l/d Ratio on Normalized W Velocity at z-axis

4.1.2.6. Normalized Velocity Magnitude

The normalized velocity magnitude distributions of injectors with different orifice l/d ratios are given in Figure 4.32. It shows similar trends to axial velocity distribution as expected.

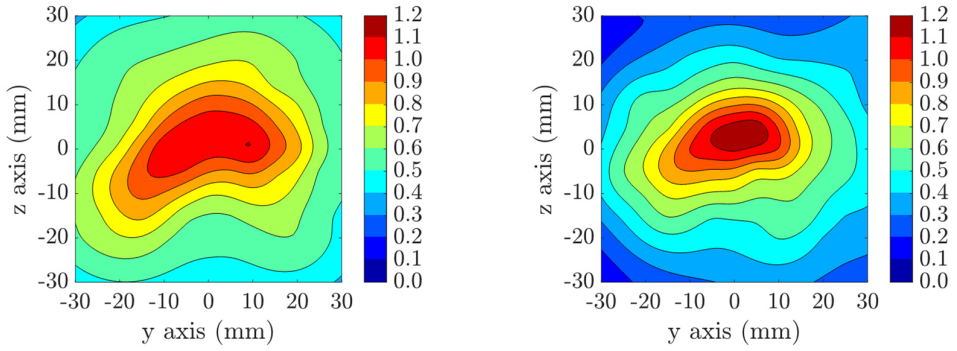

a) Injector T601035, orifice l/d ratio = 3 b) Injector T601055, orifice l/d ratio = 5

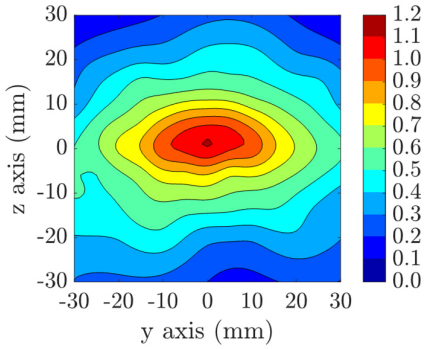

c) Injector T601085, orifice l/d ratio = 8

Figure 4.32. The Effect of Orifice l/d Ratio on Normalized Velocity Magnitude

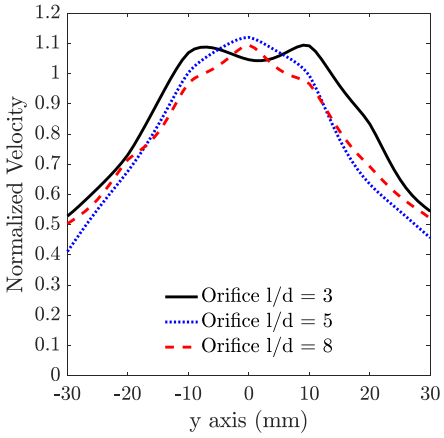

Figure 4.33. Comparison of the Effect of Orifice l/d Ratio on Normalized Velocity Magnitude at y-axis

Figure 4.33 shows the velocity magnitude distribution along the y-axis. The velocity magnitude distribution shows the same trends with the normalized axial velocity distribution.

4.1.2.7. SMD Distribution

Figure 4.34 shows the SMD distributions of injectors with different orifice l/d ratios.

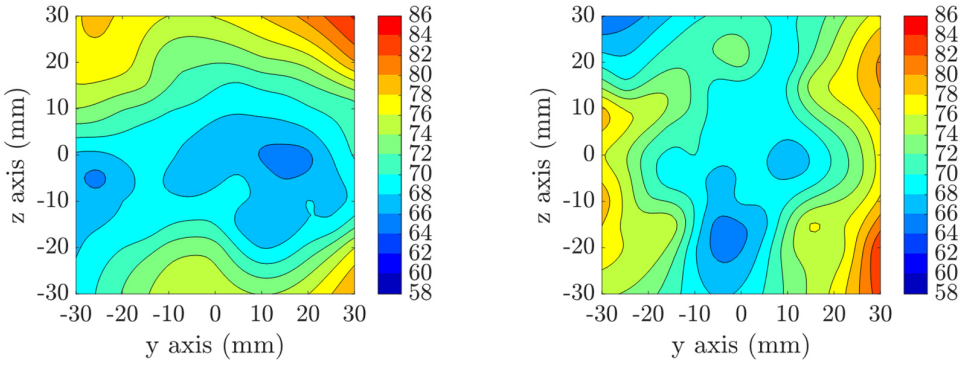

a) Injector T601035, orifice l/d ratio = 3 b) Injector T601055, orifice l/d ratio = 5

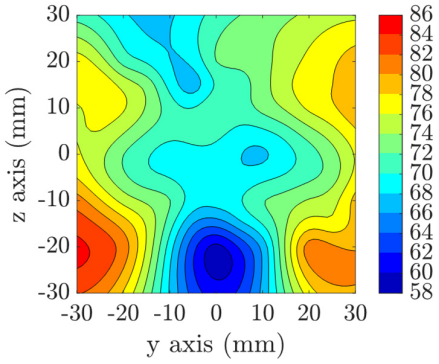

c) Injector T601085, orifice l/d ratio = 8

Figure 4.34. The Effect of Orifice l/d Ratio on SMD

The SMD distributions with the l/d ratios of 5 and 8 show similar trends. On the other hand, the minimum values of the SMD for the triplet injector with the l/d ratio

of 3 disperse along the y-axis, which shows more of a random distribution of the spray at the measurement plane.

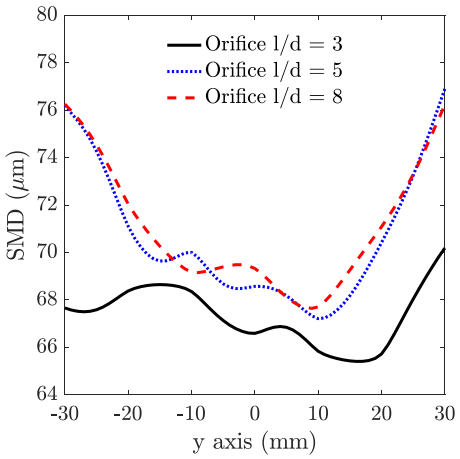

Figure 4.35. Comparison of the Effect of Orifice l/d Ratio on SMD at y-axis

The SMD distributions with different orifice l/d ratios are given in Figure 4.35. Since the magnitude of the velocity components becomes smaller in the injector with an orifice l/d ratio of 3, the SMD changes less along the y-axis. As seen before, similar velocity distributions of injectors with l/d ratios of 5 and 8 result in similar SMD distributions.

4.1.2.8. Rosin-Rammler Distribution

The Rosin-Rammler distributions of injectors with different orifice l/d ratios are shown in Figure 4.36. It is seen that, although X values show differences, q values remain very similar with a change in the orifice l/d ratio.

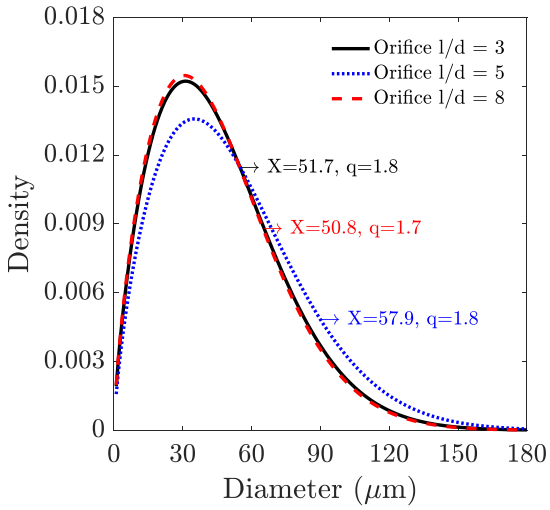

Figure 4.36. Comparison of Rosin-Rammler Distributions

4.1.2.9. Total Normalized Droplet Count

The change in the total normalized droplet count as a function of orifice l/d ratio is given in Figure 4.37. The total normalized droplet count is inversely proportional to the orifice l/d ratio.

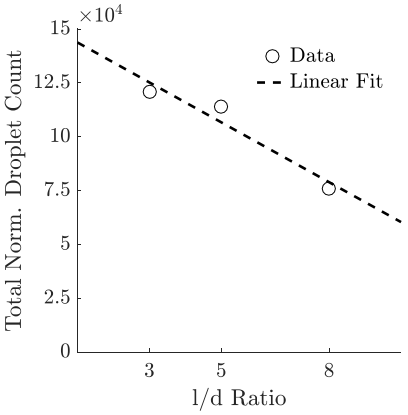

Figure 4.37. Comparison of the Effect of Orifice l/d Ratio on Total Normalized Droplet Count

4.1.2.10. Mean D10

The arithmetic mean diameter (D_{10}) as a function of orifice l/d ratio is given in Figure 4.38. It is inversely proportional to the orifice l/d ratio.

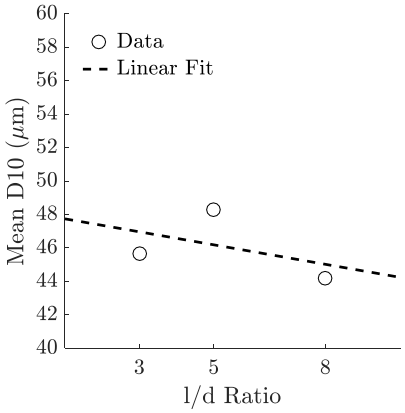

Figure 4.38. Comparison of the Effect of Orifice l/d Ratio on Mean D10

4.1.2.11. Mean SMD

The change in the mean SMD as a function of orifice l/d ratio is given in Figure 4.39. The mean SMD is proportional to the orifice l/d ratio.

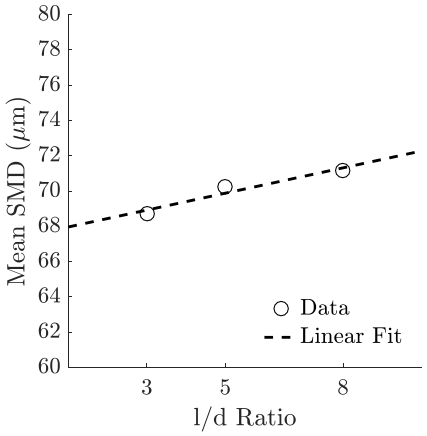

Figure 4.39. Comparison of the Effect of Orifice l/d Ratio on Mean SMD

4.1.2.12. Spray Angle

The effect of the orifice l/d ratio on the spray angle is given in Figure 4.40. The spray angle increases with an increase in the orifice l/d ratio similar to the normalized mass flux distribution.

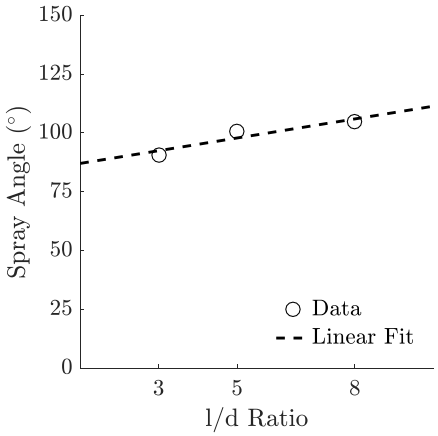

Figure 4.40. Comparison of the Effect of Orifice l/d Ratio on Spray Angle

4.1.3. The Effect of Orifice Diameter

In this section, the effect of orifice diameter of triplet injectors on normalized mass flux, velocity, droplet count distributions, droplet statistics and spray angles will be discussed. The impingement distance, orifice l/d ratio, impingement angle and momentum ratio were kept constant while the following results were obtained.

4.1.3.1. Normalized Mass Flux Distribution

Figure 4.41 shows the normalized mass flux distribution of the sprays from the triplet injectors with different orifice diameters. In each case, the inner orifice had the same diameter with the outer orifices. For the minimum orifice diameter, although the overall area the mass flux is distributed does not change significantly, the normalized mass flux becomes relatively more evenly distributed. This response

to the change of the orifice diameter is in the same trend with the one seen in the doublet injectors by Heidmann et al. (Heidmann and Humphrey, 1952). They also observed that the disperse of the spray changes with the orifice diameter. Since the momentum ratio in each case is kept almost constant, Re number changes in each test case. With the increase of orifice diameter, Reynolds number decreases from the order of 30000 to the order of 20000 at the outer orifices, and from the order of 12000 to the order of 8000 in the inner orifices. Hence, the disturbances on the liquid sheet become more apparent.

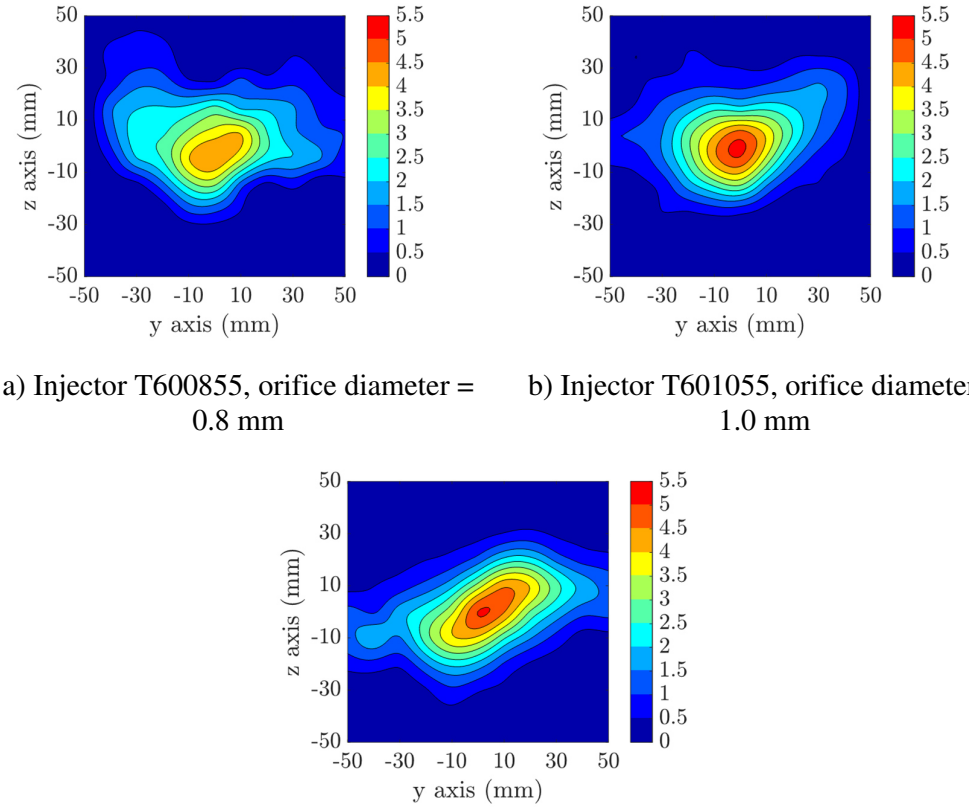

a) Injector T600855, orifice diameter = 0.8 mm

b) Injector T601055, orifice diameter = 1.0 mm

c) Injector T601255, orifice diameter = 1.2 mm

Figure 4.41. The Effect of Orifice Diameter on Normalized Mass Flux Distribution

Figure 4.42 shows the normalized mass flux distributions with different orifice diameters. Other than the highest mass flux at the center, there is no obvious change on the mass flux distributions along the z-axis.

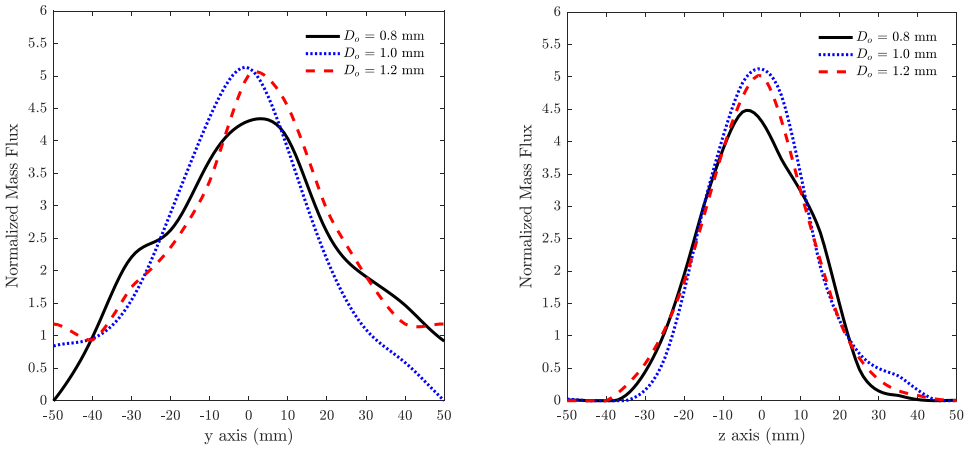

a) along y-axis b) along z-axis

Figure 4.42. Comparison of the Effect of Orifice Diameter on Normalized Mass Flux Distributions at y and z-axes

4.1.3.2. Normalized Droplet Count

The normalized droplet count distributions obtained by the injectors with different orifice diameters are given in Figure 4.43. Distribution plots show that orifice diameter has a significant effect on the normalized droplet count. Similar to the normalized mass flux distribution, the normalized droplet count improves with a decrease in the orifice diameter.

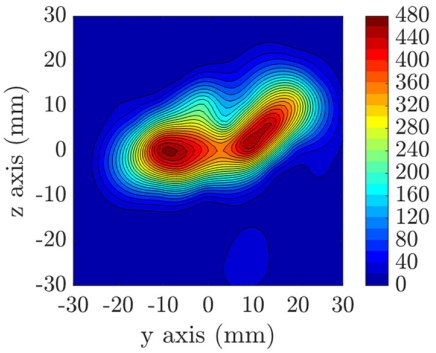

a) Injector T600855, orifice diameter = 0.8 mm

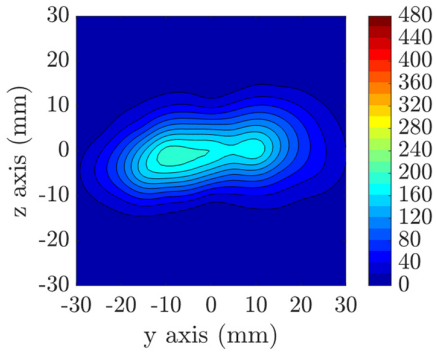

b) Injector T601055, orifice diameter = 1.0 mm

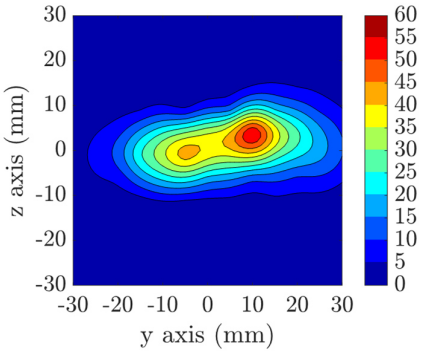

c) Injector T601255, orifice diameter = 1.2 mm

Figure 4.43. The Effect of Orifice Diameter on Normalized Droplet Count

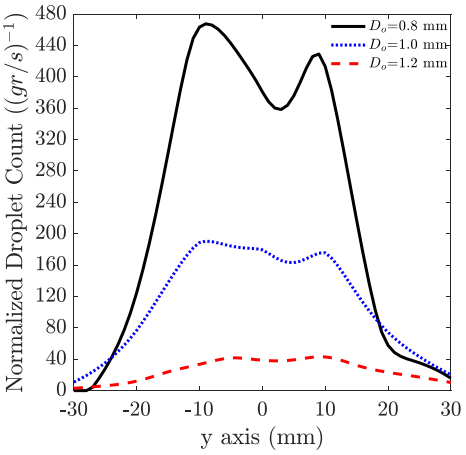

Figure 4.44. Comparison of the Effect of Orifice Diameter on Normalized Droplet Count at y-axis

Figure 4.44 shows the comparison of the effect of orifice diameter on the normalized droplet count along the y-axis. The highest normalized droplet count is increased by almost 300% with a decrease in the orifice diameter by 20% from 1 mm to 0.8 mm, and is decreased by 80% with an increase in the orifice diameter by 20% from 1 mm to 1.2 mm.

4.1.3.3. Normalized Axial Velocity

Figure 4.45 shows the axial velocity distribution of injectors with different orifice diameters. With the decrease of the orifice diameter, the maximum axial velocity becomes higher, as expected.

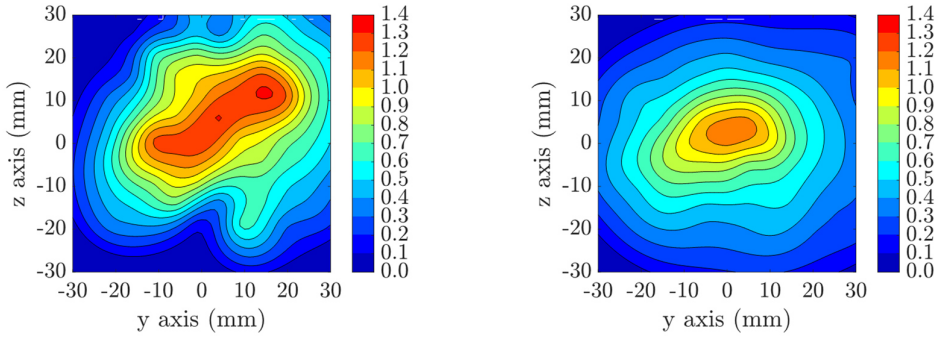

a) Injector T600855, orifice diameter = 0.8 mm

b) Injector T601055, orifice diameter = 1.0 mm

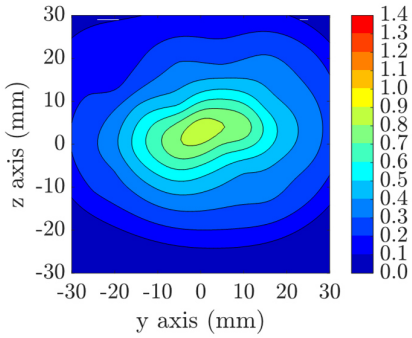

c) Injector T601255, orifice diameter = 1.2 mm

Figure 4.45. The Effect of Orifice Diameter on Normalized Axial Velocity

Figure 4.46 shows the comparison of the effect of the orifice diameter on the normalized axial velocity along the y-axis. The maximum axial velocity increases by 20% with the decrease of the orifice diameter by 20% from 1 mm to 0.8 mm, and decreases by 25% with the increase of the orifice diameter by 20% from 1mm to 1.2 mm.

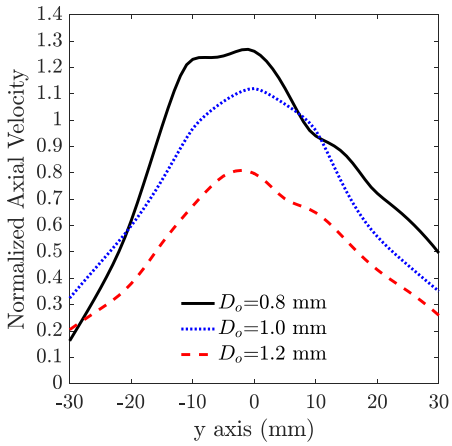

Figure 4.46. Comparison of the Effect of Orifice Diameter on Normalized Axial Velocity at y-axis

4.1.3.4. Normalized V Velocity

Figure 4.47 shows the normalized V velocity distribution obtained from the injectors with different orifice diameters. The normalized V velocity distribution shows similar trends with the normalized mass flux distribution. In terms of the magnitude, V velocity decreases with the increase of the orifice diameter.

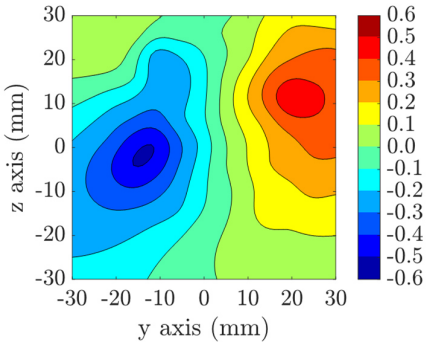

a) Injector T600855, orifice diameter = 0.8 mm

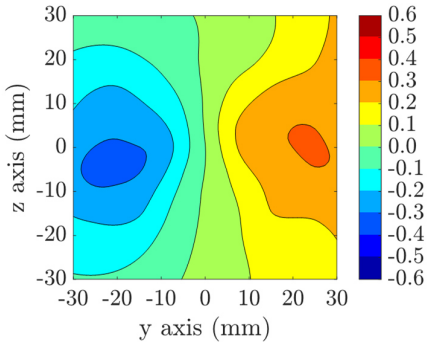

b) Injector T601055, orifice diameter = 1.0 mm

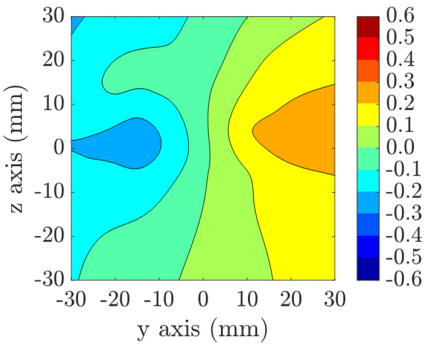

c) Injector T601255, orifice diameter = 1.2 mm

Figure 4.47. The Effect of Orifice Diameter on Normalized V Velocity

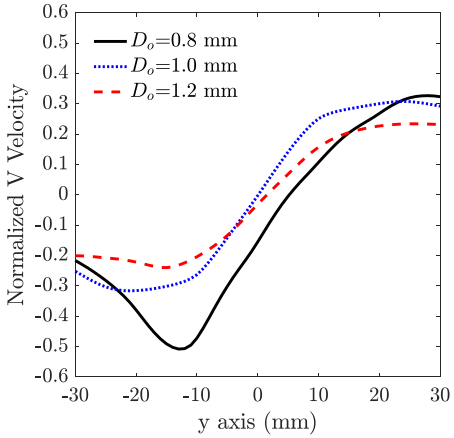

Figure 4.48. Comparison of the Effect of Orifice Diameter on Normalized V Velocity at y-axis

In Figure 4.48, the comparison of the normalized V velocity distribution along the y-axis with respect to the change in the orifice diameters of injectors is given. Since the distribution of the 0.8 mm injectors is tilted on the right section, the maximum V velocity of this case is not reflected on the y-axis in the comparison. However, the comparison of the V velocity magnitude of the left section shows a trend depending on the orifice diameter. With the increase of the orifice diameter, the magnitude of V velocity becomes smaller. The change is obvious between 1 mm and 0.8 mm with an increase of 70% with 0.8 mm. The increase of the orifice diameter from 1 mm to 1.2 mm results in a decrease of 30% in the V velocity magnitude.

4.1.3.5. Normalized W Velocity

Figure 4.49 shows the normalized W velocity distributions for different orifice diameters. The normalized W velocity distribution decreases with an increase in the orifice diameter in terms of the magnitude as expected due to the results of the normalized mass flux distributions of the same injectors.

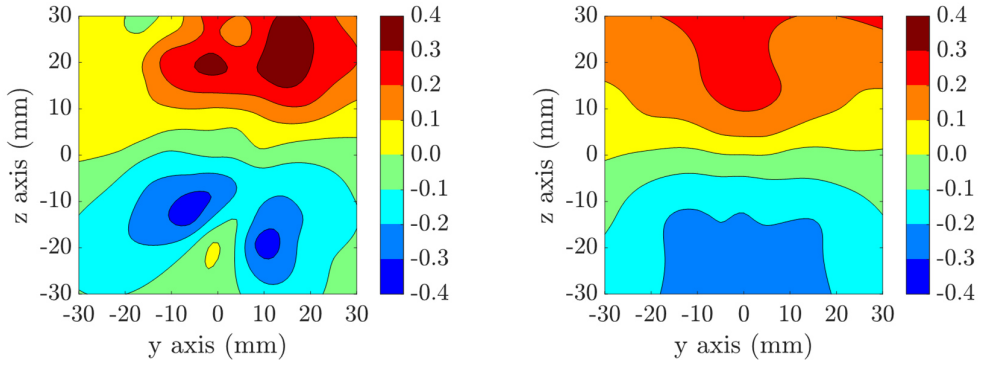

a) Injector T600855, orifice diameter = 0.8 mm

b) Injector T601055, orifice diameter = 1.0 mm

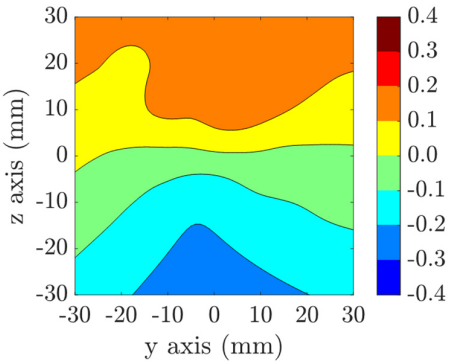

c) Injector T601255, orifice diameter = 1.2 mm

Figure 4.49. The Effect of Orifice Diameter on Normalized W Velocity

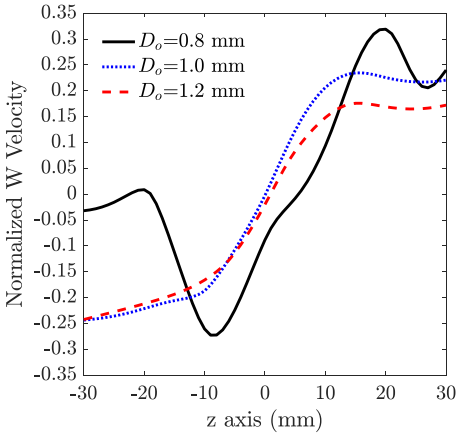

Figure 4.50. Comparison of the Effect of Orifice Diameter on Normalized W Velocity at z-axis

In Figure 4.50, the normalized W velocity distribution along the z-axis can be seen. The normalized W velocity distribution along z-axis shows that it is inversely proportional to the orifice diameter in terms of magnitude, which is linked to the normalized droplet count distribution.

4.1.3.6. Normalized Velocity Magnitude

Figure 4.51 shows the normalized velocity magnitude distributions obtained by the triplet injectors with different orifice diameters.

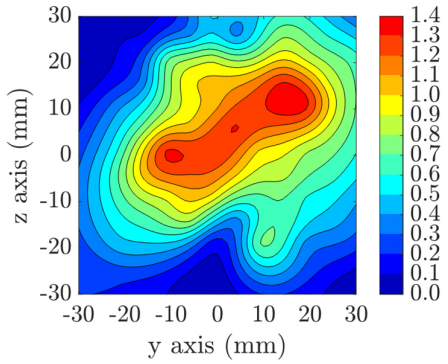

a) Injector T600855, orifice diameter = 0.8 mm

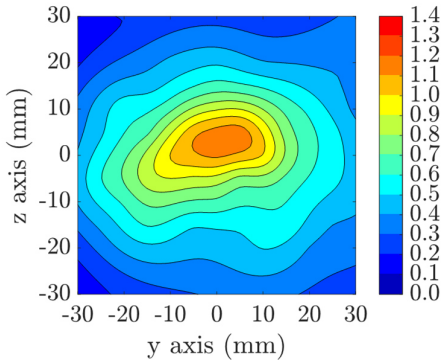

b) Injector T601055, orifice diameter = 1.0 mm

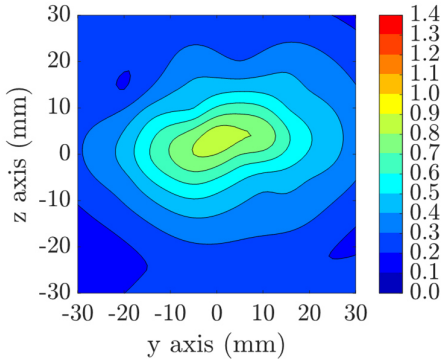

c) Injector T601255, orifice diameter = 1.2 mm

Figure 4.51. The Effect of Orifice Diameter on Normalized Velocity Magnitude

The normalized velocity magnitude distributions show similar trends with other velocity distributions as expected.

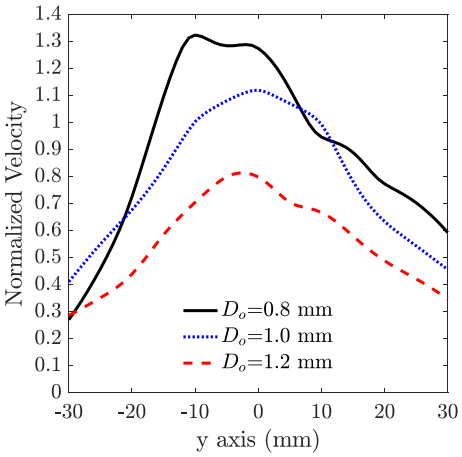

Figure 4.52. Comparison of the Effect of Orifice Diameter on Normalized Velocity Magnitude at y-axis

In Figure 4.52, the comparison of normalized velocity magnitude distribution along the y-axis is given. With a decrease of orifice diameter from 1 mm to 0.8 mm, the maximum value of the normalized velocity magnitude increases by 20%. An increase in the orifice diameter from 1 mm to 1.2 mm results in a decrease by 30% in the normalized velocity magnitude.

4.1.3.7. SMD Distribution

Figure 4.53 shows the SMD distribution with injectors of different orifice diameters.

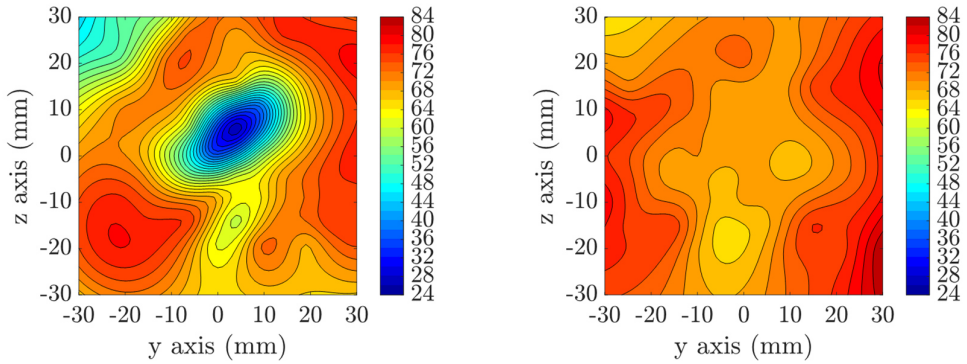

a) Injector T600855, orifice diameter = 0.8 mm

b) Injector T601055, orifice diameter = 1.0 mm

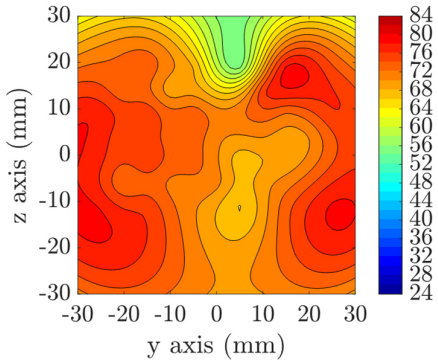

c) Injector T601255, orifice diameter = 1.2 mm

Figure 4.53. The Effect of Orifice Diameter on SMD

The SMD distributions show similar results with velocity distributions. The change in the orifice diameter from 1 mm to 0.8 mm reduces the SMD at the center, however, the increase from 1 mm to 1.2 mm causes only a slight change in the SMD.

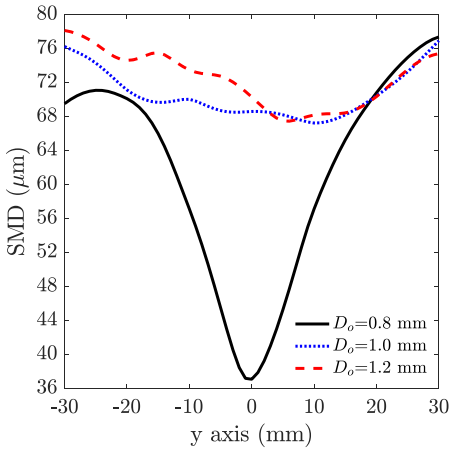

Figure 4.54. Comparison of the Effect of Orifice Diameter on SMD at y-axis

Figure 4.54 shows the comparison of the effect of the orifice diameter on SMD along the y-axis. The decrease in the orifice diameter from 1 mm to 0.8 mm leads to a decrease of the minimum SMD by half although the increase from 1 mm to 1.2 mm of the orifice diameter doesn't affect the SMD distribution.

4.1.3.8. Rosin-Rammler Distribution

The Rosin-Rammler distributions of injectors with different orifice diameters are shown in Figure 4.55.

Decrease in the orifice diameter causes an increase in the q parameter, which indicates that the spray becomes more uniform.

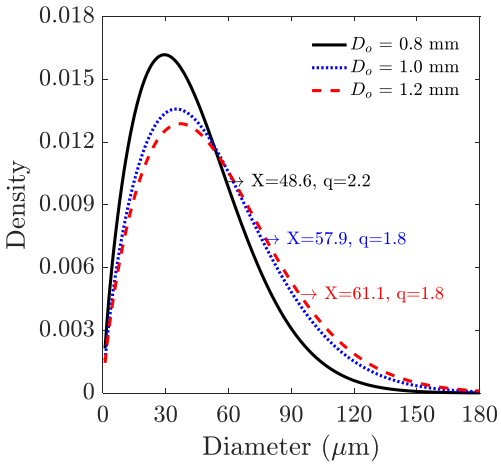

Figure 4.55. Comparison of Rosin-Rammler Distributions

4.1.3.9. Total Normalized Droplet Count

The change in the total normalized droplet count as a function of the orifice diameter is given in Figure 4.56.

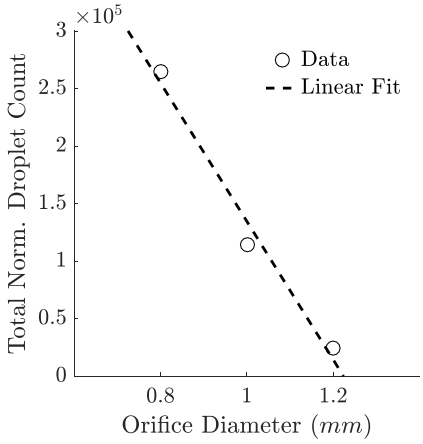

Figure 4.56. Comparison of the Effect of Orifice Diameter on Total Normalized Droplet Count

Impingement distance, orifice l/d ratio, impingement angle and momentum ratio were kept constant while the following results were obtained. The total normalized droplet count is significantly decreasing with the orifice diameter increase.

4.1.3.10. Mean D10

The change in the mean diameter as a function of the orifice diameter is given in Figure 4.57.

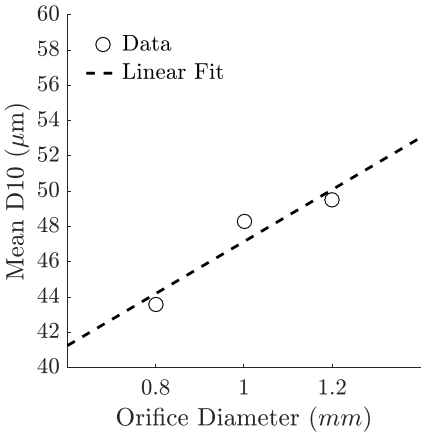

Figure 4.57. Comparison of the Effect of Orifice Diameter on Mean D10

In a similar fashion, the impingement distance, orifice l/d ratio, impingement angle and momentum ratio were kept constant in obtaining these results. The mean diameter increases with an increase in orifice diameter.

4.1.3.11. Mean SMD

The change in the mean SMD as a function of orifice diameter is given in Figure 4.58. The mean SMD is proportional to orifice diameter. The orifice diameter has the greatest effect on the mean SMD over all other parameters examined in this thesis study.

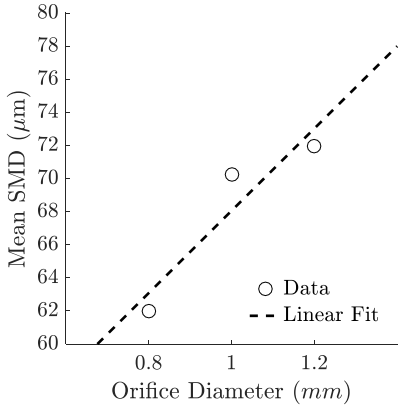

Figure 4.58. Comparison of the Effect of Orifice Diameter on Mean SMD

4.1.3.12. Spray Angle

Next, the change in the spray angle with respect to the orifice diameter is given in Figure 4.59. As it is seen, the spray angle is proportional to the orifice diameter.

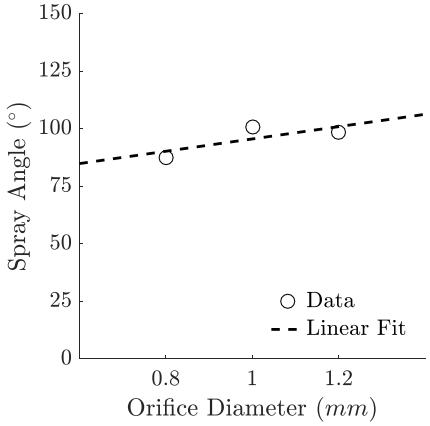

Figure 4.59. Comparison of the Effect of Orifice Diameter on Spray Angle

4.1.4. The Effect of Impingement Angle

In this section, the effect of impingement angle for triplet injectors on normalized mass flux, velocity, droplet count distributions, droplet statistics and spray angles

will be discussed. Impingement distance, orifice l/d ratio, orifice diameter and momentum ratio were kept constant while the following results were obtained.

4.1.4.1. Normalized Mass Flux Distribution

Figure 4.60 shows the effect of the impingement angle on the spray shape. The measurements for the injector with 45° impingement angle had to be performed at a plane 160 mm downstream of the impingement point instead of 80 mm, but the results are projected to 80 mm with the method explained below to make a one-to-one comparison.

The findings of Hines et al. (Hines, Schuman, Ford and Fertig, 1972) suggest that the mass flux distributions obtained from triplet injectors can be defined by Equations *(29)* and *(30)*.

$$w_o = \frac{w_{001_o}}{z^2} \mathrm{e}^{\left(-a_o\left(\frac{x}{z}\right)^2 - b_o\left(\frac{y}{z}\right)^2\right)} \qquad (29)$$

$$w_i = \frac{w_{001_i}}{z^2}\left[1 + c_i\left(\frac{x}{z}\right)^2\right] \mathrm{e}^{\left(-a_i\left(\frac{x}{z}\right)^2 - b_i\left(\frac{y}{z}\right)^2\right)} \qquad (30)$$

Here, w_{001} is the normalization factor equivalent to mass flux, and a, b, and c are the spray coefficients defined for the inner and outer orifices that are deduced from the experimental data. Hines et al. (Hines, Schuman, Ford and Fertig, 1972) defines the z-axis as the vertical direction that the spray develops, with x and z-axes being switched compared to the coordinate system used in the current setup. Taking this into account, the spray coefficients for the injector with 45° impingement angle are determined using the mass flux measurements at x=160 mm downstream of the impingement point, as follows: a_o=11.4, b_o=145.2, a_i=19.9, b_i=342.8, and c_i=14.8. Then, the measurements were projected onto x=80 mm using this set of coefficients.

Figure 4.60 shows that with the increase of the impingement angle, the normalized mass flux distributions become more evenly distributed. The mass flow rates and orifice properties are kept almost constant for all injectors. The driven parameter in

the distribution is the lateral momentum at the impingement point that triggers the impact waves on the liquid sheet and results in the break up into ligaments and droplets. Decrease in the impingement angle causes the lateral momentum originating from the outer orifices to decrease, thus, the mass flux grows in the axial direction without a break up for a longer time and cannot be evenly distributed until the jet reaches the measurement plane.

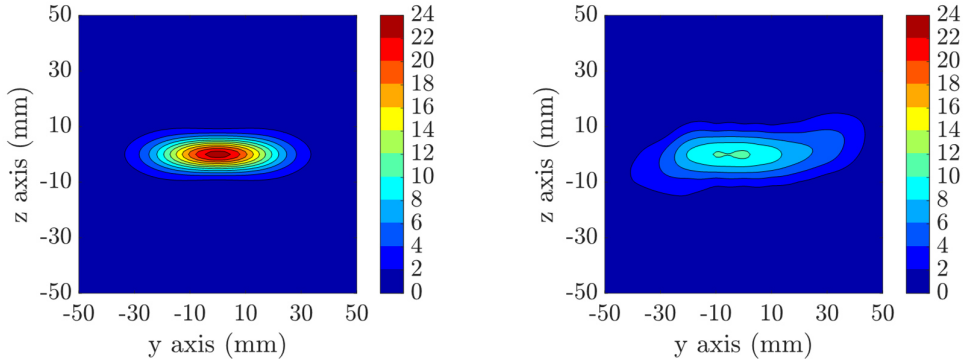

a) Injector T451055, impingement angle = 45°

b) Injector T601055, impingement angle = 60°

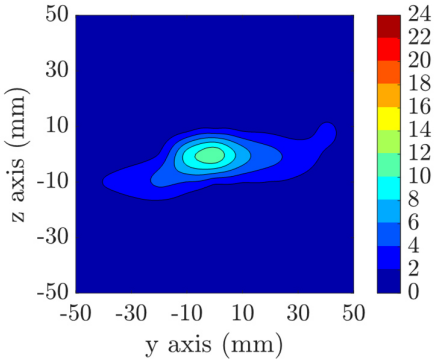

c) Injector T901055, impingement angle = 90°

Figure 4.60. The Effect of Impingement Angle on Normalized Mass Flux Distribution

Figure 4.61 shows the normalized mass flux distributions obtained from the triplets with different impingement angles. There is a sharp drop in the peak value of the mass flux as the impingement angle is increased from 45° to 60°, but further increase

from 60° to 90° does not create an observable difference in the peak value. On the other hand, a more even distribution is observable with the 60° angle compared to the 90° angle at this MR level.

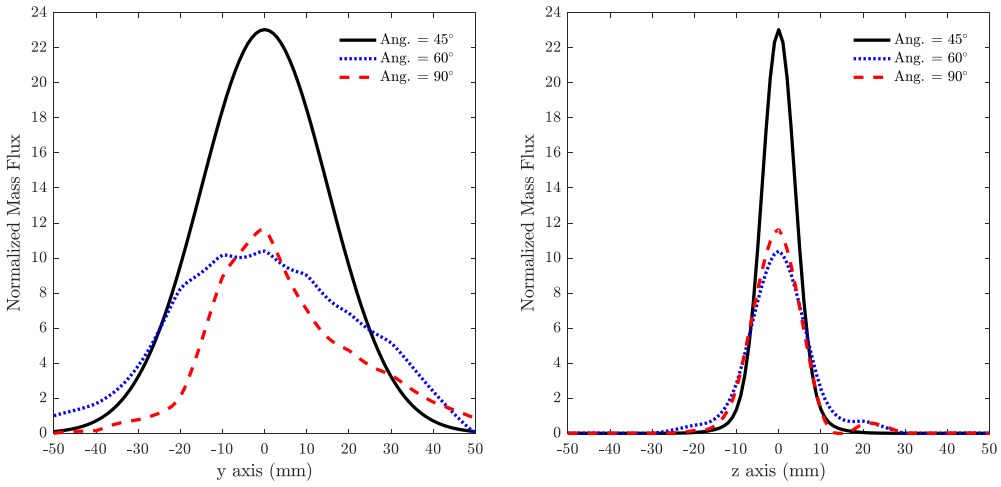

a) along y-axis b) along z-axis

Figure 4.61. Comparison of the Effect of Impingement Angle on Normalized Mass Flux Distributions at y and z-axes

4.1.4.2. Normalized Droplet Count

Figure 4.62 shows the normalized droplet count distribution of injectors with different impingement angles. The normalized droplet count distributions show that the normalized droplet count is proportional to the impingement angle. There are two distinct peaks appearing for the 45° impingement case. As the angle is increased, the droplet count increases at these spots and the spray spreads over a wider region as well in the lateral direction.

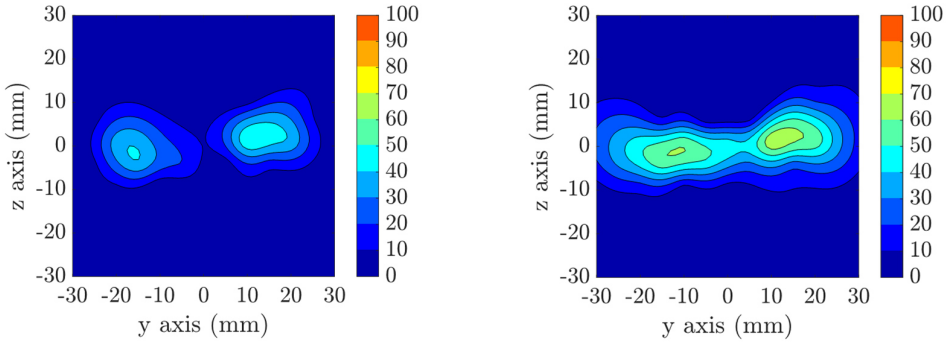

a) Injector T451055, impingement angle = 45°

b) Injector T601055, impingement angle = 60°

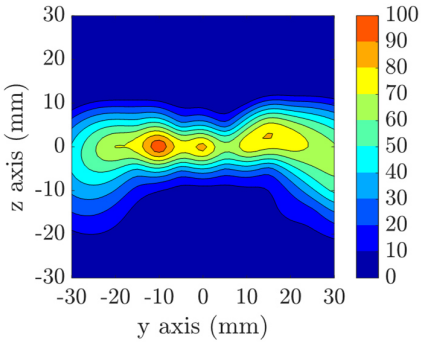

c) Injector T901055, impingement angle = 90°

Figure 4.62. The Effect of Impingement Angle on Normalized Droplet Count

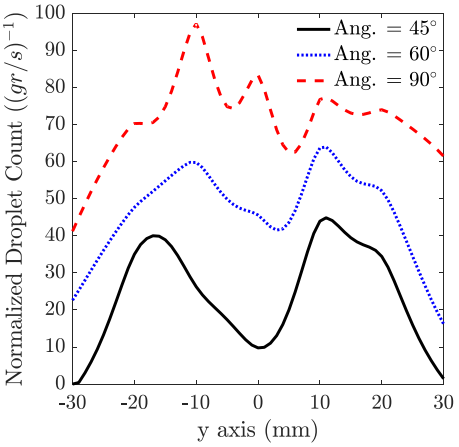

Figure 4.63. Comparison of the Effect of Impingement Angle on Normalized Droplet Count at y-axis

Figure 4.63 combines these three distributions, where the two peaks are the most visible for the 45° angle. The normalized droplet count is also the lowest for this case. Increase in the impingement distance from 45° to 60° leads to 70% increase in the normalized droplet count. With further increase up to 90°, the maximum normalized droplet count becomes 3 times higher than that of the case with 45°.

4.1.4.3. Normalized Axial Velocity

The normalized axial velocity distributions of injectors with different impingement angles are given in Figure 4.64. It is seen that the increase in the impingement angle causes a slight decrease in the normalized axial velocity.

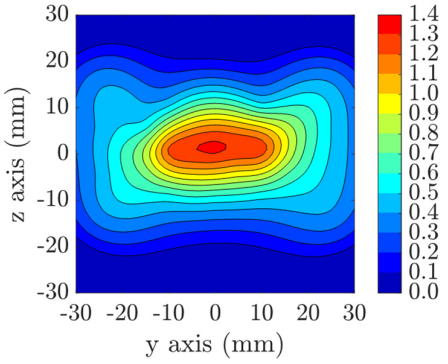

a) Injector T451055, impingement angle = 45°

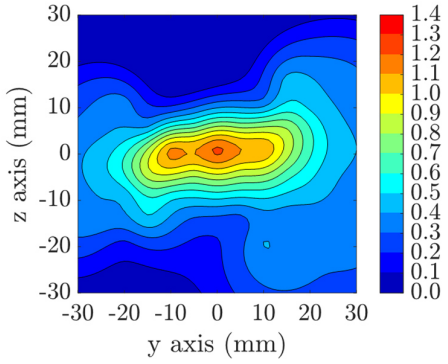

b) Injector T601055, impingement angle = 60°

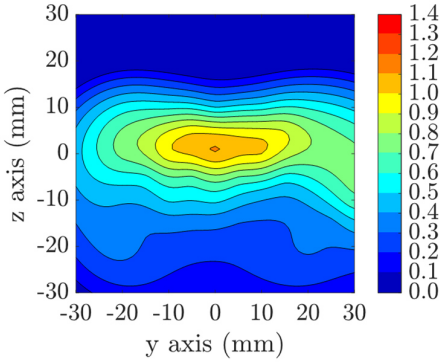

c) Injector T901055, impingement angle = 90°

Figure 4.64. The Effect of Impingement Angle on Normalized Axial Velocity

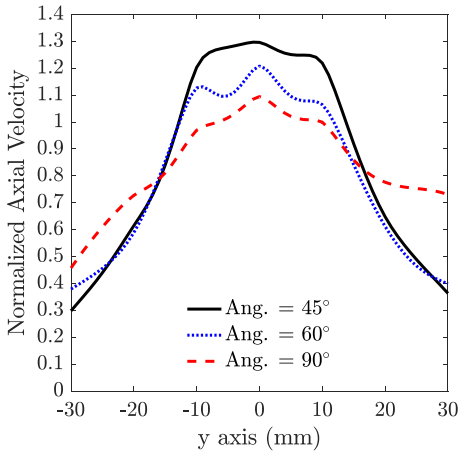

Figure 4.65. Comparison of the Effect of Impingement Angle on Normalized Axial Velocity at y-axis

In Figure 4.65, the normalized axial velocity profiles of injectors with different impingement angles are compared at the momentum ratio that was around 2. Decrease in the impingement angle from 90° to 45° results in 30% increase in the normalized axial velocity.

4.1.4.4. Normalized V Velocity

The normalized V velocity distribution of injectors with different impingement angles are given in Figure 4.66. Similar to spray dispersion of the injectors, increase in the impingement angle results in an increase in the normalized V velocity distribution in terms of magnitude.

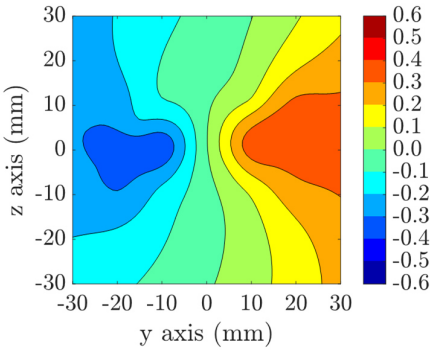

a) Injector T451055, impingement angle =45°

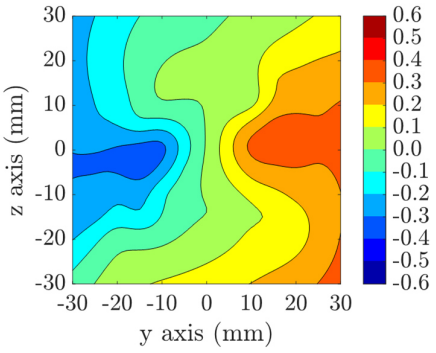

b) Injector T601055, impingement angle =60°

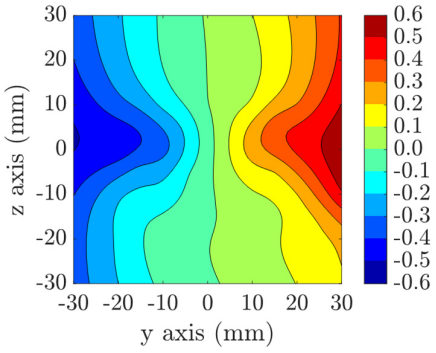

c) Injector T901055, impingement angle =90°

Figure 4.66. The Effect of Impingement Angle on Normalized V Velocity

The normalized lateral velocity profiles from all three injectors with different angles are given in Figure 4.67. In the core part of the spray, all profiles have similar trends in contrast to the significant differences observed in the normalized axial velocity distributions of Figure 4.65 in the same region. However, it becomes more clear towards the spray edges that the velocity profile for the 90° impingement angle shows rather a linear trend unlike its counterparts at 45° and 60°.

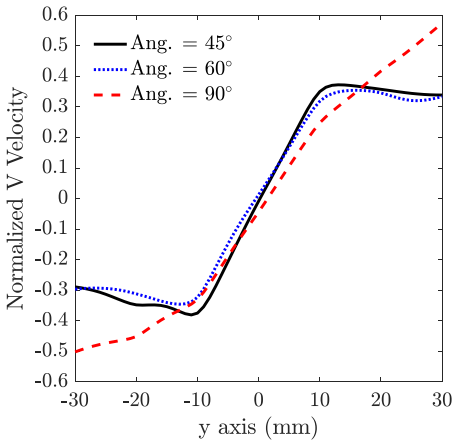

Figure 4.67. Comparison of the Effect of Impingement Angle on Normalized V Velocity at y-axis

4.1.4.5. Normalized W Velocity

The normalized W velocity distributions of injectors with different impingement angles are given in Figure 4.68. A highly correlated relation between the impingement angle and the normalized W velocity distribution cannot be observed.

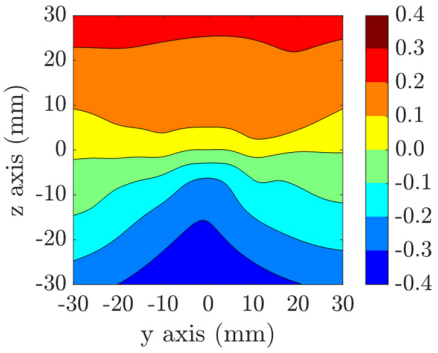

a) Injector T451055, impingement angle = 45°

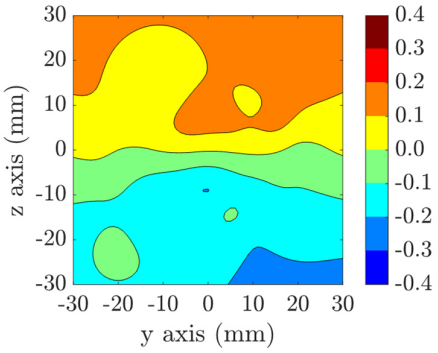

b) Injector T601055, impingement angle = 60°

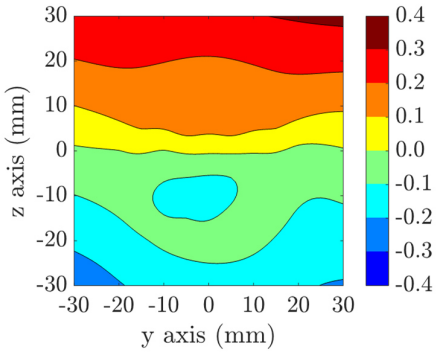

c) Injector T901055, impingement angle = 90°

Figure 4.68. The Effect of Impingement Angle on Normalized W Velocity

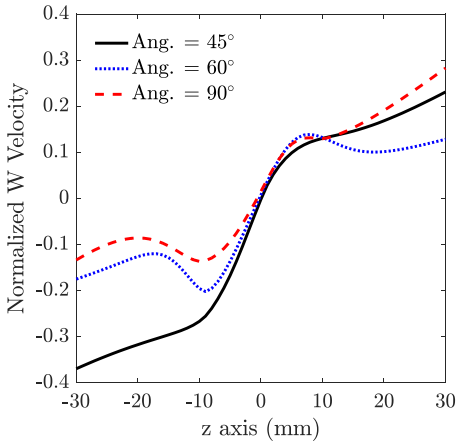

Figure 4.69. Comparison of the Effect of Impingement Angle on Normalized W Velocity at z-axis

A comparison of the effect of the impingement angle on the normalized W velocity along z-axis is given in Figure 4.69. Similar to what is observed with the contour plots, a direct relation cannot be observed.

4.1.4.6. Normalized Velocity Magnitude

The normalized velocity magnitude distribution of injectors with different impingement angles are given in Figure 4.70.

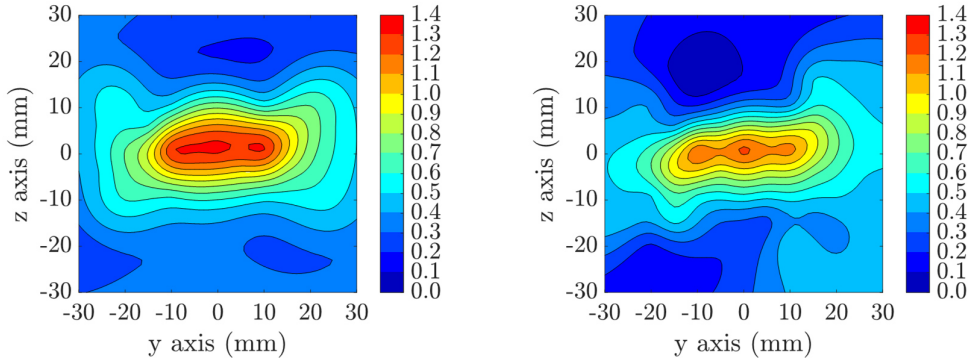

a) Injector T451055, impingement angle = 45°

b) Injector T601055, impingement angle = 60°

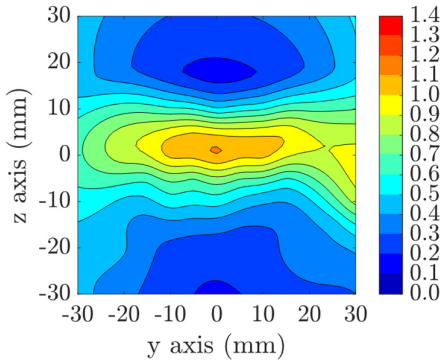

c) Injector T901055, impingement angle = 90°

Figure 4.70. The Effect of Impingement Angle on Normalized Velocity Magnitude

The normalized velocity magnitude decreases with an increase in the impingement angle.

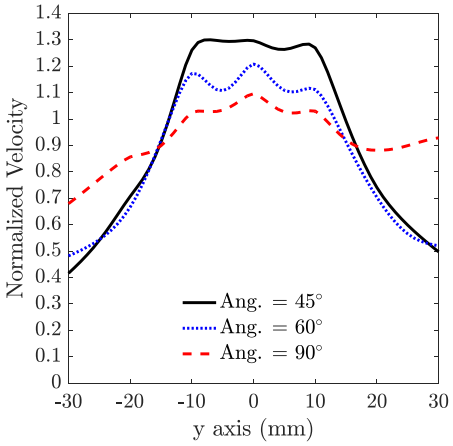

Figure 4.71. Comparison of the Effect of Impingement Angle on Normalized Velocity Magnitude at y-axis

In Figure 4.71, the comparison of the effect of impingement angle on the normalized velocity magnitude along the y-axis is given. The results show similarity to the axial velocity distributions as expected.

4.1.4.7. SMD Distribution

The SMD distribution of injectors with different triplet injectors are given in Figure 4.72.

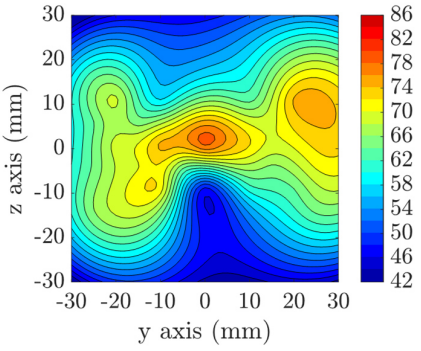

a) Injector T451055, impingement angle = 45°

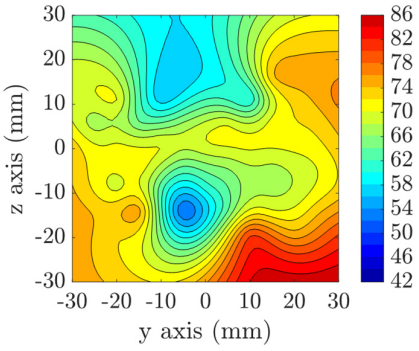

b) Injector T601055, impingement angle = 60°

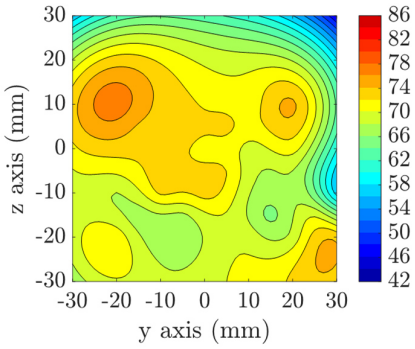

c) Injector T901055, impingement angle = 90°

Figure 4.72. The Effect of Impingement Angle on SMD

In contrary to previous findings, the highest SMD for the 45-impingement angle injector is seen at the center, which shows that effective atomization cannot be obtained. The SMD distribution indicating smaller values along the z-axis can be seen with the 60-impingement angle injector compared to the 90-impingement angle. In the 90-impingement angle injector, the resultant spray and atomized droplets spread on a larger area in a more uniform fashion.

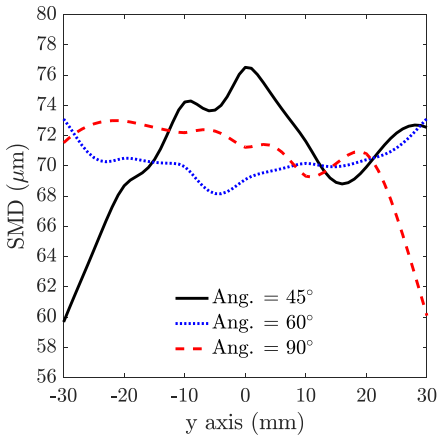

Figure 4.73. Comparison of the Effect of Impingement Angle on SMD at y-axis

Figure 4.73 shows the SMD profiles of the three tests with different impingement angles at the same flow conditions. At the core part, the highest SMD belongs to the

45° impingement angle and the lowest value is obtained at the 60° impingement angle, yet, an important difference in 60° and 90° injectors cannot be obtained.

4.1.4.8. Rosin-Rammler Distribution

The Rosin-Rammler distributions of injectors with different impingement angles are shown in Figure 4.74. While the q parameter doesn't change significantly with the impingement angle, X parameter increases in coherent to previous findings.

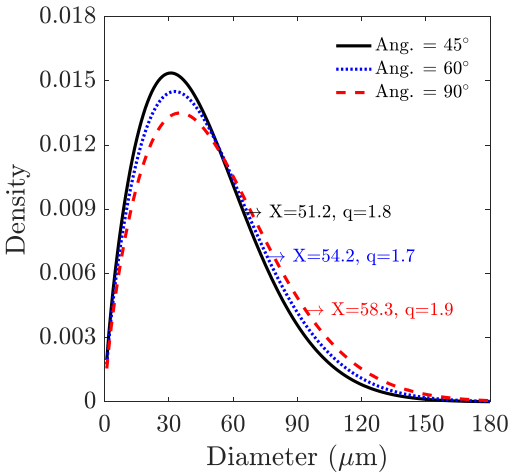

Figure 4.74. Comparison of Rosin-Rammler Distributions

4.1.4.9. Total Normalized Droplet Count

The change in the total normalized droplet count with the impingement angle is given in Figure 4.75. The total normalized droplet count increases with the impingement angle.

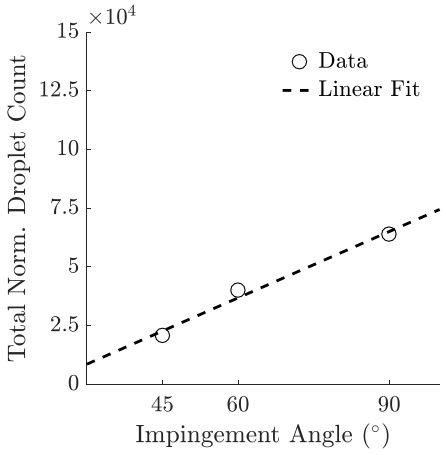

Figure 4.75. Comparison of the Effect of Impingement Angle on Total Normalized Droplet Count

4.1.4.10. Mean D10

The change in the arithmetic mean diameter as a function of impingement angle is given in Figure 4.76. The mean D10 has an increasing trend with the impingement angle.

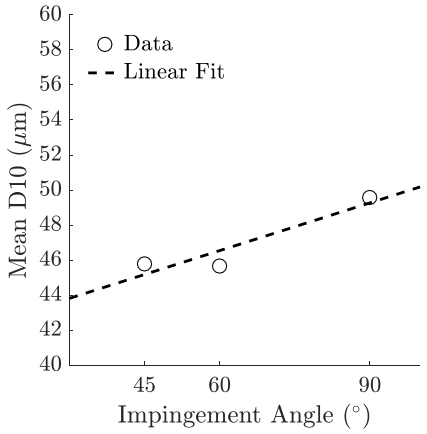

Figure 4.76. Comparison of the Effect of Impingement Angle on Mean D10

4.1.4.11. Mean SMD

The change in mean SMD as a function of impingement angle is given in Figure 4.77.

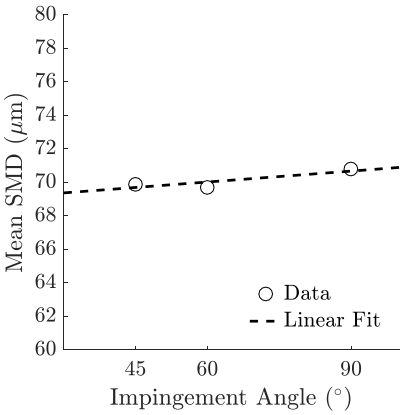

Figure 4.77. Comparison of the Effect of Impingement Angle on Mean SMD

The mean SMD gradually increases with an increase in the impingement angle.

4.1.4.12. Spray Angle

The change in the spray angle with respect to the impingement angle is given in Figure 4.78. The impingement angle increases with an increase in the impingement angle.

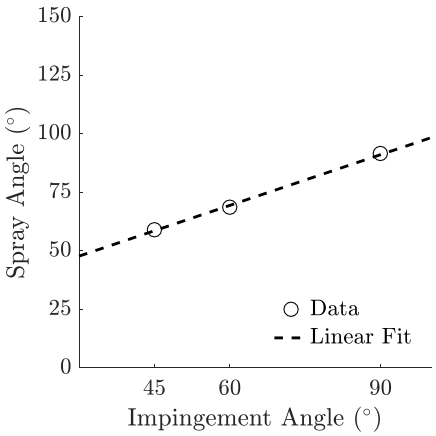

Figure 4.78. Comparison of the Effect of Impingement Angle on Spray Angle

4.1.5. The Effect of Momentum Ratio (60° Impingement Angle Injector)

In this section, the effect of momentum ratio on triplet injector with 60° impingement angle on normalized mass flux, velocity, droplet count distributions, droplet statistics and spray angles will be discussed. Impingement distance, orifice l/d ratio, orifice diameter and impingement angle were kept constant while the following results were obtained. It should be noted that in obtaining the MR values, the mass flow rate through the inner orifice was decreased first by 29.5% and then by 27.3% for the first three cases while the mass flow rate through the outer orifices was increased by 3.8% and 1%, respectively. For the last case with MR = 12.91, this value was maintained by increasing the mass flow rate through the outer orifice by 20.2% and decreasing the mass flow rate through the inner orifice by 3.4%.

4.1.5.1. Normalized Mass Flux Distribution

In Figure 4.79, contour plots for the normalized mass flux distributions at three different momentum ratios are given for the triplet injector with 60° impingement angle.

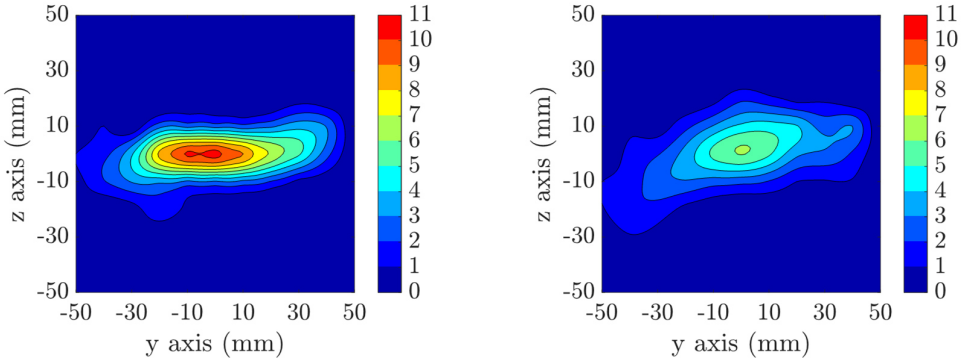

a) Injector T601055, MR = 1.99 b) Injector T601055, MR = 4.32

c) Injector T601055, MR = 8.34 d) Injector T601055, MR = 12.91

Figure 4.79. The Effect of Momentum Ratio on Normalized Mass Flux Distribution

At the momentum ratio of MR=1.99, the spray seems to have more of an elliptical distribution. As the momentum ratio increases, however, the observed distribution transforms into a rather circular shape. The contours reflect a narrower spray distribution in the horizontal direction with an increase in the momentum ratio due to the fact that the spray becomes so dilute in the outskirts that the normalized mass flux becomes smaller than 1 although it spreads on a greater region.

In Figure 4.80, the normalized mass flux distribution along the spray fan centerline is given for all momentum ratio values. There is an observable decrease in the peak value of the normalized mass flux as the momentum ratio is increased. The distributions become more uniform suggesting improved mixing.

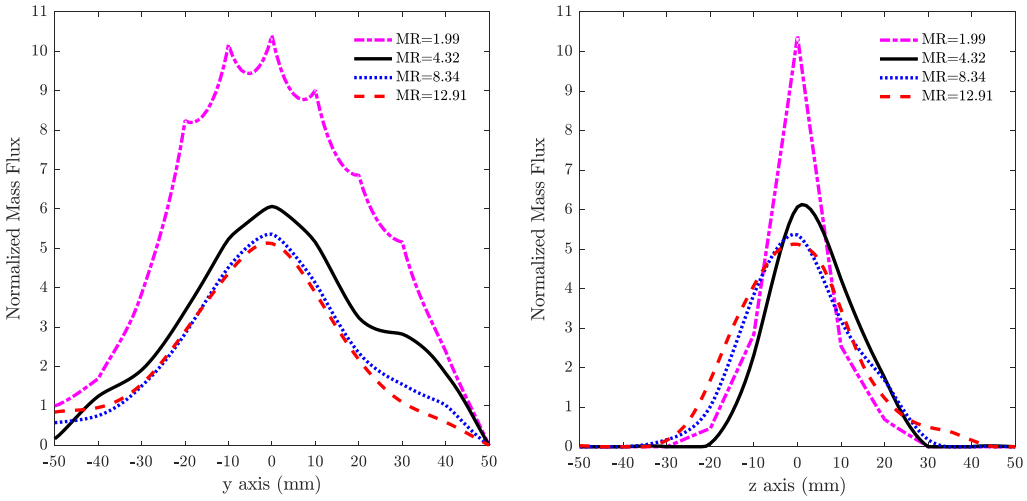

a) along y-axis b) along z-axis

Figure 4.80. Comparison of the Effect of Momentum Ratio on Normalized Mass Flux Distributions at y and z-axes

The response of the normalized mass flux distribution to increasing the momentum ratio is similar to the one obtained with doublet injectors by Vassallo et al. (Vassallo, Ashgriz, and Boorady, 1992). Also, they showed that the increase in the flow rate results in a decrease in the droplet diameter and an increase in the droplet density and velocity.

4.1.5.2. Normalized Droplet Count

Figure 4.81 shows the normalized droplet count distribution of injectors with different momentum ratios. As expected, the normalized droplet count increases with the increase in momentum ratio.

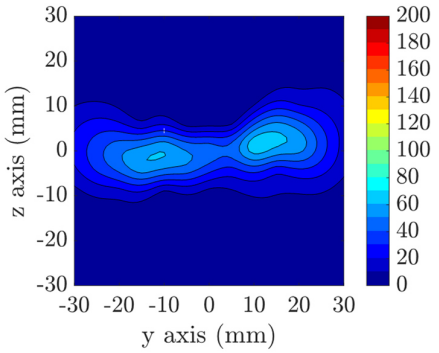

a) Injector T601055, MR = 1.99

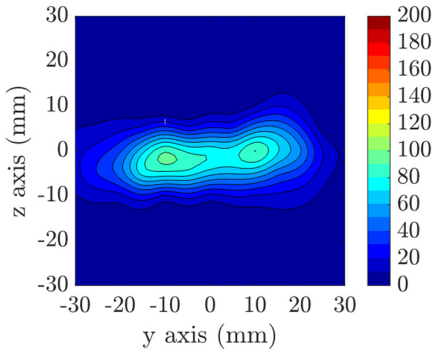

b) Injector T601055, MR = 4.32

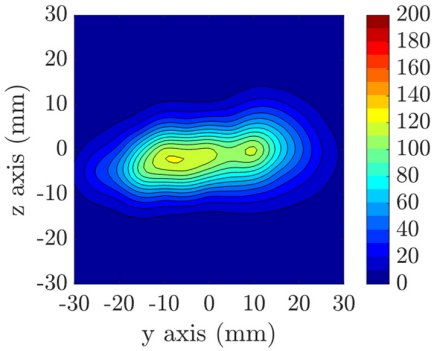

c) Injector T601055, MR = 8.34

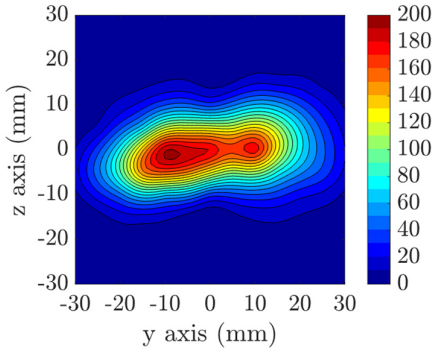

d) Injector T601055, MR = 12.91

Figure 4.81. The Effect of Momentum Ratio (60° Impingement Angle Injector) on Normalized Droplet Count

In Figure 4.82, the distributions of the normalized droplet count for the 60° impingement angle are presented. The contours suggest a continuous increase in the droplet count with momentum ratio, revealing that the optimum point has not been reached yet even at the highest MR.

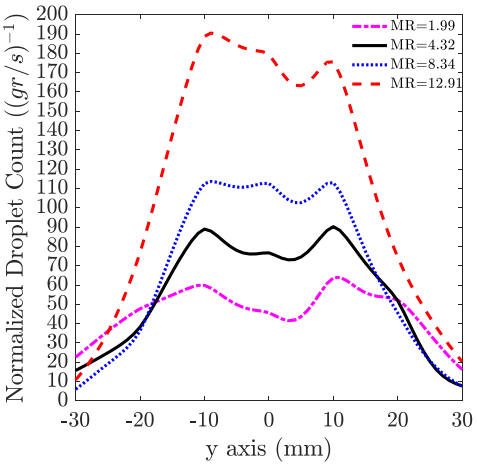

Figure 4.82. Comparison of the Effect of Momentum Ratio (60° Impingement Angle Injector) on Normalized Droplet Count at y-axis

Although the mass flux distributions at MR=8.34 and MR=12.91 showed similarities in terms of shape and magnitude, the droplet count achieved at MR=12.91 is significantly higher compared to that at MR=8.34 according to Figure 4.82. This is because while the higher momentum ratio results in better atomization giving a larger number of droplets in the vicinity of the impingement point (x=30 mm in Figure 4.82), the differences in the momentum flux start to diminish as the flow slows down and spray keeps evolving further downstream (x=80 mm). Unlike the mass flux and axial velocity profiles, the normalized droplet count profiles in Figure 4.82 have two separate peak points at approximately +/- 10 mm away from the center. These locations do not change with momentum ratio; however, the droplet count is affected noticeably. These regions of high droplet count across the volume of the spray reflect the most effective mixing of the jets.

4.1.5.3. Normalized Axial Velocity

The normalized axial velocity distributions of injectors with different impingement angles are given in Figure 4.83. A distinct change with respect to momentum ratio on the normalized axial velocity is not observed.

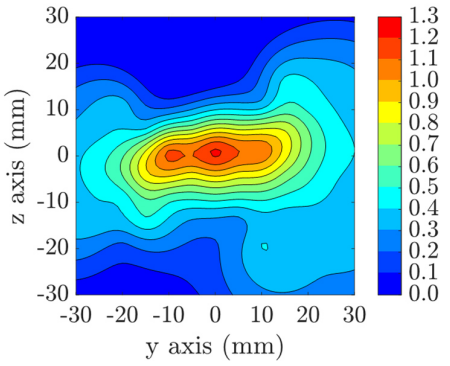

a) Injector T601055, MR = 1.99

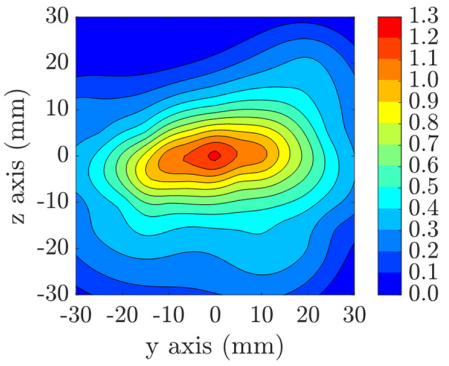

b) Injector T601055, MR = 4.32

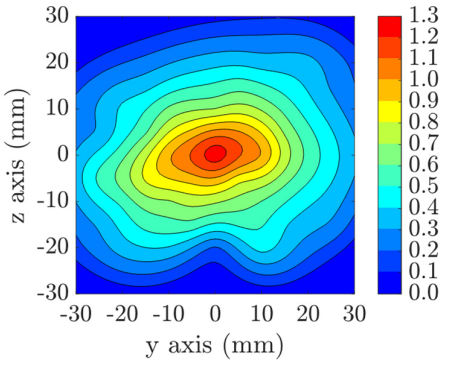

c) Injector T601055, MR = 8.34

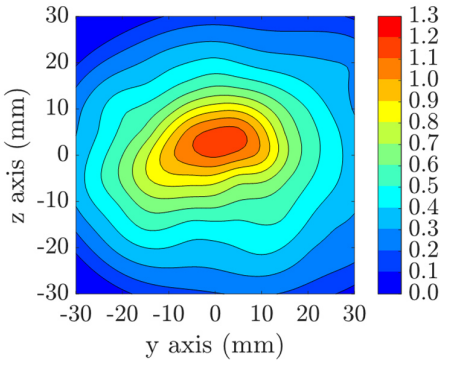

d) Injector T601055, MR = 12.91

Figure 4.83. The Effect of Momentum Ratio (60° Impingement Angle Injector) on Normalized Axial Velocity

In Figure 4.84, the axial velocity profiles obtained in the tests with the injectors with 60° impingement angle are given. For the 60° impingement angle, the velocity reaches its maximum at the center as expected and reduces by more than 50 % in the lateral direction at 30 mm away from the origin. In terms of the distribution, the results show similarities to those for the normalized mass flux. However, while the peak values of the axial velocity component stay rather at similar levels as MR is increased from 4.32 to 8.34 at Plane 1, this causes a clear drop in the peak values of the normalized mass flux, as the spray keeps developing downstream of the impingement point.

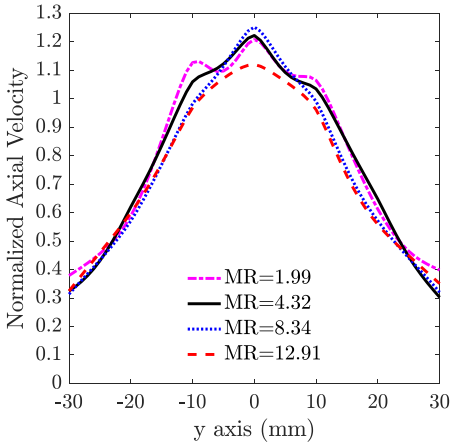

Figure 4.84. Comparison of the Effect of Momentum Ratio (60° Impingement Angle Injector) on Normalized Axial Velocity at y-axis

In the lateral direction, the axial velocity curves seem to be fairly collapsing for all MR values.

4.1.5.4. Normalized V Velocity

The normalized V velocity distribution of injectors with different impingement angles are given in Figure 4.85. The behavior of the distribution stays the same for all cases.

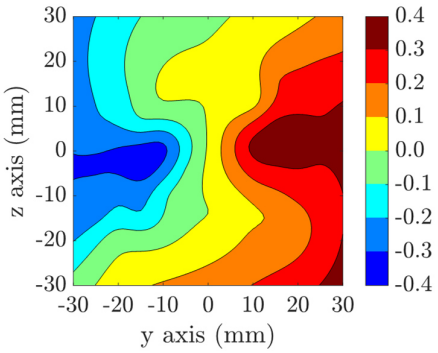

a) Injector T601055, MR = 1.99

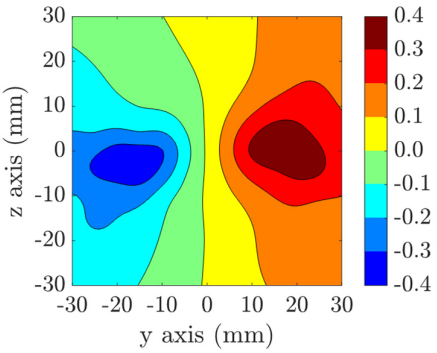

b) Injector T601055, MR = 4.32

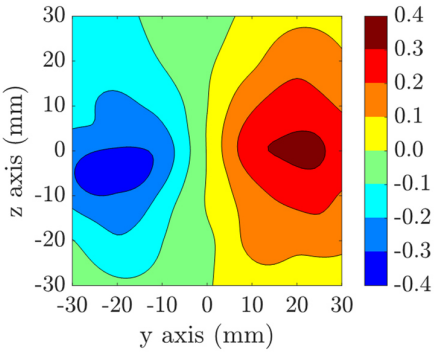

c) Injector T601055, MR = 8.34

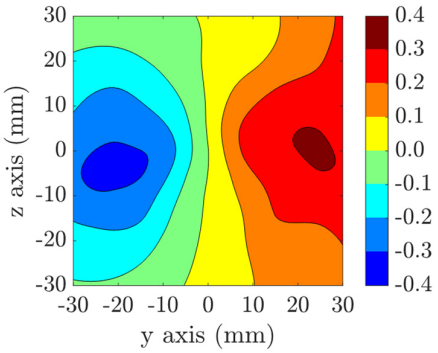

d) Injector T601055, MR = 12.91

Figure 4.85. The Effect of Momentum Ratio (60° Impingement Angle Injector) on Normalized V Velocity

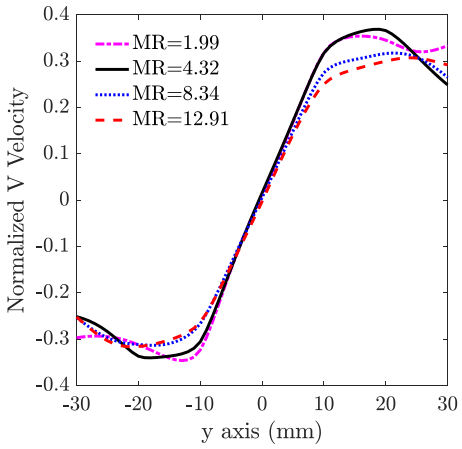

Figure 4.86. Comparison of the Effect of Momentum Ratio (60° Impingement Angle Injector) on Normalized V Velocity at y-axis

According to Figure 4.86, for the 60° impingement angle, the increase in the momentum ratio does not affect the behavior of the normalized lateral velocity profile in the core part of the spray. Besides, as moved out of this core part, only small deviations seem to exist. In terms of magnitude, the peak points are reached around 15 mm away from the center for all cases, followed by a slight decrease. These observations imply that the momentum change has a slight effect on the characteristics of the normalized lateral velocity for the triplet injectors with 60° impingement angle.

4.1.5.5. Normalized W Velocity

In Figure 4.87, the normalized W velocity distribution of injectors with different impingement angles are given.

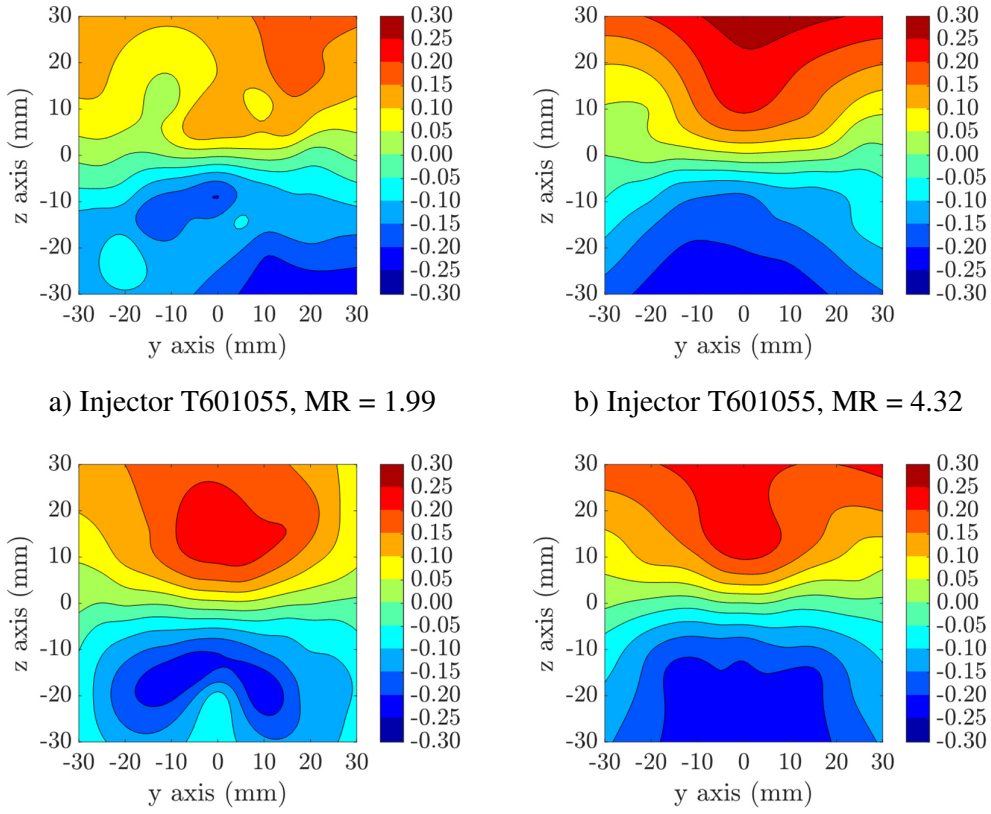

a) Injector T601055, MR = 1.99

b) Injector T601055, MR = 4.32

c) Injector T601055, MR = 8.34

d) Injector T601055, MR = 12.91

Figure 4.87. The Effect of Momentum Ratio (60° Impingement Angle Injector) on Normalized W Velocity

Considering the smaller spread with MR=1.99 in the z direction, it may be interpreted as this is due to its lower W velocity magnitude than the others. Figure 4.88 shows the effect of momentum Ratio on the normalized W velocity along the z-axis.

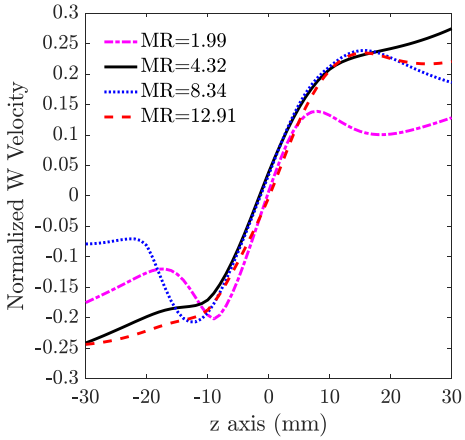

Figure 4.88. Comparison of the Effect of Momentum Ratio (60° Impingement Angle Injector) on Normalized W Velocity at z-axis

4.1.5.6. Normalized Velocity Magnitude

Figure 4.89 shows the normalized velocity distribution of injectors with different momentum ratios. In agreement with the previous velocity comparisons, no significant differences are observed in the normalized velocity magnitudes.

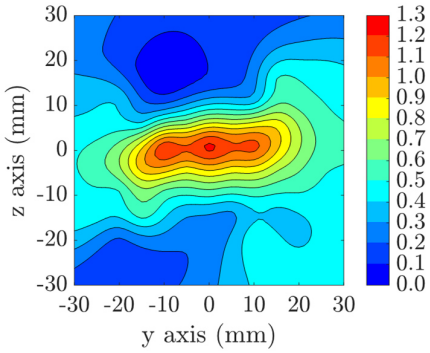

a) Injector T601055, MR = 1.99

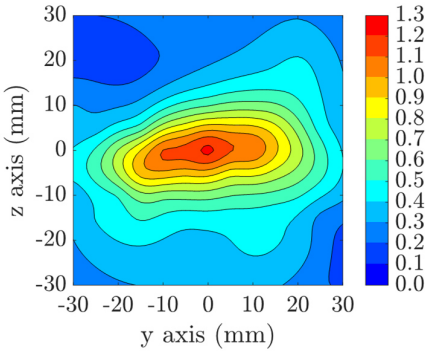

b) Injector T601055, MR = 4.32

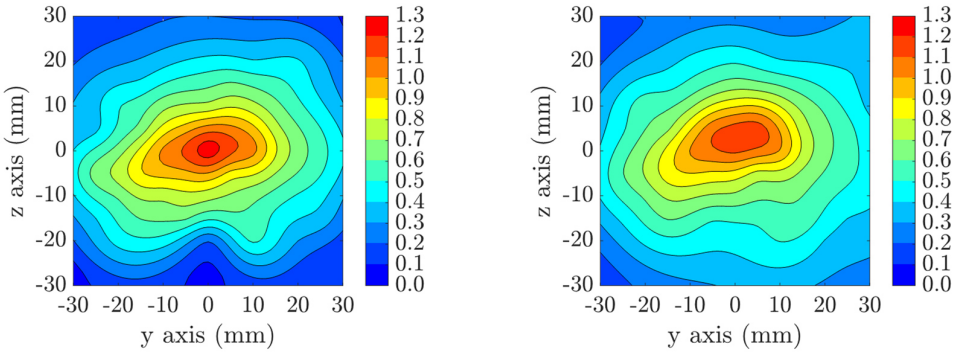

c) Injector T601055, MR = 8.34 d) Injector T601055, MR = 12.91

Figure 4.89. The Effect of Momentum Ratio (60° Impingement Angle Injector) on Normalized Velocity Magnitude

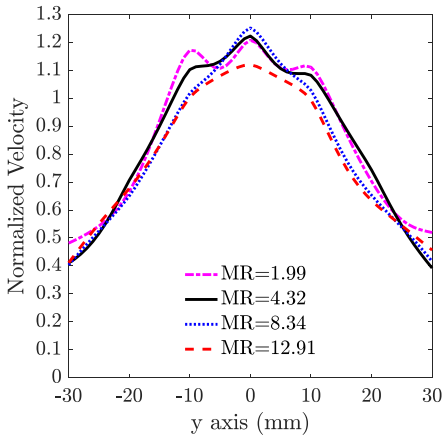

Figure 4.90. Comparison of the Effect of Momentum Ratio (60° Impingement Angle Injector) on Normalized Velocity Magnitude at y-axis

The comparison of the effect of momentum ratio along the y-axis is given in Figure 4.90. The findings also indicate that the distribution of the normalized velocity magnitude is almost independent of the change in momentum ratio.

4.1.5.7. SMD Distribution

The SMD distribution of injectors with different momentum ratios are given in Figure 4.91. The minimum values observed with MR=1.99 may be the result of the

lack of droplets compared to the other cases. The evaluation on the SMD distribution is performed by taking the normalized droplet count into consideration. It seems that the SMD distributions are very close to each other among test cases.

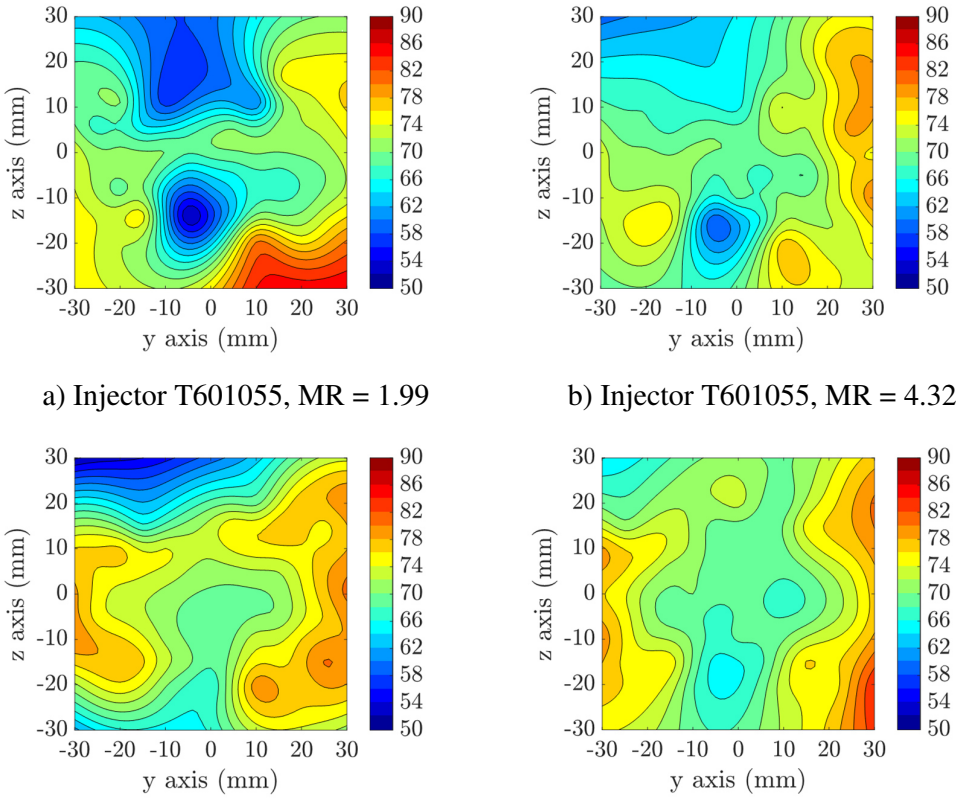

a) Injector T601055, MR = 1.99

b) Injector T601055, MR = 4.32

c) Injector T601055, MR = 8.34

d) Injector T601055, MR = 12.91

Figure 4.91. The Effect of Momentum Ratio (60° Impingement Angle Injector) on SMD

According to Figure 4.92, for the 60° impingement angle, the trends of the SMD distribution along z=0 are similar and the diameter of the droplets are also very close between the cases. It seems that the minimum SMD levels are generally reached at the highest MR. The general trends suggest an increase in the SMD levels away from the center as expected since the droplet count is reduced there as the mixing of the jets deteriorates. The deviation observed in the SMDs between the cases reaches up to 5 µm.

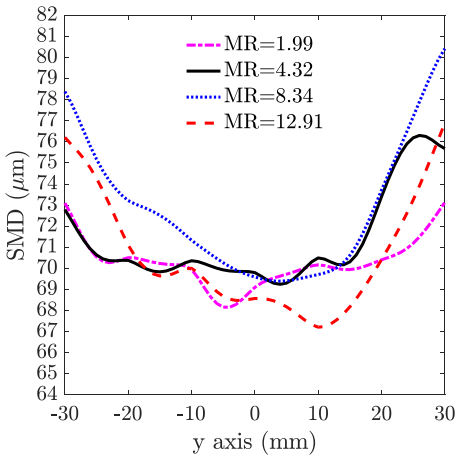

Figure 4.92. Comparison of the Effect of Momentum Ratio (60° Impingement Angle Injector) on SMD at y-axis

4.1.5.8. Rosin-Rammler Distribution

The Rosin-Rammler distributions of injectors with different momentum ratios are shown in Figure 4.93.

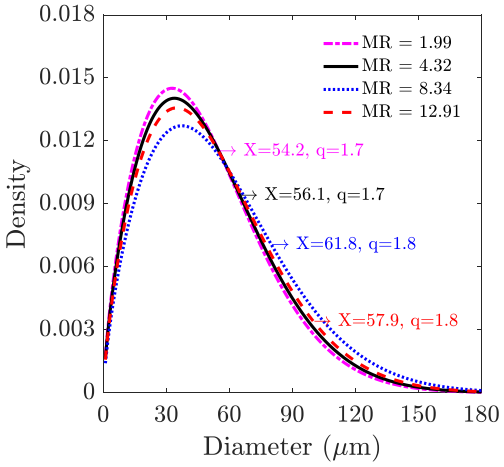

Figure 4.93. Comparison of Rosin-Rammler Distributions

Results indicated that the X and q constants are changing between 54.2 to 61.8 and 1.7 to 1.8, respectively, with an increase in MR from 1.99 to 12.91.

4.1.5.9. Total Normalized Droplet Count

The total normalized droplet count of 60° injector will be discussed with 90° injectors in Section 4.1.5.9.

4.1.5.10. Mean D10

The mean droplet diameter of 60° injector will be discussed with 90° injectors in Section 4.1.5.10.

4.1.5.11. Mean SMD

The mean SMD of 60° injector will be discussed with 90° injectors in Section 4.1.5.11.

4.1.5.12. Spray Angle

The spray angle of 60° injector will be discussed with 90° injectors in Section 4.1.5.12.

4.1.6. The Effect of Momentum Ratio (90° Impingement Angle Injector)

In this section, the effect of momentum ratio on the normalized mass flux, velocity, droplet count distributions, droplet statistics and spray angles for the triplet injector with 90° impingement angle will be discussed. Impingement distance, orifice l/d ratio, orifice diameter and impingement angle were kept constant while the following results were obtained. In obtaining the MR values in the increasing order from MR = 3.19 to MR = 11.73, the mass flow rate through the outer orifices was increased by 42%, 20%, and 20.8%, respectively, while the mass flow rate through

the inner orifice was increased by 1.7%, maintained at the same value, and then further increased by 5.5%, respectively.

4.1.6.1. Normalized Mass Flux Distribution

In Figure 4.94, the normalized mass flux distributions for the triplet injector with 90° impingement angle at different momentum ratios are given. Trends are similar to those observed in the distributions with 60° impingement angle, in terms of the spray distribution and the highest mass flux at the center of the spray. The elliptical distribution transforms into a circular shape as MR is increased.

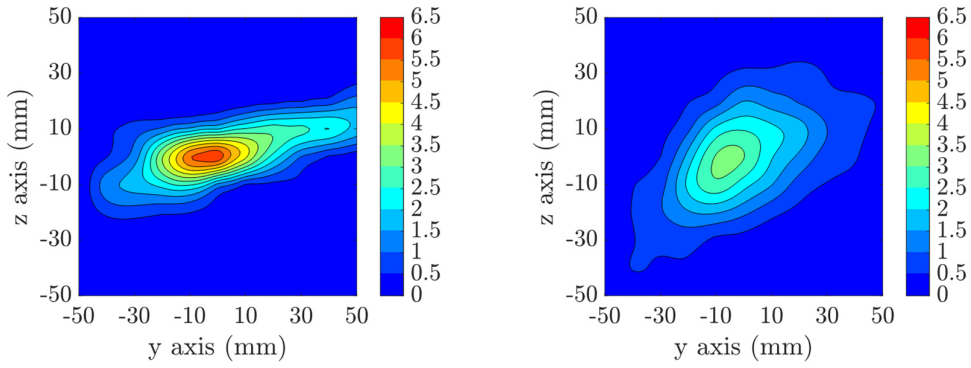

a) Injector T901055, MR = 3.19

b) Injector T901055, MR = 6.21

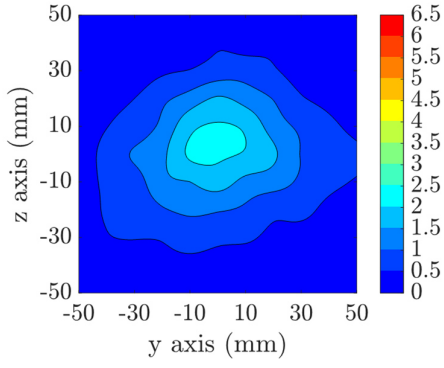

c) Injector T901055, MR = 8.93

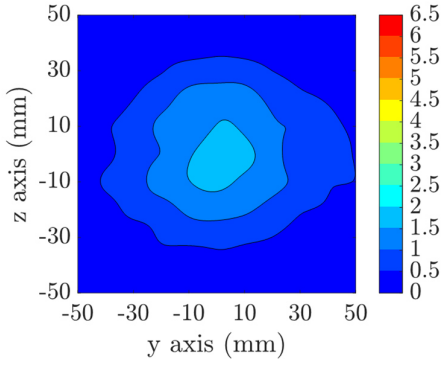

d) Injector T901055, MR = 11.73

Figure 4.94. The Effect of Momentum Ratio on Normalized Mass Flux Distribution

Figure 4.95 depicts a sharp drop in the normalized mass flux value at z=0 as the momentum ratio is increased from MR=2.07 to MR=6.21. Further increase in MR keeps decreasing the uneven distribution of the mass flux, however, the observed drop is less significant.

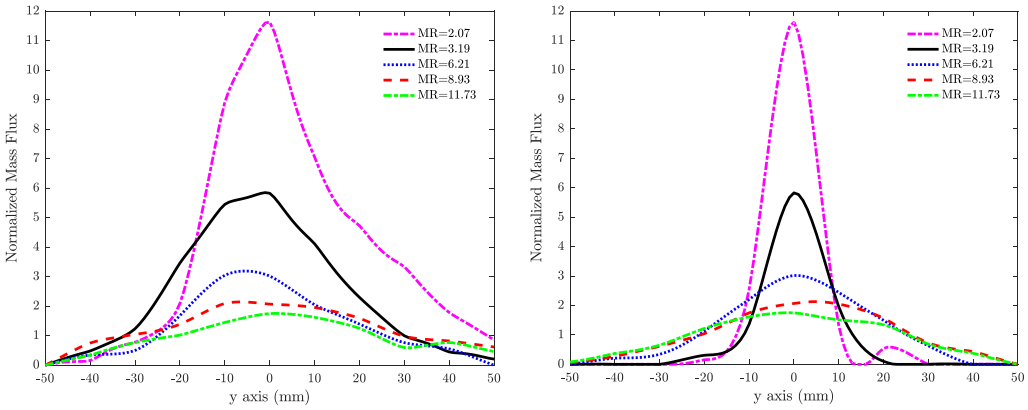

a) along y-axis b) along z-axis

Figure 4.95. Comparison of the Effect of Momentum Ratio on Normalized Mass Flux Distributions at y and z-axes

4.1.6.2. Normalized Droplet Count

The normalized droplet count distribution of injector with different momentum ratios is given in Figure 4.96.

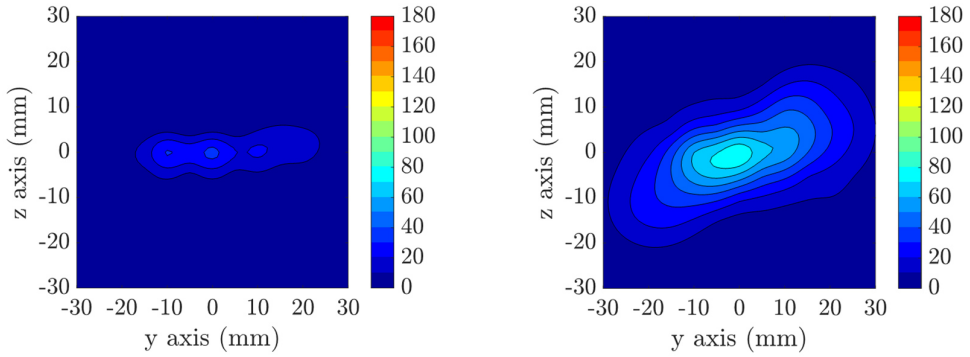

a) Injector T901055, MR= 3.19

b) Injector T901055, MR= 6.21

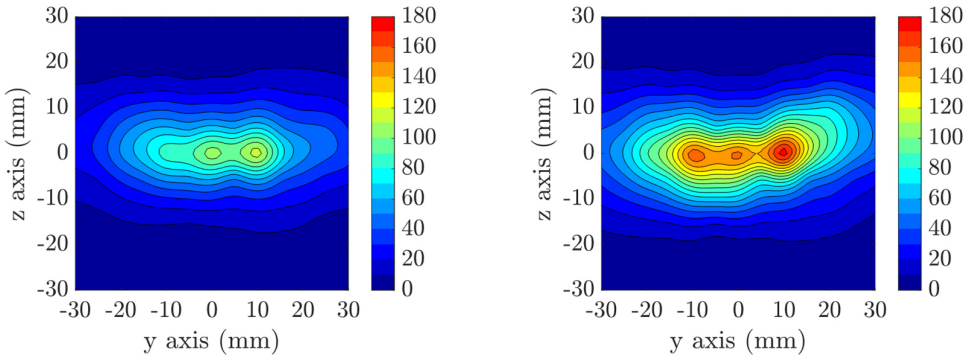

c) Injector T901055, MR= 8.93

d) Injector T901055, MR= 11.73

Figure 4.96. The Effect of Momentum Ratio (90° Impingement Angle Injector) on Normalized Droplet Count

Results clearly show that the momentum ratio has an important effect on the normalized droplet count. There is a continuous increase in the droplet count with momentum ratio as observed in the contours. Figure 4.97 shows that at z=0, the normalized droplet count increases with momentum ratio, as was observed for the case of 60° impingement angle.

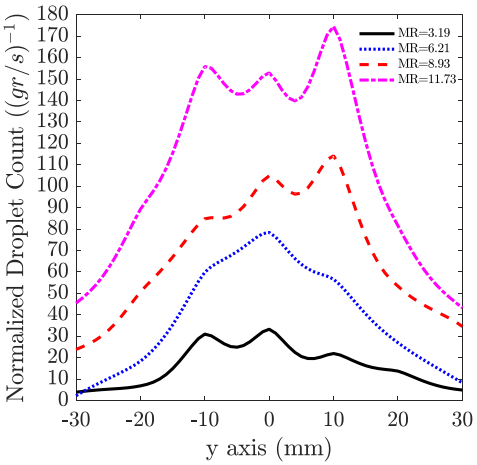

Figure 4.97. Comparison of the Effect of Momentum Ratio (90° Impingement Angle Injector) on Normalized Droplet Count at y-axis

4.1.6.3. Normalized Axial Velocity

The normalized axial velocity distribution of injectors with different momentum ratios are given in Figure 4.98. The normalized axial velocity distribution shows similarities to the normalized mass flux distributions. Other than there is only a slight change with an increase in the momentum ratio, no observable difference among cases can be obtained.

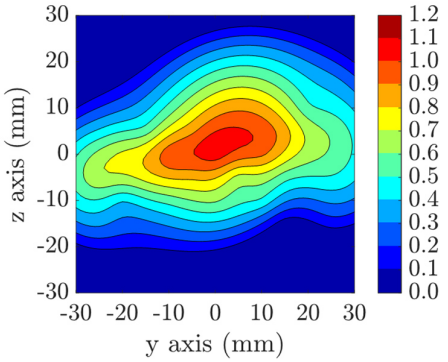

a) Injector T901055, MR= 3.19

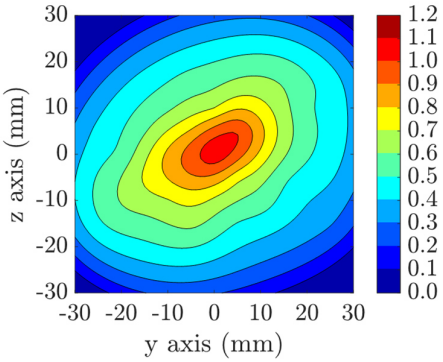

b) Injector T901055, MR= 6.21

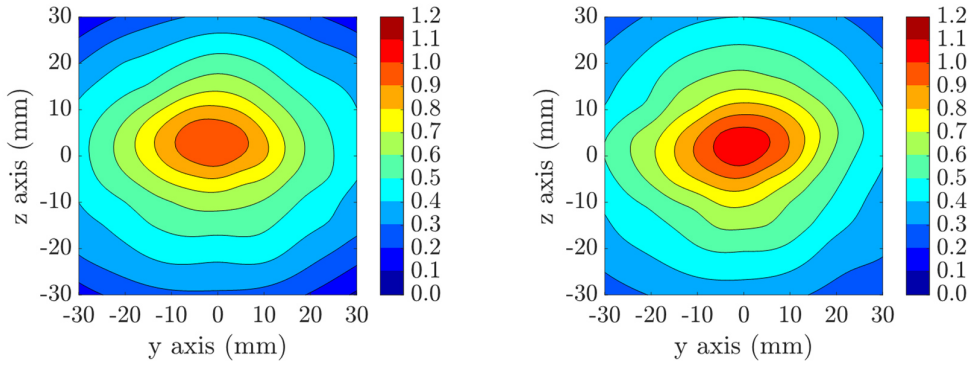

c) Injector T901055, MR= 8.93 d) Injector T901055, MR= 11.73

Figure 4.98. The Effect of Momentum Ratio (90° Impingement Angle Injector) on Normalized Axial Velocity

Figure 4.99 shows similar trends in the normalized axial velocity distribution along the y-axis for all cases. However, compared to the 60° impingement angle case, the differences between the cases seem to have slightly increased with the 90° impingement angle.

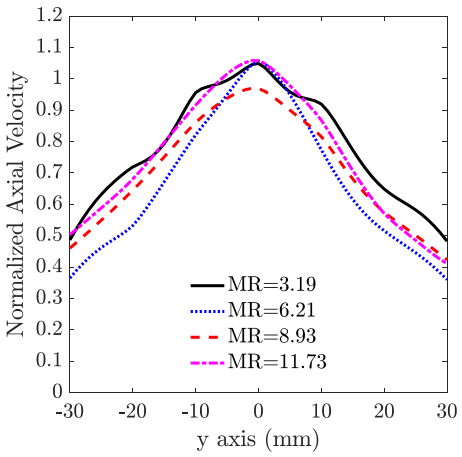

Figure 4.99. Comparison of the Effect of Momentum Ratio (90° Impingement Angle Injector) on Normalized Axial Velocity at y-axis

4.1.6.4. Normalized V Velocity

The normalized V velocity distributions of injector with different momentum ratios are given in Figure 4.100.

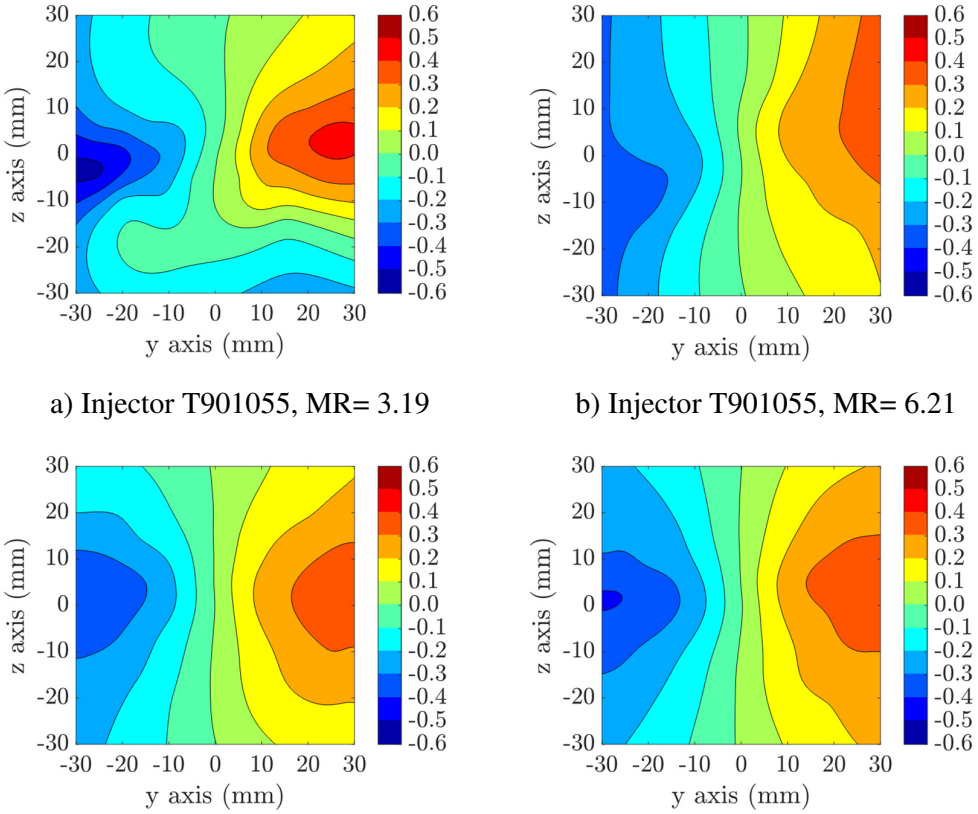

a) Injector T901055, MR= 3.19

b) Injector T901055, MR= 6.21

c) Injector T901055, MR= 8.93

d) Injector T901055, MR= 11.73

Figure 4.100. The Effect of Momentum Ratio (90° Impingement Angle Injector) on Normalized V Velocity

Due to relatively lower normalized droplet count in MR=3.19, actual velocity trends may not be captured as well less away from the spray centerline. Other than this difference, the behavior of the normalized V velocity distribution stays the same among the test cases.

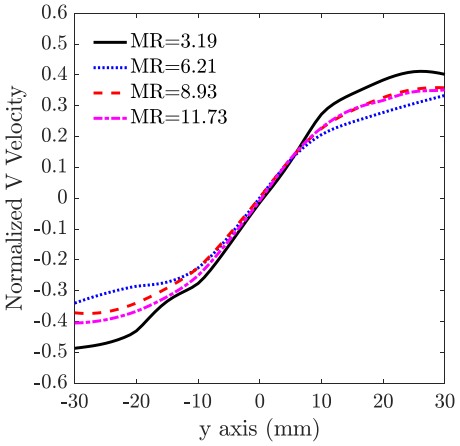

Figure 4.101. Comparison of the Effect of Momentum Ratio (90° Impingement Angle Injector) on Normalized V Velocity at y-axis

Figure 4.101 indicates that for the 90° impingement angle, the change in the momentum ratio has a small effect on the normalized lateral velocity.

4.1.6.5. Normalized W Velocity

Figure 4.102 shows the normalized W velocity distributions of injector with different momentum ratios.

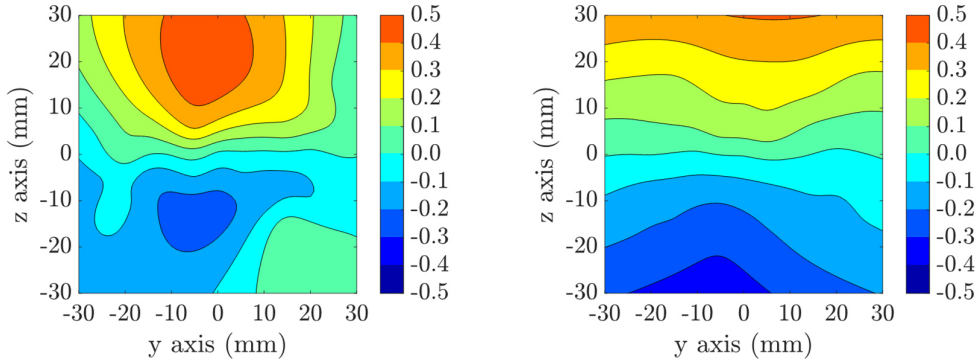

a) Injector T901055, MR= 3.19

b) Injector T901055, MR= 6.21

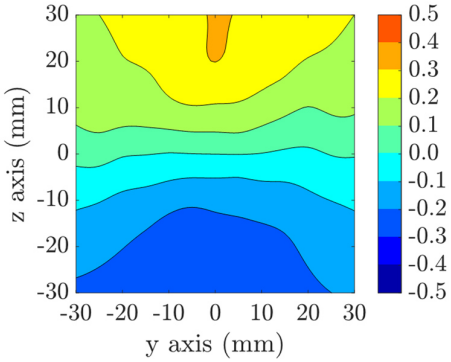

c) Injector T901055, MR= 8.93

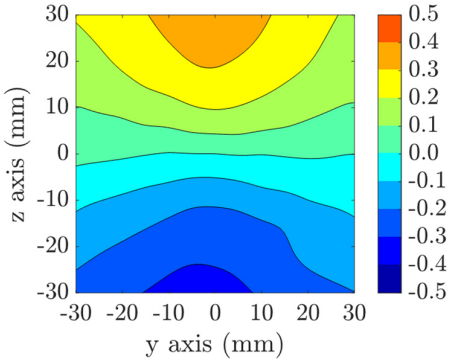

d) Injector T901055, MR= 11.73

Figure 4.102. The Effect of Momentum Ratio (90° Impingement Angle Injector) on Normalized W Velocity

Similar to the normalized V velocity distribution results, some unrealistic velocity distribution results obtained in the case of MR=3.19. Other three results with MR=6.21, MR=8.93 and MR=11.73 shows similar distributions.

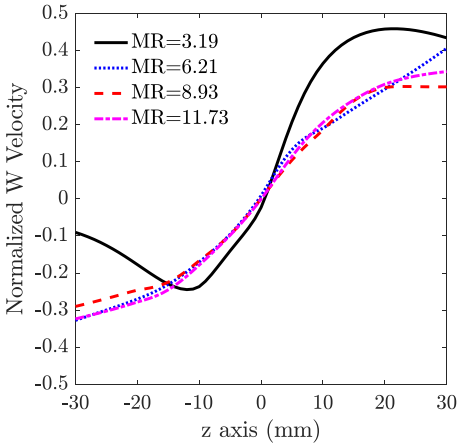

Figure 4.103. Comparison of the Effect of Momentum Ratio (90° Impingement Angle Injector) on Normalized W Velocity at z-axis

As it is seen before with the 60° impingement angle injector case, Figure 4.103 also indicates that there is no strong relation between momentum ratio and normalized W velocity distribution.

4.1.6.6. Normalized Velocity Magnitude

The normalized velocity magnitude distribution of 90° impingement angle with different momentum ratios can be seen in Figure 4.104. What is observed with the velocity magnitude distribution is in agreement with previous findings.

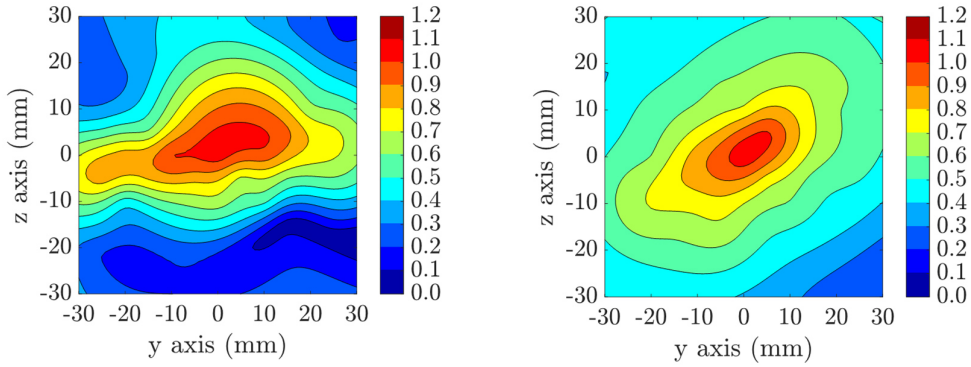

a) Injector T901055, MR= 3.19

b) Injector T901055, MR= 6.21

c) Injector T901055, MR= 8.93

d) Injector T901055, MR= 11.73

Figure 4.104. The Effect of Momentum Ratio (90° Impingement Angle Injector) on Normalized Velocity Magnitude

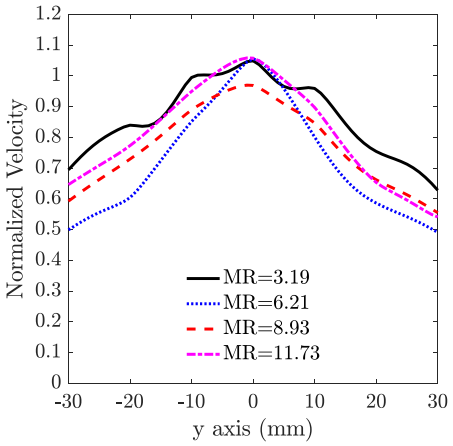

Figure 4.105. Comparison of the Effect of Momentum Ratio (90° Impingement Angle Injector) on Normalized Velocity Magnitude at y-axis

The comparison of the effect of momentum ratio is given in Figure 4.105.

4.1.6.7. SMD Distribution

The SMD distributions of injector with different momentum ratios are given in Figure 4.106. Due to relatively lower count of droplets, the SMD values observed with MR=3.19 test case do not reflect a realistic distribution. Other than this, the behavior of the contour plots shows that there is a slight decrease in terms of SMD in return of an increase in the momentum ratio.

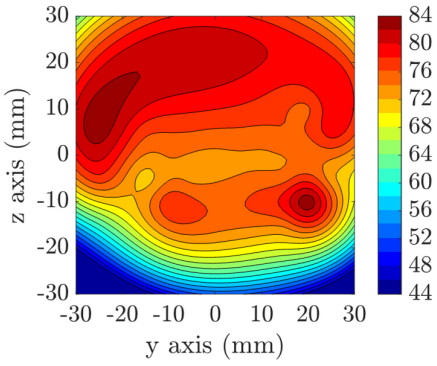

a) Injector T901055, MR= 3.19

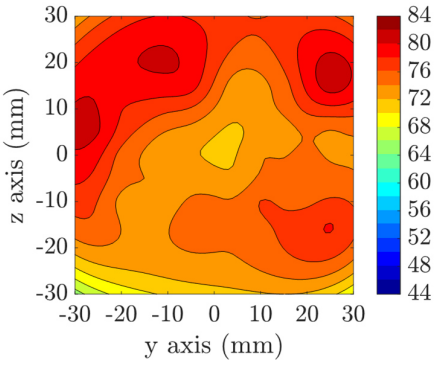

b) Injector T901055, MR= 6.21

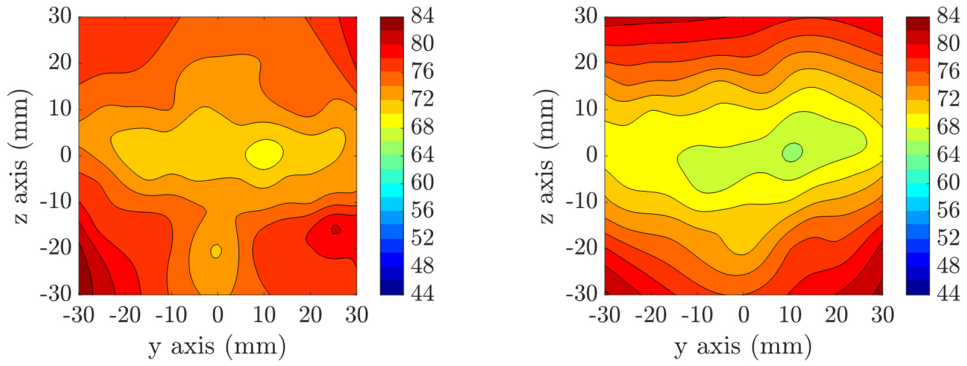

c) Injector T901055, MR= 8.93 d) Injector T901055, MR= 11.73

Figure 4.106. The Effect of Momentum Ratio (90° Impingement Angle Injector) on SMD

The level of decrease in the SMD with respect to momentum ratio can be seen in Figure 4.107. With an increase in the momentum ratio from 3.19 to 11.73, the minimum SMD is decreased gradually from 74 µm to 66 µm.

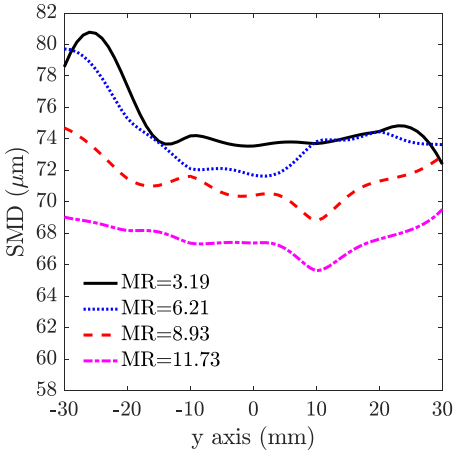

Figure 4.107. Comparison of the Effect of Momentum Ratio (90° Impingement Angle Injector) on SMD at y-axis

4.1.6.8. Rosin-Rammler Distribution

The Rosin-Rammler distributions of injectors with different momentum ratios are shown in Figure 4.108. With momentum ratio, X shows a tendency to decrease while the q parameter increases, respectively.

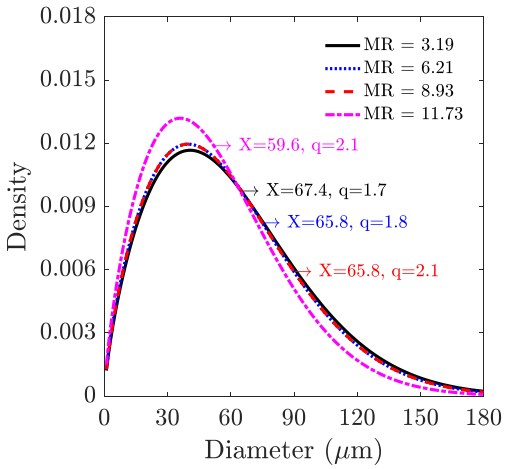

Figure 4.108. Comparison of Rosin-Rammler Distributions

4.1.6.9. Total Normalized Droplet Count

The change in total normalized droplet count with respect to momentum ratio is given in Figure 4.109. The total normalized droplet count is proportional to the momentum ratio for both injectors with different impingement angles.

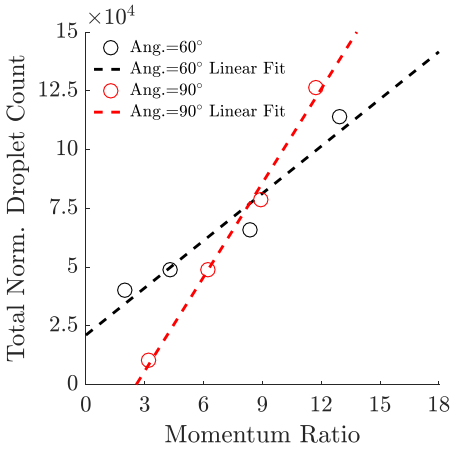

Figure 4.109. Comparison of the Effect of Momentum Ratio on Total Normalized Droplet Count

4.1.6.10. Mean D10

The change in the arithmetic mean diameter as a function of the momentum ratio is given in Figure 4.110. The mean D10 is proportional to the momentum ratio for the 60° impingement angle, while it is almost independent of the momentum ratio for the 90° impingement angle.

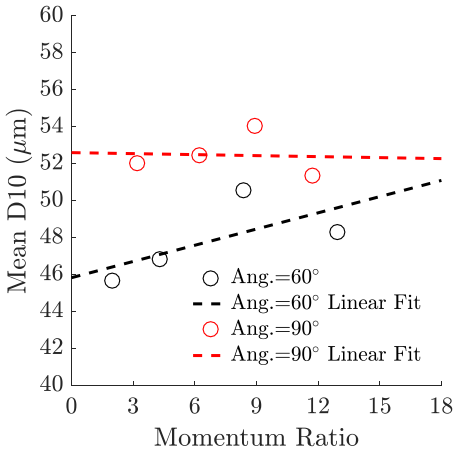

Figure 4.110. Comparison of the Effect of Momentum Ratio on Mean D10

4.1.6.11. Mean SMD

The change in the mean SMD with respect to the momentum ratio is given in Figure 4.111. Impingement distance, orifice l/d ratio, orifice diameter and impingement angle were kept constant while the following results were obtained.

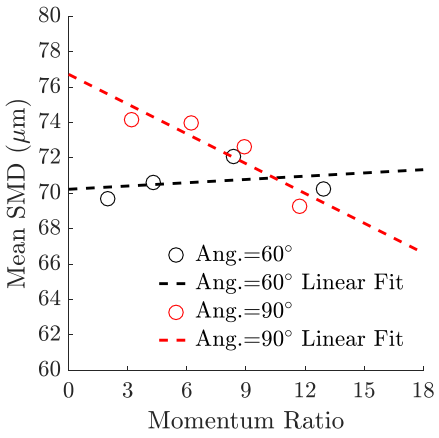

Figure 4.111. Comparison of the Effect of Momentum Ratio on Mean SMD

An increase in the momentum ratio slightly increases the mean SMD for the 60° impingement angle injector, while it clearly decreases the mean SMD for the 90° impingement angle injector.

4.1.6.12. Spray Angle

The changes in the spray angles with respect to the momentum ratio are given in Figure 4.112. The dispersion of the spray along the y-axis increases as the momentum ratio increases. It is seen that the injector with the higher impingement angle gives slightly higher spray angles.

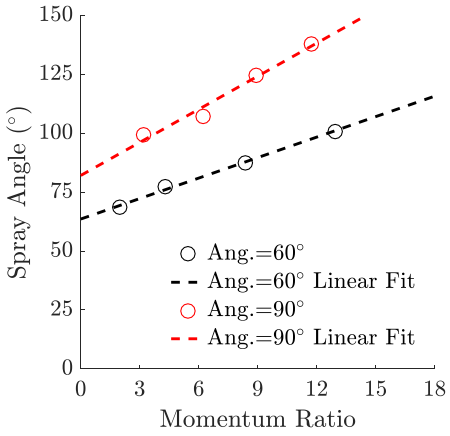

Figure 4.112. Comparison of the Effect of Momentum Ratio on Spray Angle

4.1.7. Measurements at 15 mm for Test Case T601055 With MR=1.99

In addition to the PDA measurements performed at 30 mm below the impingement point for the test T601055 with MR=1.99, another data set was obtained at 15 mm to be used in the CFD comparison. In this section, the normalized droplet count, SMD, velocity components and magnitude distributions are given.

The normalized droplet count distribution of T601055 with MR of 1.99 at 15 mm away from the impingement distance is shown in Figure 4.113.

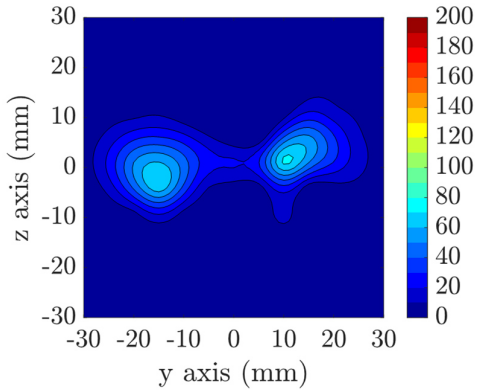

Figure 4.113. Normalized Droplet Count Distribution of T601055 with MR=1.99 at 15 mm Below Impingement Point

The normalized velocity distributions are given in Figure 4.114.

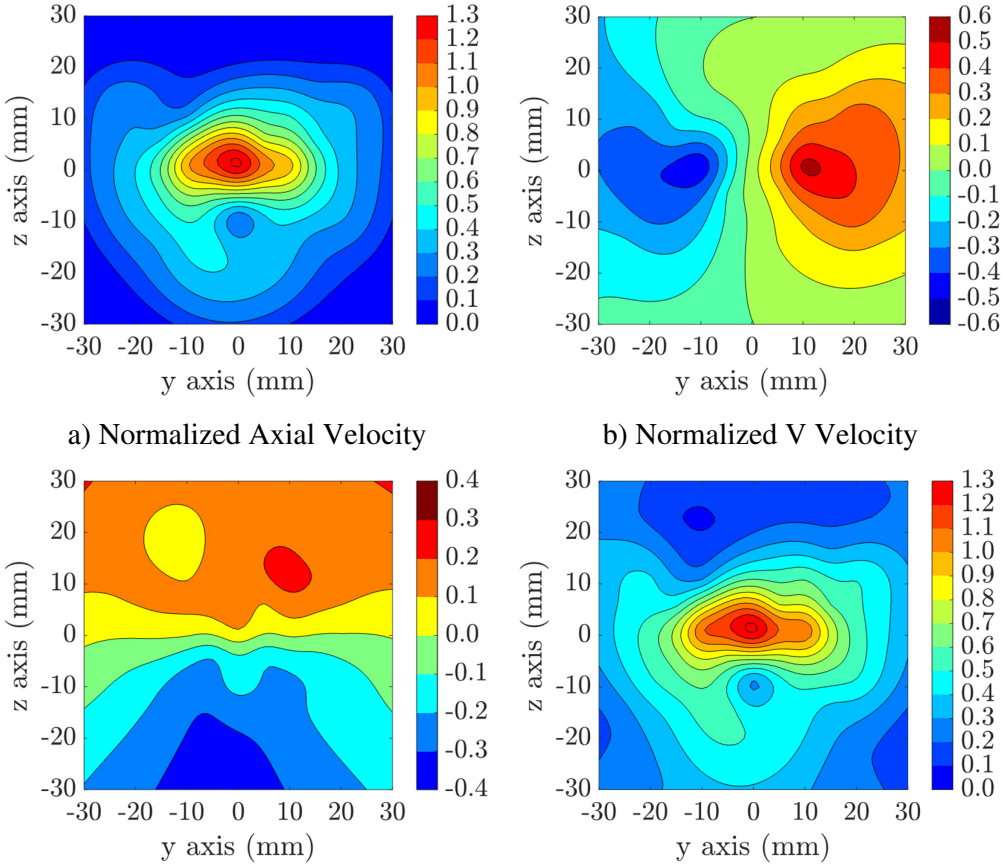

a) Normalized Axial Velocity

b) Normalized V Velocity

c) Normalized W Velocity

d) Normalized Velocity Magnitude

Figure 4.114. Normalized Velocity Distributions of T601055 with MR=1.99 at 15 mm Below Impingement Point

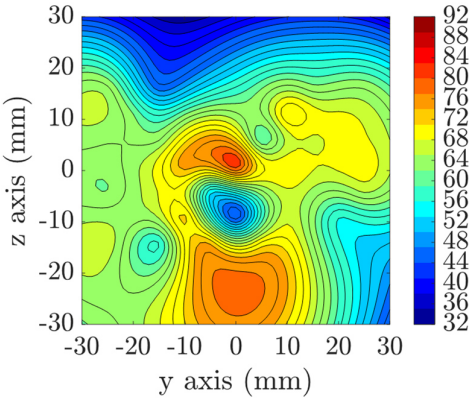

Figure 4.115. Normalized SMD Distribution of T601055 with MR=1.99 at 15 mm Below Impingement Point

The normalized SMD distribution of T601055 at 15 mm away from the impingement point can be seen in Figure 4.115. The SMD reaches 84 µm at the center while it is about 65 µm at ±15 mm away from the center along the y-axis where the highest droplet counts are obtained. Local SMD values less than 40 µm are obtained below the center and at the edges of the measurement plane due to lack of droplets.

4.1.8. Conclusion on Triplet Injectors

For triplet injectors, the results of the mass flux distributions show that the most effective parameter on the mass flux distribution is the impingement angle. As the injector with 45° impingement angle produces a very nonuniform distribution on the measurement plane, an increase in the impingement angle makes the distribution more uniform. In terms of mass flux distribution, the second most effective parameter is evaluated as the momentum ratio. The investigation of the effects of this parameter is completed with two triplet injectors of 60° and 90° impingement angles and both sets of tests show that triplet injectors improve the uniformity of the mass flux distribution in return of the increase in the momentum ratio. While the increase in the impingement distance contributes to the uniformity, it is inversely proportional with the orifice l/d ratio and the orifice diameter.

The impingement angle is found to increase the normalized droplet count. This may be linked to the decrease of the normalized axial velocity and increase in the lateral velocity along the spray centerline as the impingement angle increases. Despite the dependency of the normalized mass flux and droplet count distributions on the impingement angle, the SMD doesn't show an apparent trend in response to the impingement angle. As the coincident axial velocity distributions indicate the similarity of the area that the mass flux is distributed, the increasing lateral velocity profile from center to the edges may be contributing to the enhancement of the normalized mass flux and droplet count distributions. The SMD distributions obtained with different momentum ratios show similarities along the spray centerline with the injector with 60° impingement angle. However, the SMD levels decrease with momentum ratio with the injector of 90° impingement angle.

The increase in the impingement distance reduces the normalized droplet count over the measurement area significantly and causes the mass flux distributions to be slightly more uniform. These trends may be linked to the decrease of both axial and lateral velocity profiles. While the decrease in former may lead to more uniform distribution in terms of mass flux, the decrease in latter results in the reduction of the normalized droplet count. The SMD distribution doesn't show a trend as a function of the impingement distance.

Increase of the orifice l/d ratio results in a more stable jet at the exit of the orifice, hence, resulting in better atomization due to the impact of these jets. This is observable in the axial and lateral velocity distributions, which are almost the same in cases with the orifice l/d ratios of 5 and 8, while the profiles are different for the orifice l/d ratio of 3. Further increase in the orifice l/d from 5 to 8 decreases the normalized droplet count. This result may indicate that with further increase, the liquid sheet breakup length gets longer and the measurement cannot be performed at the fully-atomized region.

As a predicted result of increasing the orifice diameter by keeping the momentum ratio constant, the axial and lateral velocity profiles decrease along the spray

centerline. Therefore, droplet count decreases accordingly. The most effective parameter on the SMD is the orifice diameter. The decrease in the orifice diameter to 0.8 mm leads to significantly low SMD levels in triplet injectors.

Another macroscopic evaluation on the spray dispersion is performed by using the snapshots of the spray taken by a video camera. These comparisons were performed from only one side view of the spray; hence, one should be aware that the other view of the spray was not evaluated, which is important especially in triplets, due to the asymmetric distributions of these injectors. With this manner, while the increase in the impingement distance decreases the spray angle, an increase in all other parameters investigated, the orifice l/d ratio, orifice diameter, impingement angle and momentum ratio, increases the spray angle.

4.2. Pentad Injectors

In this section, the effects of impingement distance, orifice l/d ratio, orifice diameter, impingement distance and momentum ratio on the spray characteristics of pentad injectors will be discussed in terms of mass flux, velocity distributions, droplet statistics and spray angles.

Figure 4.116 shows the distribution of pentad injectors. In the figure, blue circles represent the injector orifices. Since the orifices are positioned along both y and z axes, the resultant spray grows along the diagonals. Hence, in this section, the comparison of different test cases will be evaluated along the y' and z' axes.

The normalized mass flux distributions of pentad injectors are investigated in order to analyze the effect of impingement distance, orifice l/d ratio, orifice diameter, impingement angle and momentum ratio. The measurements are performed at 480 mm below the impingement point in all injectors except the one with 90° of impingement angle. The reason for that will be explained in the related section.

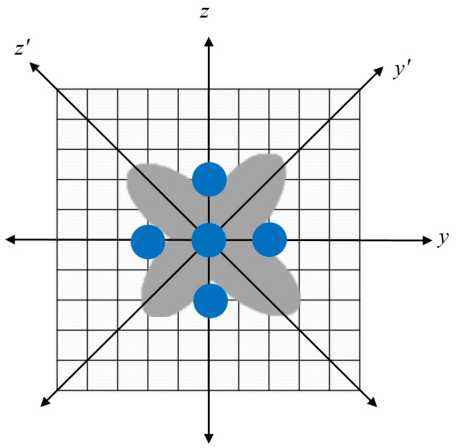

Figure 4.116. The Schematic of the Distribution of Pentad Injectors

Velocity distributions and droplet statistics were obtained by PDA at a plane 30 mm below the impingement point of each injector without any exceptions. Pentad injectors produce a very dense spray core at the center of the distributions. The measurements done with the PDA system show that due to the thick liquid sheet at the center, the laser beams cannot penetrate through the sheet and therefore cannot reach out to the droplets in some specific areas. This problem can be visualized as shown in Figure 4.117.

In the figure, the measurement instant in four regions of the spray dispersed is given. On the upper left section, the laser beams cannot penetrate through the liquid sheet and cannot reach the droplets. Besides, the receiver cannot observe the light reflecting from the droplets. On the upper right section, even if the lasers can reach the droplets, the receiver cannot see the lasers because of the thick laser sheet. The lower left section allows the receiver to collect the light reflecting from the droplets, however, the laser beams cannot reach the droplets in this part. On the lower right section of the pentad injectors, the lasers from the transmitters can reach the droplets and the receiver is also in a position that can collect the light reflecting from the droplets. Due to this issue, data could not be obtained properly on these three quarters of the spray.

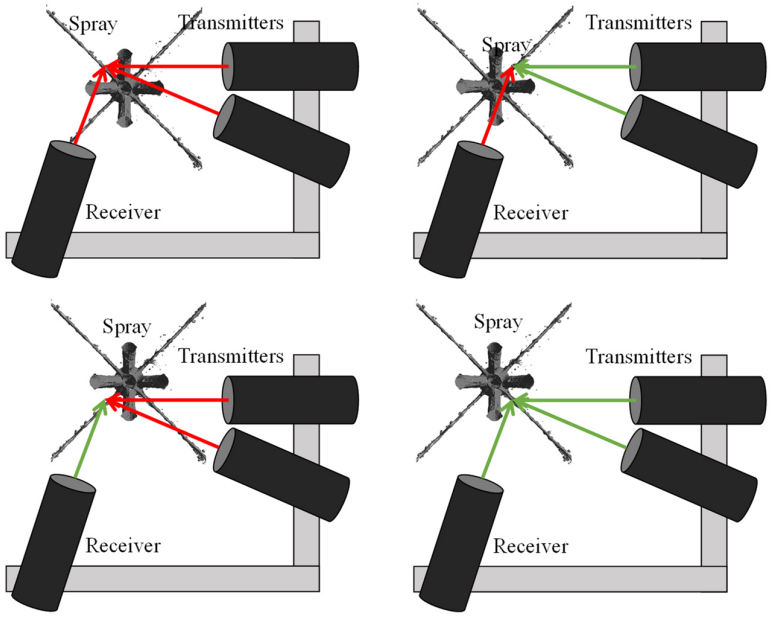

Figure 4.117. The Position of PDA System with Spray of a Pentad Injector

An example of the PDA measurement results can be seen in Figure 4.118.

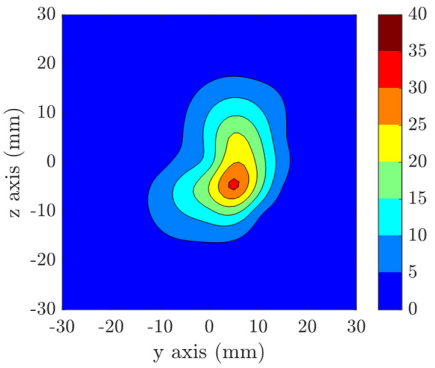

Figure 4.118. The Normalized Droplet Count Distribution

As a result, the measurements could be performed only in the lower left section of the measurement plane. Hence, the symmetry of this quarter is projected to the other quarters and the results in the following sections are presented in this fashion.

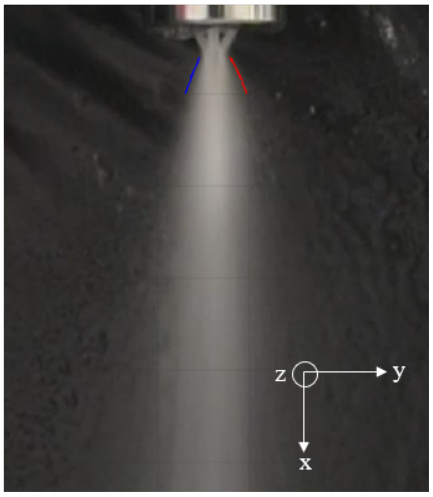

Figure 4.119. A Representation of Spray Angle Measurements in Pentad Injectors

Additionally, the spray angle measurements of pentad injectors are examined in order to investigate the effect of impingement distance, orifice l/d ratio, orifice diameter, impingement angle and momentum ratio. Similar to triplets, the spray images were taken by a video camera. A representation for the spray angle measurements in pentad injectors is given in Figure 4.119. In this study, the spray angles were measured on the xy plane, while the change in the xz plane was not studied. All results were compared based on the change of the angle along the xy plane.

Table 4.2 shows the test list of the pentad injectors. For each test configuration, measurements were performed with the patternator, PDA and the video camera. As for the triplet injectors, while the selected test parameter is investigated, all other measured parameters are kept constant. In obtaining the momentum ratio, MR, the mass flow rates supplied to the inner and outer orifices were adjusted accordingly. In order to eliminate the effect of the variations caused by the pressurizing system, the mass flux, droplet count and velocity distributions will be presented in the following sections in the normalized form.

Table 4.2. Test Map of Pentad Injectors

No	Code	Injector Type	MR	Imp. Angle (°)	Orifice Diameter (mm)	Orifice l/d Ratio	Imp. Distance (mm)
1	P601055	Pentad	4.17	60	1.0	5	5
2	P601055	Pentad	16.05	60	1.0	5	5
3	P601058	Pentad	16.03	60	1.0	5	8
4	P601051	Pentad	15.98	60	1.0	5	10
5	P601035	Pentad	16.06	60	1.0	3	5
6	P601085	Pentad	16.27	60	1.0	8	5
7	P601255	Pentad	16.32	60	1.2	5	5
8	P600855	Pentad	16.15	60	0.8	5	5
9	P451055	Pentad	16.03	45	1.0	5	5
10	P901055	Pentad	16.04	90	1.0	5	5

4.2.1. The Effect of Impingement Distance

In this section, the effect of the impingement distance of pentad injectors on the normalized droplet count, velocity and SMD distributions will be discussed. The other parameters such as the orifice l/d ratio, orifice diameter, impingement angle and momentum ratio are kept constant.

4.2.1.1. Normalized Mass Flux Distribution

Figure 4.120 shows the mass flux distribution of pentad injectors with different impingement distances.

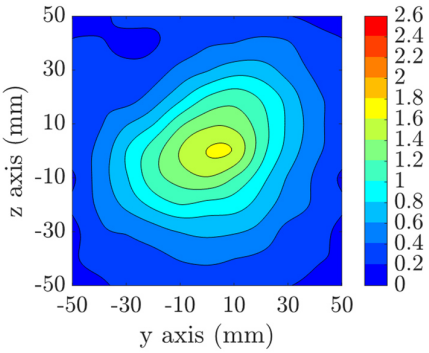

a) Injector P601055, Impingement Distance = 5 mm

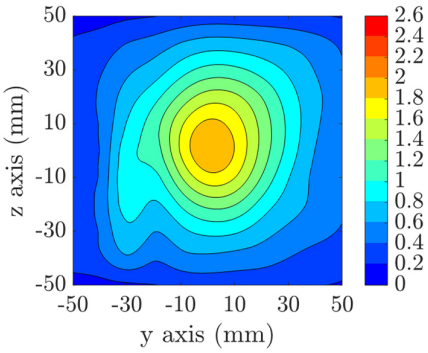

b) Injector P601058, Impingement Distance = 8 mm

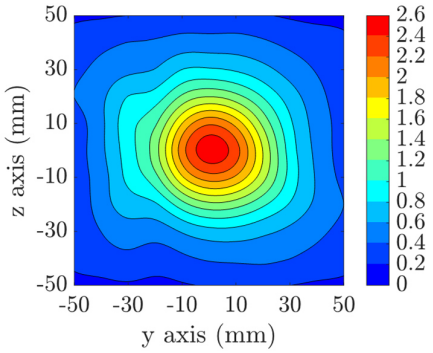

c) Injector P601051, Impingement Distance = 10 mm

Figure 4.120. The Effect of Impingement Distance on Normalized Mass Flux Distribution

In contrary to triplets, with the increase of impingement distance, the highest flux at the center increases. It is considered that due to the symmetry of the outer orifices, the normalized flux is not distributed randomly. Instead, it concentrates at the center.

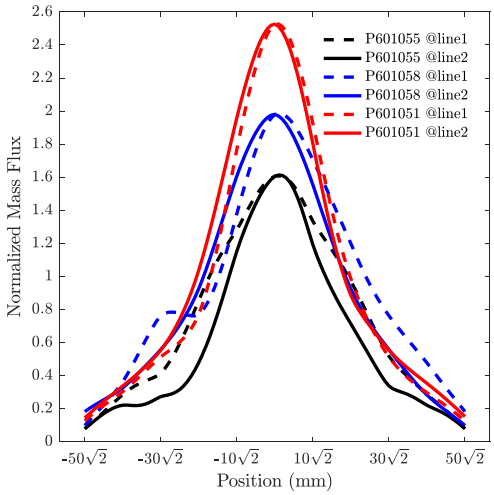

Figure 4.121. Comparison of the Effect of Impingement Distance on Normalized Mass Flux Distributions at y' and z'-axes

Figure 4.121 shows the normalized mass flux distributions of pentads with different impingement distances, where 5 mm distance is shown in black, 8 mm distance is in blue, and 10 mm distance in red. Due to the symmetry of the nature of pentads, the mass flux distribution along the y' and z' axes, which are denoted by line 1 and line 2, respectively, are given on the same plot. The y' and z' axes are obtained by converting the y and z axes with 45° in the counterclockwise direction. With the increase of the impingement distance of 5 mm to 10 mm, the highest mass flux value at the center is increased by 70%. On the outskirts of the spray, the spread of the distributions show similar trends with respect to the impingement distance.

4.2.1.2. Normalized Droplet Count

Figure 4.122 shows the normalized droplet count distribution of injectors with different impingement angles.

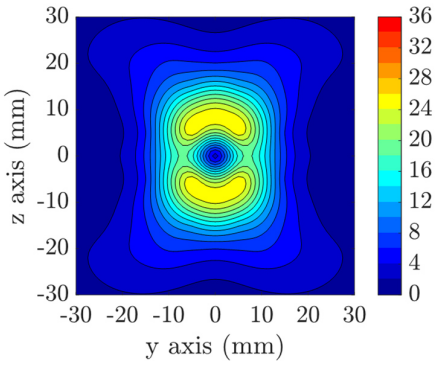

a) Injector P601055, Impingement Distance = 5 mm

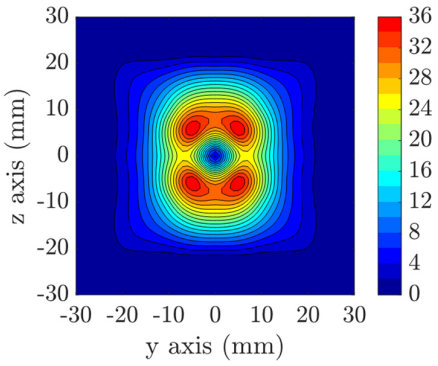

b) Injector P601058, Impingement Distance = 8 mm

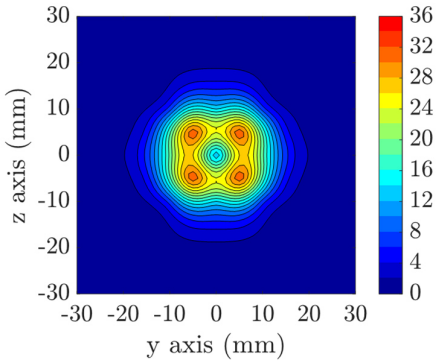

c) Injector P601051, Impingement Distance = 10 mm

Figure 4.122. The Effect of Impingement Distance on Normalized Droplet Count

In triplet injectors, with the increase of the impingement distance, the normalized droplet count becomes smaller coherent to the normalized mass flux distributions. However, the increase in the impingement distance results in an increase in mass flux distributions in pentad injectors, while it is observed that the normalized droplet count first increases as the distance is increased from 5 mm to 8 mm, then decreases with further increase in the impingement distance from 8 mm to 10 mm. Compared to the triplet injectors, the pentad injectors have two times higher mass flow rates. Hence, the liquid sheet breakup length increases and the break up of ligaments occurs further compared to triplets.

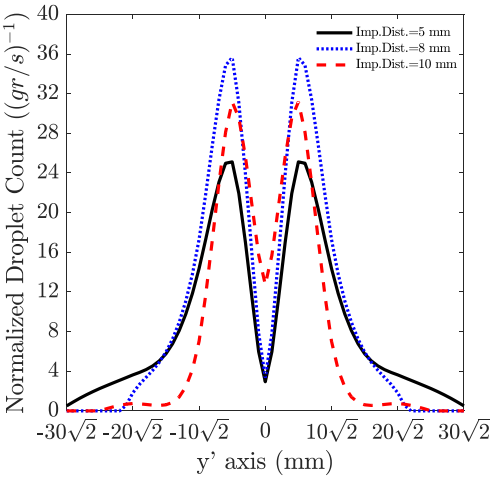

Figure 4.123. Comparison of the Effect of Impingement Distance on Normalized Droplet Count at y'-axis

Figure 4.123 shows the distribution of the normalized droplet count distribution along the y'-axis. It shows that further increase of the impingement distance from 8 mm to 10 mm leads to a decrease in normalized droplet count.

4.2.1.3. Normalized Axial Velocity

The normalized axial velocity distribution of injectors with different impingement distances is given in Figure 4.124. Similar velocity distributions are obtained for all test cases. In Figure 4.125, the comparison of the effect of the impingement distance on the normalized axial velocity along the y'-axis is given. The decrease of the peak axial velocity occurring at 10 mm impingement distance is coherent to that observed at 10 mm in the peak normalized droplet count.

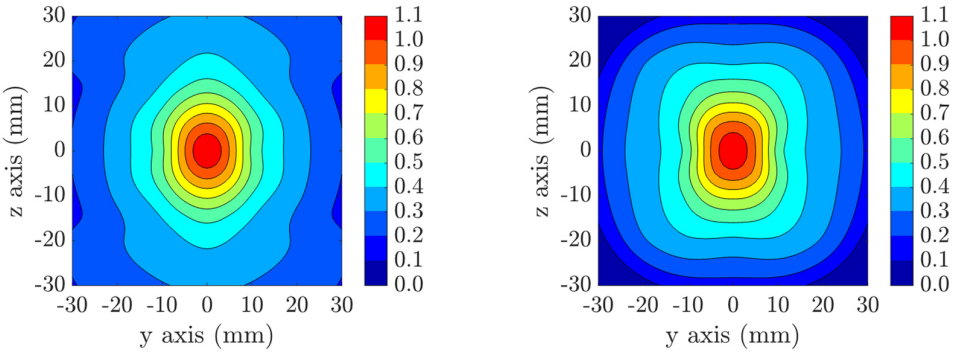

a) Injector P601055, Impingement Distance = 5 mm

b) Injector P601058, Impingement Distance = 8 mm

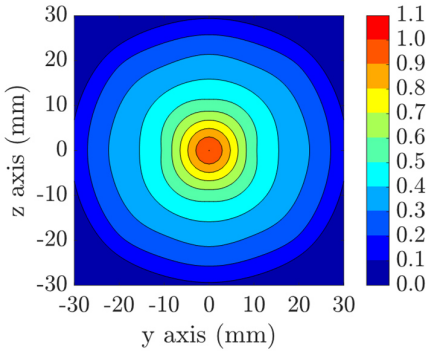

c) Injector P601051, Impingement Distance = 10 mm

Figure 4.124. The Effect of Impingement Distance on Normalized Axial Velocity

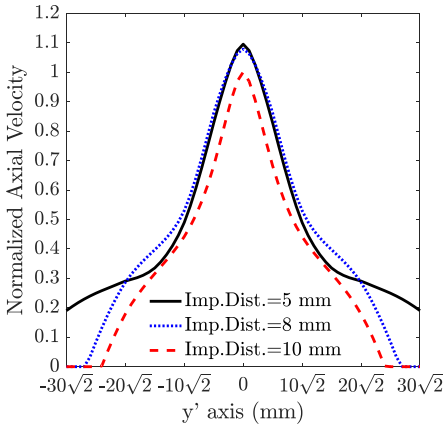

Figure 4.125. Comparison of the Effect of Impingement Distance on Normalized Axial Velocity at y'-axis

4.2.1.4. Normalized V Velocity

The normalized V velocity distributions are given in Figure 4.126. Similar distributions are obtained in all cases, with a slight increase in the velocities with the 8 mm case.

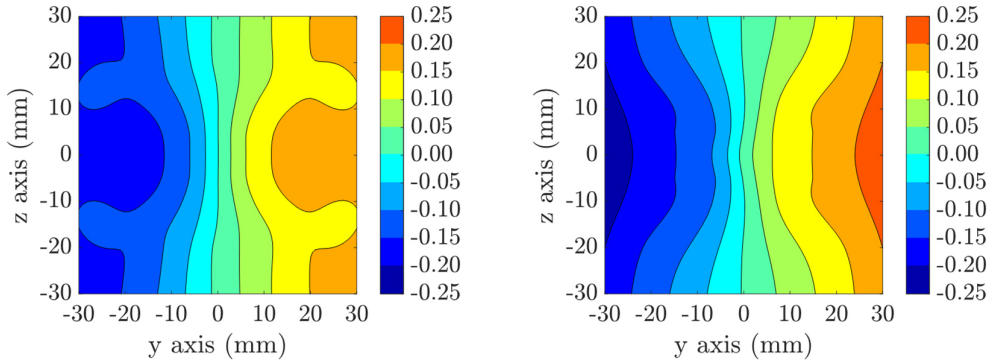

a) Injector P601055, Impingement Distance = 5 mm

b) Injector P601058, Impingement Distance = 8 mm

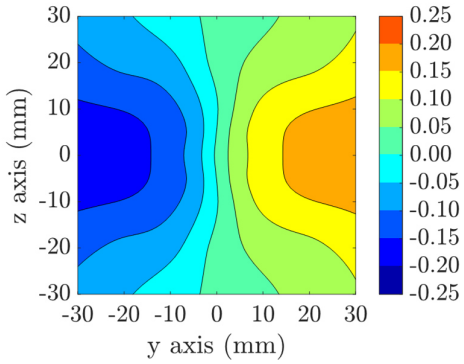

c) Injector P601051, Impingement Distance = 10 mm

Figure 4.126. The Effect of Impingement Distance on Normalized V Velocity

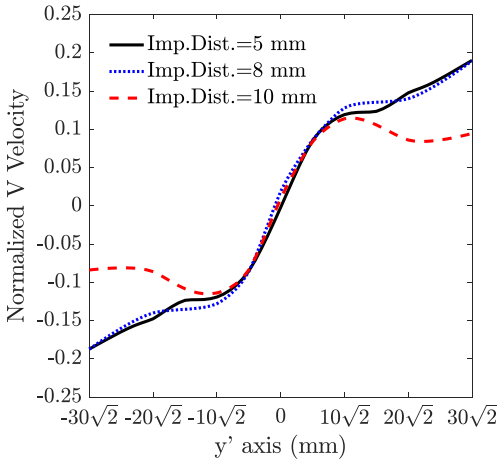

Figure 4.127. Comparison of the Effect of Impingement Distance on Normalized V Velocity at y'-axis

The comparison of the effect of the impingement distance on the normalized V velocity along the y'-axis in Figure 4.127 shows that in the central region, all velocity profiles have similar distributions. When it gets far away from the center, the case of 10 mm impingement distance shows a gradual decrease in the velocity, causing the normalized mass flux distribution to disperse on a smaller area.

4.2.1.5. Normalized W Velocity

The normalized W velocity distributions of injectors with different impingement distances are given in Figure 4.128. These distributions also show some minor increase when the impingement distance increases from 5 mm to 8 mm, and further increase from 8 mm to 10 mm results in the decrease of the normalized W velocity.

The direct comparison of the normalized W velocity distribution along the y'-axis in Figure 4.129 shows that away from the center, the increase of the impingement distance from 8 mm to 10 mm results in a decrease of the normalized W velocity.

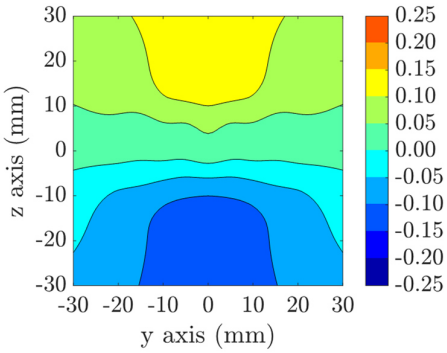

a) Injector P601055, Impingement Distance = 5 mm

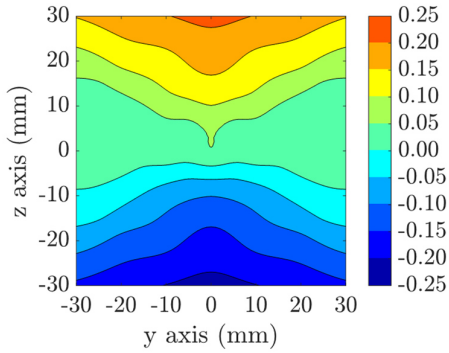

b) Injector P601058, Impingement Distance = 8 mm

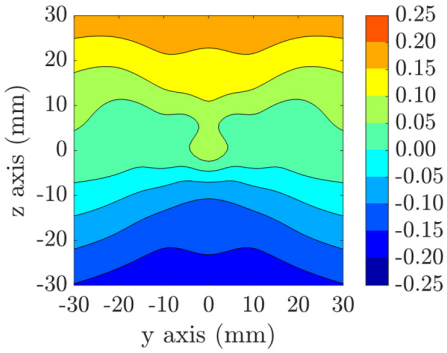

c) Injector P601051, Impingement Distance = 10 mm

Figure 4.128. The Effect of Impingement Distance on Normalized W Velocity

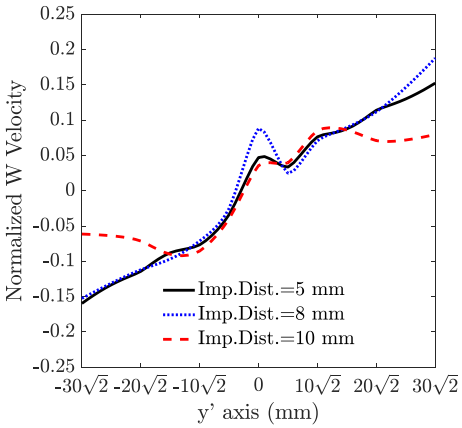

Figure 4.129. Comparison of the Effect of Impingement Distance on Normalized W Velocity at y'-axis

4.2.1.6. Normalized Velocity Magnitude

The distributions of the normalized velocity magnitude of injectors with different impingement distances are given in Figure 4.130. The distributions show similar trends to those of the normalized axial velocity and are in coherence with the previous findings.

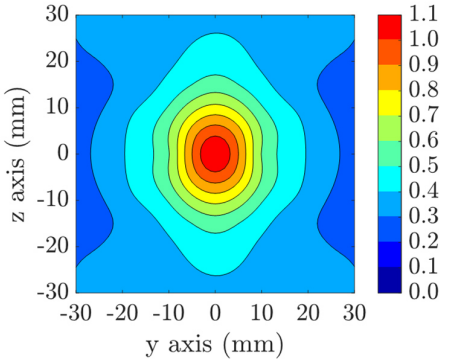

a) Injector P601055, Impingement Distance = 5 mm

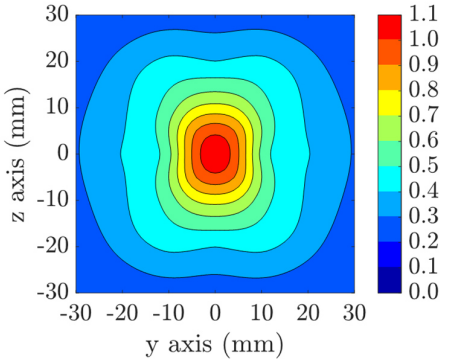

b) Injector P601058, Impingement Distance = 8 mm

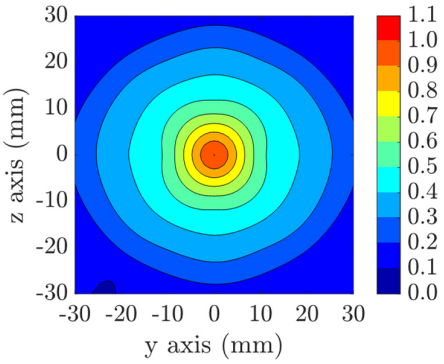

c) Injector P601051, Impingement Distance = 10 mm

Figure 4.130. The Effect of Impingement Distance on Normalized Velocity Magnitude

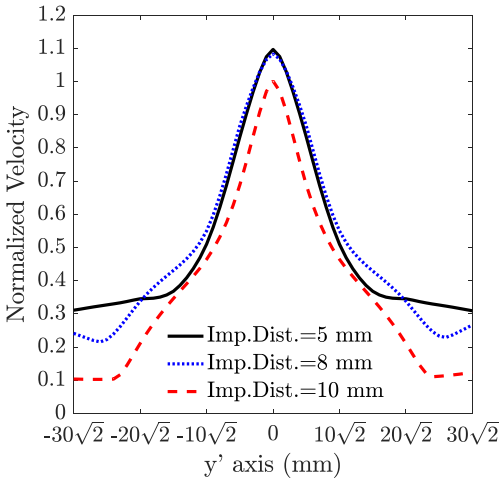

Figure 4.131. Comparison of the Effect of Impingement Distance on Normalized Velocity Magnitude at y'-axis

The comparison of the distributions along the y'-axis given in Figure 4.131 shows that at the center, the peak normalized axial velocity is decreased by 10% with the increase of the impingement distance from 8 mm to 10 mm.

4.2.1.7. SMD Distribution

The SMD distributions produced by the injectors with different impingement distances are given in Figure 4.132.

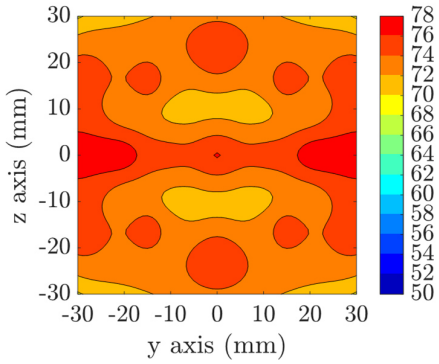

a) Injector P601055, Impingement Distance = 5 mm

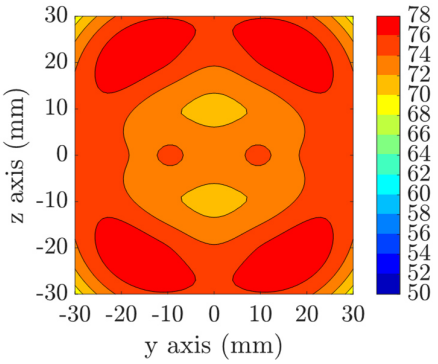

b) Injector P601058, Impingement Distance = 8 mm

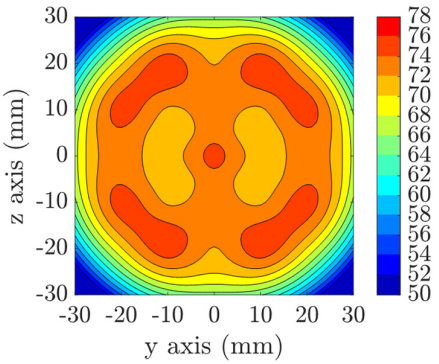

c) Injector P601051, Impingement Distance = 10 mm

Figure 4.132. The Effect of Impingement Distance on SMD

The observed trend is that the locations on the measurement plane with relatively low SMD values generally correspond to the locations where the droplet count is relatively higher in Figure 4.132 in each distribution. It should be noted that at 10 mm impingement distance, some unrealistic minimum SMD values are seen due to the lack of droplets at those regions.

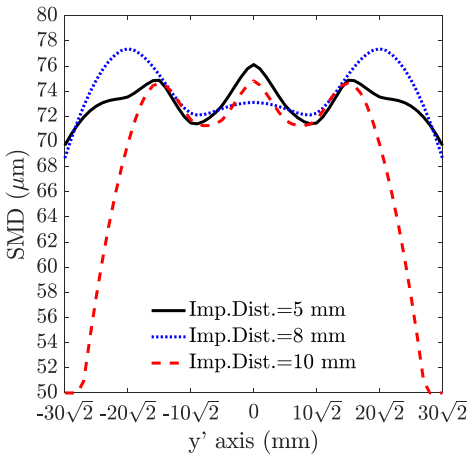

Figure 4.133. Comparison of the Effect of Impingement Distance on SMD at y'-axis

The comparison of the SMD distributions along the y'-axis given in Figure 4.133 shows that the minimum SMD values coincide for all three impingement distances and that the peak points of the curves seem to be nearly reversed.

4.2.1.8. Rosin-Rammler Distribution

The Rosin-Rammler distributions of the injectors with different impingement distances are shown in Figure 4.134. The distributions show that the droplet size does not change with respect to the impingement distance in pentad injectors.

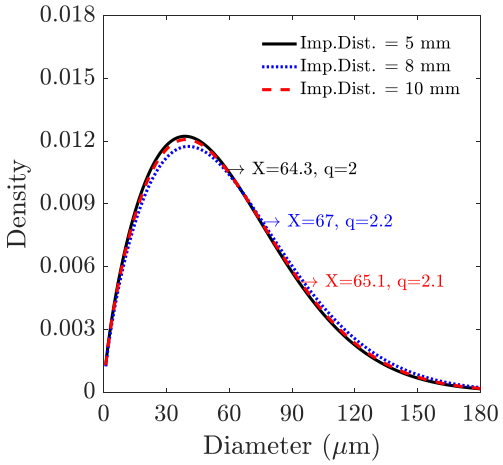

Figure 4.134. Comparison of Rosin-Rammler Distributions

4.2.1.9. Total Normalized Droplet Count

The total normalized droplet count as a function of the impingement distance is given in Figure 4.135. The orifice l/d ratio, orifice diameter, impingement angle and momentum ratio were all kept constant while the following results were obtained. The total normalized droplet count is inversely proportional to the impingement distance.

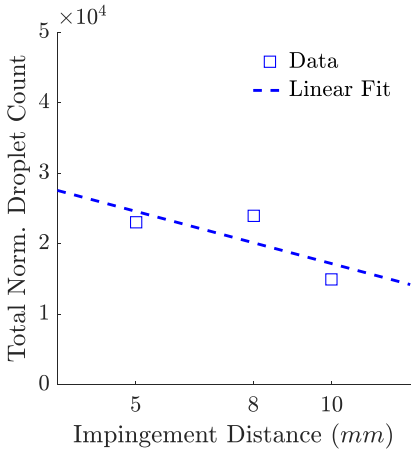

Figure 4.135. Comparison of the Effect of Impingement Distance on Total Normalized Droplet Count

4.2.1.10. Mean D10

The change in the arithmetic mean diameter, D10, as a function of the impingement distance is given in Figure 4.136.

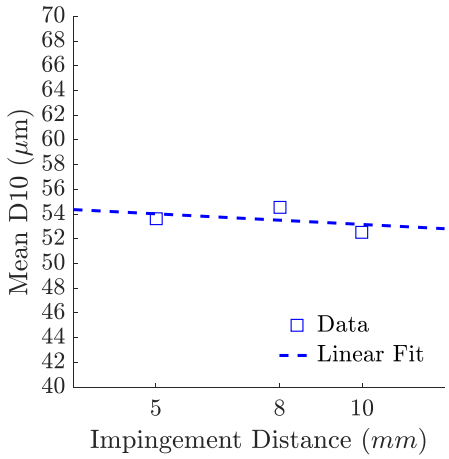

Figure 4.136. Comparison of the Effect of Impingement Distance on Mean D10

In pentads, D10 slightly decreases with respect to the impingement distance.

4.2.1.11. Mean SMD

The change in the mean SMD as a function of the impingement distance is given in Figure 4.137. Similar to the triplets, the mean SMD is almost insenstive to the impingement distance.

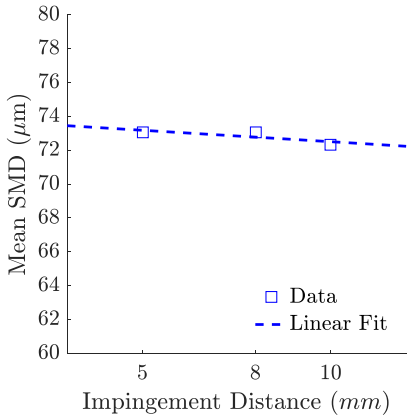

Figure 4.137. Comparison of the Effect of Impingement Distance on Mean SMD

4.2.1.12. Spray Angle

The effect of the impingement distance on the spray angle is given in Figure 4.138. With the increase of the impingement distance, the spray angle becomes smaller although it causes the spray to disperse on a greater area in the other direction.

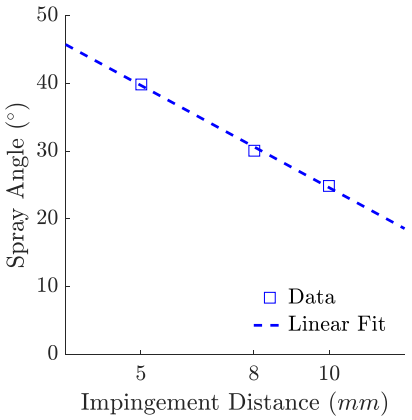

Figure 4.138. Comparison of the Effect of Impingement Distance on Spray Angle

4.2.2. The Effect of Orifice l/d Ratio

In this section, the effect of the orifice l/d ratio will be investigated in terms of the normalized droplet count, velocity and SMD distributions. The impingement distance, orifice diameter, impingement angle and momentum ratio are kept constant.

4.2.2.1. Normalized Mass Flux Distribution

In this section, the effect of the orifice l/d ratio on triplet injectors will be discussed.

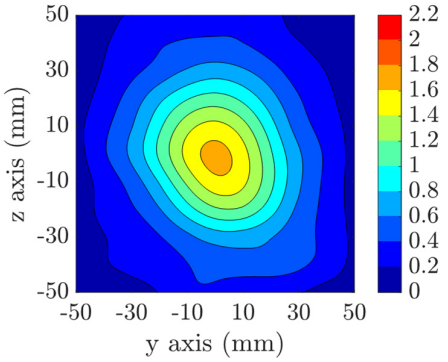

a) Injector P601035, orifice l/d ratio = 3

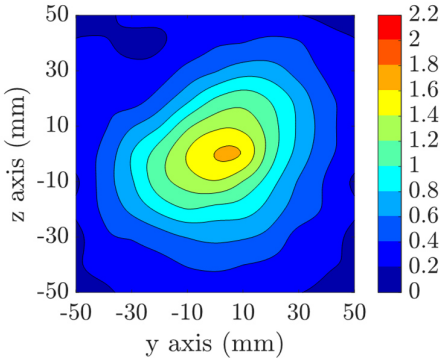

b) Injector P601055, orifice l/d ratio = 5

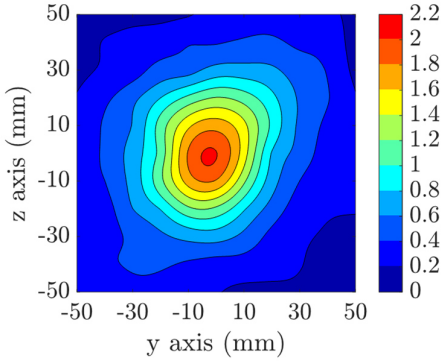

c) Injector P601085, orifice l/d ratio = 8

Figure 4.139. The Effect of Orifice l/d Ratio on Normalized Mass Flux Distribution

Figure 4.139 shows the mass flux distribution obtained by the pentad injectors with different orifice l/d ratios. In each case, the inner orifice had the same l/d ratio with the outer orifices. As it is seen, with the increase of the l/d ratio, the highest flux value at the center increases slightly. These results show similar trends with triplet injector test cases. With the increase of the length of the orifice, the disturbances on the liquid jet forms far away from the exit of the orifices. As a result, the liquid sheet breakup length increases and the mass flux disperses on a smaller area.

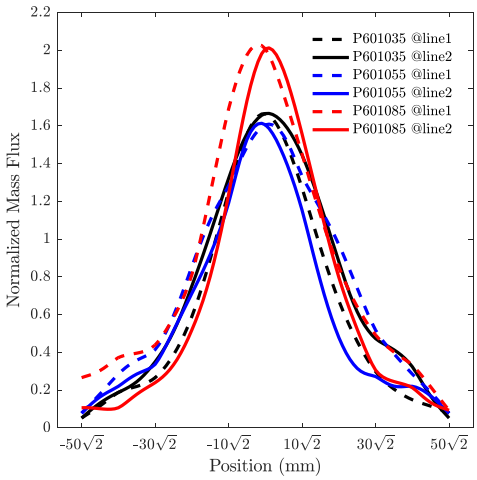

Figure 4.140. Comparison of the Effect of Orifice l/d Ratio on Normalized Mass Flux Distributions at y' and z'-axes

Figure 4.140 shows the normalized mass flux distributions of pentads with different impingement distances, where l/d = 3 is shown in black, l/d = 5 is in blue, and l/d = 8 is in red. Due to the symmetry of the nature of pentads, the mass flux distributions along the y' and z' axes, which are denoted by line 1 and line 2, respectively, are given on the same plot. With the increase of l/d by 60% from a value of 5 to 8, the highest mass flux value observed at the center is increased by 25%. Compared to the triplets, it can be said that the change of the orifice l/d ratio becomes less important in terms of mass flux distribution.

4.2.2.2. Normalized Droplet Count

The normalized droplet count distributions of the injectors with different orifice l/d ratios are given in Figure 4.141.

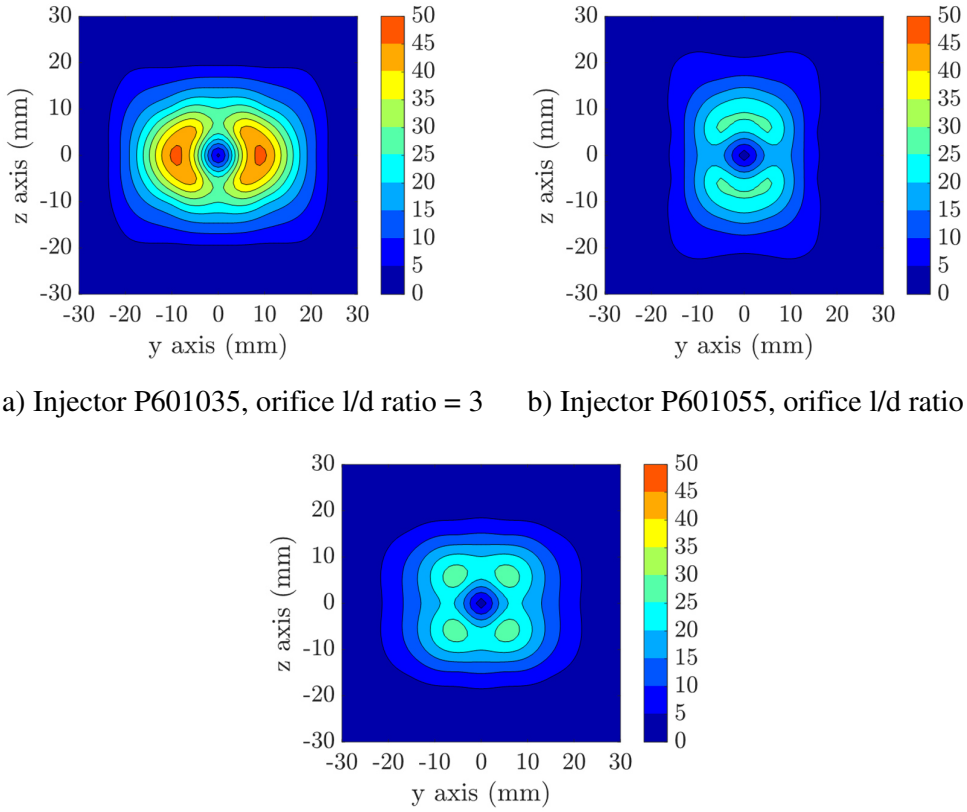

a) Injector P601035, orifice l/d ratio = 3 b) Injector P601055, orifice l/d ratio = 5

c) Injector P601085, orifice l/d ratio = 8

Figure 4.141. The Effect of Orifice l/d Ratio on Normalized Droplet Count

In triplet injectors, the highest count was obtained for l/d = 5, and further increase to l/d = 8 caused a reduction in the count. Here with the pentad injectors, it is observed that the highest count is observed for l/d = 3, and an increase to l/d = 5 decreases the droplet count while further increase to l/d = 8 does not show an obvious change anymore.

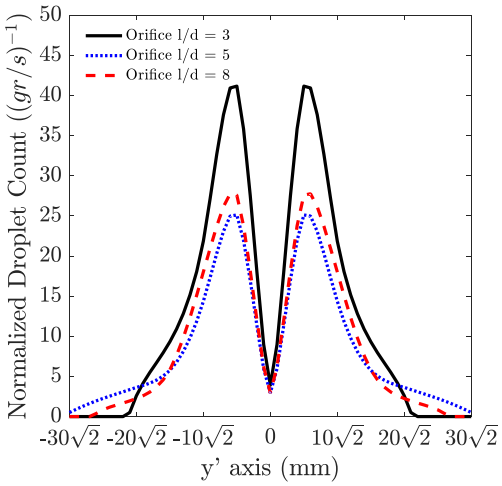

Figure 4.142. Comparison of the Effect of Orifice l/d Ratio on Normalized Droplet Count at y'-axis

The comparison of the distribution along the y'-axis given in Figure 4.142 shows the importance of the l/d ratio on the normalized droplet count. The increase in the l/d ratio from 3 to 5 results in a decrease of the normalized count by 50%.

4.2.2.3. Normalized Axial Velocity

The normalized axial velocity distributions are given in Figure 4.143

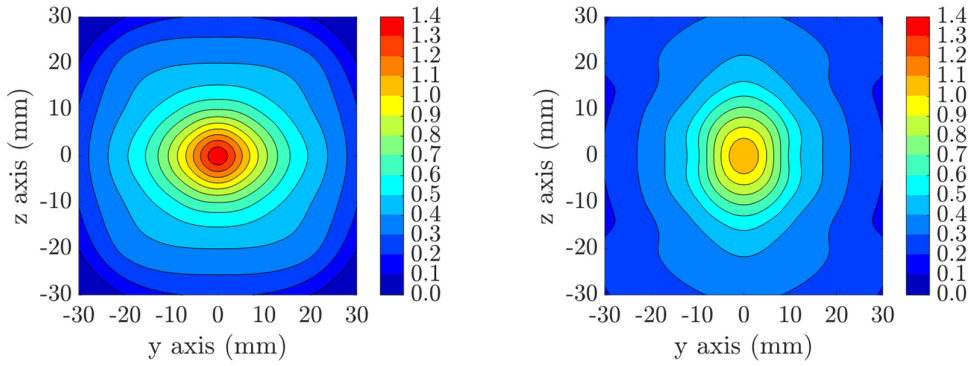

a) Injector P601035, orifice l/d ratio = 3 b) Injector P601055, orifice l/d ratio = 5

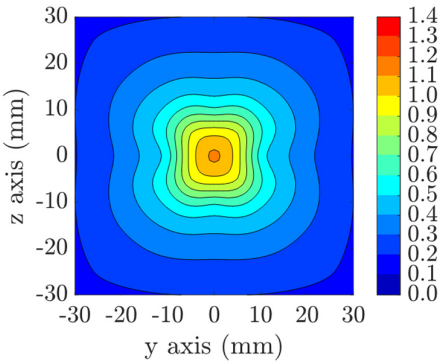

c) Injector P601085, orifice l/d ratio = 8

Figure 4.143. The Effect of Orifice l/d Ratio on Normalized Axial Velocity

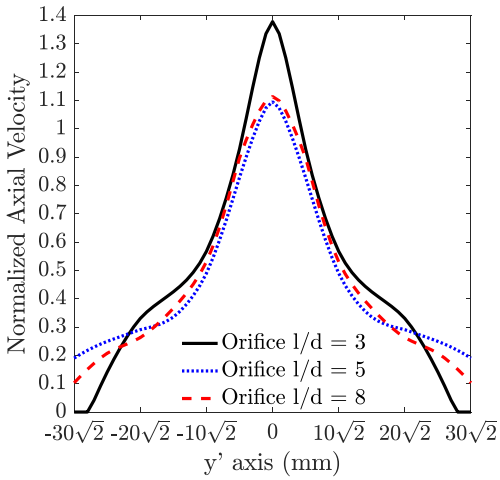

Figure 4.144. Comparison of the Effect of Orifice l/d Ratio on Normalized Axial Velocity at y'-axis

As the normalized droplet count results indicate, the normalized axial velocity is the highest at the l/d ratio of 3. The l/d ratios of 5 and 8 show similar normalized axial velocity distributions. According to Figure 4.144 along the y'-axis, the peak normalized axial velocity decreases by 30% with the increase of the orifice l/d ratio from 3 to 5.

4.2.2.4. Normalized V Velocity

The normalized V velocity distribution is given in Figure 4.145. In terms of magnitudes, the V velocity decreases with an increase in the l/d ratio. These results are in agreement with the other observations with the pentad injectors discussed before. On the other hand, this is the opposite trend to what was observed with the triplet injectors. The normalized V velocity distribution along the y'-axis given in Figure 4.146 shows similar velocity distributions at the center. The differences between the cases become clear away from the center.

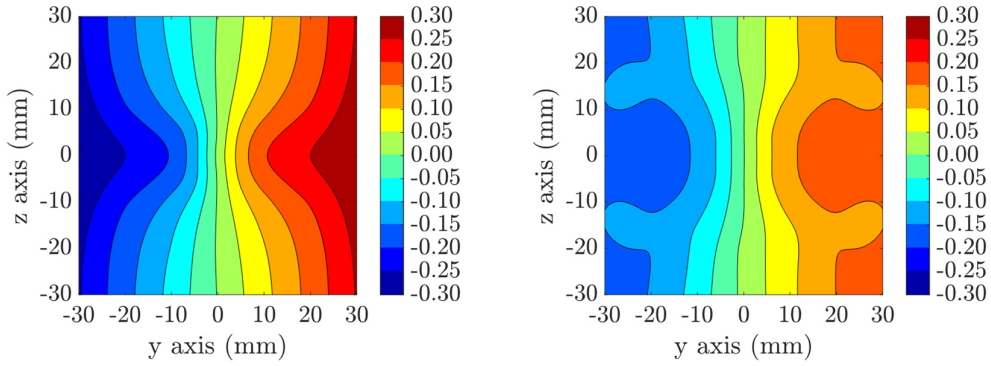

a) Injector P601035, orifice l/d ratio = 3 b) Injector P601055, orifice l/d ratio = 5

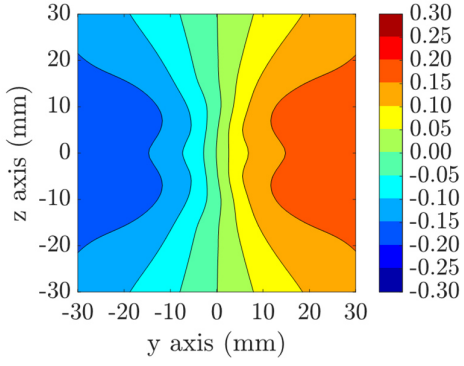

c) Injector P601085, orifice l/d ratio = 8

Figure 4.145. The Effect of Orifice l/d Ratio on Normalized V Velocity

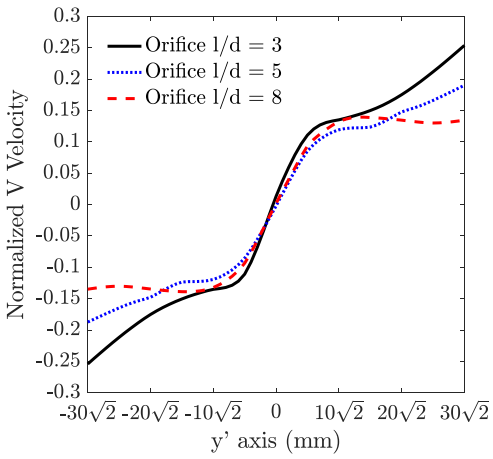

Figure 4.146. Comparison of the Effect of Orifice l/d Ratio on Normalized V Velocity at y'-axis

4.2.2.5. Normalized W Velocity

The normalized W velocity distributions produced by the pentad injectors with different l/d ratios are given in Figure 4.147. Similar to V velocity, the magnitude of the W velocity becomes smaller with an increase in the l/d ratio from 3 to 5.

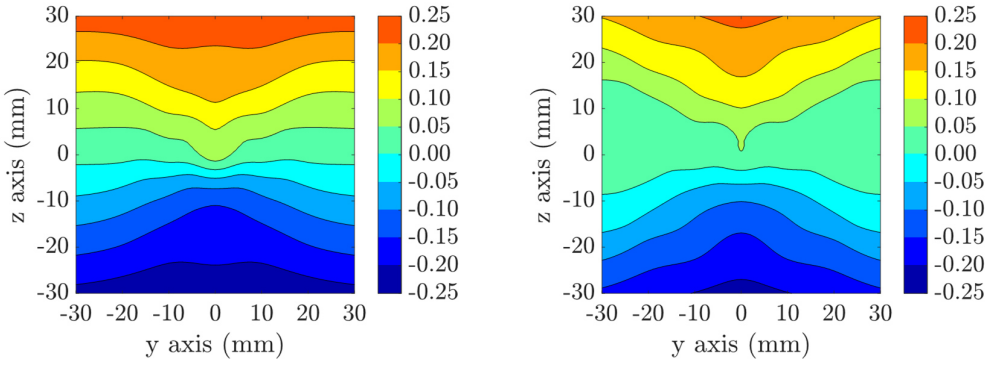

a) Injector P601035, orifice l/d ratio = 3 b) Injector P601055, orifice l/d ratio = 5

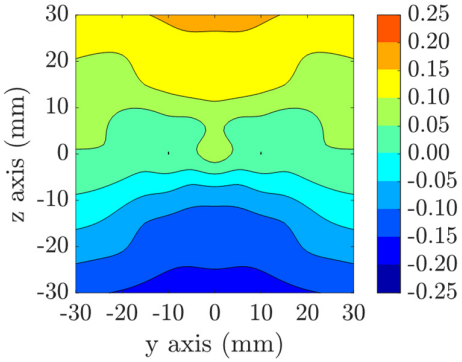

c) Injector P601085, orifice l/d ratio = 8

Figure 4.147. The Effect of Orifice l/d Ratio on Normalized W Velocity

According to Figure 4.148, the distributions with the l/d ratios of 5 and 8 show a very similar trend all along the y'-axis. As a reminder, the measurements obtained on one quarter of the measurement plane were projected onto the other quarters based on the symmetric geometry of the pentad injectors, and this should be kept in mind in the interpretation of all presented results.

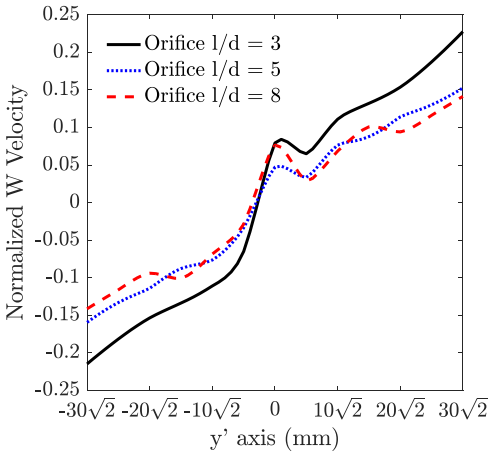

Figure 4.148. Comparison of the Effect of Orifice l/d Ratio on Normalized W Velocity at y'-axis

4.2.2.6. Normalized Velocity Magnitude

The normalized velocity magnitude distributions obtained with pentad injectors are given in Figure 4.149. The normalized velocity magnitude decreases with an increase in the l/d ratio, similar to what is observed with the axial velocity distributions..

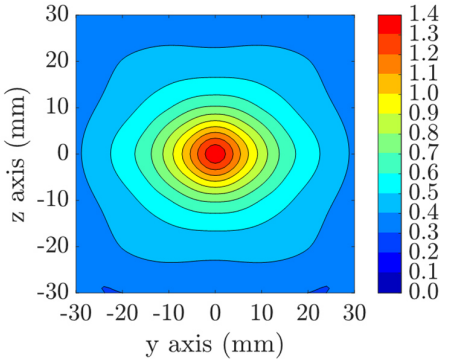

a) Injector P601035, orifice l/d ratio = 3

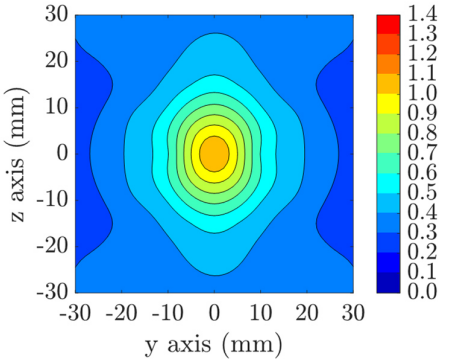

b) Injector P601055, orifice l/d ratio = 5

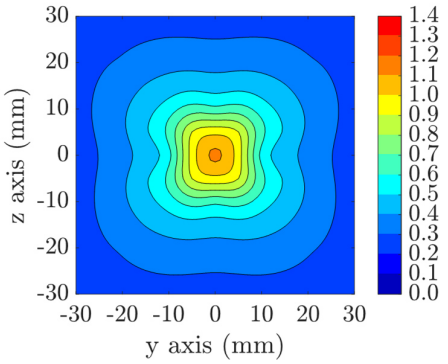

c) Injector P601085, orifice l/d ratio = 8

Figure 4.149. The Effect of Orifice l/d Ratio on Normalized Velocity Magnitude

The comparison of the distributions along the y'-axis given in Figure 4.150 show that the normalized velocity magnitude decreases by 30% as the l/d ratio increases from 3 to 5.

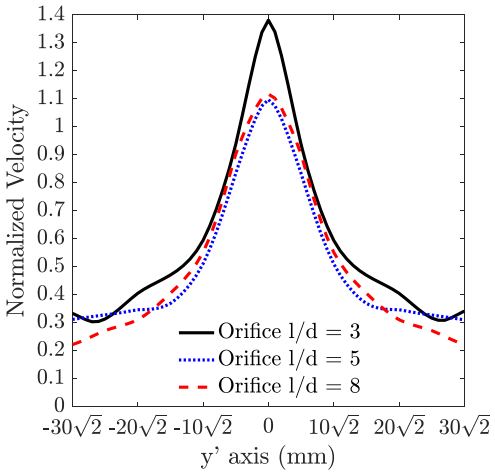

Figure 4.150. Comparison of the Effect of Orifice l/d Ratio on Normalized Velocity Magnitude at y'-axis

4.2.2.7. SMD Distribution

The SMD distributions obtained by the pentad injectors can be seen in Figure 4.151. The SMD values are relatively low in the regions where relatively high normalized droplet counts are obtained. There is an obvious increase in the SMD at l/d = 8.

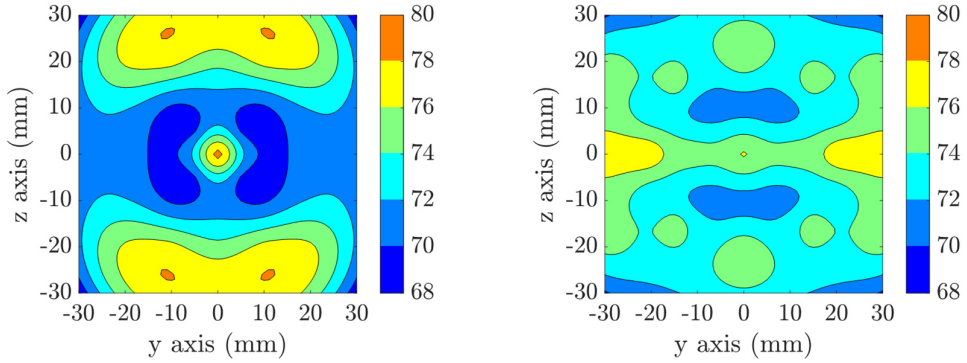

a) Injector P601035, orifice l/d ratio = 3 b) Injector P601055, orifice l/d ratio = 5

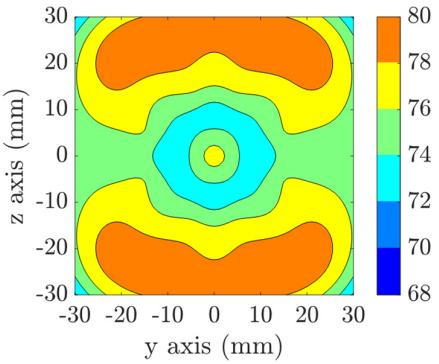

c) Injector P601085, orifice l/d ratio = 8

Figure 4.151. The Effect of Orifice l/d Ratio on SMD

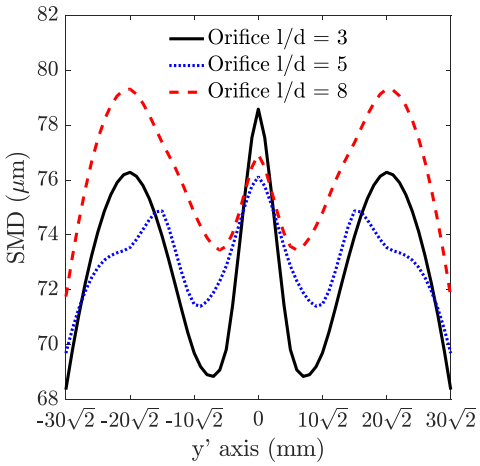

Figure 4.152. Comparison of the Effect of Orifice l/d Ratio on SMD at y'-axis

The change in the SMD distribution along the y'-axis is given in Figure 4.152. The SMD is proportional to the orifice l/d ratio, and an inverse trend of the normalized droplet count is observed.

4.2.2.8. Rosin-Rammler Distribution

The Rosin-Rammler distributions of the sprays produced by the pentad injectors with different orifice l/d ratios are shown in Figure 4.153.

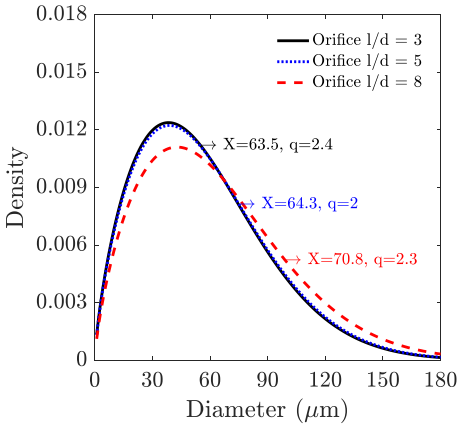

Figure 4.153. Comparison of Rosin-Rammler Distributions

While the q parameter seems to be slightly changing among the test cases, the X parameter increases, which is consistent with the observed increase in the mean droplet diameter.

4.2.2.9. Total Normalized Droplet Count

The total normalized droplet count as a function of the orifice l/d ratio is given in Figure 4.154. The impingement distance, orifice diameter, impingement angle and momentum ratio were kept constant while the following results were obtained. The total normalized droplet count is inversely proportional with the orifice l/d ratio.

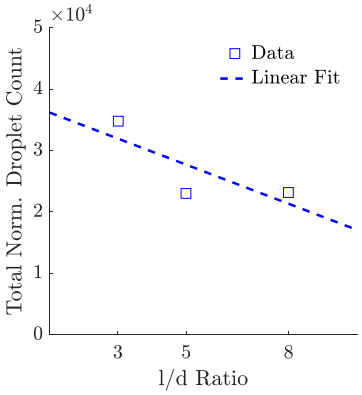

Figure 4.154. Comparison of the Effect of Orifice l/d Ratio on Total Normalized Droplet Count

4.2.2.10. Mean D10

The change in the arithmetic mean diameter, D10, as a function of the orifice l/d ratio is given in Figure 4.155. The mean diameter is proportional to the l/d ratio.

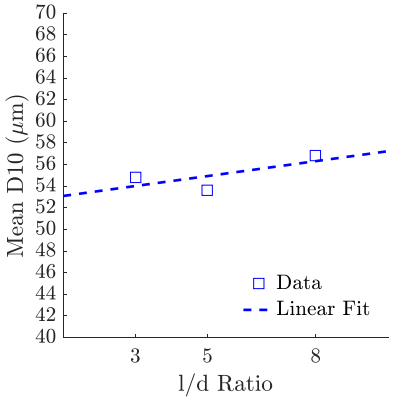

Figure 4.155. Comparison of the Effect of Orifice l/d Ratio on Mean D10

4.2.2.11. Mean SMD

The change in the mean SMD as a function of the orifice l/d ratio is given in Figure 4.156. Similar to triplet injectors, the mean SMD is proportional to the l/d ratio.

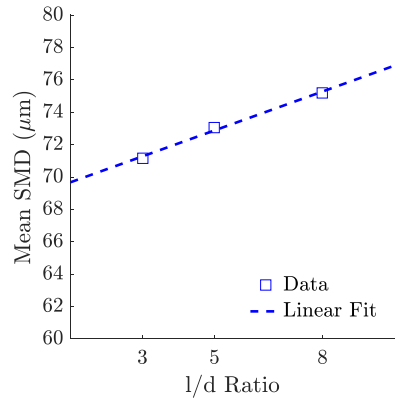

Figure 4.156. Comparison of the Effect of Orifice l/d Ratio on Mean SMD

4.2.2.12. Spray Angle

The effect of the orifice l/d ratio on the spray angle is given in Figure 4.157. The spray angle decreases with an increase in the orifice l/d ratio. This is the opposite of the trend observed with triplet injectors.

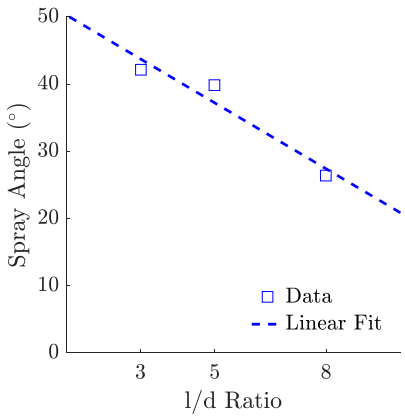

Figure 4.157. Comparison of the Effect of Orifice l/d Ratio on Spray Angle

4.2.3. The Effect of Orifice Diameter

In this section, the effect of the orifice diameter will be investigated in terms of the normalized droplet count, velocity and SMD distributions. The impingement distance, orifice l/d ratio, impingement angle and momentum ratio are kept constant.

4.2.3.1. Normalized Mass Flux Distribution

Figure 4.158 shows the mass flux distributions obtained with pentad injectors with different orifice diameters. In each case, the inner orifice had the same diameter with the outer orifices. With a decrease in the orifice diameter from 1.2 mm to 1 mm, the area that the mass flux is distributed over enlarges significantly, and the mass flux also becomes considerably more evenly distributed. Compared to triplet injectors,

the effect of the change of the orifice diameter from 1 mm to 1.2 mm is more severe on normalized mass flux distributions. This is because the outer orifices located in the same circle at intervals of 90° prevents the spray from spreading in the perpendicular direction.

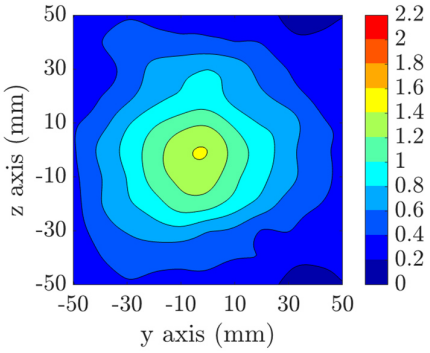

a) Injector P600855, orifice diameter = 0.8 mm

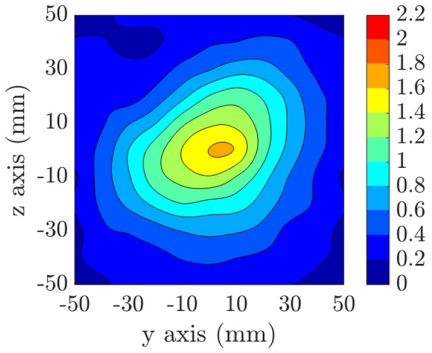

b) Injector P601055, orifice diameter = 1.0 mm

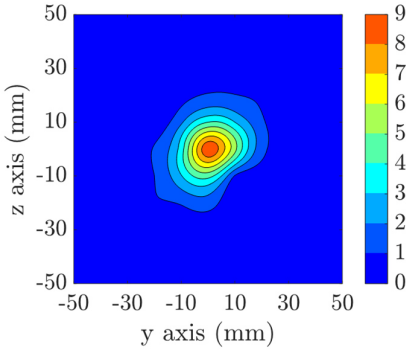

c) Injector P601255, orifice diameter = 1.2 mm

Figure 4.158. The Effect of Orifice Diameter on Normalized Mass Flux Distribution

Figure 4.159 shows the normalized mass flux distributions of pentads with different orifice diameters, where the diameter of 0.8 mm is shown in black, 1.0 mm in blue, and 1.2 mm in red. The mass flux distributions along the y' and z' axes are denoted by line 1 and line 2, respectively, The drastic change in the mass flux distribution can be seen on both axes. The effect of the orifice diameter on the mass flux distribution is significantly more obvious than triplet injectors.

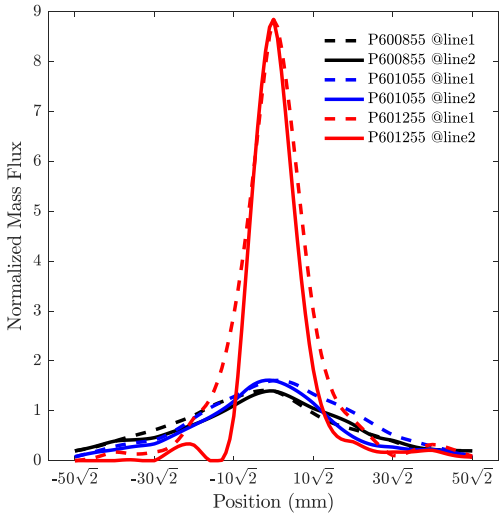

Figure 4.159. Comparison of the Effect of Orifice Diameter on Normalized Mass Flux Distributions at y' and z'-axes

4.2.3.2. Normalized Droplet Count

The normalized droplet count distributions obtained by the pentad injectors with different orifice diameters are given in Figure 4.160. A drastic change in terms of the normalized droplet count is obtained with a change in the orifice diameter.

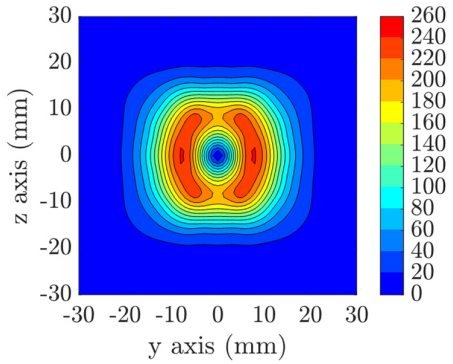

a) Injector P600855, orifice diameter = 0.8 mm

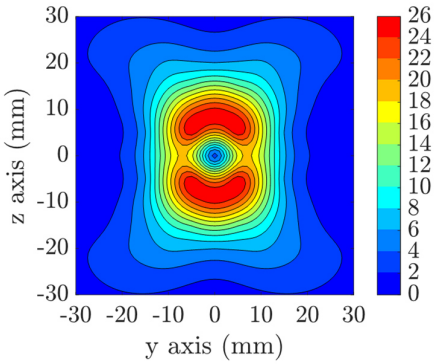

b) Injector P601055, orifice diameter = 1.0 mm

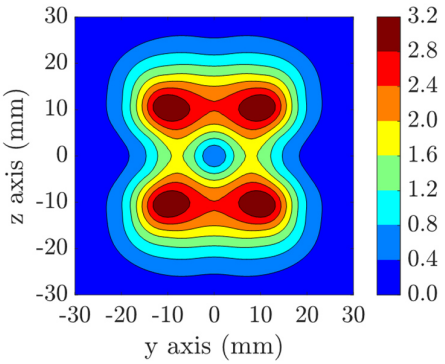

c) Injector P601255, orifice diameter = 1.2 mm

Figure 4.160. The Effect of Orifice Diameter on Normalized Droplet Count

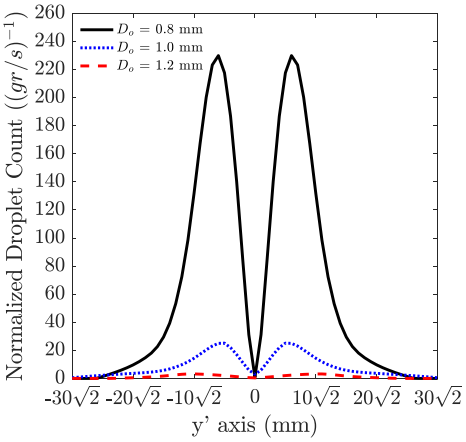

Figure 4.161. Comparison of the Effect of Orifice Diameter on Normalized Droplet Count at y'-axis

The comparison of the effect of the orifice diameter on the normalized droplet count is given in Figure 4.161. Increase of the orifice diameter from 0.8 mm to 1 mm decreases the normalized droplet count by 90%, further increase from 1 mm to 1.2 mm also causes another decrease by 90% due to the much lower number of droplets.

4.2.3.3. Normalized Axial Velocity

The normalized axial velocity distributions are given in Figure 4.162.

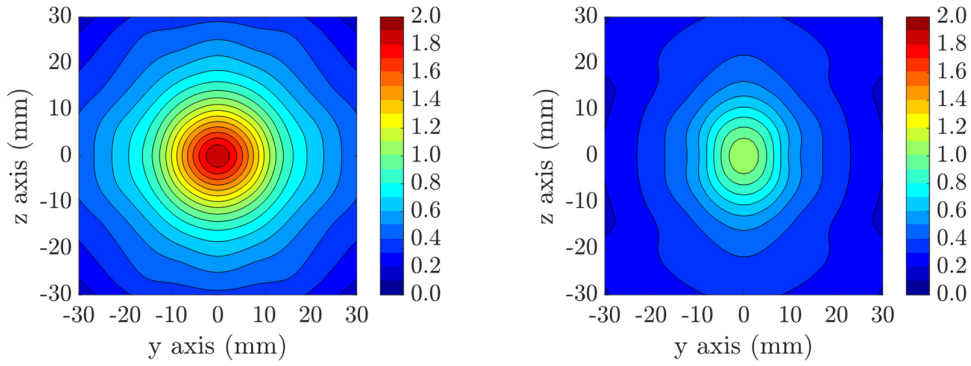

a) Injector P600855, orifice diameter = 0.8 mm

b) Injector P601055, orifice diameter = 1.0 mm

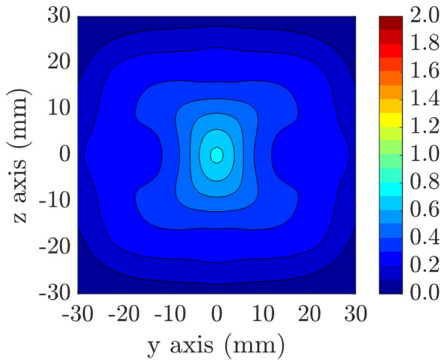

c) Injector P601255, orifice diameter = 1.2 mm

Figure 4.162. The Effect of Orifice Diameter on Normalized Axial Velocity

As expected from the normalized droplet count distribution results, with the increase of the orifice diameter, the normalized axial velocity decreases.

The comparison of the normalized axial velocity distribution along the y' axis given Figure 4.163 shows that results are inversely proportional to the orifice diameter.

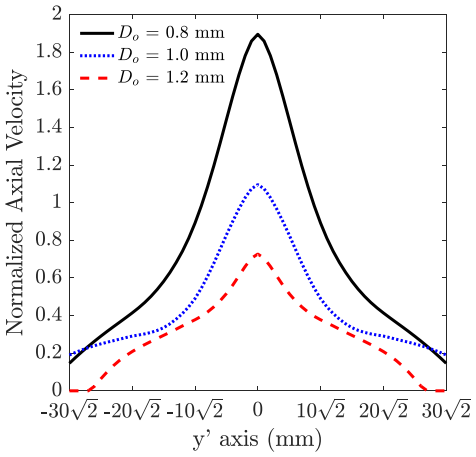

Figure 4.163. Comparison of the Effect of Orifice Diameter on Normalized Axial Velocity at y'-axis

4.2.3.4. Normalized V Velocity

The normalized V velocity distributions obtained by the pentad injectors with different orifice diameters are given in Figure 4.164.

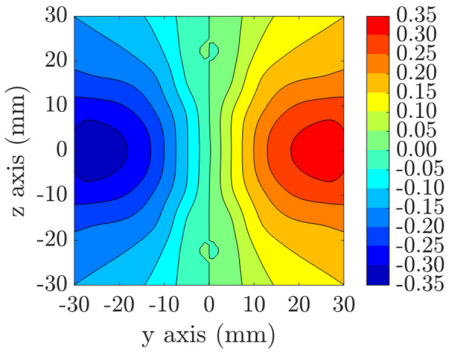

a) Injector P600855, orifice diameter = 0.8 mm

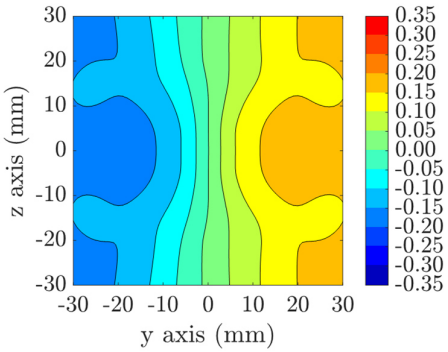

b) Injector P601055, orifice diameter = 1.0 mm

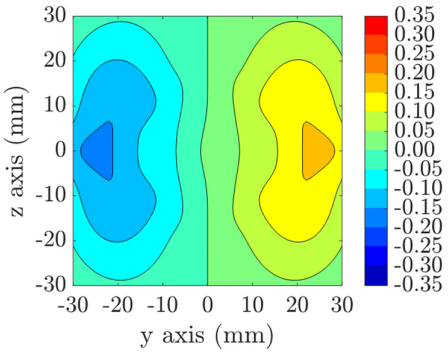

c) Injector P601255, orifice diameter = 1.2 mm

Figure 4.164. The Effect of Orifice Diameter on Normalized V Velocity

The contour plots show that with the increase of the orifice diameter, the normalized V velocity decreases similar to the axial velocity.

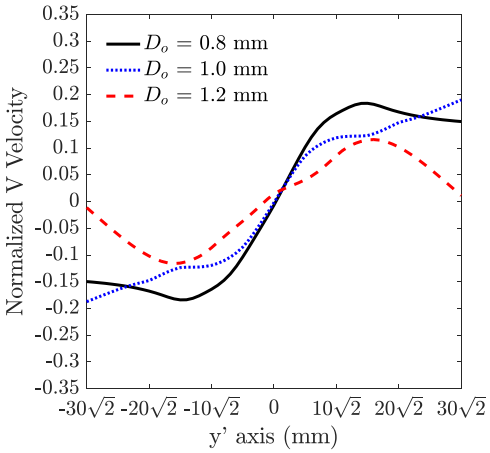

Figure 4.165. Comparison of the Effect of Orifice Diameter on Normalized V Velocity at y'-axis

Figure 4.165 shows that along the y'-axis, V velocity becomes smaller with an increase in the orifice diameter.

4.2.3.5. Normalized W Velocity

The normalized W velocity distributions provided by the pentad injectors with different orifice diameters are given in Figure 4.166.

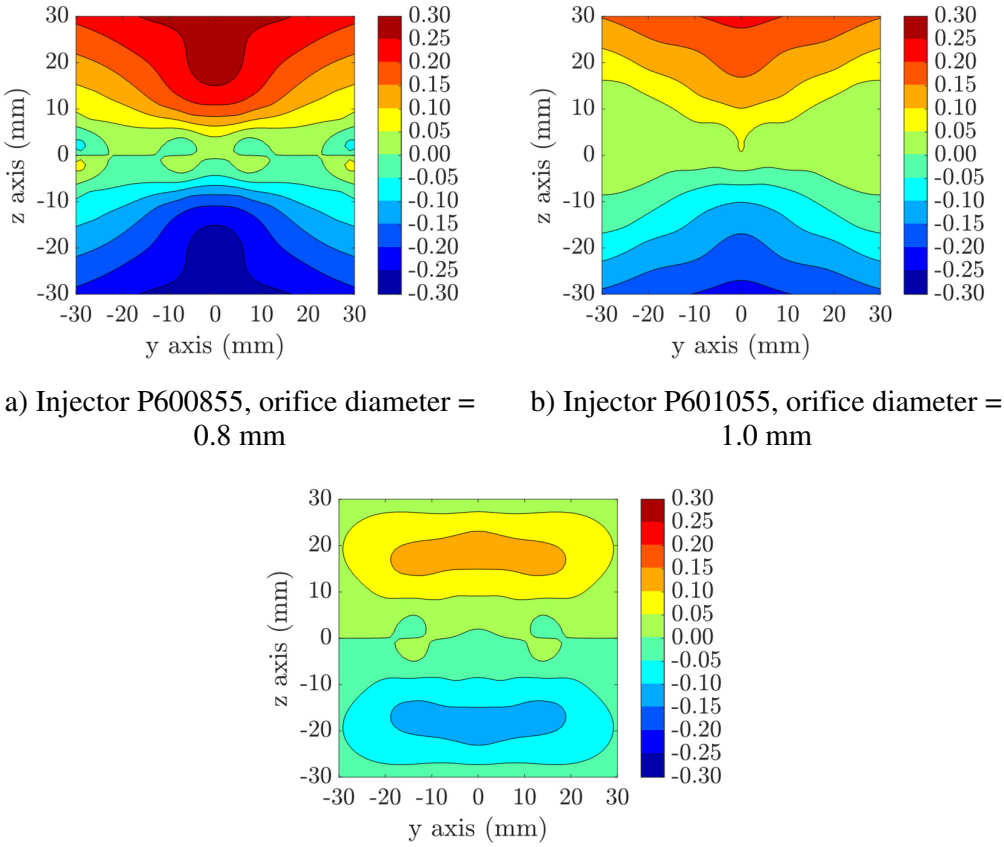

a) Injector P600855, orifice diameter = 0.8 mm

b) Injector P601055, orifice diameter = 1.0 mm

c) Injector P601255, orifice diameter = 1.2 mm

Figure 4.166. The Effect of Orifice Diameter on Normalized W Velocity

Similar to V velocity, the normalized W velocity magnitude decreases with the increase of the orifice diameter. The comparison of the normalized W velocity given in Figure 4.167 shows a similar trend to the normalized V velocity.

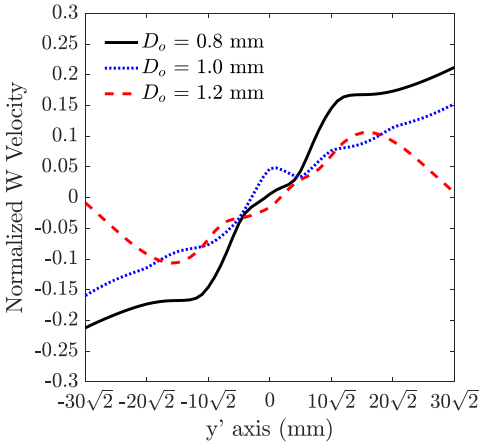

Figure 4.167. Comparison of the Effect of Orifice Diameter on Normalized W Velocity at y'-axis

4.2.3.6. Normalized Velocity Magnitude

The normalized velocity magnitude distributions are given in Figure 4.168. Similar to the other normalized velocity distributions, the normalized velocity magnitude decreases with the increase of the orifice diameter.

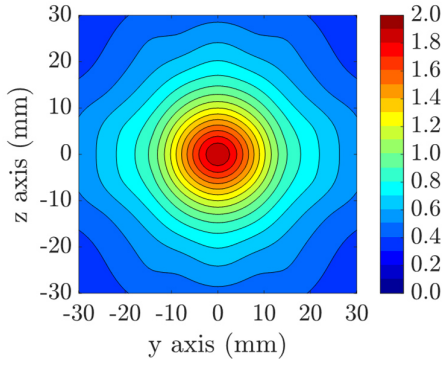

a) Injector P600855, orifice diameter = 0.8 mm

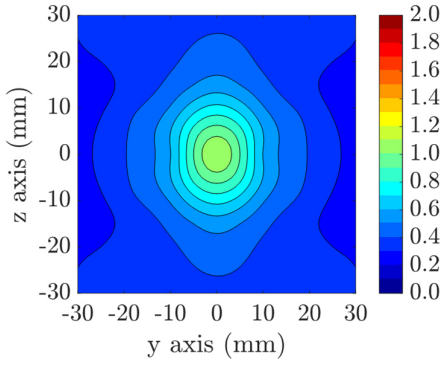

b) Injector P601055, orifice diameter = 1.0 mm

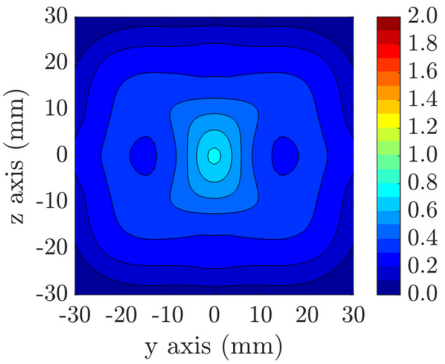

c) Injector P601255, orifice diameter = 1.2 mm

Figure 4.168. The Effect of Orifice Diameter on Normalized Velocity Magnitude

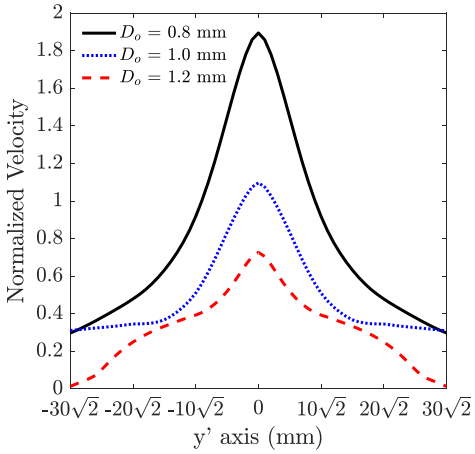

Figure 4.169. Comparison of the Effect of Orifice Diameter on Normalized Velocity Magnitude at y'-axis

The comparison of the normalized velocity distributions along the y'-axis in Figure 4.169 shows that with the increase of the orifice diameter by 0.2 mm, the normalized velocity magnitude decreases by 50%.

4.2.3.7. SMD Distribution

The SMD distributions obtained by the pentad injectors with different orifice diameters are given in Figure 4.170.

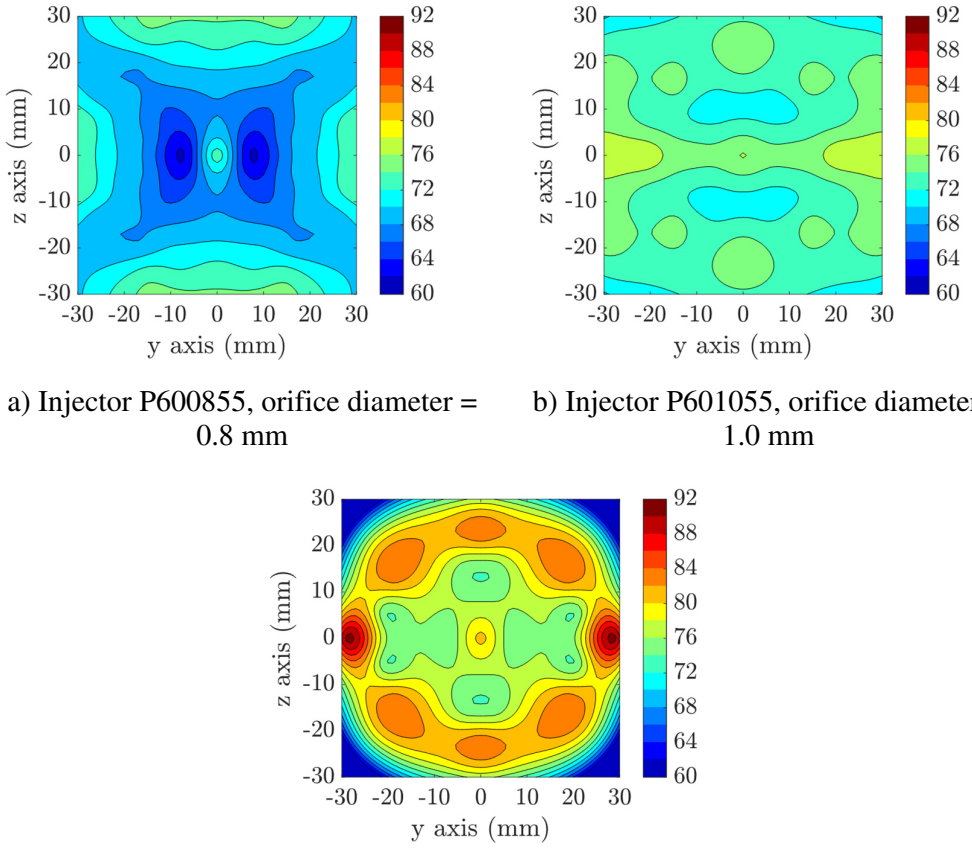

a) Injector P600855, orifice diameter = 0.8 mm

b) Injector P601055, orifice diameter = 1.0 mm

c) Injector P601255, orifice diameter = 1.2 mm

Figure 4.170. The Effect of Orifice Diameter on SMD

The minimum SMD values are obtained with the orifice diameter of 0.8 mm. Increase in the orifice diameter causes an increase in the minimum SMD. It should be noted that due insufficient number of droplets, unrealistic minimum SMD values are obtained in the injector with the 1.2 mm orifice diameter.

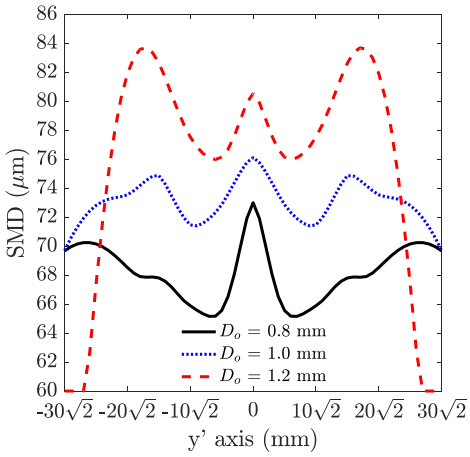

Figure 4.171. Comparison of the Effect of Orifice Diameter on SMD at y'-axis

The comparison of the SMD distributions with different orifice diameters given in Figure 4.171 show that the minimum SMD is proportional to the orifice diameter.

4.2.3.8. Rosin-Rammler Distribution

The Rosin-Rammler distributions of pentad injectors with different orifice diameters are shown in Figure 4.172.

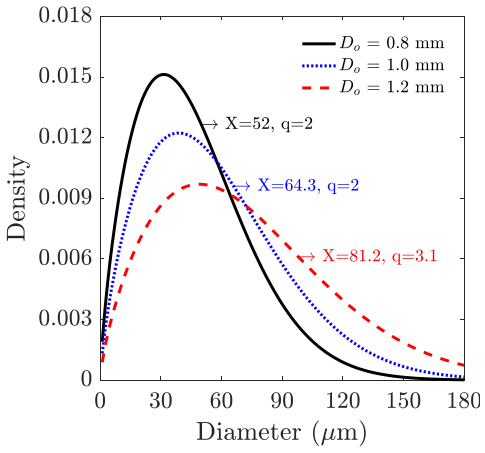

Figure 4.172. Comparison of Rosin-Rammler Distributions

It is seen that the X parameter is strongly correlated to the orifice diameter. On the other hand, between injectors with 0.8 mm and 1 mm, q doesn't change. Further increase in the orifice diameter results in a more uniformly distributed spray

4.2.3.9. Total Normalized Droplet Count

The change in the total normalized droplet count with the orifice diameter is given in Figure 4.173. Total normalized droplet count is inversely proportional to the orifice diameter.

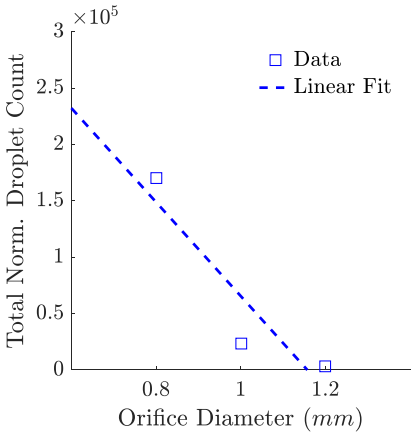

Figure 4.173. Comparison of the Effect of Orifice Diameter on Total Normalized Droplet Count

4.2.3.10. Mean D10

The arithmetic mean diameter as a function of the orifice diameter is given in Figure 4.174. The arithmetic mean diameter is proportional to the orifice diameter.

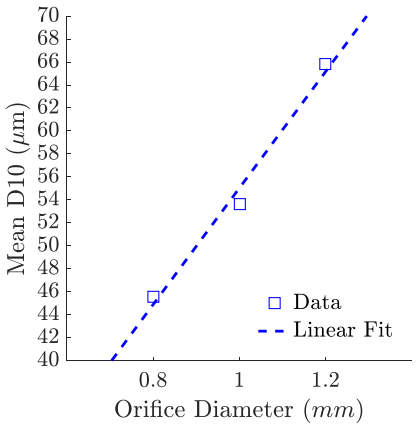

Figure 4.174. Comparison of the Effect of Orifice Diameter on Mean D10

4.2.3.11. Mean SMD

The change in the mean SMD as a function of the orifice diameter is given in Figure 4.175. The mean SMD is proportional to the orifice diameter. For pentad injectors, the orifice diameter has the greatest effect on the mean SMD over all parameters examined in this thesis study.

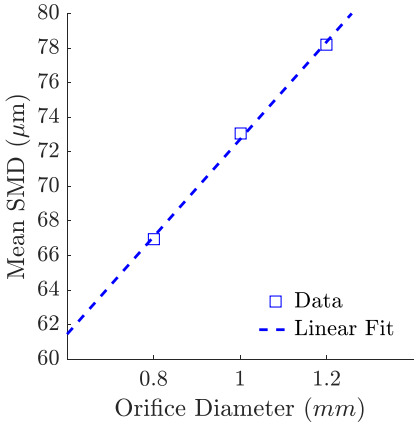

Figure 4.175. Comparison of the Effect of Orifice Diameter on Mean SMD

4.2.3.12. Spray Angle

The change in the spray angle with respect to the orifice diameter is given in Figure 4.176. As it is seen, the spray angle is inversely proportional to the orifice diameter.

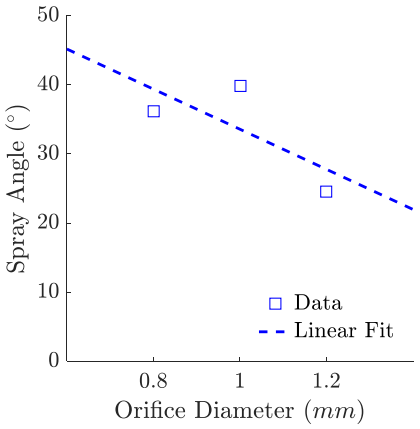

Figure 4.176. Comparison of the Effect of Orifice Diameter on Spray Angle

4.2.4. The Effect of Impingement Angle

In this section, the effect of the impingement angle will be investigated in terms of the normalized droplet count, velocity and SMD distributions. The impingement distance, orifice l/d ratio, orifice diameter and momentum ratio are kept constant.

4.2.4.1. Normalized Mass Flux Distribution

Figure 4.177 shows the mass flux distribution produced by the pentad injectors with different impingement angles. The measurements for the injector with 90° impingement angle had to be performed at a plane 150 mm downstream of the impingement point instead of 480 mm, since a large portion of the mass flux could not be collected at 480 mm by using the mechanical patternator available.

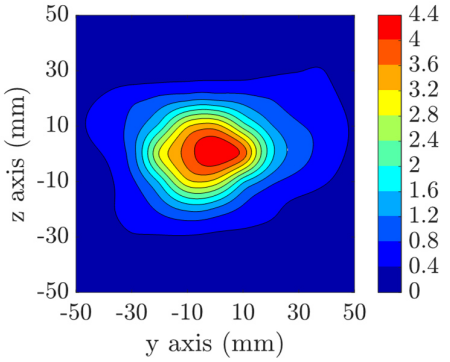

a) Injector P451055, impingement angle = 45°

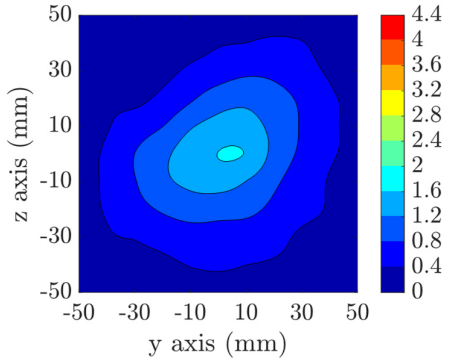

b) Injector P601055, impingement angle = 60°

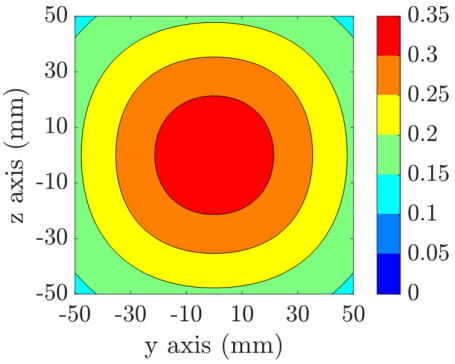

c) Injector P901055, impingement angle = 90°

Figure 4.177. The Effect of Impingement Angle on Normalized Mass Flux Distribution

Therefore, once again the study of Hines et al. (Hines, Schuman, Ford and Fertig, 1972) was used to obtain the spray dispersion parameters at the plane 150 mm below the impingement point, and then, project it onto the plane 480 mm away from the impingement point in order to compare it with the others. The findings of Hines et al. (Hines, Schuman, Ford and Fertig, 1972) suggest that the mass flux distributions obtained from pentad injectors can be defined by Equations *(31)* and *(32)*.

$$w_o = \frac{w_{001_o}}{z^2}\left\{1 + c_o\left[\left(\frac{y}{z}\right)^2 + \left(\frac{x}{z}\right)^2\right]\right\} e^{-a_o\left[\left(\frac{x}{z}\right)^2 + \left(\frac{y}{z}\right)^2\right]} \qquad (31)$$

$$w_i = \frac{w_{001_i}}{z^2}\left\{1 + c_i\left[\left(\frac{y}{z}\right)^2 + \left(\frac{x}{z}\right)^2\right]\right\} e^{-a_i\left[\left(\frac{x}{z}\right)^2 + \left(\frac{y}{z}\right)^2\right]} \quad (32)$$

Similar to the definitions previously provided in the case of triplet injectors, w_{001} is the normalization factor equivalent to mass flux, and a and c are the spray coefficients defined for the inner and outer orifices that are deduced from the experimental data. Hines et al. (Hines, Schuman, Ford and Fertig, 1972) defines the z-axis as the vertical direction that the spray develops, with x and z-axes being switched compared to the coordinate system used in the current setup. The spray coefficients for the injector with 90° impingement angle are determined using the mass flux measurements at x=150 mm downstream of the impingement point, as follows: a_o=14.5, c_o=258.3, a_i=1.3 and c_i=360.9. Then, the measurements were projected onto x=480 mm using this set of coefficients. Figure 4.174 shows that similar to the results of triplet injectors, as the impingement angle increases from 45° to 60°, there is a sharp drop in the peak value of the mass flux and the distribution becomes more uniform as a result of higher lateral momentum originating from the outer orifices. As a difference from the triplet injectors, with further of impingement angle from 60° to 90°, the peak value decreases further and the distribution becomes even more uniform.

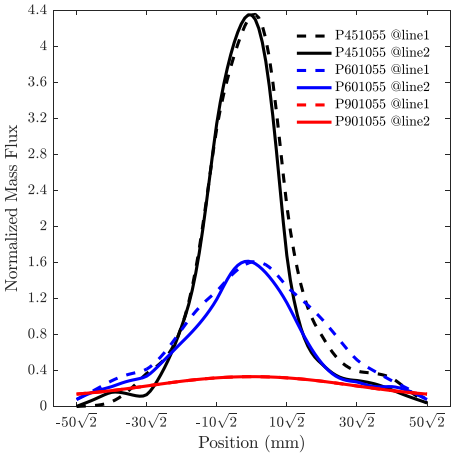

Figure 4.178. Comparison of the Effect of Impingement Angle on Normalized Mass Flux Distributions at y' and z'-axes

Figure 4.178 shows the normalized mass flux distributions obtained by pentads with different impingement angles, where 45° is shown in black, 60° in blue, and 90° in red. The mass flux distributions along the y' and z'-axes are denoted by line 1 and line 2, respectively, Increasing the impingement angle from 45° to 60° results in a significant reduction in mass flux. It seems that further increase of the impingement angle decreases the highest value of the mass flux even more than the previous one such that the most uniform distribution of the mass flux is obtained amongst all test cases.

4.2.4.2. Normalized Droplet Count

The normalized droplet count distribution is given in Figure 4.179.

Contour plots show that with the increase of the impingement angle, the normalized droplet count decreases in contrary to the triplet injectors. Although the momentum ratio is kept approximately constant for impingement angle investigations, the momentum ratio is 2 for triplet injectors and 16 for pentad injectors. This suggests that the observed results may not be purely driven by the injector type and that the effect of the impingement angle should be investigated with different momentum ratios for both triplet and pentad injectors.

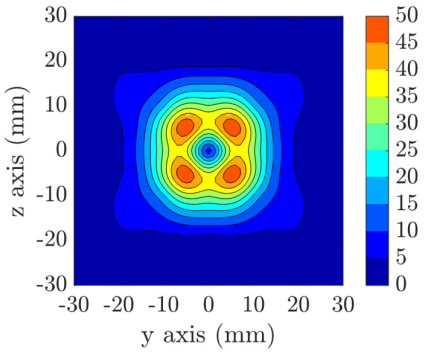

a) Injector P451055, impingement angle = 45°

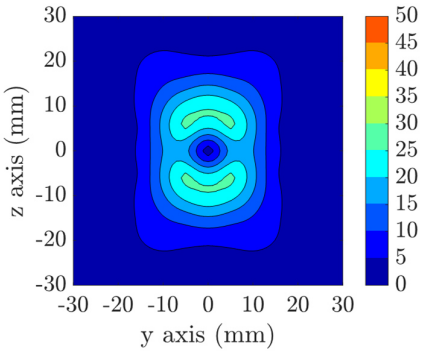

b) Injector P601055, impingement angle = 60°

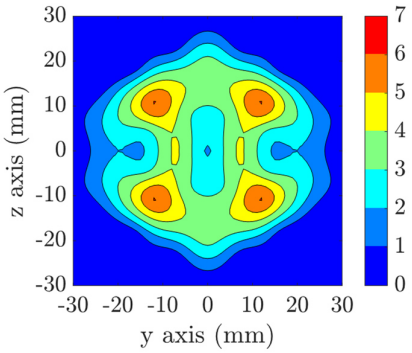

c) Injector P901055, impingement angle = 90°

Figure 4.179. The Effect of Impingement Angle on Normalized Droplet Count

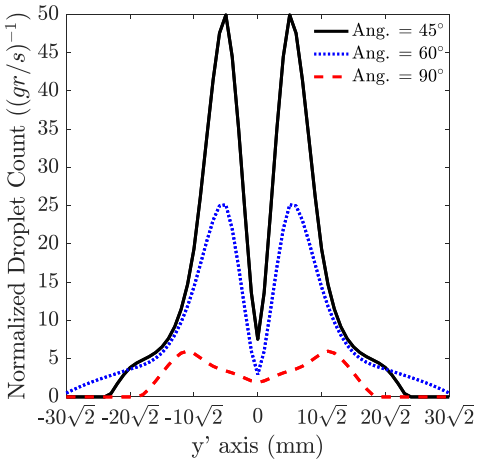

Figure 4.180. Comparison of the Effect of Impingement Angle on Normalized Droplet Count at y'-axis

Figure 4.180 shows that the increase in the impingement angle from 45° to 60° leads to a decrease in the normalized droplet count by 50%. Further increase in the impingement angle from 60° to 90° decreases the normalized droplet count by 90%.

4.2.4.3. Normalized Axial Velocity

The normalized axial velocity distributions obtained by pentad injectors with different impingement angles are given in Figure 4.181. In the same manner with the

normalized droplet count, the peak value of the normalized axial velocity decreases with an increase in the impingement angle.

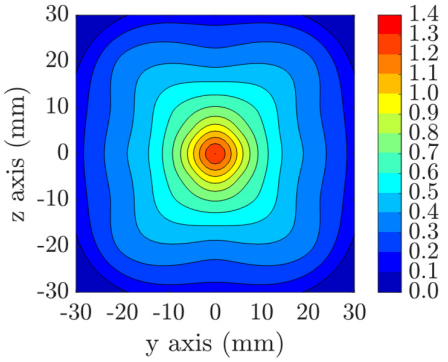

a) Injector P451055, impingement angle = 45°

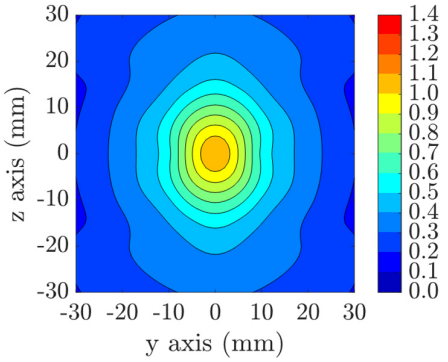

b) Injector P601055, impingement angle = 60°

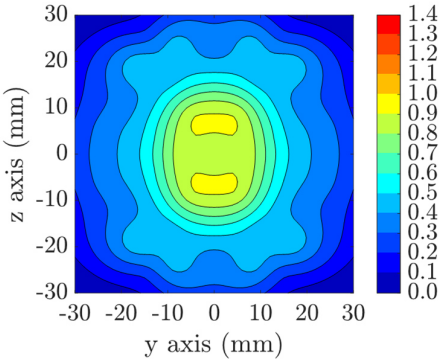

c) Injector P901055, impingement angle = 90°

Figure 4.181. The Effect of Impingement Angle on Normalized Axial Velocity

The comparison of the effect of the impingement angle on the normalized axial velocity along the y'-axis is given in Figure 4.182. In addition to the reduction in the highest values at the center with an increase in the impingement angle, there is an unexpected decrease at the center at the impingement angle of 90°. This is more likely an artificial product of the post-processing of the data due to projecting one quadrant of the measurement plane onto the other quadrants considering the geometic symmetry of the pentad injectors.

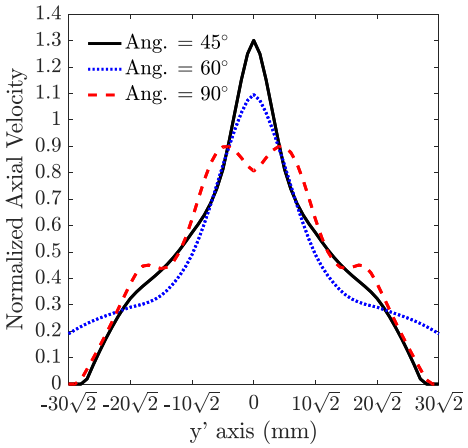

Figure 4.182. Comparison of the Effect of Impingement Angle on Normalized Axial Velocity at y'-axis

4.2.4.4. Normalized V Velocity

The normalized V velocity distributions obtained by pentad injectors with different impingement angles are given in Figure 4.183. The normalized V velocity gradually decreases with an increase in the impingement angle in terms of magnitude. These results show similarities with the droplet count distributions.

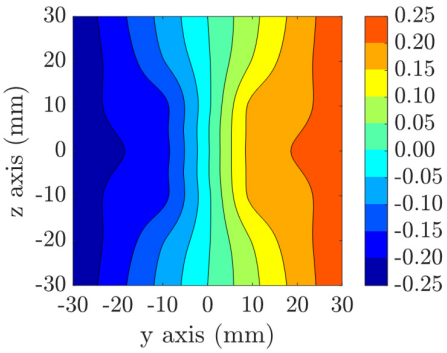

a) Injector P451055, impingement angle = 45°

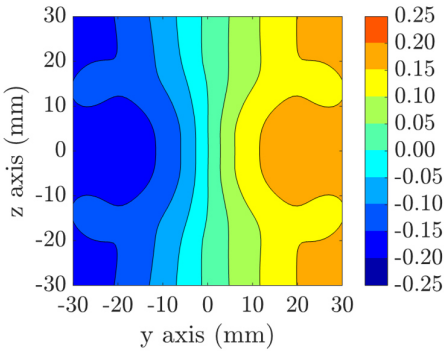

b) Injector P601055, impingement angle = 60°

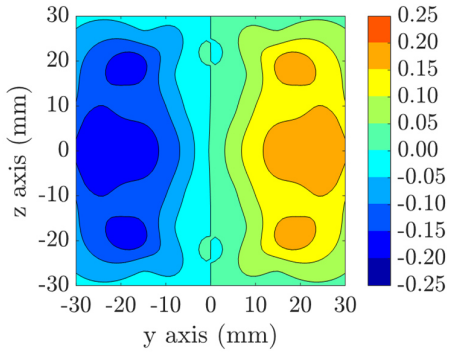

c) Injector P901055, impingement angle = 90°

Figure 4.183. The Effect of Impingement Angle on Normalized V Velocity

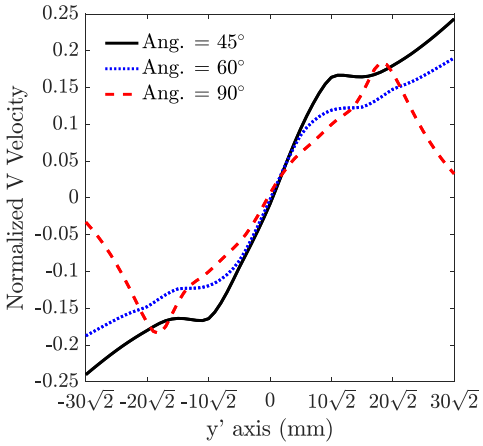

Figure 4.184. Comparison of the Effect of Impingement Angle on Normalized V Velocity at y'-axis

The comparison of the effect of impingement angle on the normalized V velocity along the y'-axis is given in Figure 4.184. V velocity becomes smaller with an increase in the impingement angle from 45° to 60°, but an observable relation cannot be obtained between the impingement angle 90° and the normalized V velocity distribution.

4.2.4.5. Normalized W Velocity

The normalized W velocity distributions of pentad injectors with different impingement angles are given in Figure 4.185.

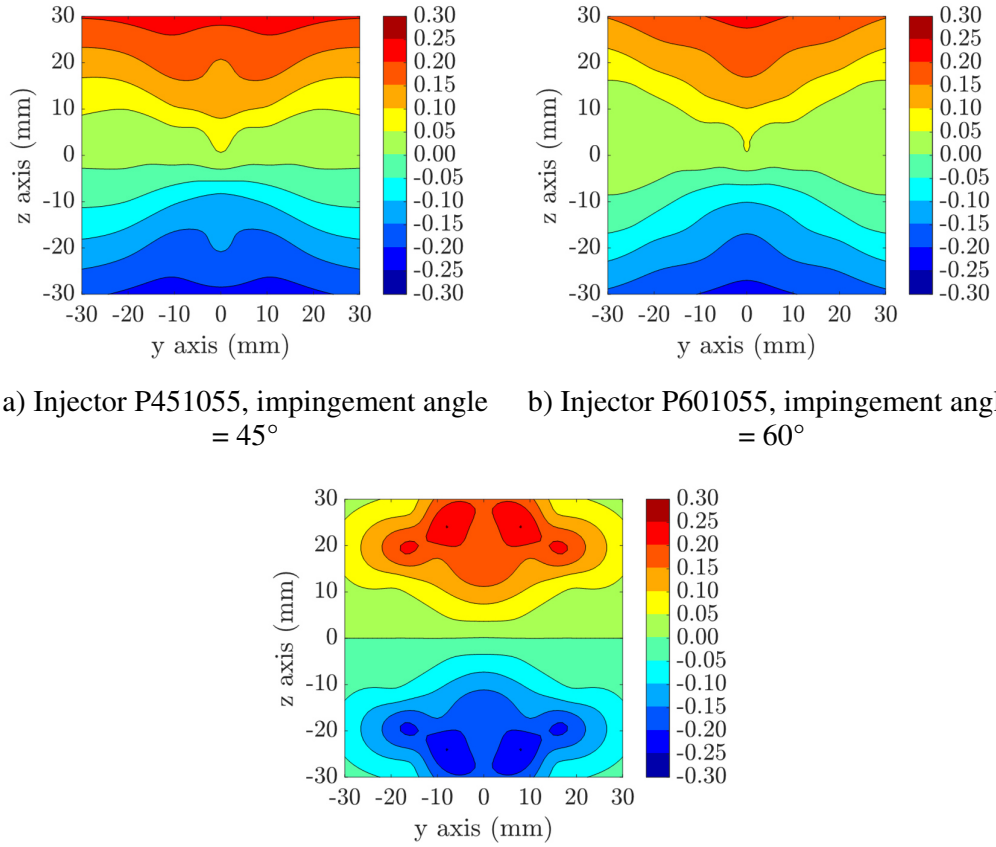

a) Injector P451055, impingement angle = 45°

b) Injector P601055, impingement angle = 60°

c) Injector P901055, impingement angle = 90°

Figure 4.185. The Effect of Impingement Angle on Normalized W Velocity

The normalized W velocity gradually decreases in terms of magnitude as the impingement angle increases from 45° to 60°. The trend for 90° is not clear.

The comparison of the effect of the impingement angle on the normalized V velocity along the y'-axis is given in Figure 4.186. Similar to the normalized V velocity, the normalized W velocity becomes smaller with an increase in the impingement angle

from 45° to 60°, but an observable relation cannot be obtained between the impingement angle 90° and the normalized W velocity distribution.

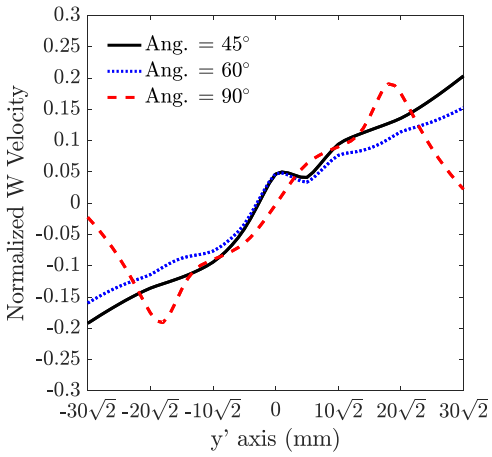

Figure 4.186. Comparison of the Effect of Impingement Angle on Normalized W Velocity at y'-axis

4.2.4.6. Normalized Velocity Magnitude

The normalized velocity magnitude distributions obtained by pentad injectors with different impingement angles are given in Figure 4.187.

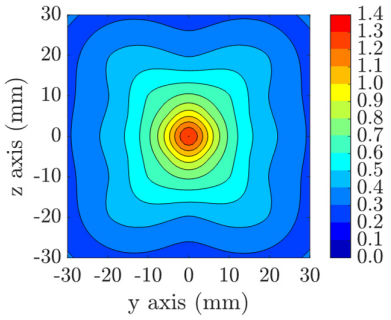

a) Injector P451055, impingement angle = 45°

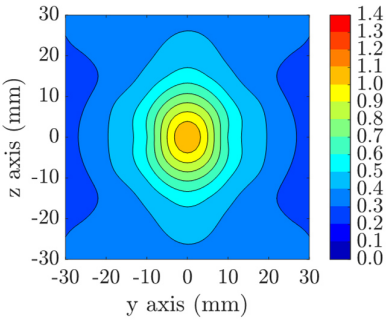

b) Injector P601055, impingement angle = 60°

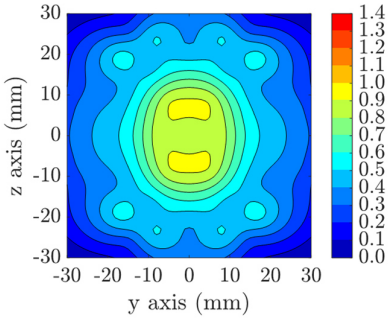

c) Injector P901055, impingement angle = 90°

Figure 4.187. The Effect of Impingement Angle on Normalized Velocity Magnitude

Similar to the previous velocity distirbutions, the normalized velocity magnitude decreases with an increase in the impingement angle. The normalized velocity distribution along the y'-axis given in Figure 4.188 shows similar trends with that of the normalized axial velocity.

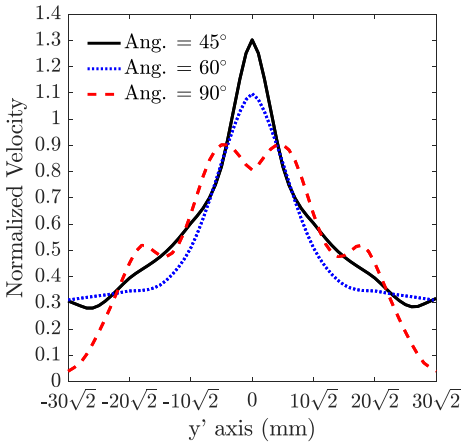

Figure 4.188. Comparison of the Effect of Impingement Angle on Normalized Velocity Magnitude at y'-axis

4.2.4.7. SMD Distribution

The SMD distribution produced by pentad injectors with different impingement angles are given in Figure 4.189.

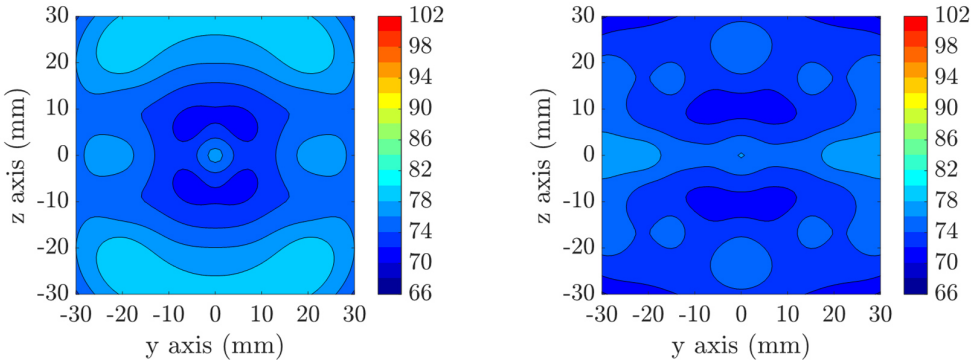

a) Injector P451055, impingement angle = 45°

b) Injector P601055, impingement angle = 60°

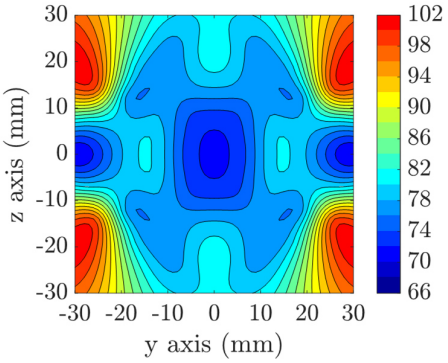

c) Injector P901055, impingement angle = 90°

Figure 4.189. The Effect of Impingement Angle on SMD

In the injector with impingement angle of 90°, some unrealistic SMD values can be seen on the corners of the distribution because of unsufficient number of droplets in those regions. Other than that, the distributions for 45° and 60° seem similar despite the huge difference that was observed in the normalized droplet counts for the two cases.

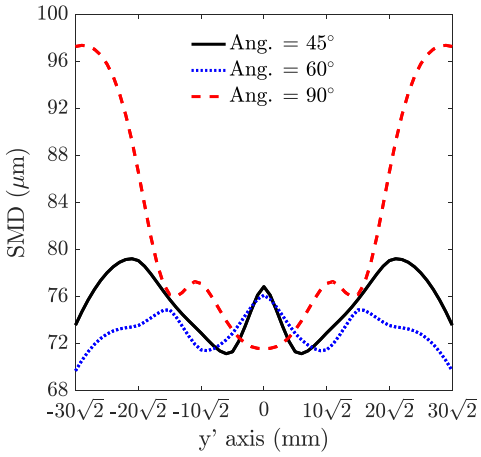

Figure 4.190. Comparison of the Effect of Impingement Angle on SMD at y'-axis

According to Figure 4.190, in the highest droplet count regions, the minimum SMD values are obtained for 45° and 60° around 70, however, a general overall trend among the distributions cannot be obtained.

4.2.4.8. Rosin-Rammler Distribution

As shown in Figure 4.191, the smallest X and q are obtained with the 60° impingement angle injector.

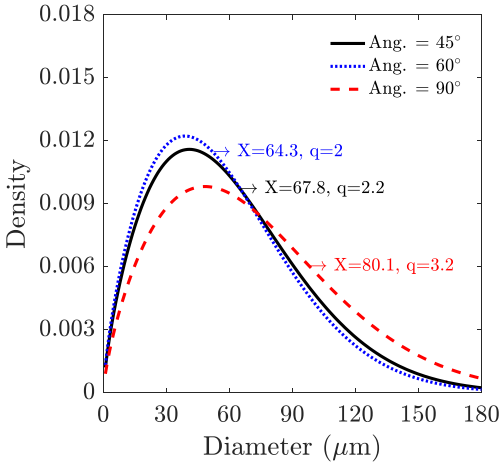

Figure 4.191. Comparison of Rosin-Rammler Distributions

4.2.4.9. Total Normalized Droplet Count

The total normalized droplet count variation with the impingement angle is given in Figure 4.192. The total normalized droplet count significantly decreases with an increase in the impingement angle.

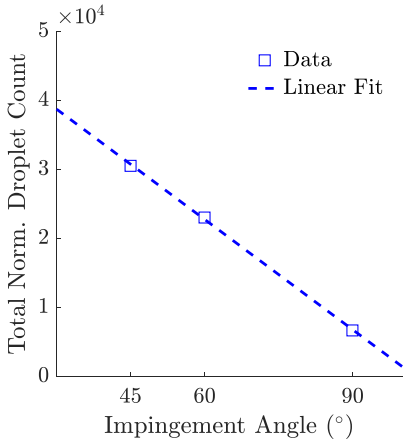

Figure 4.192. Comparison of the Effect of Impingement Angle on Total Normalized Droplet Count

4.2.4.10. Mean D10

The arithmetic mean diameter, D10, as a function of the impingement angle is given in Figure 4.193. The arithmetic mean diameter is proportional to the impingement angle.

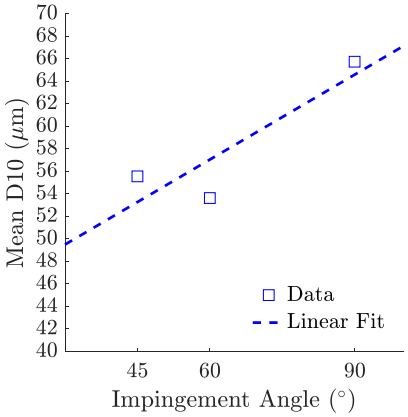

Figure 4.193. Comparison of the Effect of Impingement Angle on Mean D10

4.2.4.11. Mean SMD

The change in the mean SMD as a function of the impingement angle is given in Figure 4.194. The mean SMD increases with an increase in the impingement angle. The impingement angle affects the mean SMD of pentad injectors more compared to triplet injectors.

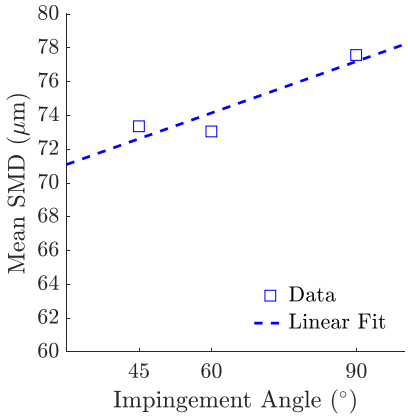

Figure 4.194. Comparison of the Effect of Impingement Angle on Mean SMD

4.2.4.12. Spray Angle

The change in the spray angle with respect to the impingement angle is given in Figure 4.195. The change in the spray angle increases with an increase in the impingement angle.

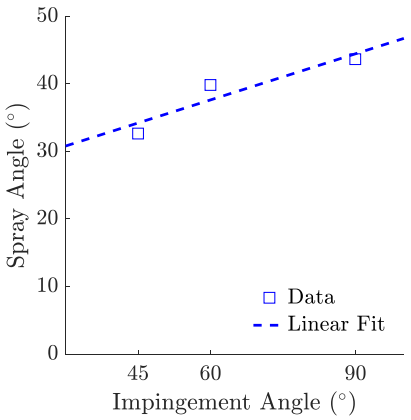

Figure 4.195. Comparison of the Effect of Impingement Angle on Spray Angle

4.2.5. The Effect of Momentum Ratio

In this section, the effect of the momentum ratio will be discussed by using the P601055 injector that has an impingement angle of 60°. There are only two momentum ratio values for which the measurements were performed. Other than the momentum ratio, all parameters such as the impingement angle, orifice diameter, orifice l/d ratio and impingement distance are kept constant. The momentum ratio was increased from MR = 4.17 to MR = 16.05 by decreasing the mass flow rate through the inner orifice by 49.2% and through the outer orifice by 0.4%.

4.2.5.1. Normalized Mass Flux Distribution

Similar to triplet injectors, an increase in the momentum ratio decreases the highest value of the normalized mass flux observed at the center as shown in Figure 4.196.

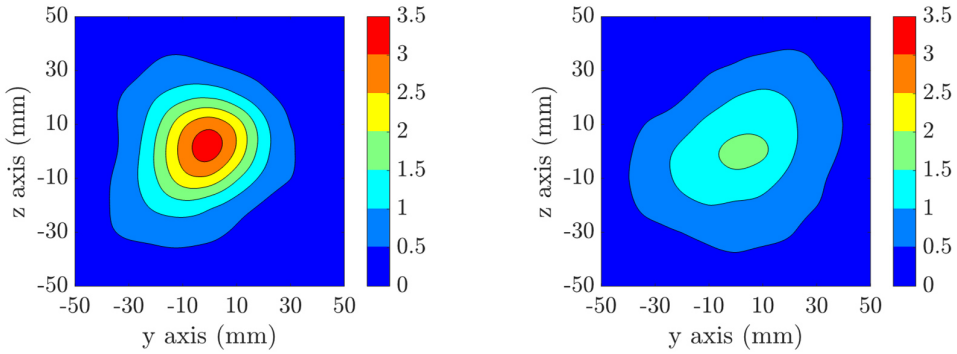

a) Injector P601055, MR= 4.17 b) Injector P601055, MR= 16.05

Figure 4.196. The Effect of Momentum Ratio on Normalized Mass Flux Distribution

Figure 4.197 shows the normalized mass flux distribution along the y' and z'-axes, which are denoted by line 1 and line 2, respectively, Similar to the triplet results, the significant decrease in the normalized mass flux is obtained at the center.

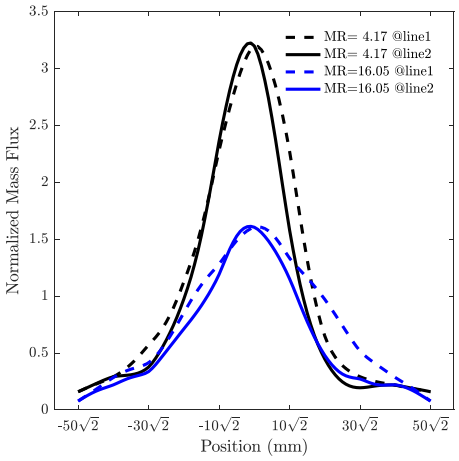

Figure 4.197. Comparison of the Effect of Momentum Ratio on Normalized Mass Flux Distributions at y' and z'-axes

4.2.5.2. Normalized Droplet Count

The normalized droplet count distributions obtained by the pentad injectors with different momentum ratios is given in Figure 4.198. The increase in the momentum ratio decreases the normalized droplet count. This is opposite to what was observed with the tiplet injectors.

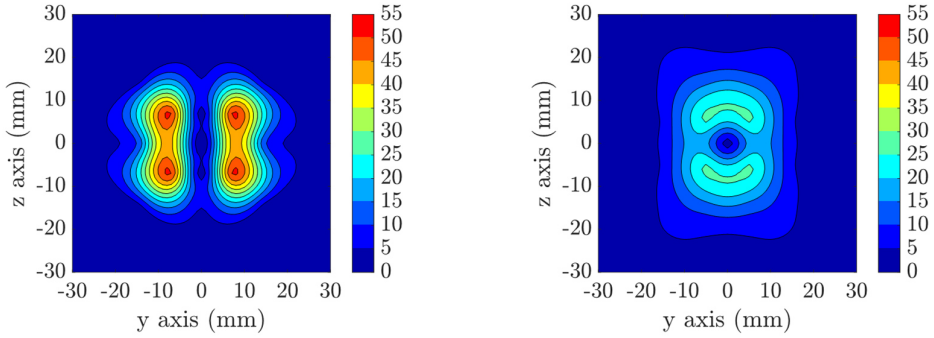

a) Injector P601055, MR = 4.17 b) Injector P601055, MR = 16.05

Figure 4.198. The Effect of Momentum Ratio on Normalized Droplet Count

The comparison along the y'-axis given in Figure 4.199 shows that four times of an increase in the momentum ratio causes the normalized droplet count to decrease by 50%.

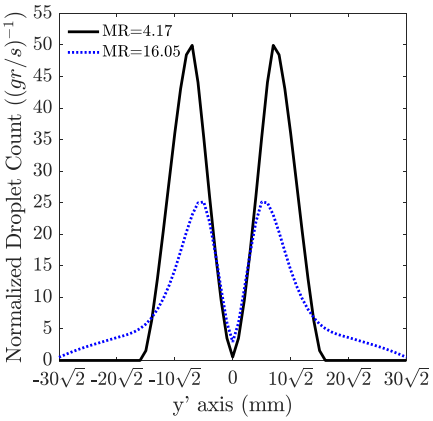

Figure 4.199. Comparison of the Effect of Momentum Ratio (60° Impingement Angle Injector) on Normalized Droplet Count at y'-axis

4.2.5.3. Normalized Axial Velocity

The normalized axial velocity distributions are given in Figure 4.200. The normalized axial velocity decreases slightly at the center with four times of an increase in the momentum ratio, whereas it slightly increases in the regions away from the center. This is also visible in Figure 4.201.

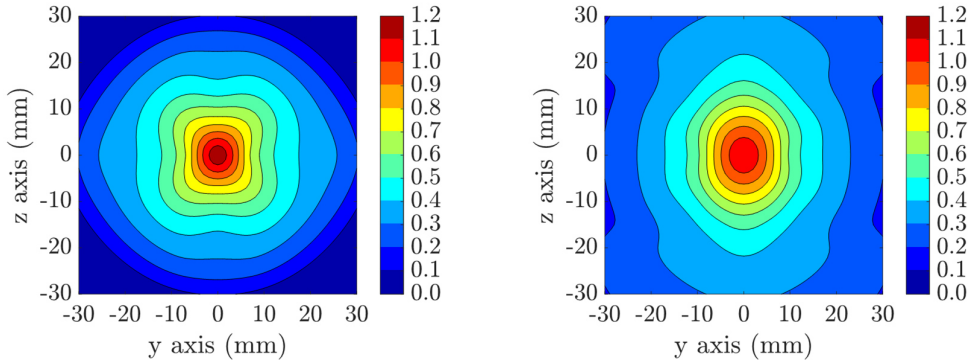

a) Injector P601055, MR= 4.17 b) Injector P601055, MR= 16.05

Figure 4.200. The Effect of Momentum Ratio (60° Impingement Angle Injector) on Normalized Axial Velocity

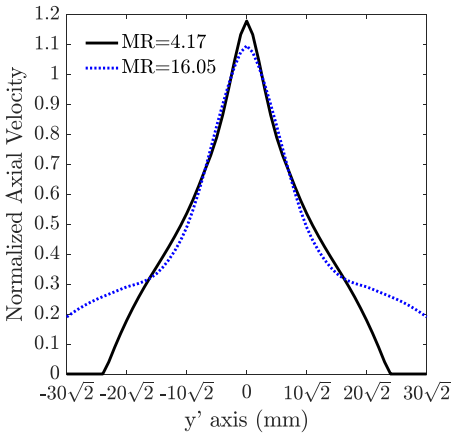

Figure 4.201. Comparison of the Effect of Momentum Ratio on Normalized Axial Velocity at y'-axis

4.2.5.4. Normalized V Velocity

The normalized V velocity distributions of different momentum ratios are given in Figure 4.202. Similar velocity distributions are obtained with slightly lower velocity levels for the higher momentum ratio. This is also observable in the trends given in Figure 4.203 along the y'-axis.

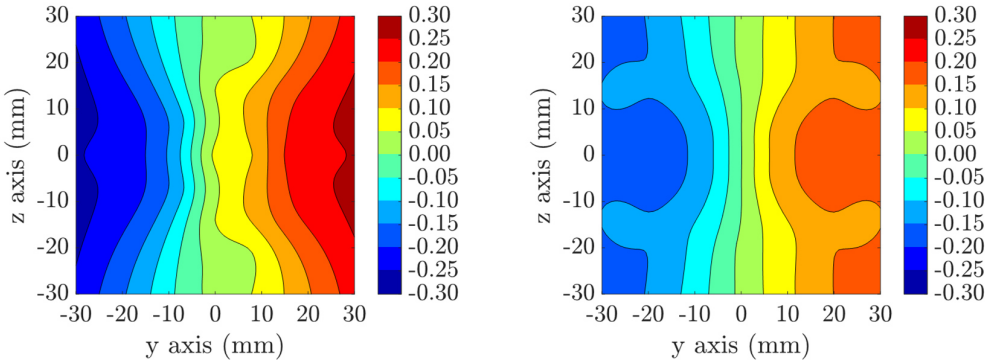

a) Injector P601055, MR= 4.17 b) Injector P601055, MR= 16.05

Figure 4.202. The Effect of Momentum Ratio (60° Impingement Angle Injector) on Normalized V Velocity

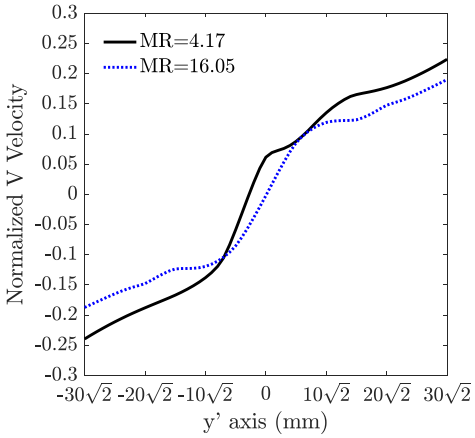

Figure 4.203. Comparison of the Effect of Momentum Ratio (60° Impingement Angle Injector) on Normalized V Velocity at y'-axis

4.2.5.5. Normalized W Velocity

The normalized W velocity distributions at different momentum ratios are given in Figure 4.204. The contour plots show that MR=4 has higher velocity magnitude compared to the other case.

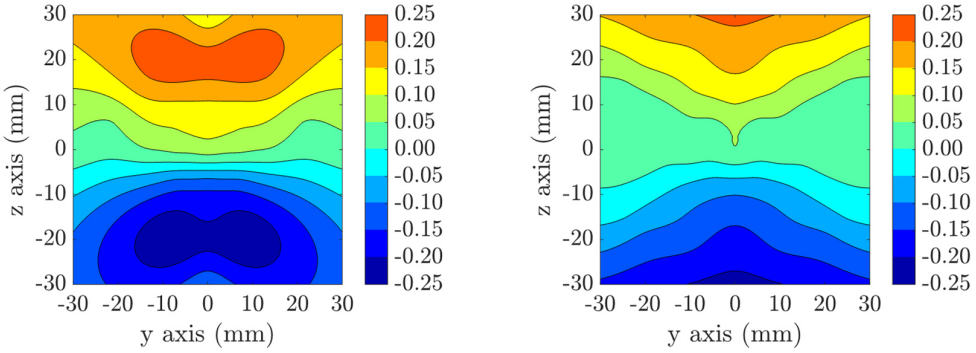

a) Injector P601055, MR = 4.17 b) Injector P601055, MR = 16.05

Figure 4.204. The Effect of Momentum Ratio (60° Impingement Angle Injector) on Normalized W Velocity

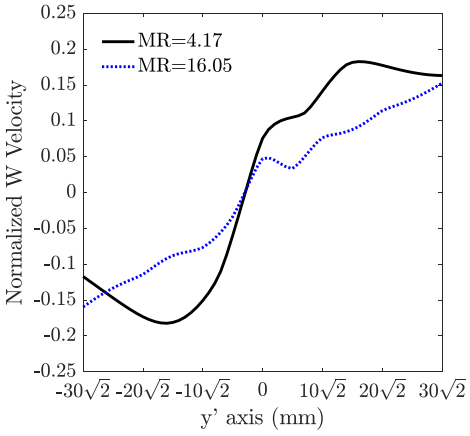

Figure 4.205. Comparison of the Effect of Momentum Ratio (60° Impingement Angle Injector) on Normalized W Velocity at y'-axis

The comparison along the y'-axis given in Figure 4.205 indicates that a higher normalized Y velocity in terms of magnitude is obtained with the lower momentum ratio, which results in a higher normalized droplet count.

4.2.5.6. Normalized Velocity Magnitude

The normalized velocity magnitude distributions are given in Figure 4.206.

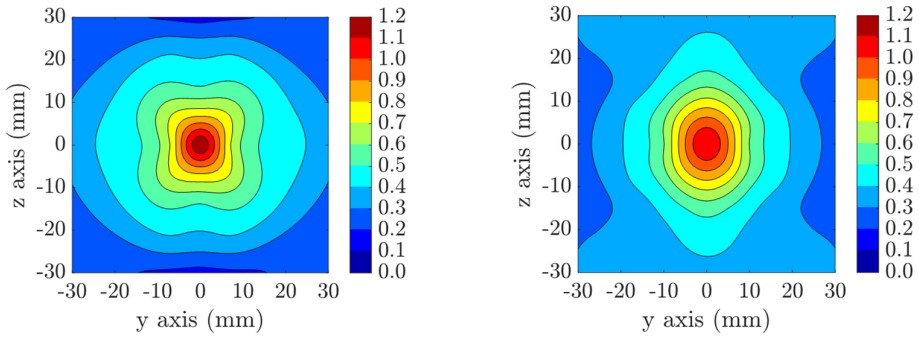

a) Injector P601055, MR = 4.17 b) Injector P601055, MR = 16.05

Figure 4.206. The Effect of Momentum Ratio on Normalized Velocity Magnitude

The contour plots show that with an increase in the momentum ratio, the normalized velocity magnitude decreases at the center, and it slightly increases in the regions away from the center.

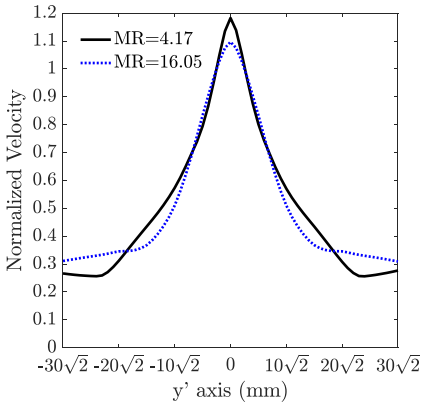

Figure 4.207. Comparison of the Effect of Momentum Ratio on Normalized Velocity Magnitude at y'-axis

According to Figure 4.207, the normalized velocity magnitude shows similarities to the normalized axial distribution at the center, however, the differences away from the center become smaller in the velocity magnitude distribution.

4.2.5.7. SMD Distribution

The SMD distributions with different momentum ratios are given in Figure 4.208.

Except the unrealistic SMD values observed on the corners of the measurement plane at MR=4, the SMD magnitudes are generally stay in similar levels.

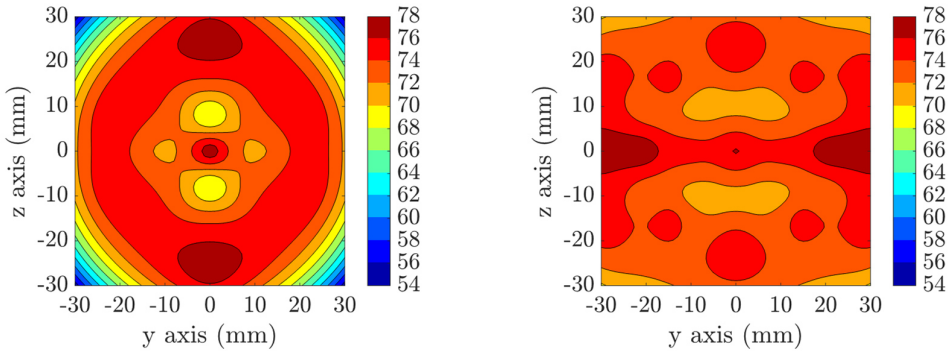

a) Injector P601055, MR = 4.17 b) Injector P601055, MR = 16.05

Figure 4.208. The Effect of Momentum Ratio on SMD Distribution

The comparison along the y'-axis given in Figure 4.209 show similarities at the center. At the regions that the highest normalized droplet counts are obtained, the local minimum SMD values decrease to 71 µm.

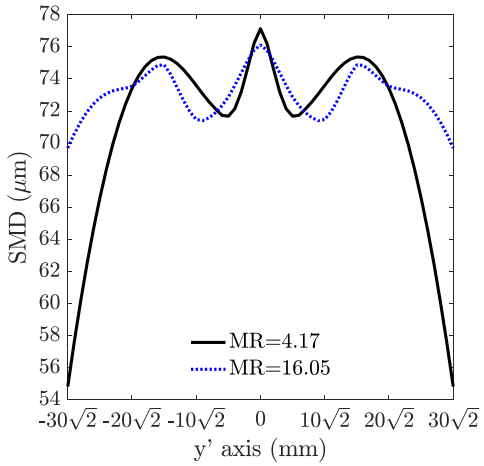

Figure 4.209. Comparison of the Effect of Momentum Ratio on SMD at y'-axis

4.2.5.8. Rosin-Rammler Distribution

The Rosin-Rammler distributions of pentad injectors with different momentum ratios are shown in Figure 4.210.

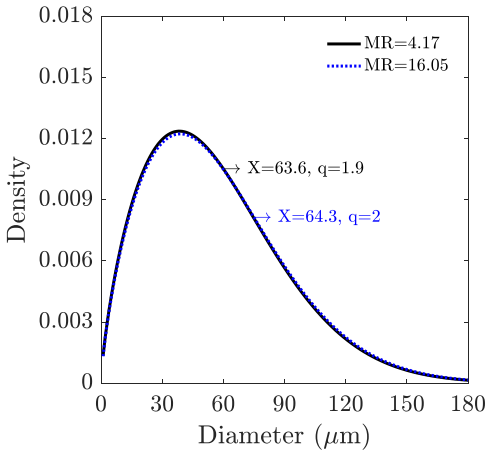

Figure 4.210. Comparison of Rosin-Rammler Distributions

The distribution appears to be identical, and the change in the momentum ratio doesn't affect the X and q parameters significantly.

4.2.5.9. Total Normalized Droplet Count

The total normalized droplet count as a function of momentum ratio is given in Figure 4.211. The total normalized droplet count decreases with an increase in momentum ratio.

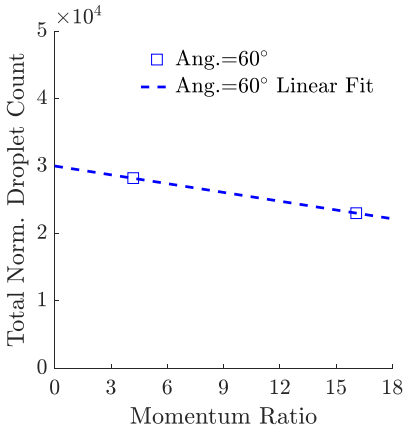

Figure 4.211. Comparison of the Effect of Momentum Ratio on Total Normalized Droplet Count

4.2.5.10. Mean D10

The arithmetic mean diameter as a function of momentum ratio is given in Figure 4.212. The arithmetic mean diameter gradually increases as the momentum ratio increases.

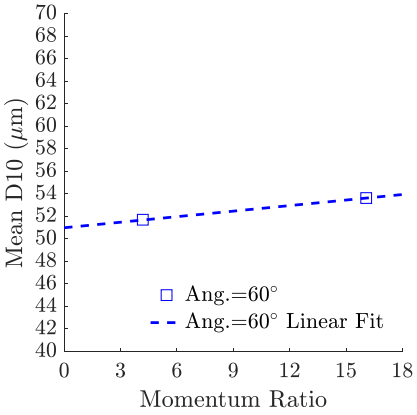

Figure 4.212. Comparison of the Effect of Momentum Ratio on Mean D10

4.2.5.11. Mean SMD

The change in the mean SMD with respect to the momentum ratio is given in Figure 4.213. It seems that the mean SMD is insensitive to the momentum ratio change.

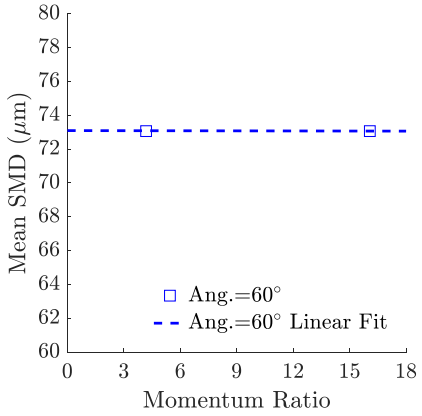

Figure 4.213. Comparison of the Effect of Momentum Ratio on Mean SMD

4.2.5.12. Spray Angle

The change in the spray angle with respect to momentum ratio is given in Figure 4.214. The dispersion of the spray along the y-axis decreases as the momentum ratio increases.

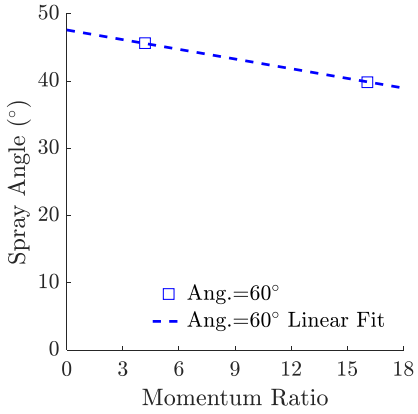

Figure 4.214. Comparison of the Effect of Momentum Ratio on Spray Angle

4.2.6. Measurements at 15 mm for Test Case P601055 With MR=4.17

In addition to the PDA measurements performed at 30 mm below the impingement point for the test P601055 with MR=4.17, another data set was obtained at 15 mm to be used in the CFD comparison. In this section, normalized droplet count, SMD, velocity components and magnitude distributions are given.

The normalized droplet count distribution is shown in Figure 4.215.

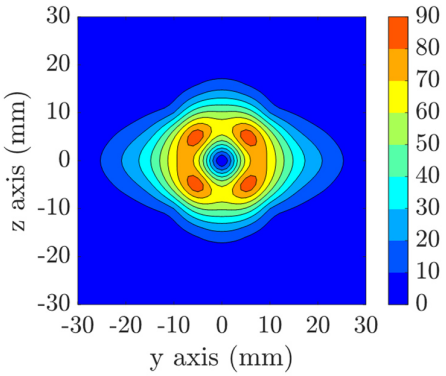

Figure 4.215. Normalized Droplet Count Distribution of P601055 with MR=4.17 at 15 mm Below Impingement Point

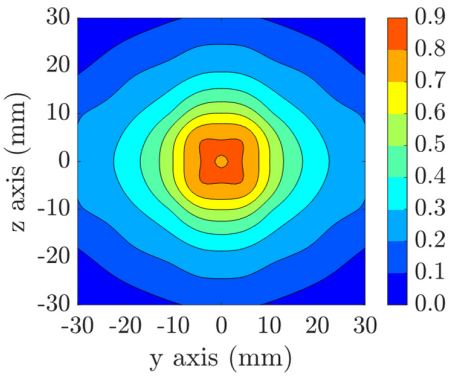

a) Normalized Axial Velocity

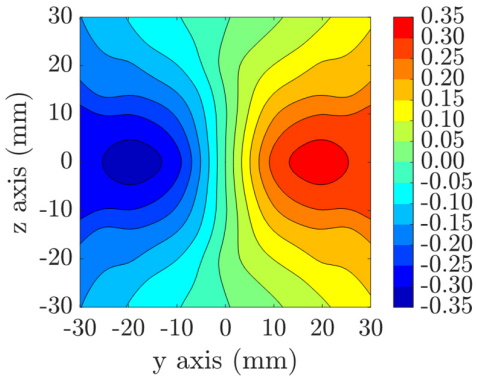

b) Normalized V Velocity

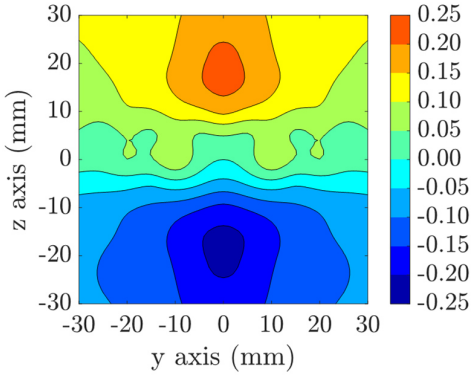

c) Normalized W Velocity

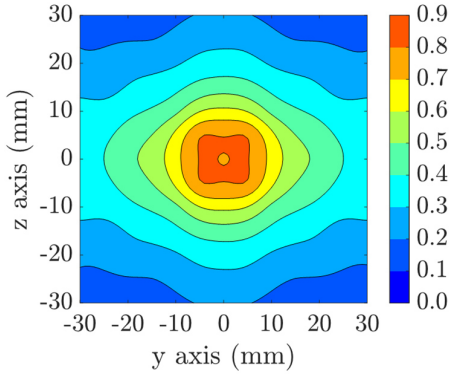

d) Normalized Velocity Magnitude

Figure 4.216. Normalized Velocity Distributions of P601055 with MR=4.17 at 15 mm Below Impingement Point

Also, the normalized velocity distributions are given in Figure 4.216.

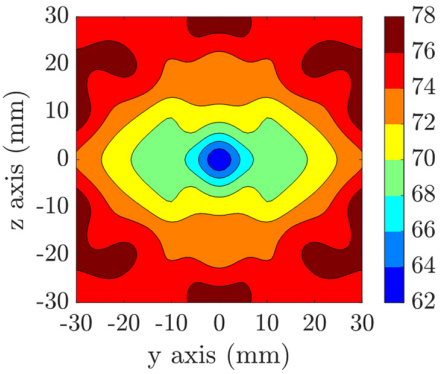

Figure 4.217. Normalized SMD Distribution of P601055 with MR=4.17 at 15 mm Below Impingement Point

The normalized SMD distribution of P601055 at 15 mm away from the impingement point can be seen in Figure 4.217.

4.2.7. Conclusion on Pentad Injectors

The effects of selected design parameters on spray characteristics such as mass flux, velocity, droplet count and size are investigated in pentads in a similar manner as triplet injectors. Similar to triplet injectors, the mass flux distribution is influenced by the impingement angle substantially. Again, in similar manner with triplets, increase in momentum ratio enhances the uniformity of the mass flux distribution in pentad injectors. While increasing the orifice diameter from 0.8 mm to 1.0 mm affects the mass flux distribution slightly, further increase in orifice diameter to 1.2 mm makes the distribution to spread over a relatively narrow area. Increase in the impingement distance causes a less uniform mass flux distribution, which is also what is observed by increasing the orifice l/d ratio from 5 to 8.

In terms of normalized droplet count distribution, increase in the impingement angle decreases the normalized droplet count. The axial velocity decreases at the center of

the spray resulting with a more uniform distribution of mass flux, and the lateral velocity profile reduces causing the normalized droplet count to decrease along the spray centerline. It should be noted that due to the perpendicular distribution of the outer orifices, the spray forms along the diagonals. Hence, the velocity profile comparisons are performed along those lines. It is considered that with the increase of the impingement angle and due to the orientation of the outer orifices, the momentum lost in the impingement region increases, hence, the magnitude of velocity decreases in all directions. As the impingement angle increases, the SMD values increase as well.

The change in normalized droplet count is also inversely proportional to the momentum ratio. With an increase in the momentum ratio, the axial velocity becomes smaller at the center and increases away from the center, which indicates the improvement of the mass flux distribution. On the other hand, magnitudes of lateral velocity profiles decrease with the increase of momentum ratio. The SMD is stays indifferent to the momentum ratio.

The investigation on the effect of impingement distance reveals that the maximum normalized droplet count is obtained with 8 mm impingement distance. The axial velocity distribution is inversely proportional with the impingement distance. However, the lateral velocity profiles along the diagonal for 5 mm and 8 mm impingement distances mimic each other closely and velocity decreases away from the center for the impingement distance of 10 mm. The impingement distance of 8 mm is found to have the highest normalized droplet count. The SMD shows only minor deviations with impingement distance along the majority of the diagonal.

The increase in the orifice l/d ratio from 3 to 5 causes a sharp drop in the normalized droplet count, but after that point from 5 to 8, the normalized droplet count is not as sensitive to the change. Both axial and lateral velocity profiles show decreasing trends with the increase of the orifice l/d ratio, which can be linked to the normalized mass flux and droplet count distributions. The SMD distribution shows a linear trend with orifice l/d ratio and an inverse trend of the normalized droplet count.

The other parameter that can be correlated with the SMD is the orifice diameter. With the increase of the orifice diameter, the SMD increases. Compared to triplet injectors, the effect of the change of the orifice diameter from 1 mm to 1.2 mm is more severe on normalized mass flux distributions. The mostly uneven normalized mass flux distribution produced with the 1.2 mm diameter results in a siginificant reduction of the normalized droplet count. Also, the normalized axial and the lateral velocity levels decrease with the increase of the orifice diameter.

Similar to triplet injectors, a set of spray angle measurements was performed for pentad injectors. It is seen that other than the impingement angle, all parameters that are the momentum ratio, orifice diameter, orifice l/d ratio and impingement distance are inversely proportional to the spray angle.

4.3. Comparison of Triplet and Pentad Injectors

In this section, the comparison of triplet and pentad injectors will be discussed in order to investigate the effects of the impingement distance, orifice l/d ratio, orifice diameter, impingement angle and momentum ratio in terms of droplet count, mean diameter, SMD and spray angles.

4.3.1. Total Normalized Droplet Count

In this section, the comparison of total normalized droplet count in triplet and pentad injectors is given.

4.3.1.1. The Effect of Impingement Distance

The comparison of total normalized droplet count as a function of the impingement distance for triplet and pentad injectors is given in Figure 4.218.

The total normalized droplet count significantly decreases with impingement distance with triplet injectors, while this drop is much less with pentad injectors.

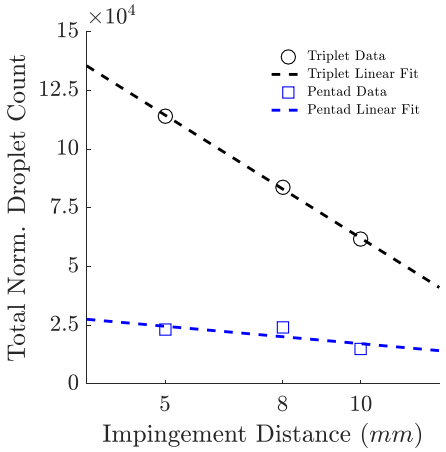

Figure 4.218. Comparison of the Effect of Impingement Distance on Total Normalized Droplet Count

4.3.1.2. The Effect of Orifice l/d Ratio

The comparison of total normalized droplet count with orifice l/d ratio is given in Figure 4.219. The total normalized droplet count shows the tendency to decrease with an increase in l/d ratio for both injector types. Similar to the previous trend, the change in triplets is more significant compared to the pentads.

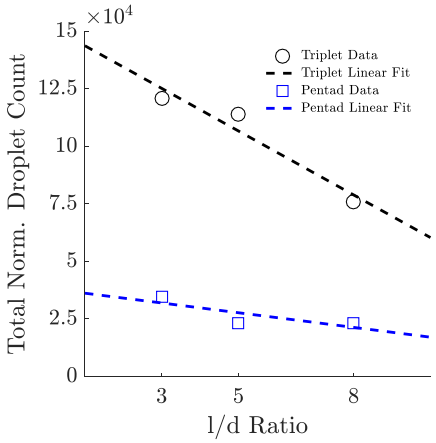

Figure 4.219. Comparison of the Effect of Orifice l/d Ratio on Total Normalized Droplet Count

4.3.1.3. The Effect of Orifice Diameter

The total normalized droplet count as a function of orifice diameter is given in Figure 4.220.

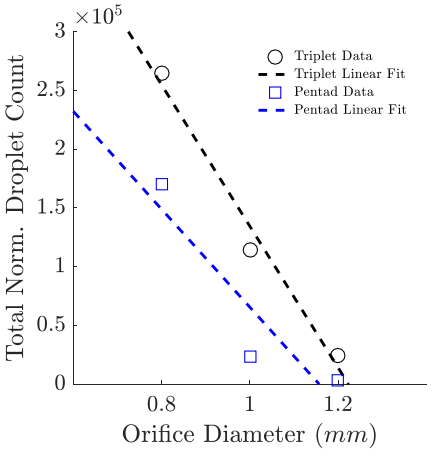

Figure 4.220. Comparison of the Effect of Orifice Diameter on Total Normalized Droplet Count

The total normalized droplet count is inversely proportional with orifice diameter in both types. The orifice diameter is the most effective parameter on total normalized droplet count for triplet and pentad injectors.

4.3.1.4. The Effect of Impingement Angle

The total normalized droplet count as a function of impingement angle is given Figure 4.221. An increase in the impingement angle results in an increase with triplet injectors and a decrease with pentad injectors.

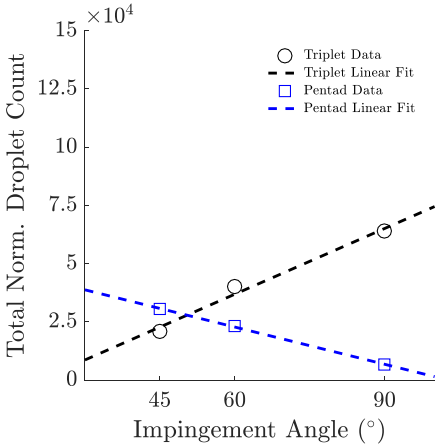

Figure 4.221. Comparison of the Effect of Impingement Angle on Total Normalized Droplet Count

4.3.1.5. The Effect of Momentum Ratio

The total normalized droplet count as a function of momentum ratio is given in Figure 4.222. In triplets, for both impingement angles, the total normalized droplet count increases with momentum ratio. On the other hand, in pentads, a slight drop in total normalized droplet count with the momentum ratio is obtained.

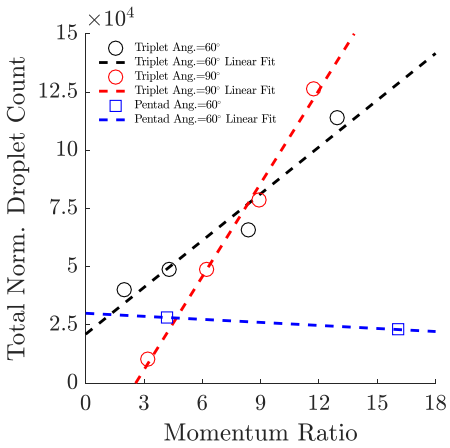

Figure 4.222. Comparison of the Effect of Momentum Ratio on Total Normalized Droplet Count

4.3.2. Mean D10

In this section, the comparisons for the arithmetic mean diameter in triplet and pentad injectors is given.

4.3.2.1. The Effect of Impingement Distance

The mean droplet diameter as a function of impingement distance for triplet and pentad injectors is given in Figure 4.223.

An increase in the impingement distance results in an increase in the arithmetic mean diameter for triplets and a slight decrease in pentads.

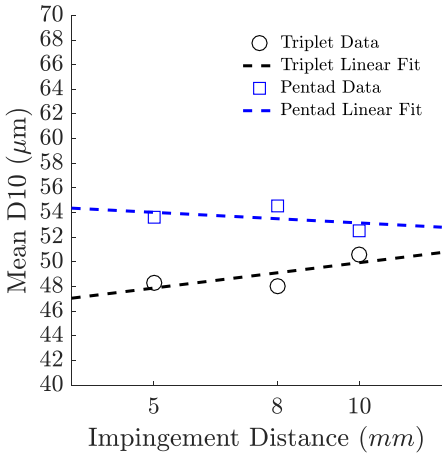

Figure 4.223. Comparison of the Effect of Impingement Distance on Mean D10

4.3.2.2. The Effect of Orifice l/d Ratio

The mean D10 as a function of orifice l/d ratio is given in Figure 4.224. By increasing the orifice l/d ratio, the mean D10 increases in pentads and decreases in triplets.

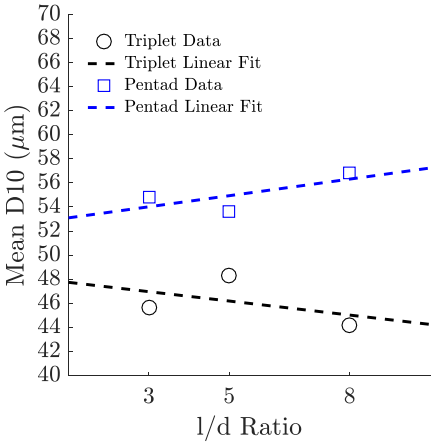

Figure 4.224. Comparison of the Effect of Orifice l/d Ratio on Mean D10

4.3.2.3. The Effect of Orifice Diameter

This time, the arithmetic mean diameter is given as a function of orifice l/d ratio in Figure 4.225.

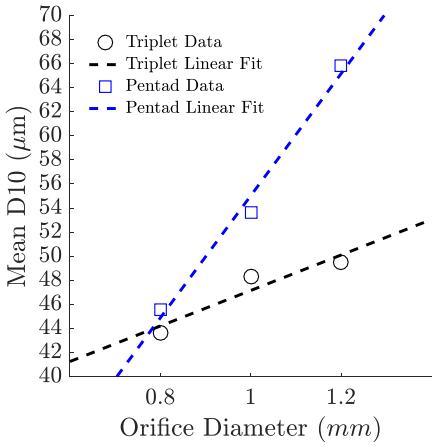

Figure 4.225. Comparison of the Effect of Orifice Diameter on Mean D10

Both injector types are proportional to the orifice diameters, however, the amount of increase in the mean diameter is more significant with pentad injectors compared to triplet injectors.

4.3.2.4. The Effect of Impingement Angle

The arrithmetic mean diameter is also analyzed in order to understand the effect of the impingement angle. Impingement distance, orifice l/d ratio, orifice diameter and momentum ratio were kept constant while the following results were obtained. The arithmetic mean diameter is proportional to the impingement angle for both injector types in Figure 4.226.

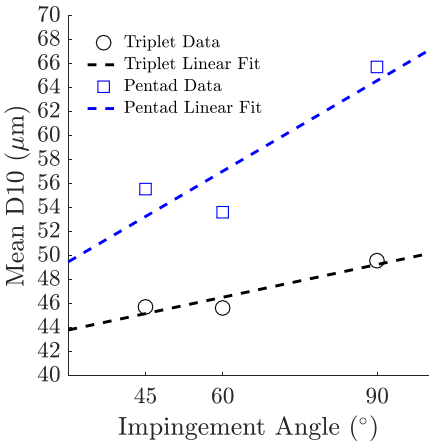

Figure 4.226. Comparison of the Effect of Impingement Angle on Mean D10

4.3.2.5. The Effect of Momentum Ratio

The mean diameter as a function of momentum ratio is given in Figure 4.227. The amount of variation in the mean diameter with the triplet injector at 90° impingement angle and with the pentad injector at 60° impingement angle is very similar. It slightly increases for triplet injectors at 60° impingement angle.

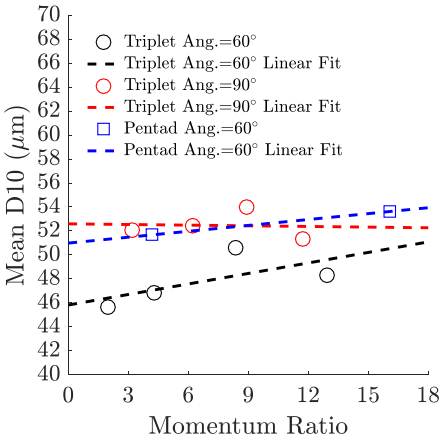

Figure 4.227. Comparison of the Effect of Momentum Ratio on Mean D10

4.3.1. Mean SMD

In this section, the mean SMD results obtained with triplet and pentad injectors will be compared with respect to impingement distance, orifice l/d ratio, orifice diameter, impingement angle and momentum ratio.

4.3.1.1. The Effect of Impingement Distance

The change in the mean SMD as a function of impingement distance is given in Figure 4.228. The mean SMD decreases slightly with impingement distance for pentad injectors and increases slightly for triplet injectors.

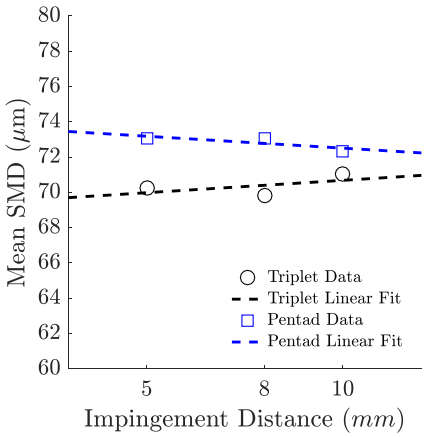

Figure 4.228. Comparison of the Effect of Impingement Distance on Mean SMD

4.3.1.2. The Effect of Orifice l/d Ratio

The change in the mean SMD as a function of orifice l/d ratio is given in Figure 4.229. The mean SMD is proportional to the orifice l/d ratio in both injector types.

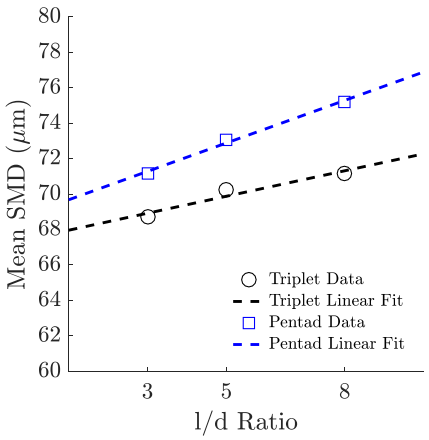

Figure 4.229. Comparison of the Effect of Orifice l/d Ratio on Mean SMD

4.3.1.3. The Effect of Orifice Diameter

The change in the mean SMD as a function of orifice diameter is given in Figure 4.230.

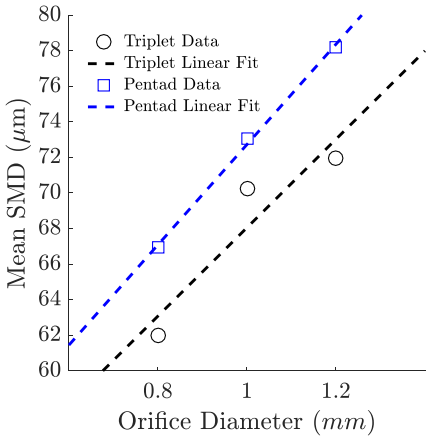

Figure 4.230. Comparison of the Effect of Orifice Diameter on Mean SMD

The mean SMD is proportional to the orifice diameter and the orifice diameter has the greatest effect on the mean SMD for both types of injectors.

4.3.1.4. The Effect of Impingement Angle

The change in the mean SMD as a function of impingement angle is given in Figure 4.231.

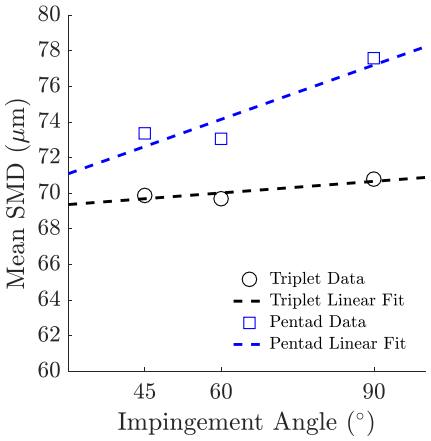

Figure 4.231. Comparison of the Effect of Impingement Angle on Mean SMD

The mean SMD increases with an increase in the impingement angle with both injectors. The change is more significant in pentad injectors than in triplet injectors.

4.3.1.5. The Effect of Momentum Ratio

The change in the mean SMD with respect to momentum ratio is given in Figure 4.232.

In triplets, an increase in the momentum ratio slightly increases the mean SMD with the 60° impingement angle injector, while it significantly decreases with the 90° impingement angle injector. On the other hand, the pentad injector is indifferent to the momentum ratio change.

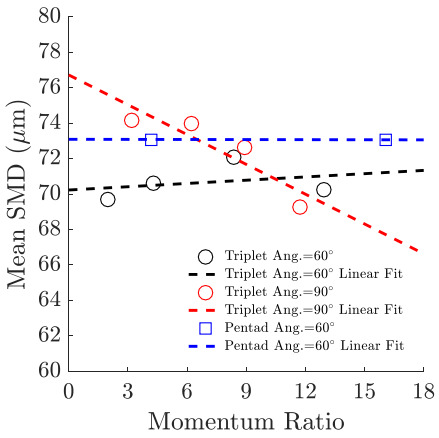

Figure 4.232. Comparison of the Effect of Momentum Ratio on Mean SMD

4.3.1. Spray Angle

In this section, the comparison of the spray angle measurements of triplet and pentad injectors will be given.

4.3.1.1. The Effect of Impingement Distance

The comparison of the change in spray angle in triplets and pentads with respect to the impingement distance is given in Figure 4.233.

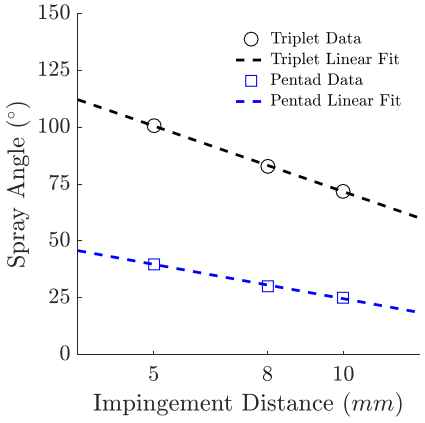

Figure 4.233. Comparison of the Effect of Impingement Distance on Spray Angle

It is seen that the spray angles of both injectors decrease with the increase of impingement distance. The change is more obvious in triplet injectors.

4.3.1.2. The Effect of Orifice l/d Ratio

The comparison of the change in spray angle in triplets and pentads with respect to the impingement distance is given in Figure 4.234.

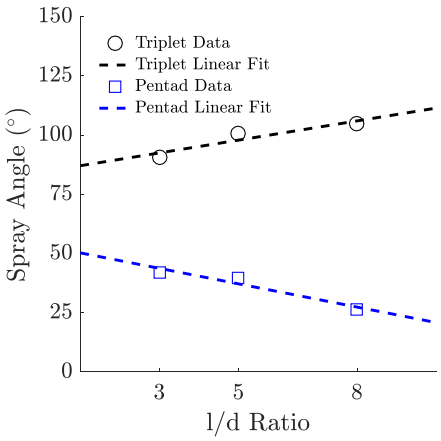

Figure 4.234. Comparison of the Effect of Orifice l/d Ratio on Spray Angle

The increase in the orifice l/d ratio causes the spray from the triplet injectors to spread over a longer distance along the y-axis, however, it decreases the spread of the spray from the pentad injectors.

4.3.1.3. The Effect of Orifice Diameter

The change in the spray angle with respect to the orifice diameter is given in Figure 4.235. The spray angle in triplet injectors increases with orifice diameter and decreases with it in pentad injectors.

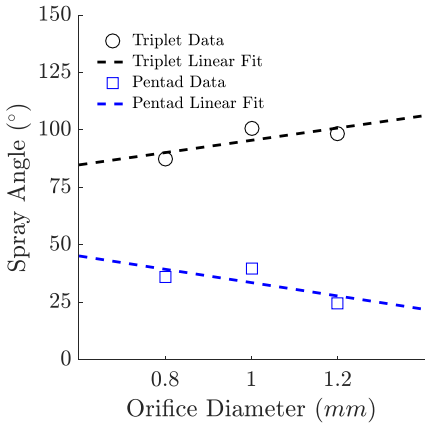

Figure 4.235. Comparison of the Effect of Orifice Diameter on Spray Angle

4.3.1.4. The Effect of Impingement Angle

The change in the spray angle with respect to the impingement angle is given in Figure 4.236.

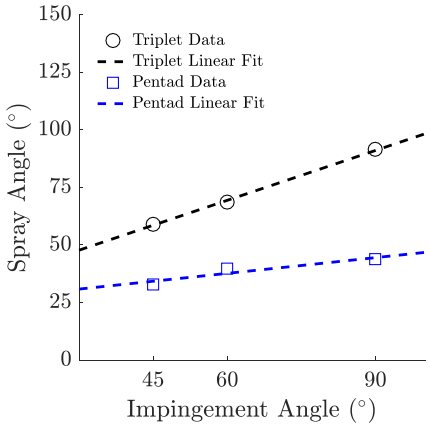

Figure 4.236. Comparison of the Effect of Impingement Angle on Spray Angle

An increase in the impingement angle increases the spray angle in both injector types. The change in the triplet injector is more obvious than the other.

4.3.1.5. The Effect of Momentum Ratio

The change in the spray angle with respect to the momentum ratio is given in Figure 4.237. Increasing the momentum ratio leads to an increase in spray angle of triplet injectors and causes a decrease in spray angle of pentad injectors.

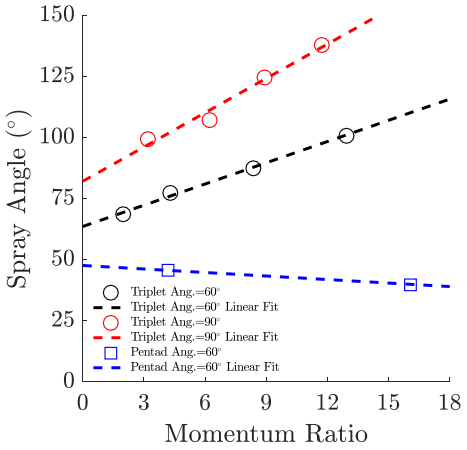

Figure 4.237. Comparison of the Effect of Momentum Ratio on Spray Angle

CHAPTER 5

NUMERICAL INVESTIGATION

In this chapter, the results of numerical analyses conducted in order to simulate the spray characteristics formed by triplet and pentad injectors were given. First of all, the numerical method selected were explained and two validation cases with doublet injectors were analyzed. The details of the numerical method, validation cases and results of the simulations were discussed in this chapter.

5.1. Numerical Tool and Computational Hardware

Numerical simulations are conducted in ANSYS Fluent v17.0 by using the CLSVOF method with the AMR technique. CLSVOF is used to bring together the advantage of the VOF method of mass conservation and the benefit of the Level Set (LS) method of capturing the liquid-gas interface. The detailed mechanism is explained in the study of Sussman et. al. (Sussman, Smith, Hussaini, Ohta, and Zhi-Wei, 2007). The study involves both the flow through the orifices and the free-stream. The k-ω SST is chosen as the turbulence model. The k-ω SST model effectively brings together the advantages of the k-ω model at the near-wall region and the k-ε model in free-stream (Wang, 2016). The curvature method with gradient of fluid volume fraction is used for the mesh refinement.

In the spray simulations, liquid jets are injected into a gaseous volume that is filled with air. Because of the multiphase nature of the problem, the Volume of Fluid Model (VOF) was used in the simulations. In the VOF model, it is assumed that fluids do not penetrated into each other. In a control volume, the fluids are described by their volume fraction and the volume-averaged properties of the fluids are defined at corresponding cells. In Fluent v17.2, the volume fraction of a fluid is defined by the following conditions (ANSYS, 2016) given in Equation *(35)*:

if

$\alpha_q = 0$	The cell doesn't contain any q[th] fluid.
$\alpha_q = 1$	The cell is filled with q[th] fluid.
$0 < \alpha_q < 1$	The cell is partially filled with q[th] fluid and partially filled with the others.

(33)

Here, q represents the number of the phase, α_q is the volume fraction of the phase q.

The continuity equation for the volume fraction of one of the phases is solved in order to track the interface between phases, which is given as follows:

$$\frac{1}{\rho_q}\left[\frac{\partial}{\partial t}\left(\alpha_q \rho_q\right) + \nabla \cdot \left(\alpha_q \rho_q \vec{v}_q\right) = S_{\alpha_q} + \sum_{p=1}^{n}\left(\dot{m}_{pq} - \dot{m}_{qp}\right)\right] \qquad (34)$$

In Equation *(34)*, $\dot{m}_{pq}$ and $\dot{m}_{qp}$ are the mass transfer from phase p to q and phase q to p, respectively. S_{α_q} is the source term, which is zero by default. $\vec{v}_q$ is the velocity of the phase q.

In the VOF model, Equation *(34)* is solved for only the secondary phase. The primary phase is calculated so as to provide Equation *(35)*,

$$\sum_{p=1}^{n} \alpha_q = 1 \qquad (35)$$

The geometric reconstruction scheme is used with the VOF model. In this approach, it is assumed that the interface between the two phases has a linear slope and the advection of the secondary phase to the cell faces are calculated based on this interface (ANSYS, 2016).

All material properties are volume-fraction-averaged. For instance, the density calculation is given as follows:

$$\rho = \sum \alpha_q \rho_q \qquad (36)$$

In Equation *(36)*, ρ is the density.

The momentum equation solved for the VOF model is given in Equation *(37)*:

$$\frac{\partial}{\partial t}(\rho\vec{v}) + \nabla \cdot (\rho\vec{v}\vec{v}) = -\nabla p + \nabla \cdot [\mu(\nabla\vec{v} + \nabla\vec{v}^T)] + \rho\vec{g} + \vec{F} \qquad (37)$$

One momentum equation is solved for the simulation, and the velocity field is shared among the phases.

The level-set method is used to track the interface between the two phases, which estimates the interface curvature and surface tension caused by the curvature. The level-set function, φ is a function of a signed distance to the interface and it gives zero level-set at the interface. In Equation *(38)*, level-set function is defined as (ANSYS, 2016):

$$\begin{array}{lll} & \varphi(x,t) = +|d| & \text{x belongs to primary phase.} \\ \text{if} & \varphi(x,t) = 0 & \text{x belongs to interface, } \Gamma. \\ & \varphi(x,t) = -|d| & \text{x belongs to secondary phase.} \end{array} \qquad (38)$$

Here, x is the position, t is time, d is the distance from the interface, Γ is the interface.

Also, the level-set function can be defined as follows with Equation *(39)*:

$$\frac{\partial\varphi}{\partial t} + \nabla \cdot (\vec{u}\varphi) = 0 \qquad (39)$$

Here, $\vec{u}$ is the velocity field.

Momentum equation is given in Equation *(40)*:

$$\frac{\partial(\rho\vec{u})}{\partial t} + \nabla \cdot (\rho\vec{u}\vec{u}) = -\nabla p + \nabla \cdot \mu[\nabla\vec{u} + (\nabla\vec{u})^T] - \vec{F}_{sf} + \rho\vec{g} \qquad (40)$$

Here, $\vec{F}_{sf}$ is the force arising from surface tension effects, which is defined by Equation *(41)* as:

$$\vec{F}_{sf} = \sigma\kappa\delta(\varphi)\vec{n} \qquad (41)$$

Here, σ is the surface tension coefficient, κ is local mean interface curvature and $\vec{n}$ is local interface normal. $\delta(\varphi)$ is defined by Equation *(42)* as:

$$\delta(\varphi) = \begin{cases} 0 & |\varphi| \geq \alpha \\ \dfrac{1 + \cos(\pi\varphi/\alpha)}{2\alpha} & |\varphi| < \alpha \end{cases} \tag{42}$$

Here, α is the interface thickness.

Local interface normal is calculated by Equation *(43)* as:

$$\vec{n} = \left.\frac{\nabla\varphi}{|\nabla\varphi|}\right|_{\varphi=0} \tag{43}$$

Local mean interface curvature is calculated by Equation *(44)* :

$$\kappa = \nabla \cdot \left.\frac{\nabla\varphi}{|\nabla\varphi|}\right|_{\varphi=0} \tag{44}$$

Density correction is applied according to Equation *(45)* as follows:

$$\vec{F}_{sf} = \frac{\rho}{0.5(\rho_1 + \rho_2)}\sigma\kappa\delta(\varphi)\vec{n} \tag{45}$$

Here, ρ is the volume-averaged density, ρ_1 is the density of primary phase and ρ_2 is the density of secondary phase.

The Heaviside scaling function is introduced to surface tension force by Equation *(46)* as follows:

$$\vec{F}_{sf} = 2H_\varphi\sigma\kappa\delta(\varphi)\vec{n}\vec{n} \tag{46}$$

H_φ is defined by Equation *(47)*:

$$H_\varphi = \begin{cases} 0 & |\varphi| > a\ (gas\ phase) \\ 1 & |\varphi| > a\ (liquid\ phase) \\ \dfrac{1}{2}\left[1 + \dfrac{\varphi}{a} + \dfrac{1}{\pi}\sin\left(\dfrac{\pi\varphi}{a}\right)\right] & |\varphi| \leq a \end{cases} \tag{47}$$

The k-ω SST model was implemented to the simulations as the turbulence model. The k-ω SST brings together the advantages of the standard k-ω model in the near-wall region and the k-ε model isconverted into k- ω model by a blending function where k is the turbulence kinetic energy, ε is the dissipation rate and ω is the specific dissipation rate that can be defined as the ratio of ε to k. Also, a damped cross-diffusion term is added in the ω equation with the SST model. The transport equations of the SST k- ω model are given in Equations *(48)* and *(49)* (ANSYS, 2016):

$$\frac{\partial}{\partial t}(\rho k) + \frac{\partial}{\partial x_i}(\rho k u_i) = \frac{\partial}{\partial x_j}\left(\Gamma_k \frac{\partial k}{\partial x_j}\right) + G_k - Y_k + S_k \qquad (48)$$

Here, G_k is the production of turbulence kinetic energy, Γ_k is the effective diffusivity of k, Y_k shows the dissipation of k due to turbulence, S_k is the user-defined source term.

$$\frac{\partial}{\partial t}(\rho \omega) + \frac{\partial}{\partial x_j}\left(\rho \omega u_j\right) = \frac{\partial}{\partial x_j}\left(\Gamma_\omega \frac{\partial \omega}{\partial x_j}\right) + G_\omega - Y_\omega + D_\omega + S_\omega \qquad (49)$$

In Equation (47), G_ω is the generation of ω, Γ_ω is the effective diffusivity of ω, Y_ω is the dissipation of ω due to turbulence. D_ω shows the cross-diffusion term and S_ω is the user-defined source term.

The effective diffusivity terms are defined through Equations *(50)* and *(51)* as follows (ANSYS, 2016):

$$\Gamma_k = \mu + \frac{\mu_t}{\sigma_k} \qquad (50)$$

$$\Gamma_\omega = \mu + \frac{\mu_t}{\sigma_\omega} \qquad (51)$$

Here, σ_k and σ_ω are the turbulent Prandtl numbers for k and ω. μ and μ_t are the viscosity and turbulent viscosity, respectively. μ_t is calculated in Equation *(52)*:

$$\mu_t = \frac{\rho k}{\omega} \frac{1}{\max\left[\frac{1}{a^*}, \frac{SF_2}{a_1 \omega}\right]} \tag{52}$$

In this equation, S shows the strain rate magnitude and F_2 is the blending function.

a^* is the coefficient used to damp the turbulent viscosity and defined by Equation *(53)*:

$$\alpha^* = \alpha_\infty^* \left(\frac{\alpha_0^* + \frac{Re_t}{R_k}}{1 + \frac{Re_t}{R_k}} \right) \tag{53}$$

where

$$Re_t = \frac{\rho k}{\mu \omega} \tag{54}$$

$$R_k = 6 \tag{55}$$

$$\alpha_0^* = \frac{\beta_i}{3} \tag{56}$$

and β_i equals to 0.072.

In the k-ω model, for high-Reynolds numbers;

$$a^* = a_\infty^* = 1 \tag{57}$$

The turbulent Prandtl numbers are defined by Equations (56) and (57) as follows:

$$\sigma_k = \frac{1}{\frac{F_1}{\sigma_{k,1}} + \frac{1 - F_1}{\sigma_{k,2}}} \tag{58}$$

$$\sigma_\omega = \frac{1}{\frac{F_1}{\sigma_{\omega,1}} + \frac{1 - F_1}{\sigma_{\omega,2}}} \tag{59}$$

The definitions of the blending functions are given in Equations *(60)* - *(64)*:

$$F_1 = \tanh(\Phi_1^4) \tag{60}$$

where

$$\Phi = \min[\max\left(\frac{\sqrt{k}}{0.09\omega y}, \frac{500\mu}{\rho y^2 \omega}\right), \frac{4\rho k}{\sigma_{\omega,2} D_\omega^+ y^2}] \tag{61}$$

D_ω^+ is defined as follows:

$$D_\omega^+ = \max\left[2\rho \frac{1}{\sigma_\omega, 2} \frac{1}{\omega} \frac{\partial k}{\partial x_j} \frac{\partial \omega}{\partial x_j}, 10^{-10}\right] \tag{62}$$

Also,

$$F_2 = \tanh(\Phi_2^2) \tag{63}$$

where

$$\Phi_2 = \max\left[2\frac{\sqrt{k}}{0.09\omega y}, \frac{500\mu}{\rho y^2 \omega}\right] \tag{64}$$

Here, y is the distance to the next surface. D_ω^+ shows the positive portion of the cross-diffusion term.

G_k is the production of turbulence kinetic energy and is defined in Equation *(65)*:

$$\mathrm{G_k} = \mu_t S^2 \tag{65}$$

Here, S is the modulus of the mean rate-of-strain tensor.

G_ω shows the production of ω and is defined in Equation (64):

$$\mathrm{G}_\omega = \frac{\alpha \alpha^*}{\nu_t} G_k \tag{66}$$

α_∞ definition is provided in Equations *(67)* - *(69)*:

$$\alpha_\infty = F_1 \alpha_{\infty,1} + (1 - F_1)\alpha_{\infty,2} \tag{67}$$

where

$$\alpha_{\infty,1} = \frac{\beta_{i,1}}{\beta_{\infty}^{*}} - \frac{\kappa^2}{\sigma_{\omega,1}\sqrt{\beta_{\infty}^{*}}} \quad (68)$$

$$\alpha_{\infty,2} = \frac{\beta_{i,2}}{\beta_{\infty}^{*}} - \frac{\kappa^2}{\sigma_{\omega,2}\sqrt{\beta_{\infty}^{*}}} \quad (69)$$

Here, κ is 0.41.

The dissipation of turbulence kinetic energy is given in Equations *(70)* - *(72)*

$$Y_k = \rho\beta^* k\omega \quad (70)$$

β^* is defined as:

$$\beta^* = \beta_i^*[1 + \zeta^* F(M_t)] \quad (71)$$

β_i^* is given as follows:

$$\beta_i^* = \beta_{\infty}^* \left(\frac{\frac{4}{15} + \left(\frac{Re_t}{R_\beta}\right)^4}{1 + \left(\frac{Re_t}{R_\beta}\right)^4} \right) \quad (72)$$

where ζ^*, R_β and β_∞^* are equal to 1.5, 8, 0.09.

The dissipation of ω is given in Equation *(73)*:

$$Y_k = \rho\beta\omega^2 \quad (73)$$

Then, β_i is defined by Equation *(74)*:

$$\beta_i = F_1\beta_{i,1} + (1 - F_1)\beta_{i,2} \quad (74)$$

The model constants are given in Table 5.1.

In order to obtain the droplets and liquid sheet of the spray properly, the domain should be resolved with a fine mesh, which increases the computational cost. The adaptive mesh refinement technique was used in these simulations in order to

decrease the numerical error in the solutions with minimum computational cost possible. Fluent software offers several mesh adaption methods. In this study, the dynamic gradient adaption is enabled. The curvature method with gradients of the volume fraction of the secondary phase is used by specifying the adaption time interval and maximum level of refinement.

Table 5.1. SST k-ω Model Constants

$\sigma_{k,1}$	$\sigma_{\omega,1}$	$\sigma_{k,2}$	$\sigma_{\omega,2}$	a_1	$\beta_{i,1}$	$\beta_{i,2}$
1.176	2.0	1.0	1.168	0.31	0.075	0.0828

In the curvature method, the undivided Laplacian of the selected solution, in this case the volume fraction of the secondary phase, is multiplied by a characteristic length scale. The gradient function in two dimensions is given in Equation *(75)*:

$$|e_{i2}| = (A_{cell})^{\frac{r}{2}} |\nabla^2 f| \qquad (75)$$

Here, e_{i2} shows the error indicator, A_{cell} is the cell area, r is the gradient volume weight which is unity by default and $\nabla^2 f$ presents the undivided Laplacian of the selected solution.

In this study, the computational resources of METU Center for Wind Energy Research (RÜZGEM) were used.

5.2. Validation of the Numerical Technique with the Use of a Doublet Injector

In this study, numerical simulations are conducted to investigate the necessary mesh size in order to capture the spray characteristics such as liquid sheet breakup, surface wave and droplet diameter. The SMD results of the simulations are compared with the experimental data given in Zheng et al.'s study (Zheng, Nie, Feng, and Wu, 2015). Liquid sheet characteristics and velocity distributions obtained by Zheng et al. (Zheng, Nie, Feng, and Wu, 2015) and Balasubramanian et al. (Balasubramanian,

Kumar, Nakod, Schütze, and Rajan, 2020) are used to analyze the results obtained in the current simulations.

5.2.1. Validation Study 1

A like doublet injector with impingement angle, 2α of 80° studied by Zheng et al. (Zheng, Nie, Feng, and Wu, 2015) is chosen for the mesh sensitivity study. The schematic of the cross-section of the resultant spray in the computational domain is given in Figure 5.1. Water is used as the working fluid in a like-doublet injector with an impingement angle, 2α, of 80°. Density and viscosity of the water are defined as 998.2 kg/m^3 and 0.001003 kg/ms in Fluent, respectively. The surface tension between water and air is defined as 0.0725 N/m. The mean Re is calculated as 25389 and We as 8960, respectively. A mass flow rate, $\dot{m}_i$, of 0.020 kg/s is supplied at the inlet of each orifice having a diameter, d_o, of 1 mm, at a turbulence intensity of 5%. The pre-impingement length, L_{imp}, is defined as 5 mm. The surface normals of the inlet and exit of the orifices are modeled to be perpendicular to the volume that the liquid jets are injected into, so that a normal velocity distribution along the orifices and a realistic liquid jet behavior with droplet formation at the exit of the orifices can be established. The domain is filled with air, and the ambient pressure boundary condition of 1 atm is assigned to the outlet to match the case study. All boundary surfaces other than the inlets and orifice walls are defined as the outlet as shown in Figure 5.1. Wall boundary condition is applied along the orifices.

The SMD measurements are performed at Plane 1, which is 30 mm away from the impingement point. Line 1 passes through the stagnation point along the z-axis and Line 2 is parallel to Line 1 and passes through the impingement point that is also the origin of the domain. In the current study, the stagnation point was defined as the point that has the highest local pressure inside the impact region of liquid jets. This location was found to be varying between 0.65 mm and 1 mm above the impingement point among the studied cases. Zheng et al. (Zheng, Nie, Feng, and Wu, 2015) presents results along the line through the stagnation point as well, but

with no information on its location. The computational domain is 37.5 mm x 24 mm x 10 mm in x, y and z directions, respectively. Because of the highly three-dimensional behavior of spray atomization, a three-dimensional analysis is conducted.

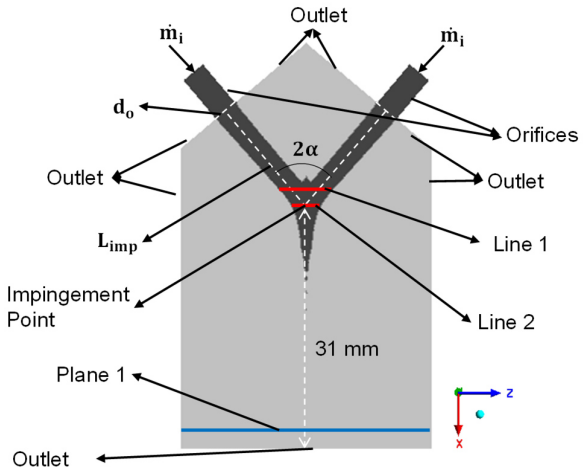

Figure 5.1. The cross-section of the computational domain (not to scale)

The computations are conducted with ANSYS Fluent v17.0 by using the CLSVOF method with the AMR technique. Since the current study involves both flow through orifices and free-stream, the k-ω SST is chosen as the turbulence model. The curvature method with gradient of fluid volume fraction is used for mesh refinement and the variable time stepping method is enabled with a global Courant number of 2.

5.2.1.1. Use of Adaptive Mesh Refinement

A three-level adaptive mesh is used in the liquid volume for all analyses. The minimum cell sizes of 100, 80, 60, 50, 40 and 30 μm were achieved in the analyses of M1, M2, M3, M4, M5 and M6, respectively. The orifice domains were further resolved with the minimum cell size mentioned at each analysis so that the velocity profile of the liquid jet could be captured at the exit of the orifices. Inner iterations

were repeated until the mass, momentum, k-ω and LS function residuals were reduced to level of around 0.001. The initial number of nodes and the final number of nodes at t=1.6 ms, which corresponds to a time after the first droplet reaches the bottommost of the domain, are given in Table 5.2 for each case. The number of nodes is not expected to change significantly beyond that point. Table 5.2 also shows the equivalent number of nodes that would be required in a uniform mesh using the minimum cell size if the adaptive mesh technique was not used. The comparison of the two mesh types shows that the number of nodes required for the coarsest uniform mesh is higher even than that required for the finest adaptive mesh. Besides, the difference in the number of nodes between adaptive mesh and uniform mesh increases drastically as the minimum cell size is further decreased. This shows that the adaptive mesh refinement makes the atomization simulations affordable in terms of computational costs.

Table 5.2. Adaptive Mesh

	M1	**M2**	**M3**	**M4**	**M5**	**M6**
Minimum Cell Size	100 μm	80 μm	60 μm	50 μm	40 μm	30 μm
Initial Number of Nodes - AMR	34426	58812	133270	213906	393278	886660
Final Number of Nodes - AMR	887109	1415936	2627055	3759786	6652385	11329490
Total Number of Nodes - Uniform Mesh	12218430	23652066	55616960	95930796	187326376	441557132

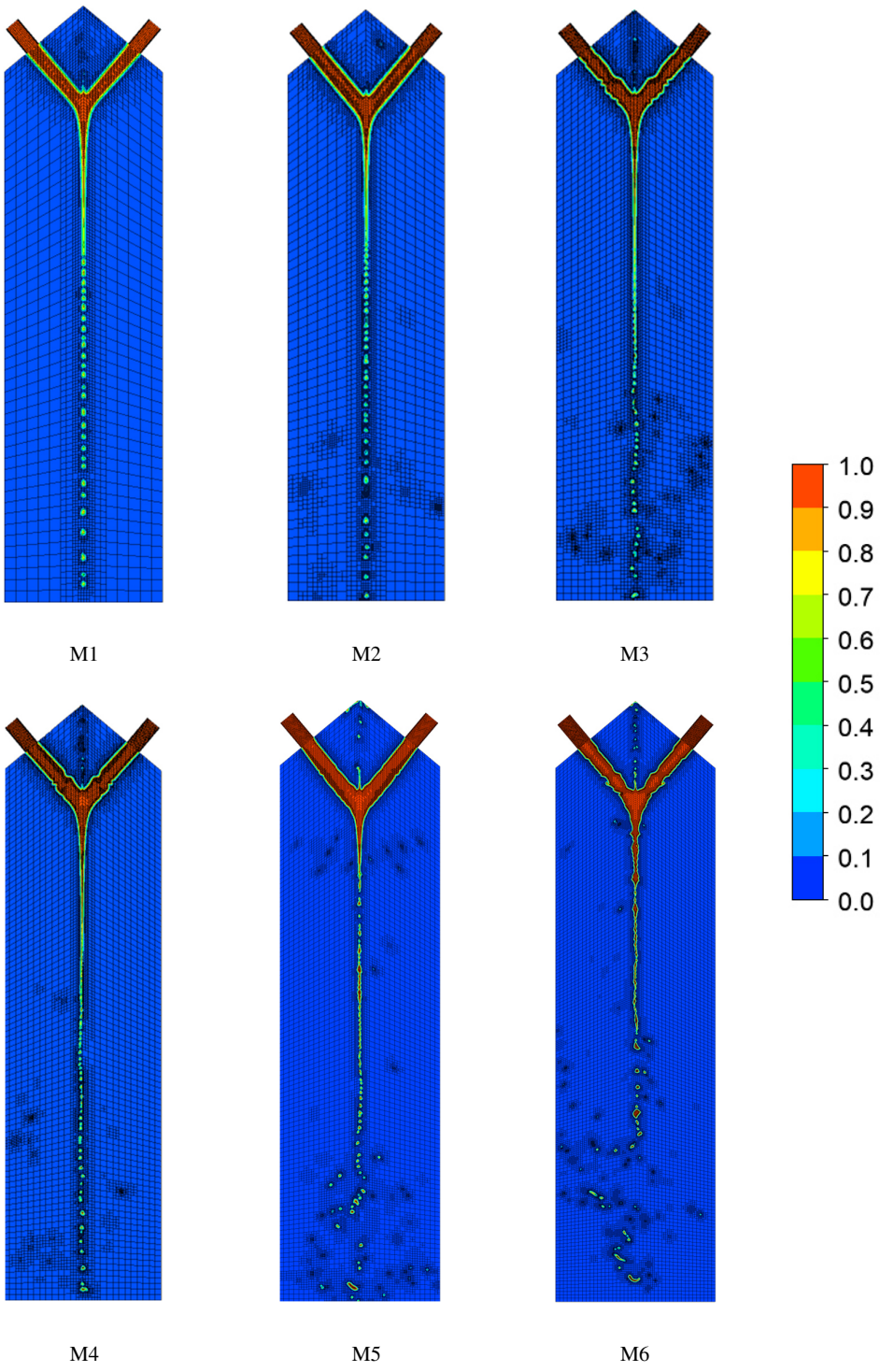

Figure 5.2. Cross-section of the Fluid Volumes with Meshes at t=1.6 ms

In Figure 5.2, the fluid volumes of water are given at a cross-section of the domain along the direction of the flow. Cells with a volume of fraction of 1 include only water. All values other than 1 indicate the cells where water and air coexist. Each volume shows the mesh for each analysis at the time of 1.6 milliseconds as repetitive liquid sheet breakups are acquired.

A blow-up view of the water-air interface is given in Figure 5.3 for cases M5 and M6. In the vicinity of this region, it can be seen that the cell sizes become smaller and merge at the center of the spray reducing the overall number of nodes. As the minimum cell size decreases from M1 to M6, the interface between water and air is further resolved and the symmetrical behavior of the liquid sheet across the domain vanishes. Due to the impact of the two liquid jets, the mixing of these jets propagates in both axial and lateral directions until the formed liquid sheet breaks into ligaments due to the formation of the surface waves, resulting in a thin liquid sheet below the impingement point.

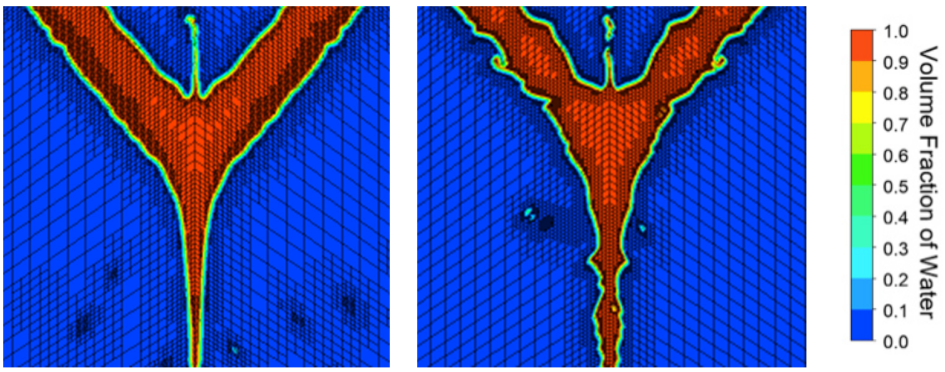

Figure 5.3. Blow-up View of Adapted Cells in M5 and M6 at t=1.6 ms

Cases M1 and M2 cannot resolve the liquid sheet well enough to capture the fluctuations on the surface of the sheet. Those fluctuations are observed at 20 mm downstream of the impingement point for the first time in case M3 as shown in Figure 5.2 with the horizontal line, and are also captured by the other cases with smaller cell sizes.

The range of minimum cell sizes used in this study was considered by taking into account the other findings in the literature. Zheng et al. (Zheng, Nie, Feng and Wu, 2015) modeled a fluid volume with dimensions of 35 mm x 24 mm x 10 mm and used 2.1 million mesh cells with a minimum cell size of 40 µm. Balasubramanian et al. (Balasubramanian, Kumar, Nakod, Schütze, and Rajan, 2020) resolved a similar domain with a radius of 24 mm and a length of 35 mm with 800000 cells and used the adaptive mesh refinement with a minimum cell size of 40 µm until 3 ms, applying further refinement to reduce the minimum cell size to 20 µm for the rest of the analysis. In another study, Chen et al. (Chen, Ma, and Yang, 2012) used the adaptive mesh technique with three refinement levels with minimum cell sizes of 80, 40 and 20 µm. Arienti et al. (Arienti, Li, Soteriou, Eckett, Sussman, and Jensen, 2013) also used the AMR technique to resolve a fluid domain of 12 mm x 16 mm x 24 mm enabling three refinement levels. Considering almost the half size of the domain used by Zheng et al. (Zheng, Nie, Feng and Wu, 2015) mentioned above and the simplified orifice geometry in order to reduce the overall computational cost, the minimum cell sizes of 62.5 µm, 31.25 µm and 15.625 µm could be studied. In this study, the full-scale domain of 37.5 mm x 24 mm x 10 mm is modeled in all analyses to capture the asymmetric nature of the problem. Hence, due to limited computational resources and costs, minimum cell sizes smaller than shown in Table 1 were not studied. As given in Table 1, the case with the minimum cell size of 30 µm (M6) reaches the number of nodes of 10.5 millions with adaptive mesh, while this number is only 6.3 millions for the case with 40 µm cell size (M5). The average percentage of differences in the predicted velocity magnitudes along Line 2 is calculated as 18.1% between M4 (50 µm cell size) and M5. This reduced to 4.7% between M5 and M6. Comparisons of these cases with available data from literature will be presented in the following sections. Considering the close agreement of the results from cases M5 and M6, it is apparent that the selection of case M5 will bring the benefits of significantly lower computational costs compared to the latter.

5.2.1.2. General Spray Characteristics

Figure 5.4 shows the snapshots of the isosurfaces of volume fraction of liquid phase for each case. As described by Balasubramanian et al. (Balasubramanian, Kumar, Nakod, Schütze, and Rajan, 2020), the liquid sheet thickness varies due to the surface waves, forming holes at the thinner parts of the liquid stream. These holes expand in both lateral and axial directions due to the velocity difference in the liquid sheet and form ligaments. In a similar manner, ligaments break up into small droplets. The core region of the liquid sheet is obtained in all cases as shown in Figure 5.4, however, the details of the break-up mechanism such as the surface waves forming due to the impact of liquid jets and the liquid sheet deformation into ligaments are not resolved in the core region as much as in M5 and M6.

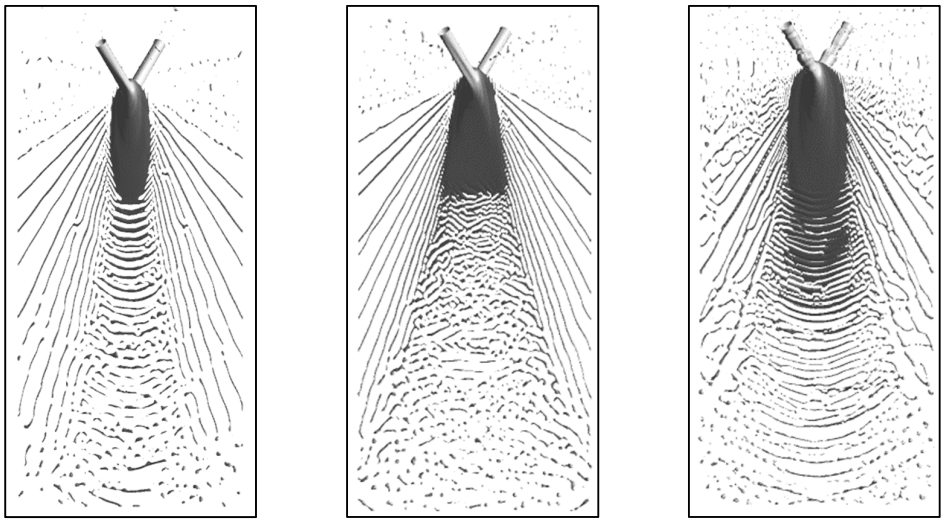

M1 M2 M3

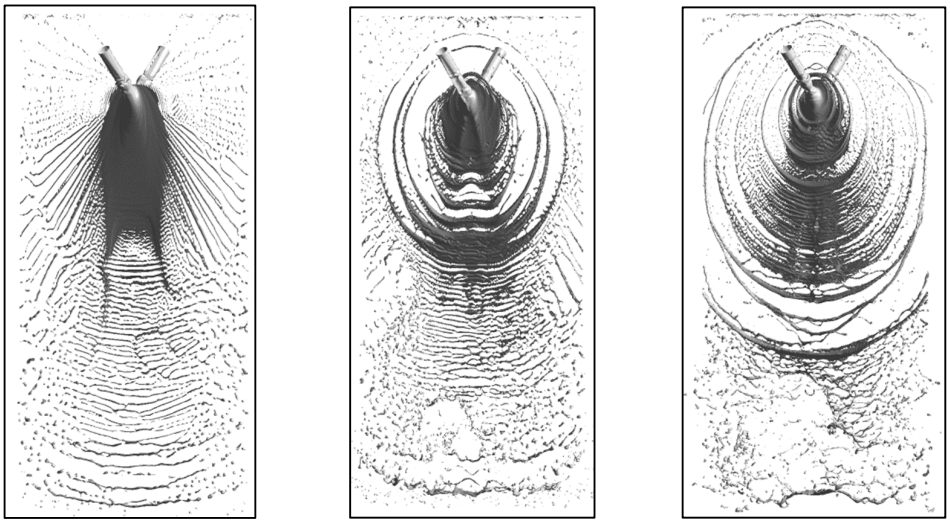

M4 M5 M6

Figure 5.4. Comparison of Snapshots of Sprays at t=1.6 ms

In their computations, Zheng et al. (Zheng, Nie, Feng, and Wu, 2015) used a fixed mesh of 2.1 million cells with a minimum cell size of 40 μm and performed their analysis up to around 1.3 ms. On the other hand, Balasubramanian et al. (Balasubramanian, Kumar, Nakod, Schütze, and Rajan, 2020) used an adaptive mesh as done in the current study, while further reducing the minimum cell size to 20 μm and performing the analysis up to 5 ms.

The break-up length in current cases cannot be compared to the results of the experiment performed by Zheng et al. (Zheng, Nie, Feng, and Wu, 2015) since quantitative data were not provided. Their numerical results indicate the existence of large droplets both in the vicinity of the impingement location and across the computational domain, which does not agree with neither current findings or with those of Balasubramanian et al. This could be due to the relatively coarse mesh that was adopted by Zheng et al. On the other hand, when the given spray snapshots of M5 and M6 are visually examined, more similarities to the results obtained by Balasubramanian et al. are observed in terms of break-up length and droplet density in the vicinity of the liquid core region.

5.2.1.3. Snapshots of Spray View by Simulation M5 With Respect to Time

Simulation M5 is selected to demonstrate the evolution of spray with respect to time for further insight. The snapshots at each time interval are given in Figure 5.5.

Fluctuations in the liquid core and small droplets exist even at 0.6 ms. The first liquid sheet breakup becomes observable at 1 ms. The liquid sheet length increases until 1.2 ms without a major change in the spray structure. The initial hole that forms surrounding the vicinity of the impingement point at 1.2 ms enlarges and triggers the surface waves as can be seen at 1.3 ms. Beyond this instant in time, additional holes are observed to be forming with time. Fluctuations on the liquid sheet due to these surface waves cause the liquid sheet to break up into more ligaments at 1.5 ms. After that, the successive breakup of the liquid sheet keeps progressing at 1.6 ms as a result of the formation of additional holes.

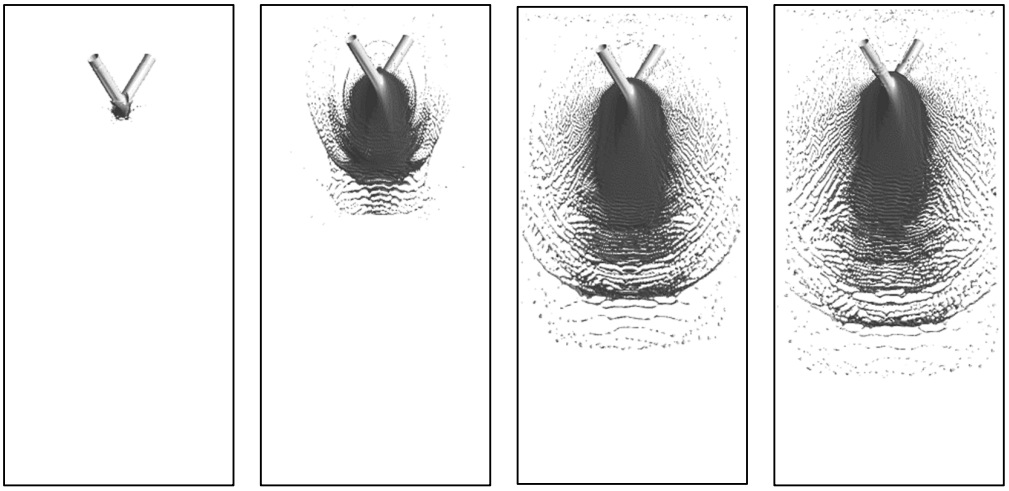

t=0.3 ms t=0.6 ms t=0.9 ms t=1.0 ms

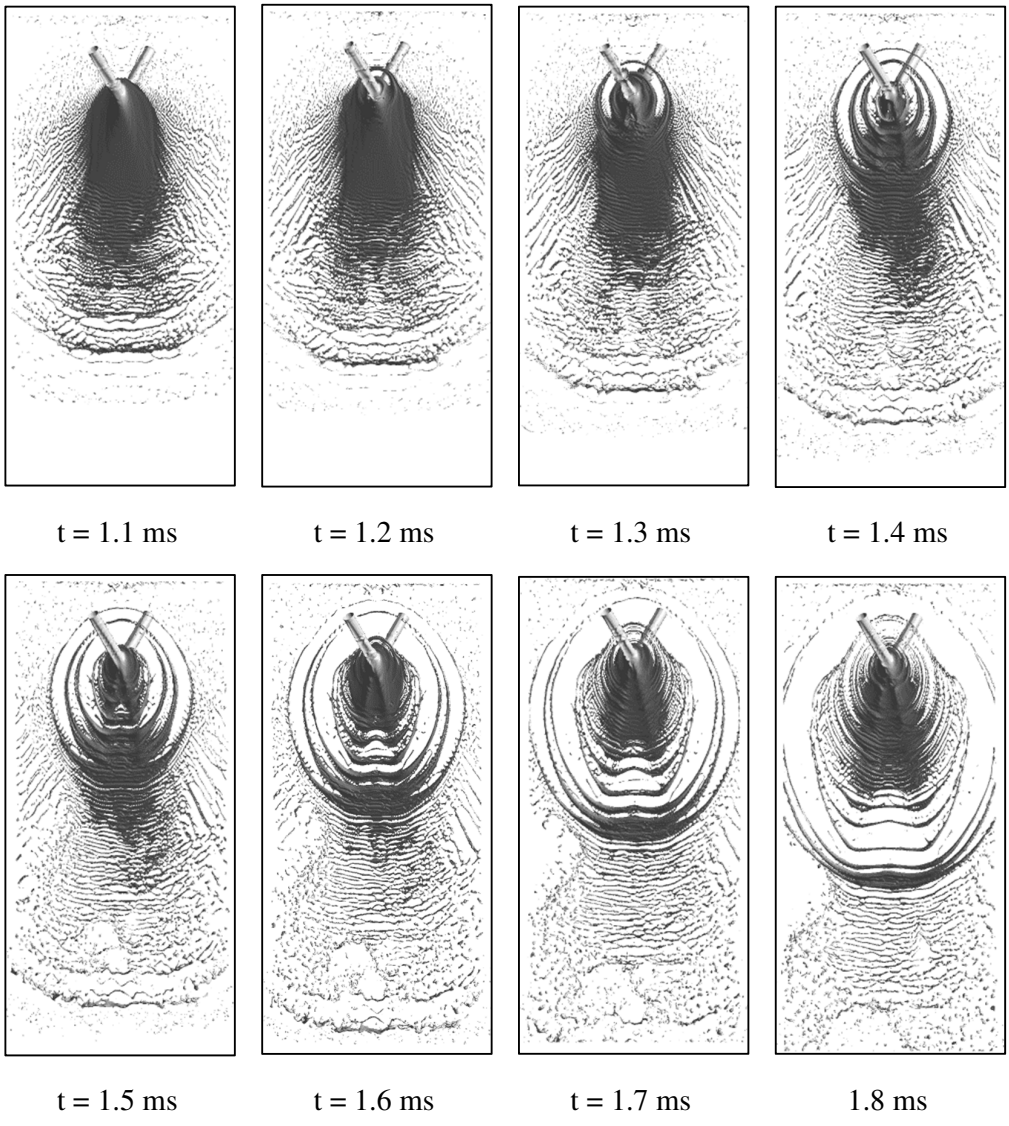

Figure 5.5. Spray View with Respect to Time (M5)

5.2.1.4. Comparison of Droplet Size

Droplets passing through Plane 1 are used in comparison of the SMD calculations. The studies of Zheng et al. (Zheng, Nie, Feng, and Wu, 2015) and Balasubramanian et al. (Balasubramanian, Kumar, Nakod, Schütze, and Rajan, 2020) will be referred

to as Study 1 and Study 2, respectively, hereafter for simplicity. It should be noted that there are unfortunately limited experimental data that could be used in the validation of current computations.

Table 5.3 presents the values from both studies along with the results from cases M5 and M6 of the current study. All percentage differences given are calculated with respect to the experimental data of Study 1. Study 1 also provides a statistically averaged numerical value for the SMD over different time instants, which has a difference of about 11% from the measured value at 30 mm. The authors attribute these differences to the reasons such as omitting the flow development inside the injectors in their computations, measurement errors, and limited grid resolution. In the current study, an average SMD was calculated using the time intervals between when the first droplet passes through the considered plane and the end of an analysis.

Table 5.3. Comparison of SMD Results With Study 1 (Zheng, Nie, Feng, and Wu, 2015) and Study 2 (Balasubramanian, Kumar, Nakod, Schütze, and Rajan, 2020)

Distance from impingement point (mm)		**Study 1 (Exp.)**	**Study 1 (Num.)**	**Study 2 (Num.)**	**M5 (Current Study)**	**M6 (Current Study)**
10	**SMD (µm)**	129	147.1	144	135	143
	Difference (%)		14	11.6	4.3	10.8
20	**SMD (µm)**	125	149.2	147	162	111
	Difference (%)		19.4	17.6	29.7	10.8
30	**SMD (µm)**	127	140.9	182	143	139
	Difference (%)		10.9	43.3	12.6	9.4

Good agreement on the SMD results are observed for both cases of M5 and M6 with a difference of only 1.5 % and 1.3% from the numerical results of Study 1, and with a difference of 12.6% and 9.4% from the experimental value for each case, respectively. On the other hand, although the liquid sheet characteristics of current simulations of M5 and M6 were found to be in agreement with Study 2, a larger

deviation is observed here with Study 2 in the SMD results. This can be explained to be due to the use of the VOF-DPM method in that study, as the authors explain. In this method, since the droplets are tracked with DPM, the ligaments and droplets are transported from the VOF domain to the DPM domain when the predefined conditions are reached, which may lead to a loss in the droplet count or to a change in the droplet diameter. The authors also mention the uncertainty that might be caused by the mesh selection that was driven by limited resources. Also it should be noted that, in contrary to Study 1, in the current study, a distinct atomization zone could not be observed at 10 mm and 20 mm below the impingement point since the computational domain was mainly filled by ligaments at those locations and there was considerably a much smaller number of droplets compared to those found at 30 mm distance.

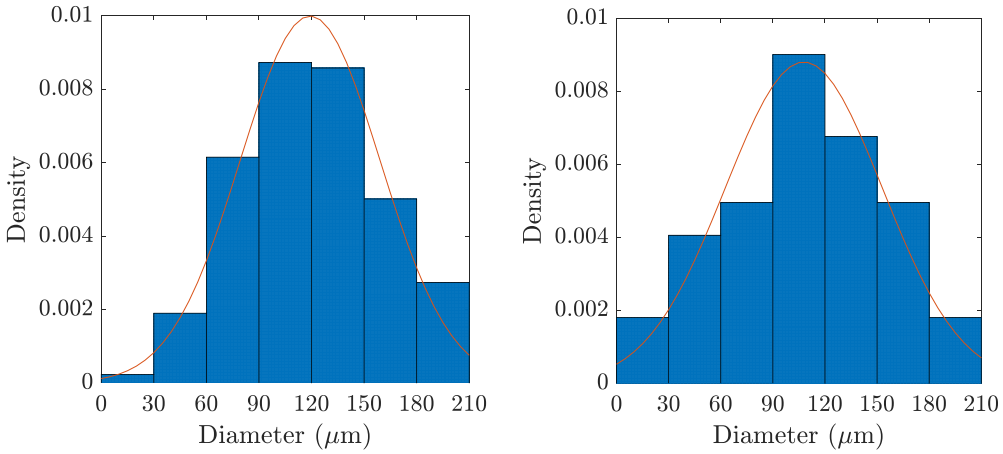

M5 M6

Figure 5.6. Density Histograms of Simulations

In Figure 5.6, the droplet size distribution of M5 and M6 are given on a probability density scale. The analysis with M5 provides a normal diameter distribution according to the Anderson-Darling goodness-of-fit hypothesis test with a p-value of 0.063. The mean diameter (D10) is 119.2 µm with a standart deviation of 39.9 µm. X and q parameters of Rosin-Rammler distributions are found as 139 µm and 3.2. Mean diameter of normal distribution reduces by 10% to 107.8 µm in M6, and the

standart deviation increases by 5 μm with a p-value of 0.068. In other words, the minimum mesh cell sizes of 40 μm and 30 μm give compatible results, as will be also demonstrated in the velocity comparisons in the next section.

5.2.1.5. Comparison of Velocity Distributions

Figure 5.7 shows the velocity distributions along Line 1 and Line 2 that were denoted in Figure 5.1. Both of these lines reside inside the liquid volume, with Line 1 having a length of 2 mm and Line 2 a length of 1.3 mm. Figure 5.7a shows the distribution of the velocity magnitude along the line passing through the stagnation point, Line 1, which has the highest local pressure in the liquid sheet. As mentioned before, this line passes through approximately 1 mm above the impingement point in the current study, but it should be noted that this value in Study 1 is not known. In Figure 5.7a, results from all cases in the current study are somewhat in agreement with Study 1 at the center. However, the discrepancy between Study 1 and the cases M5 and M6 draw apart away from the center. This is also observed in the comparison of the z-component of the velocity along Line 1 given in Figure 5.7b. The coarse meshes give a very close result to that of Study 1. This is not unexpected considering the relatively coarse mesh used in the mentioned study. In both comparisons, M5 and M6 show very close velocity distributions to one another along the line. Figure 5.7c and Figure 5.7d present the velocity magnitude and the velocity component in z direction along Line 2, which passes through the impingement point. Due to the impact of the two jets, the velocity magnitude decreases around the impingement point staying between 22 and 25 m/s around the center for all cases, but differences between them become more apparent away from the center. It seems that the velocity magnitude distributions predicted by current analyses are in better agreement with Study 2 than with Study 1, while Study 1 does not seem to properly capture the general trends. M5 differs by 8.8% on average from Study 2, while this value is reduced by half with M6. On the other hand, unlike the velocity distribution, the velocity component in z direction for all cases agree with

those from both of the studies with a maximum deviation of 5 m/s. Velocity in the z-direction is almost equal to zero at the center, which seems to be underpredicted by Study 2, and increases further away from the center.

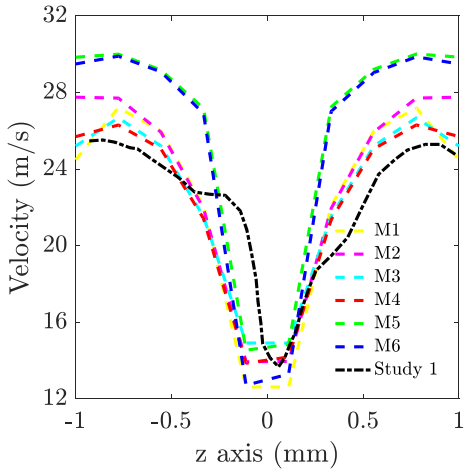

a) Velocity Magnitude Along Line 1

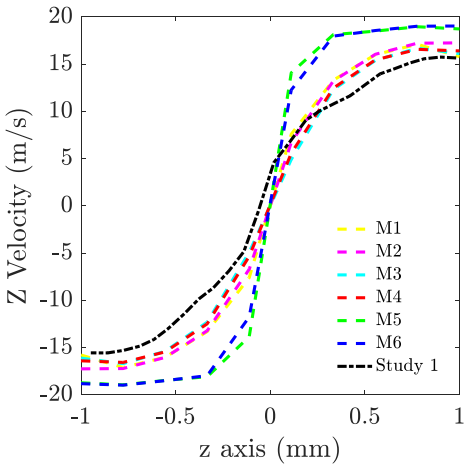

b) Z Velocity Along Line 1

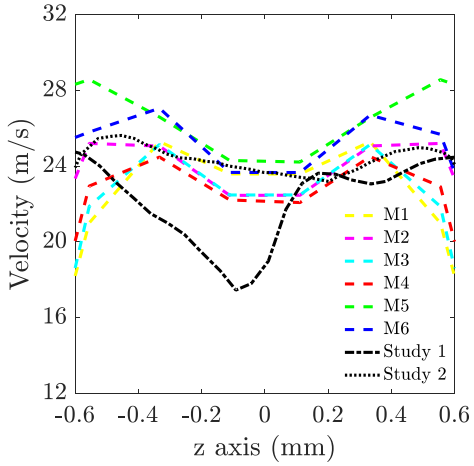

c) Velocity Magnitude Along Line 2

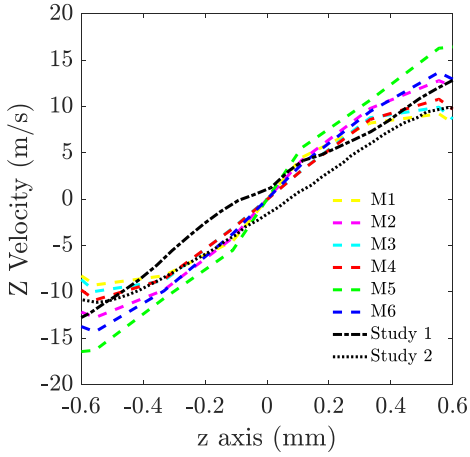

d) Z Velocity Along Line 2

Figure 5.7. Comparison of Velocity Distributions With Study 1 (Zheng, Nie, Feng, and Wu, 2015) and Study 2 (Balasubramanian, Kumar, Nakod, Schütze, and Rajan, 2020)

Since there is no experimental data available for velocity distributions, the deviations among current computations and these reference studies are considered to be a result

of the differences in the meshes, methods, and the turbulence models used in those studies. Although the CLSVOF method was used in Study 1 (Zheng, Nie, Feng, and Wu, 2015) similar to the current study, the AMR was not applied. The total number of mesh cells used was 2.1 millions, which is much less than the corresponding number of mesh cells of 4.9 and 8.4 millions for M5 and M6 used in this study, respectively, with the use of AMR. There is also no information provided on the turbulence model used in that study. On the other hand, in Study 2 (Balasubramanian, Kumar, Nakod, Schütze, and Rajan, 2020), the VOF-DPM method with the AMR is used for the analysis that had a minimum cell size of 20 µm, and a hybrid Reynolds-Averaged Navier-Stokes (RANS) with Large Eddy Simulation (LES) turbulence model was implemented. Despite all these discrepancies, these findings present additional insight and provide useful data to be used in comparisons in future studies.

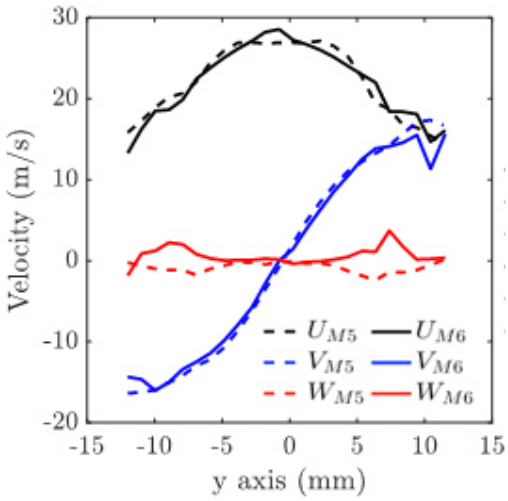

Figure 5.8. Comparison of Velocity Distributions at x=20 mm With M5 and M6

In Figure 5.8Figure 5.14, the comparison of velocity variation inside the liquid sheet at 20 mm below the impingement point along y-axis is given. U, V, and W are the velocity components in x, y, and z directions, respectively. Similar trends are observed for velocity distributions in both cases. The average percentage of

difference between the two is 5.2% for the U component, and is calculated as 13.5% for the V component due to lower velocity levels observed.

5.2.2. Validation Study 2

For this case, another computational domain is modeled that resembles that of the first validation case, but reflects the geometric dimensions used in the experiments of Anderson et al. (Anderson, Ryan, Santoro, and Hewitt, 1995). It has an orifice diameter of 0.635 mm, a pre-impingement length of 25.4 mm, an orifice length-to-diameter ratio of 80, and an impingement angle of 60°. The distance from the impingement point to the bottom of the domain is 28 mm. The height of the meshed volume is 57 mm from tip to bottom, and extends by 30 mm in lateral directions. Including the full length of the orifices, the overall dimensions of the computational domain becomes 77 mm x 95 mm x 30 mm in x, y, and z directions, respectively. The working fluid in this case is also water. Instead of mass flow rate, a jet velocity of 18.5 m/s is defined at each orifice inlet in order to match the experimental test setup. Computations are performed with the same methods and techniques described in the first case. The schematic of the computational domain is given Figure 5.9.

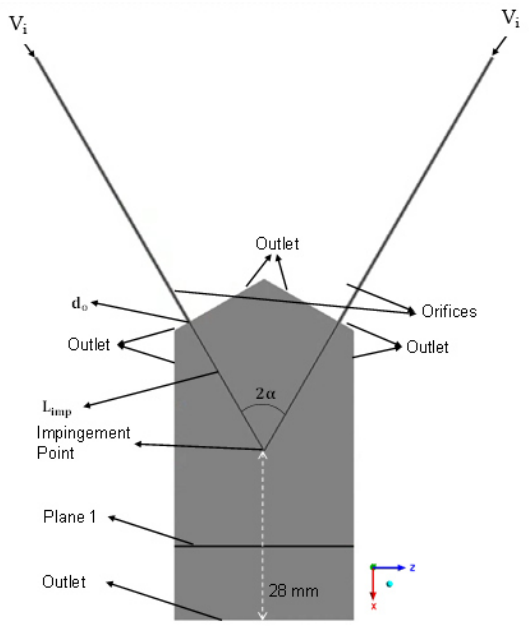

Figure 5.9. The Cross-section of the Computational Domain

5.2.2.1. Use of Adaptive Mesh Refinement (AMR)

A five-level adaptive mesh is used in the liquid volume for all analyses. This time, taking into account the findings of the previous study, the mesh sensitivity study is limited to three minimum cell sizes, being 50, 40, and 30 μm denoted by the analyses M4, M5, and M6, respectively, to be consistent with the nomenclature used in the first validation. In Table 5.4, the initial number of nodes and the final number of nodes at t=4.5 ms is given for each case. Comparing the number of nodes for the intermediate mesh (M5) and the fine mesh (M6), a significant reduction is obvious.

Table 5.4. Number of Nodes for Each Case Used in Mesh Sensitivity

	M4	**M5**	**M6**
Minimum Cell Size	50 μm	40 μm	30 μm
Initial Number of Nodes - AMR	678885	1232235	2504172
Final Number of Nodes - AMR	2037678	2948089	6821037
Total Number of Nodes - Uniform Mesh	479684966	934007872	2213867670

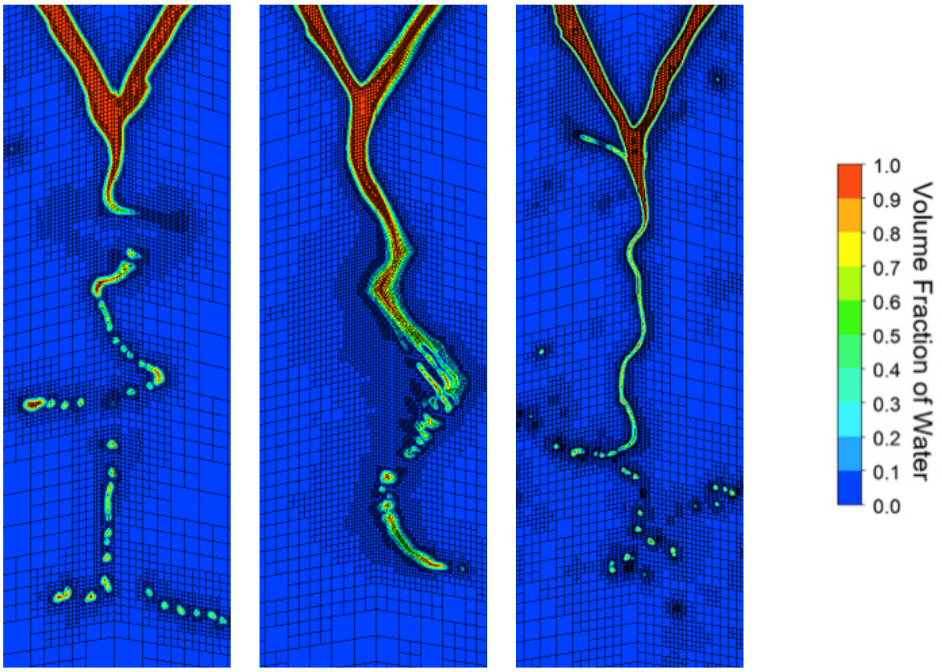

M4 M5 M6

Figure 5.10. Blow-up View of Cross-Section of the Fluid Volumes With Meshes at t=4.5 ms in Validation 2

In the same manner, inner iterations were repeated until the mass, momentum, k-ω and LS function residuals were reduced to level of around 0.001. The average percentage of differences in the predicted velocity magnitudes along the spray centerline in x direction is calculated as 3.5% between M4 and M5, and 6.1% between M5 and M6 given the larger difference between these two mesh sizes. Figure 5.10 shows the blown-up cross-sectional views of all three meshes at t=4.5 ms.

5.2.2.2. Comparison of Droplet Size

The experimental data used in the comparison given in Figure 5.11 were obtained by Anderson et al. (Anderson, Ryan, Santoro, and Hewitt, 1995) along the spray centerline at 41 mm downstream of the impingement point. The droplet size was

measured in terms of the arithmetic mean diameter (D10). Since the distance between the impingement point and the bottom of the domain in the current study is 28 mm, the results are collected at a plane 16 mm downstream of the impingement point instead.

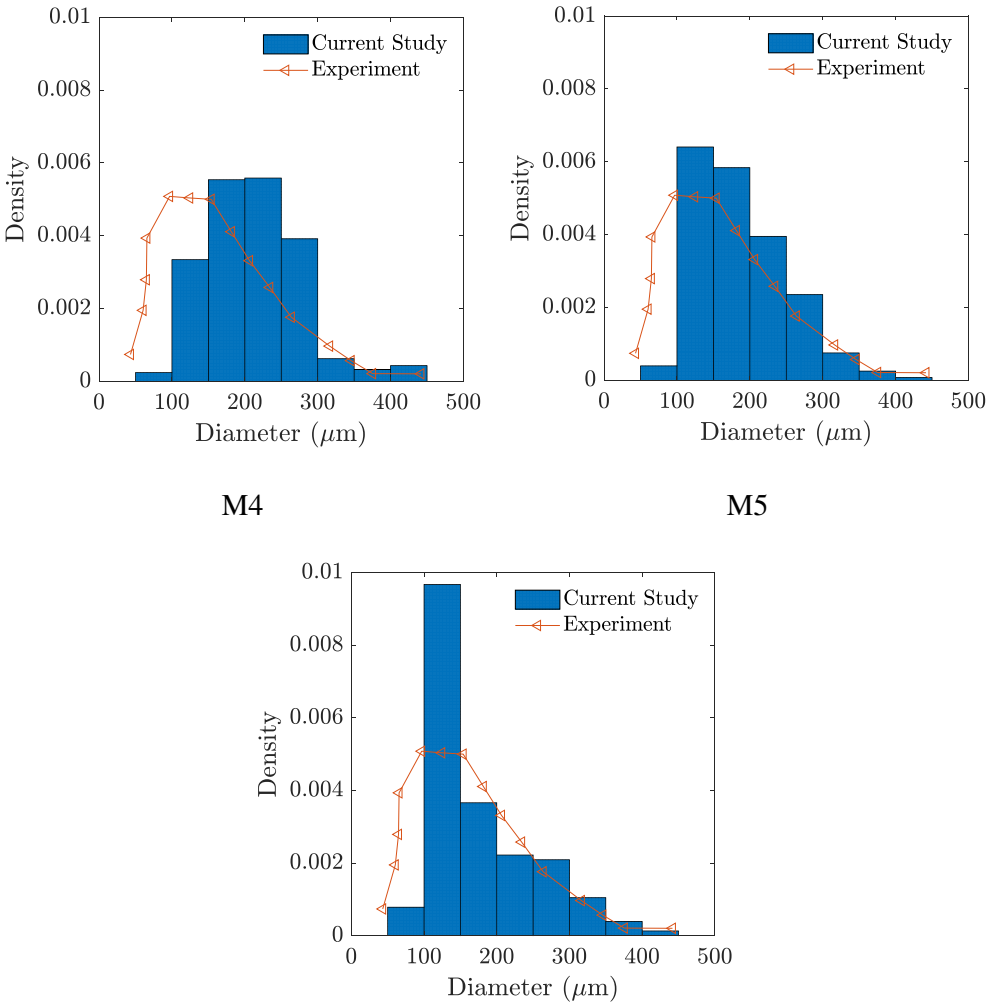

Figure 5.11. Comparison of Droplet Size Distributions of Meshes Used in Validation 2 With Experimental Data of Anderson et al. (Anderson, Ryan, Santoro, and Hewitt, 1995)

Arienti et al. (Arienti, Li, Soteriou, Eckett, Sussman, and Jensen, 2013) performed a similar comparison with the same experimental data at the same locations, and stated that the time-averaged diameter distributions do not change between the two planes. Hence, the droplet size distribution of D10 is compared with the computation results as given in Figure 5.11 where the histogram bars show the result of each analysis and the orange curve shows the experimental data.

Table 5.5. Comparison of D10 Results With Experimental Data of Anderson et al. (Anderson, Ryan, Pal, and Santoro, 1992)

	Experiment	**M4**	**M5**	**M6**
D10 (μm)	182.3	212.2	185.3	172
Difference (%)		16.4	1.6	5.7

Arienti et al. (Arienti, Li, Soteriou, Eckett, Sussman, and Jensen, 2013) performed a similar comparison with the same experimental data at the same locations, and stated that the time-averaged diameter distributions do not change between the two planes. Hence, the droplet size distribution of D10 is compared with the computation results as given in Figure 5.11 where the histogram bars show the result of each analysis and the orange curve shows the experimental data.

Table 5.5 shows the comparison of the mean droplet diameter (D10) predicted in simulations with the experimental data given in the study of Anderson et al. (Anderson, Ryan, Pal, and Santoro, 1992). Both the experimental and the numerical values shown in Table 4 were acquired at 16 mm below the impingement point. In the current study, an average of the droplet diameters was calculated using the time intervals between when the first droplet passes through the considered plane and the end of an analysis. The percentage differences given are calculated with respect to the experimental data. The accuracy of the predictions clearly improves in

simulations M5 and M6 compared to M4. Also, the Rosin-Rammler distribution constants, X and q are found as 180 µm and 3.46, respectively.

In summary, findings show that the CLSVOF method with the AMR technique can be considered to simulate the atomization process of impinging jets in doublet injectors with reasonable accuracy. A minimum cell size of 40 µm is found to provide reasonable accuracy with an acceptable computational cost. Therefore, triplet and pentad simulations given in the following sections were performed by using a mesh with minimum cell sizes of 40 µm.

5.3. Triplet Analysis

A triplet injector simulation is conducted with the inputs given in Table 5.6. The schematic of the cross-section of the resultant spray in the computational domain is given in Figure 5.12. Water is used as the working fluid in a triplet injector with an impingement angle, 2α, of 60°. The density and viscosity of the water are already defined as 998.2 kg/m3 and 0.001003 kg/ms in Fluent. The surface tension between water and air is defined as 0.0725 N/m. The mean Re and We are calculated as 19904 and 5507, respectively.

Table 5.6. Inputs of the Analysis

Velocity inlet of each orifice	20 m/s
Pressure outlet of domain	1 atm
Density of water	998.2 kg/m^3
Viscosity of water	0.001003 kg/m-s
Surface tension between water and air	0.0725 N/m

A velocity boundary condition of 20 m/s is applied at the inlet of each orifice having a diameter, d_o, of 1 mm. The pre-impingement length, L_{imp}, and orifice l/d ratio are defined as 5 mm. The surface normals of the inlet and exit of the orifices are

modeled to be perpendicular to the volume that the liquid jets are injected into, so that a normal velocity distribution along the orifices and a realistic liquid jet behavior with droplet formation at the exit of the orifices can be established. The domain is filled with air, and the ambient pressure boundary condition of 1 atm is defined at the outlet that is all the boundary surfaces other than the inlets and walls of the orifices. Wall boundary condition is applied along the orifices.

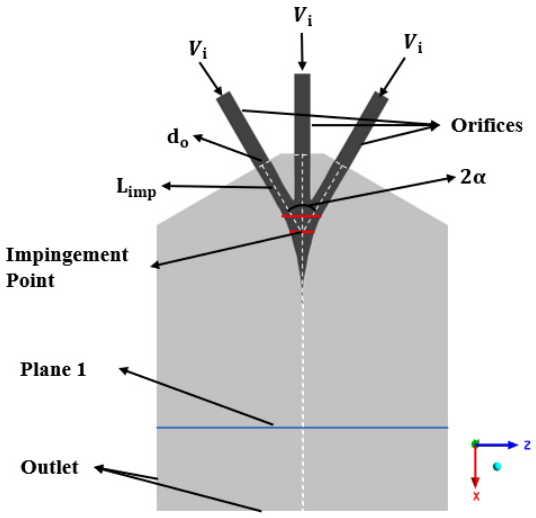

Figure 5.12. Cross-section of the Computational Domain

The computational domain is 45 mm x 100 mm x 40 mm in x, y and z directions, respectively. Because of the highly three-dimensional behavior of spray atomization, a three-dimensional analysis is conducted. The SMD measurements are performed at Plane 1, which is 15 mm away from the impingement point. The distance from the top of the domain and the impingement point is 10 mm. The bottom surface is 20 mm below Plane 1. The full length of the domain is not shown in the figure.

5.3.1.1. Use of Adaptive Mesh Refinement (AMR)

In Figure 5.13,the fluid volume of water is given at a cross-section of the domain along the direction of the flow at the time of around 1.6 milliseconds.

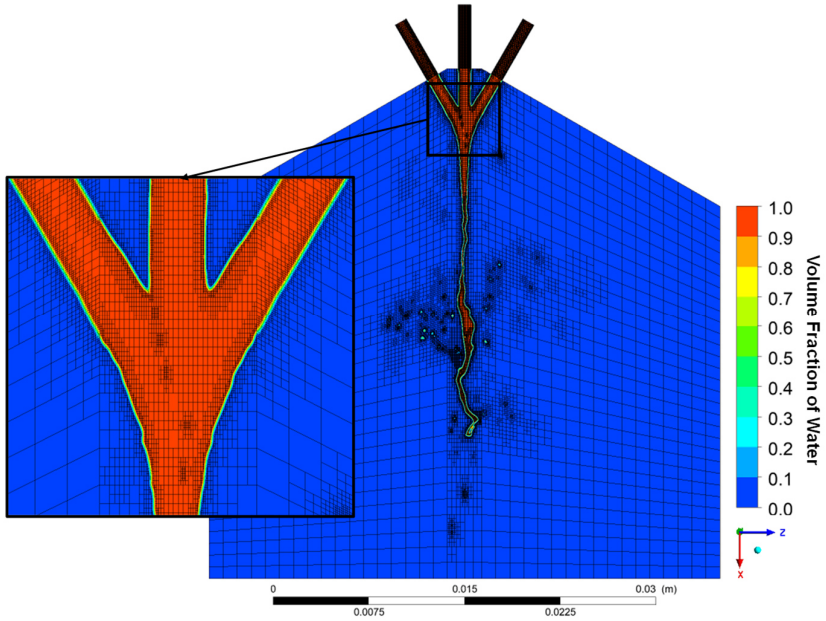

Figure 5.13. Cross-section of the Fluid Volume with Mesh

At this second, the number of nodes reaches 6 million. As it is seen in the figure, in the vicinity of the interface of water and air, the cell sizes become smaller and merge at the center of the spray reducing the overall number of nodes. Due to the impact of liquid jets, the mixing of these jets propagates in both axial and lateral directions until it breaks into ligaments because of the surface waves and forms a thin liquid sheet under the impingement point. The current simulation enables to resolve the liquid sheet good enough to capture the fluctuations on the surface of the sheet by using the adaptive mesh technique that allows to conduct the simulation with the smallest number of nodes possible.

5.3.1.2. Snapshots of Spray View with respect to Time

In Figure 5.14, the simulation of the spray evolution of the triplet injector is given with respect to time.

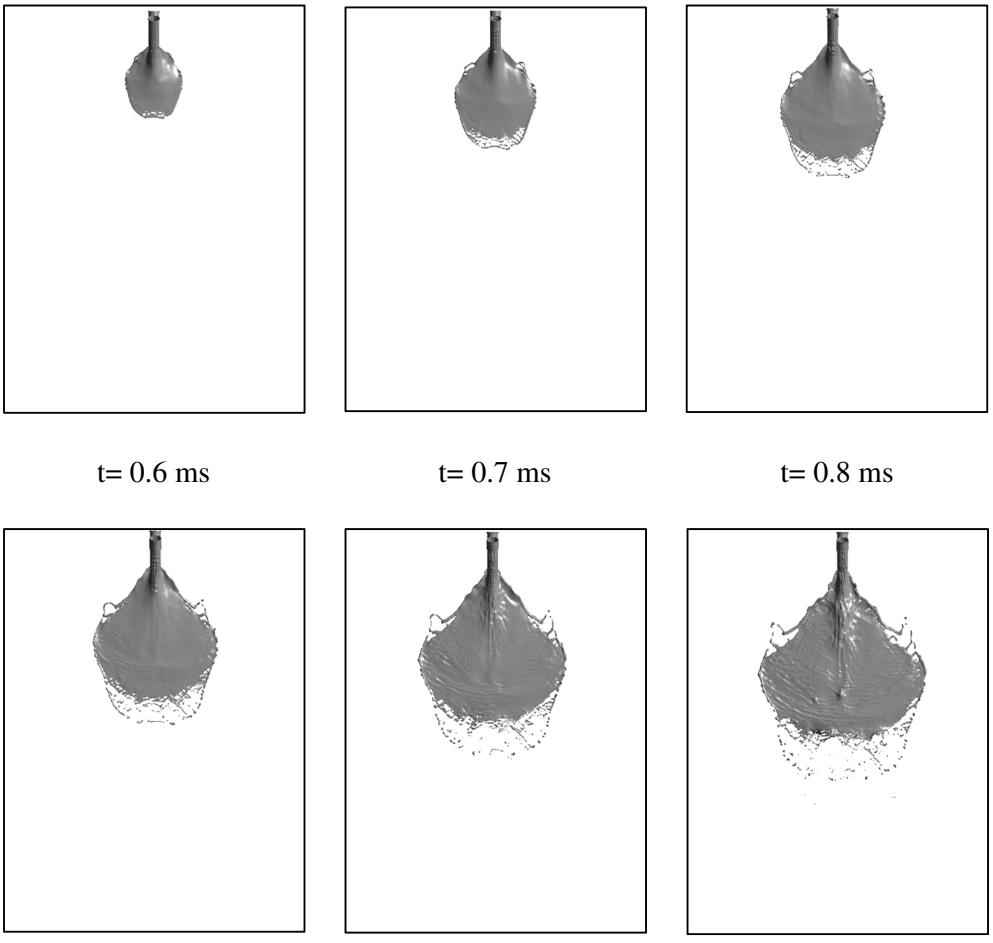

t= 0.6 ms t= 0.7 ms t= 0.8 ms

t= 0.9 ms t= 1.0 ms t= 1.1 ms

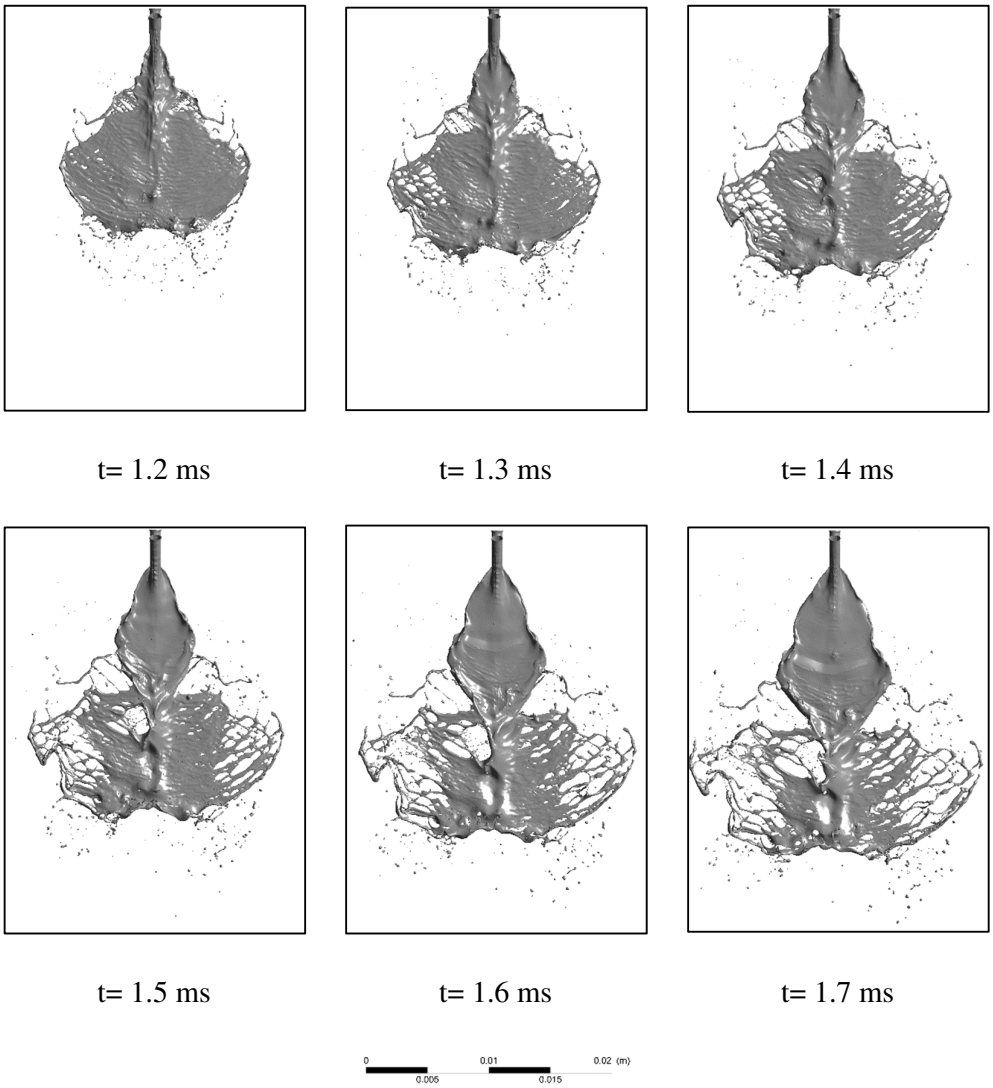

Figure 5.14. Spray Evolution with respect to Time

Fluctuations in the liquid core and small droplets exist even at 0.6 ms. Holes at the tip of the liquid sheet result in small droplets. The oscillations started at 0.7 ms results into larger holes that grows until 1.7 ms. During this evolution of the spray, a drastic change in the spray width is observed.

5.3.1.3. Comparison of Droplet Size

Droplets passing through Plane 1 are used for the comparison of the mean droplet size and Sauter mean diameter (SMD) calculations obtained with the numerical simulation and experimental data from the test T601055 with MR=1.99. In addition to the PDA measurements performed at 30 mm below the impingement point, another data set was obtained at 15 mm to be used in this CFD comparison. Due to long duration of the CFD runs, the analyses were initiated before the experimental data were obtained, hence, the inlet velocity through each orifice slightly differs from 20 m/s. Table 5.7 presents the values from both experimental and numerical studies. In calculations, droplets at time intervals between t=1.2 ms and t=1.7 ms were considered. The difference between the simulation result and experimental data is found by using Equation *(76)*.

$$Difference = \frac{abs(D_{experiment} - D_{simulation})}{D_{experiment}} \times 100 \qquad (76)$$

Table 5.7. Comparison of Droplet Statistics

	D_{10} (μm)	D_{32} (μm)
Experimental Data	44.3	69
Numerical Result	44.4	73.0
Difference %	0.2	5.8

As it is seen in Table 5.7, the difference between the simulation result and experimental data in terms of the mean droplet size and SMD is 0.2% and 5.8%, respectively. This result shows that the numerical technique used in the simulation provides reasonable accuracy in the investigation of droplet distributions.

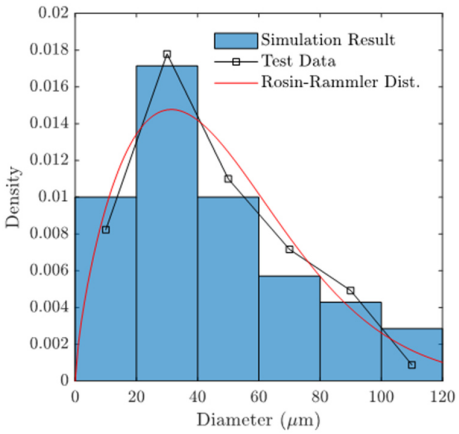

Figure 5.15. Density Histograms of Diameter of Droplets

Figure 5.15 shows the density histograms of the droplet diameter with the experimental data and numerical result on Plane 1. It should be noted that the largest droplet size measured by the PDA system used in the current study is limited to 103.7 µm, therefore, the droplets evaluated in the analysis are restricted in the same manner. The red curve given in Figure 5.15 represents the Rosin-Rammler distribution for the experiment. The distribution constants for the experiment is found to be 47.8 µm for X and 1.8 for q. According to simulation results, X and q are calculated as 52.9 µm and 1.7, respectively.

5.3.1.4. Comparison of Velocity Distributions

Figure 5.16 shows the velocity distributions of experimental data and numerical results. In obtaining this graph, the droplets are averaged along the y-axis at intervals, with each location spanning a distance of ± 1 mm, since the droplets did not pass through all of the points in between along the y-axis. Also, it is seen that away from the center, the calculated axial velocity reduces with a sharp drop compared to the experimental data. This shows that the spray will enlarge along the y-axis more. It is seen that the deviation in the axial velocities between the experiment and the simulation is around 5 m/s at the center. It should be noted that the representative numerical result was found by averaging several droplets, which

might be also contributing to this difference. However, it is seen that similar trends can be obtained. Along the majority of the y-axis, the V and W velocities are in agreement with the experimental data in terms of distribution trends and magnitude.

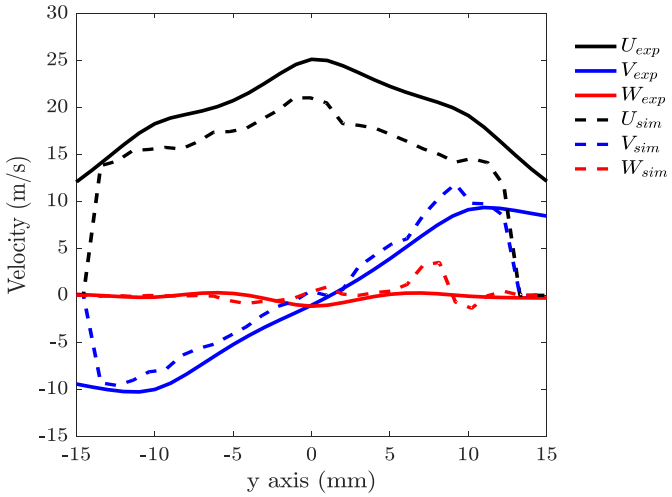

Figure 5.16. Comparison of Velocity Distributions of Experimental Data and Numerical Results

5.3.1.5. Comparison of Snapshots from Simulation and High-Speed Camera

In Figure 5.17, the snapshot of the isosurface of volume fraction of liquid phase at t=1.7 ms is compared to the snapshot of the spray taken by the high-speed camera. The breakup of the liquid sheet starts at the edges on both snapshots as a result of the oscillations on the boundaries. On contrary to the simulation of the like doublet done by Balasubramanian et al. (Balasubramanian, Kumar, Nakod, Schütze, and Rajan, 2020), in the current simulation, holes on the liquid core are not observed since the liquid sheet is relatively thick due to the central jets compared to the doublets. Instead, at around 11 mm away from the impingement point as shown with the red line, the liquid sheet becomes thinner and holes start to appear on the sheet. The blue line shows the measurement plane located at 15 mm below the impingement point. Although the formation of ligaments starts as soon as the breakup of the liquid sheet

starts, the full separation of the ligaments are obtained neither in the simulation nor in the snapshot taken by the high-speed camera. The axial momentum of the resultant spray increases while the lateral momentum that causes the impact waves does not change as much. Hence, the effect of impact waves on the liquid sheet reduces and the liquid sheet keeps its integrity, especially at the center where the central jet is directly injected. As moved away from the center, the formation of the holes, ligaments and droplets are observed similar to the doublet case analyzed by Balasubramanian et al. (Balasubramanian, Kumar, Nakod, Schütze, and Rajan, 2020).

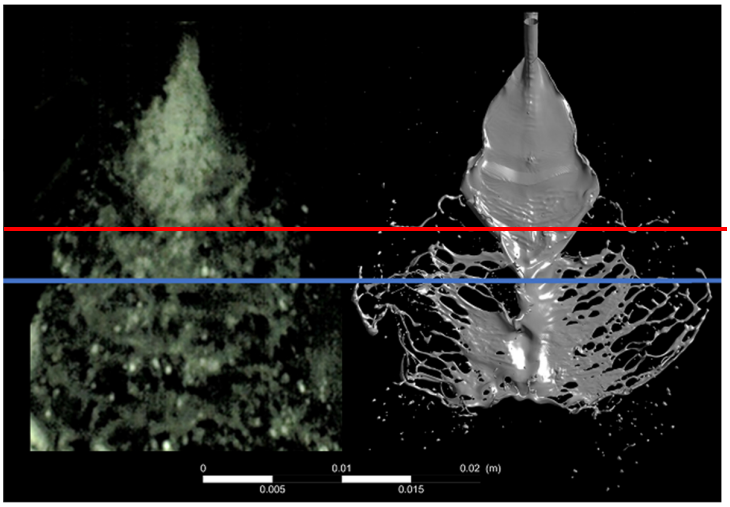

Figure 5.17. Comparison of the Snapshots Taken From the Simulation and Video Captured by High-Speed Camera

5.4. Pentad Analysis

In this section, a simulation with a pentad injector is performed with the same inputs used for the triplet injector given in Table 5.8. The schematic of the cross-section of the resultant spray in the computational domain is given in Figure 5.18. Water is used as the working fluid in a pentad injector with an impingement angle, 2α, of 60°.

The density and viscosity of the water are already defined as 998.2 kg/m3 and 0.001003 kg/ms in Fluent. The surface tension between water and air is defined as 0.0725 N/m. The mean Re and We are calculated as 19904 and 5507, respectively. A velocity boundary condition of 20 m/s is applied at the inlet of each orifice having a diameter, d_o, of 1 mm. The pre-impingement length, L_{imp}, and orifice l/d ratio are defined as 5 mm. The surface normals of the inlet and exit of the orifices are modeled to be perpendicular to the volume that the liquid jets are injected into, so that a normal velocity distribution along the orifices and a realistic liquid jet behavior with droplet formation at the exit of the orifices can be established. The domain is filled with air, and the ambient pressure boundary condition of 1 atm is defined at the outlet that is all the boundary surfaces other than the inlets and walls of the orifices. Wall boundary condition is applied along the orifices.

Table 5.8. Inputs of the Analysis

Velocity inlet of each orifice	20 m/s
Pressure outlet of domain	1 atm
Density of water	998.2 kg/m^3
Viscosity of water	0.001003 kg/m-s
Surface tension between water and air	0.0725 N/m

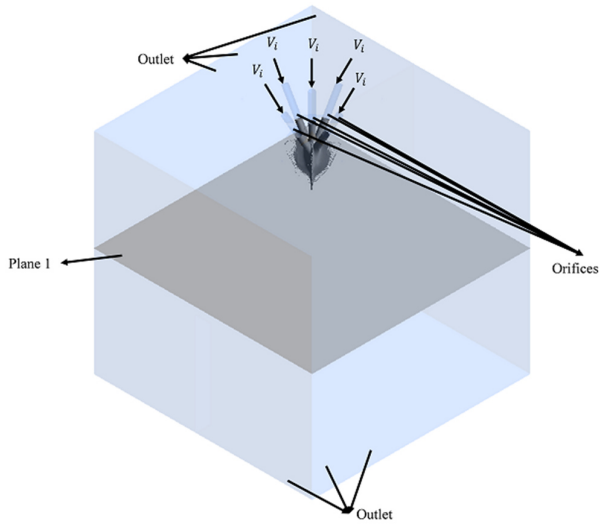

Figure 5.18. Cross-Section View of Computational Domain

The computational domain is modeled similarly, with additional inlets to replicate the injector configuration. Its dimensions are 45 mm x 40 mm x 40 mm in x, y and z directions, respectively. Because of the highly three-dimensional behavior of spray atomization, a three-dimensional analysis is conducted. The SMD measurements are performed at Plane 1, which is 15 mm away from the impingement point. The distance from the top of the domain and the impingement point is 10 mm. The bottom surface is 20 mm below Plane 1.

5.4.1.1. Use of Adaptive Mesh Refinement (AMR)

In Figure 5.19, the fluid volume of water is given at a cross-section of the domain along the direction of the flow at the time of around 1.33 milliseconds.

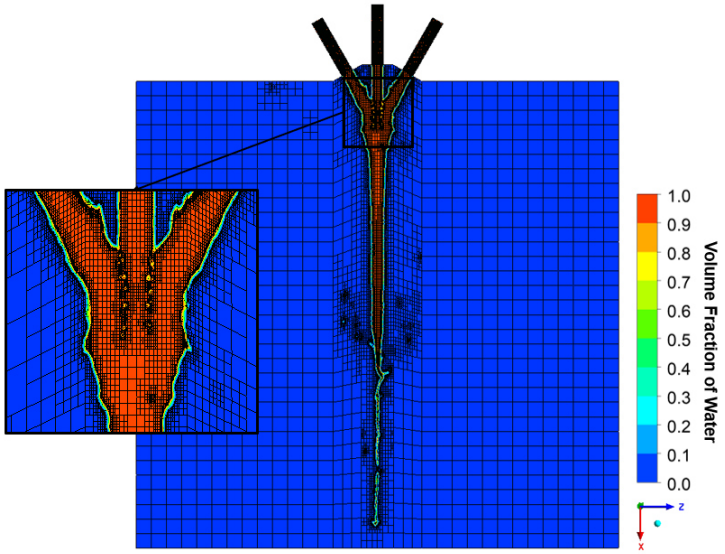

Figure 5.19. Cross-section of the Fluid Volume with Mesh

At this second, the number of nodes reaches 6.8 millions. Similar to the previous findings, in the vicinity of the interface of water and air, the cell sizes become smaller and merge at the center of the spray reducing the overall number of nodes. Due to the impact of four outer liquid jets, the mixing of these jets propagates in the axial direction and also at 45° angles to the orifices in the lateral directions. Then, the liquid sheet breaks into ligaments because of the surface waves and forms a thin liquid sheet. This time, the atomization starts at a plane that is very close to the orifices because the liquid sheet is very thick along the axial direction due to the increased overall mass flow rate, however, it becomes thinner on the lateral direction quickly. Thus, the successive break up of the liquid sheet starts at those regions. The current simulation enables to resolve the liquid sheet at a reasonable level to capture the fluctuations on the surface of the sheet by using the adaptive mesh technique that allows to conduct the simulation with the smallest number of nodes possible.

5.4.1.2. Snapshots of Spray View with respect to Time

In Figure 5.20, the simulation of the spray evolution of the pentad injector is given with respect to time.

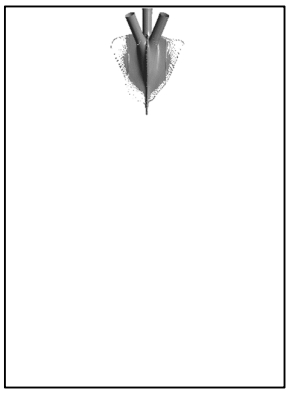

t= 0.60 ms

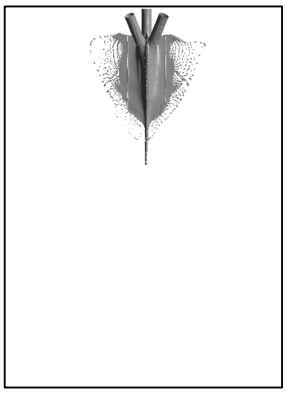

t= 0.72 ms

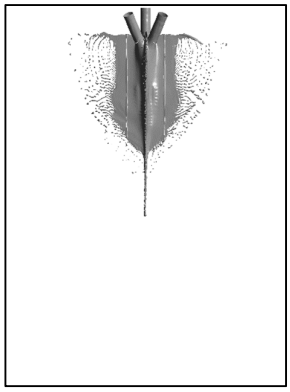

t= 0.86 ms

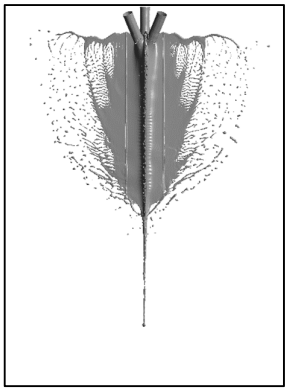

t= 1.17 ms

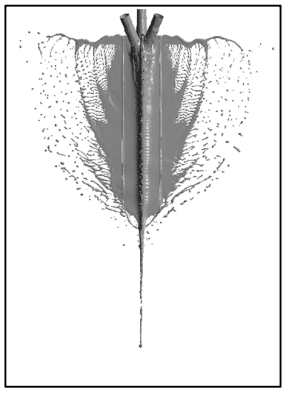

t= 1.23 ms

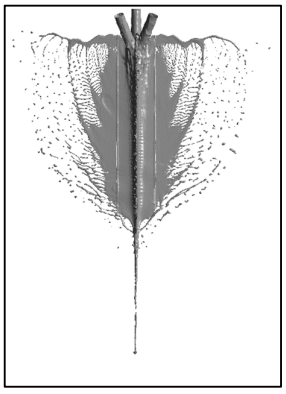

t= 1.25 ms

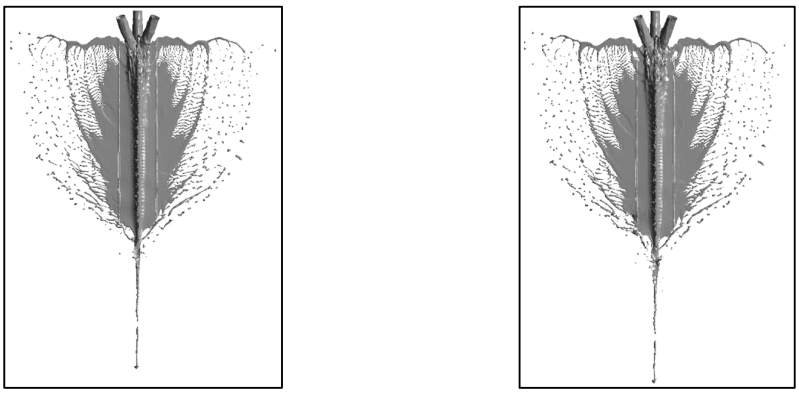

t= 1.28 ms t= 1.33 ms

Figure 5.20. Spray Evolution with respect to Time

The atomized droplets exist even at 0.6 ms in the lateral directions. As it is seen, the liquid sheet keeps it volume until 1.17 ms without any breakups in the axial direction. Although the spray moves faster in the axial direction, the atomization starts earlier in the lateral direction as a result of the increased lateral momentum and perpendicular orientation of the outer orifices. Ligaments formation is observed at t=1.17 ms and the new ones are formed until the end of the simulation.

5.4.1.3. Comparison of Droplet Size

The droplets passing through Plane 1 are used for comparison of the mean droplet size and Sauter mean diameter (SMD) calculations obtained with numerical simulation and experimental data from the test P601055 with MR=4.17. As in the case of T601055 test, another data set was obtained at 15 mm below the impingement point for the test P601055 as well to be used in this CFD comparison. Since the analyses were initiated before the experimental data were obtained, the inlet velocity through each orifice differs only by a small percentage from 20 m/s. Table 5.9 presents the values from both experimental and numerical studies. In calculations, droplets at time intervals between t=1.2 ms and t=1.3 ms were considered.

Table 5.9. Comparison of Droplet Statistics

	D_{10} (μm)	D_{32} (μm)
Experimental Data	49.4	71.3
Numerical Result	53.4	72.6
Difference %	8.1	1.8

As it is seen in Table 5.9 the difference between the simulation result and experimental data in terms of mean droplet size and SMD is 8.1% and 1.8%, respectively.

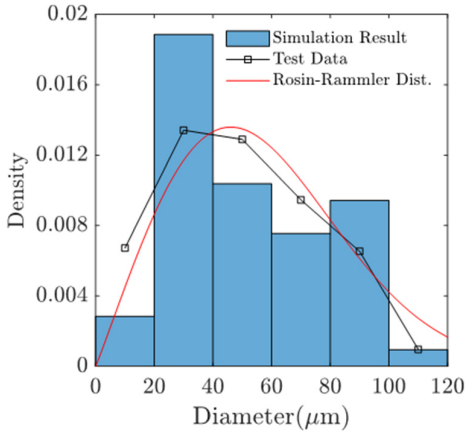

Figure 5.21. Density Histograms of Diameter of Droplets

Figure 5.21 shows the comparison of the droplet diameter with experimental data and numerical result on plane 1. Due to the previously mentioned limitation of droplet size measurements obtained by the PDA system to 103.7 µm, the droplets evaluated in the analysis are restricted in the same manner. In the figure, it is seen that there is a deviation between numerical result and the test data. Due to limited number of droplet data obtained in the simulation, the difference between the two distributions is greater compared to that observed in the triplet case. The red curve given in Figure 5.21 represents the Rosin-Rammler distribution for the experiment. The distribution constants for the experiment is found to be 64 µm for X and 2 for q.

According to simulation results, X and q are calculated as 59.3 μm and 2.1, respectively.

CHAPTER 6

CONCLUSION

In this thesis, the spray characteristics of triplet and pentad types of impinging injectors were examined through a series of experiments and numerical simulations. The parameters selected for analyzing spray characteristics are the impingement distance of the injector, l/d ratio of the orifices, diameter of orifices, impingement angle of the injector and momentum ratio of the propellants.

Experiments on triplet injectors showed that smaller orifice diameter enhances the uniformity of the mass flux distribution, increases the total droplet count and fineness of the mean droplet diameter. Also, an increase in the momentum ratio and impingement angle from 45° to 60° improves the uniformity of the mass flux distribution. Increase in the momentum ratio and impingement angle also increases the total droplet count. On the other hand, while the mean droplet diameter increases with impingement angle and momentum ratio at the 60° impingement angle, it is almost independent of the momentum ratio at the 90° impingement angle. Although the increase in the orifice l/d ratio decreases the mean droplet diameter, it increases uneven distribution of spray in addition to causing the reduction of the droplet count. Increasing the impingement distance slightly contributes to the uniformity of the distribution; however, it decreases the droplet count and coarsens the mean droplet diameter. Hence, for triplet injector design, the use of smallest orifice diameter, impingement distance and orifice l/d ratio with the highest impingement angle and momentum ratio could be suggested.

The same injector design parameters were investigated on the pentad injectors. Increase in momentum ratio enhances the uniformity of distribution with a small decrease in the normalized count. Impingement angle also contributes to the even distribution; however, it causes a significant reduction in the total normalized droplet count. Similar to triplets, smaller orifice diameter improves the droplet

count, mean diameter and mass flux distribution. Increasing the impingement distance and orifice l/d ratio both result in a decrease in the overall normalized droplet count. Increasing the impingement distance also decreases the uniformity of the mass flux distribution. Similar decrease in the uniformity is observed for the highest value of the orifice l/d ratio as well. Therefore, it could be suggested that the pentad injectors are designed with the smallest orifice diameter, impingement distance, orifice l/d ratio, impingement angle and with the highest momentum ratio.

The experimental results show that the fixed parameters may affect the results obtained with the selected design parameters. For example, the effect of an increase in the momentum ratio can change between two injectors with different impingement angles. This observation indicates that the number of tests should be increased in order to have a better understaning of spray characteristics. Also, it is seen that the SMD values can be altered considerably by only few parameters. This is because the droplet diameter obtained with the spray is highly dependent on the liquids that are used through the inner and outer orifices. In this research, the same liquid was used through both orifices. Hence, in order to understand the effect of the SMD, simulants with different density, viscosity and surface tension should be studied. The use of different simulants through the inner and outer orifices will also give a better understanding on the mixing mechanism.

In order to investigate the droplet statistics of injectors, a CLSVOF method with the AMR technique is used. At first, the selected numeric method is tested and validated with two different sets of experimental data from like-doublet impingement cases in the literature. It is seen that the droplet distributions can be obtained with reasonable accuracy by using this numerical technique with an affordable computational cost by means of the AMR technique. Also, the snapshots from the simulations are compared to the ones captured by the high-speed camera during the experiments. It is observed that the fundamental spray characteristics could be generally captured with the simulations.

In the second part of the numerical study, simulations were performed for the triplet and pentad injectors, and the results were compared to the experimental data obtained in this research. The numerical findings are in agreement with experimental data with reasonable accuracy. One observation is that in order to improve the droplet distribution results, the number of droplet count must be increased by increasing the simulation run time. Also, the numerical method can be further tested with other injector configurations and test cases. The use of different liquids in the simulations will also provide important insight to understanding of the spray characteristics of impinging injectors.

REFERENCES

Anderson, W. E., Ryan, H. M., Pal, S., and Santoro, R. J. (1992). Fundamental Studies of Impinging Liquid Jets. *30th Aerospace Sciences Meeting and Exhibit*. doi:10.2514/6.1992-458

Anderson, W. E., Ryan, H. M., Santoro, R. J., and Hewitt, R. A. (1995). Combustion Instability Mechanisms in Liquid Rocket Engines Using Impinging Jet Injectors. *31st Joint Propulsion Conference and Exhibit*. doi:10.2514/6.1995-2357

Arienti, M., Li, X., Soteriou, M. C., Eckett, C. A., Sussman, M., and Jensen, R. J. (2013). Coupled Level-Set/Volume-of-Fluid Method for Simulation of Injector Atomization. *Journal of Propulsion and Power*, *29*(1), pp. 147–157. https://doi.org/10.2514/1.b34198

Ashgriz, N., Brocklehurst, W., and Talley, D. (1995). On the Mixing Mechanisms in a Pair of Impinging Jets. 31st Joint Propulsion Conference and Exhibit. doi:10.2514/6.1995-2421

Ashgriz, N. (2016). Chapter 30: Impinging Jet Atomization. In *Handbook of Atomization and Sprays* (pp. 685-705). New York, NY: Springer.

Asihmin, V. I., Geller, Z. I., and Skobel'cyn, Y. A., Discharge of a Real Fluid From Cylindrical Orifices (in Russian), *Oil Ind.*, Vol 9, Moscow, 1961.

Atyam, D. M., and Sojka, P. E. (2017). Characterization of Direct Metal Laser Sintered Impinging Injectors: Like-Doublet, Unlike Triplet, Unlike Quadlet, Unlike Pentad. *53rd AIAA/SAE/ASEE Joint Propulsion Conference*. doi:10.2514/6.2017-4602

Balasubramanian, A. K., Kumar, V., Nakod, P., Schütze, J., and Rajan, A. (2020). Multiscale Modelling of a Doublet Injector Using Hybrid VOF-DPM Method. *AIAA Scitech 2020 Forum*. doi:10.2514/6.2020-2284

Bhatti, M. S. and Shah, R. K. (1987). "Turbulent and Transition Flow Convective Heat Transfer in Ducts." In Handbook of Single-Phase Convective Heat Transfer, ed. Kakaç, S., Shah, R. K. and Aung, W. New York: Wiley Interscience.

Cenik, B., Suer, T. U., and Uslu, S., (2019). Atomization and Combustion Characteristics of Impinging Injectors in Liquid Rocket Engines, *10th Ankara International Aerospace Conference, Ankara, Turkey, Sep 2019*

Chen, X., Ma, D., and Yang, V. (2012). Dynamics and Stability of Impinging Jets, *ILASS Americas, 24th Annual Conference on Liquid Atomization and Spray Systems, San Antonio, TX, May 2012*

Cho, Y., Lee, S., and Yoon, W. (2004). Orifice Diameter Ratio Effect on the Mixing Performances for Split Triplet Injectors. Journal of Propulsion and Power, 20(1), 69-75. doi:10.2514/1.918

Elverum, G. W., Jr., and Morey, T. F. (1959). *Criteria for Optimum Mixture-Ratio Distribution using Several Types of Impinging-Stream Injector Elements* (Memorandum No. 30-5). Pasadena, California: Jet Propulsion Laboratory, California Institute of Technology.

Ferrenberg, A., Hunt, K., and Duesberg, J. (1985). *Atomization and Mixing Study* (Rep. No. RI/RD85-312). Canoga Park, CA: Rockwell International, Rocketdyne Division.

Gill, G. S., and Nurick, W. H. (1976). *Liquid Rocket Engine Injectors* (pp. 2-18, Publication No. NASA SP-8089). Cleveland, Ohio: National Aeronautics and Space Administration.

Heidmann, M., & Humphrey, J. (1952). Fluctuations in a spray formed by two impinging jets. *Journal of the American Rocket Society*, *22*(3), 127–131. https://doi.org/10.2514/8.4445

Heidmann, M. F., Priem, R. J., and Humphrey, J. C. (1957). *A Study of Sprays Formed by Two Impinging Jets* (Rep. No. NACA TN 3835). Cleveland, Ohio: National Advisory Committee for Aeronautics.

Hines, W. S., Schuman, M. D., Ford, W. M., and Fertig, K. D. (1972). “Extension of a Thrust Chamber Compatibility Model,” Rocketdyne, Rep. No. AFRPL-TR-72-19, Canoga Park, CA.

Hoehn, F. W., Rupe, J. H., and Sotter, J. G. (1972). *Liquid-Phase Mixing of Bipropellant Doublets* (Rep. No. 32-1546). Pasadena, California: Jet Propulsion Laboratory, California Institute of Technology.

Huzel, D. K. and Huang, D. H. (1992). Chapter 4.5: Injector Design. In *Modern Engineering for Design of Liquid-Propellant Rocket Engines* (Vol. 147, pp. 105-115). SW, Washington DC: Amer. Inst.of Aeronautics & Astronautics.

Indiana, C., Bellenoue, M., and Boust, B. (2015). Experimental Investigations of Drop Size Distributions With Impinging Liquid Jets using Phase Doppler Anemometer. *International Journal of Energetic Materials and Chemical Propulsion, 14*(3), 241-264.

doi:10.1615/intjenergeticmaterialschemprop.2015011292

Inoue, C., Nozaki, K., Fujii, G., and Daimon, Y. (2017). Water Flow Diagnostics for Predicting Bi-Propellant Thruster Performance. 53rd AIAA/SAE/ASEE Joint Propulsion Conference. doi:10.2514/6.2017-4934

iX Cameras. (2020). ixCameras i-SPEED 716 High Speed Camera. https://www.ix-cameras.com/downloads/716-Datasheet.pdf (accessed August 26, 2021)

Jung, K., Lim, B., Yoon, Y., and Koo, J. (2005). Comparison of Mixing Characteristics of Unlike Triplet Injectors Using Optical Patternator. Journal of Propulsion and Power, 21(3), 442-449. doi:10.2514/1.12884

Jung, K., Khil, T., and Yoon, Y. (2006). Effects of Orifice Internal Flow on Breakup Characteristics of Like-Doublet Injectors. *Journal of Propulsion and Power, 22*(3), 653-660. doi:10.2514/1.20362

Kang, S., Lee, E., Kwon, K., Oh, J., and Yu, M. (2002). Twin Spray Characteristics Between Two Impinging F-O-O-F Type Injectors. *KSME International Journal, 16*(5), 732-742. doi:10.1007/bf03184823

Kiaoulias, D., Travis, T., Moore, J., and Risha, G. (2019). Evaluation of Orifice Inlet Geometries on Single Liquid Injectors Through Cold-Flow Experiments. *Experimental Thermal and Fluid Science, 103*, 78-88. doi:10.1016/j.expthermflusci.2019.01.009

Kline, S. J., and McClintock, F. A. (1953). "Describing Uncertainties in Single-Sample Experiments," *Mechanical Engineering*, Vol.75, no. 1, pp. 3-8.

Lai, W., Huang, W., and Chu, C. (2004). Atomization and Mixing Characteristics of an Unlike-Doublet Impinging-Jet. *International Journal of Turbo and Jet Engines, 21*(2). doi:10.1515/tjj.2004.21.2.127

Lichtarowicz, A., Duggins, R. K., and Markland, E., (1965). Discharge Coefficients for Incompressible Non-Cavitating Flow Through Long Orifices, *J. Mech. Eng. Sci.*, Vol. 7, No. 2, pp. 210–219.

Lefebvre, A. H. and McDonell, V. G. (2017). Chapter 3: Drop Size Distributions of Sprays. In *Atomization and Sprays* (pp. 55–70). CRC Press.

Mouis, A. G. F., Pal, S., and Santoro, R. J., (1995). Impinging Jet Injector Atomization Studies in a Rocket Environment. AIAA/ASME/SAE/ASEE Joint Propulsion Conference. Washington, D.C: AIAA. doi:10.2514/6.1995-2356

Nakayama, Y. (1961). Action of the Fluid in the Air Micrometer: First report, characteristics of small diameter nozzle and orifice, *Bull. Jpn. Soc. Mech. Eng.*, Vol. 4, pp. 516–524.

Nikon. AF-S DX NIKKOR 35mm f/1.8G. https://imaging.nikon.com/lineup/lens/f-mount/singlefocal/normal/af-s_dx_35mmf_18g/ (accessed August 26, 2021)

Rupe, J. H. (1953). *The Liquid-Phase Mixing of a Pair of Impinging Streams* (Rep. No. 20-195). Pasedana, California: Jet Propulsion Laboratory, California Institute of Technology.

Ryan, H., Anderson, W., Pal, S., and Santoro, R. (1993). Atomization Characteristics of Impinging Liquid Jets. *31st Aerospace Sciences Meeting*. doi:10.2514/6.1993-230

Sussman, M., Smith, K., Hussaini, M., Ohta, M., and Zhi-Wei, R. (2007). A Sharp Interface Method for Incompressible Two-Phase Flows. *Journal of Computational Physics, 221*(2), 469-505. doi:10.1016/j.jcp.2006.06.020

Sweeney, B. A., and Frederick, R. A. (2015). Experimental Study on the Effects of Varying the Impingement Distance of Like-Doublet Injectors. 51st AIAA/SAE/ASEE Joint Propulsion Conference. doi:10.2514/6.2015-3846

Sweeney, B. A., and Frederick, R. A. (2016). Jet Breakup Length to Impingement Distance Ratio for Like Doublet Injectors. *Journal of Propulsion and Power, 32*(6), 1516-1530. doi:10.2514/1.b36137

Tokina. Specifications. Tokina AT-X 24-70 F2.8 PRO FX (24-70mm f/2.8). https://tokinalens.com/product/at_x_24_70_f2_8_pro_fx/#specifications (accesses August 26, 2021)

Vassallo, P., Ashgriz, N., and Boorady, F. A. (1992). Effect of Flow Rate on the Spray Characteristics of Impinging Water Jets. Journal of Propulsion and Power, 8(5), 980-986. doi:10.2514/3.23582

Wang, Z. (2016). Chapter 2.4: Atomization Modeling for Liquid Rocket Engine Atomizers. In *Internal Combustion Processes of Liquid Rocket Engines* (pp. 59-75). Singapore: John Wiley & Sons Singapore Pte.

Won, Y. D., Cho, Y. H., Lee, S. W., and Yoon, W. S. (2002). Effect of Momentum Ratio on the Mixing Performance of Unlike Split Triplet Injectors. *Journal of Propulsion and Power, 18*(4), 847-854. doi:10.2514/2.6008

Xia, Y., Khezzar, L., Alshehhi, M., and Hardalupas, Y. (2017). Droplet Size and Velocity Characteristics of Water-Air Impinging Jet Atomizer. International Journal of Multiphase Flow, 94, 31-43.

doi:10.1016/j.ijmultiphaseflow.2017.04.014

Xia, Y., Khezzar, L., Alshehhi, M., and Hardalupas, Y. (2018). Atomization of Impinging Opposed Water Jets Interacting With an Air Jet. *Experimental Thermal and Fluid Science, 93*, 11-22.

doi:10.1016/j.expthermflusci.2017.12.010

Xia, Y., Khezzar, L., Bojanampati, S., and Molki, A. (2019). Breakup of the Water Sheet Formed by Two Liquid Impinging Jets. *International Journal of Chemical Engineering, 2019*. doi:https://doi.org/10.1155/2019/9514848

Zheng, G., Nie, W., Feng, S., and Wu, G. (2015). Numerical Simulation of the Atomization Process of a Like-Doublet Impinging Rocket Injector. Procedia Engineering, 99, 930-938. doi:10.1016/j.proeng.2014.12.624

Zhi-qing, W. (1982). "Study on Correction Coefficients of Laminar and Turbulent Entrance Region Effects in Round Pipes". Applied Mathematical Mechanics, 3. p. 433.